Karlsruhe Institute of Technology

Modeling and measurement of Rydberg-State mediated Background at the KATRIN Main Spectrometer

Zur Erlangung des akademischen Grades eines

Doktors der Naturwissenschaften

von der Fakultät für Physik

des Karlsruher Instituts für Technologie

genehmigte

DISSERTATION

von

Diplom Physiker Nikolaus Rainer-Maria Trost

aus Helmstedt

Erstgutachter:	Prof. Dr. G. Drexlin Institut für Experimentelle Teilchenphysik, KIT
Zweitgutachter:	Prof. Dr. U. Husemann Institut für Experimentelle Teilchenphysik, KIT

Tag der mündlichen Prüfung: 19. Oktober 2018

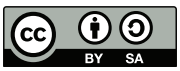

Hiermit versichere ich, dass ich die vorliegende Dissertationsschrift selbständig und nur unter Verwendung der angegebenen Quellen und Hilfsmittel verfasst habe.

Karlsruhe, 02.10.2018

Zusammenfassung

In der Teilchenphysik und Kosmologie kommt Neutrinos eine besondere Rolle zu: Obwohl sie die zahlenmäßig häufigsten (bekannten) Teilchen im Universum sind, sind ihre grundlegenden Eigenschaften am wenigsten genau bestimmt. Dies betrifft einerseits ihre Massen, für die es im Gegensatz zu allen anderen bekannten Teilchen bis heute nur eine Obergrenze von $\approx 2\mathrm{eV/c^2}$ gibt, und dies trotz der eindeutigen Evidenz für eine von Null verschiedene Masse, die sich aus der Beobachtung von Neutrinooszillationen ergibt. Andererseits ist auch die Frage, ob sie als Majorana-Teilchen ihre eigenen Antiteilchen sind oder nicht bisher offen – eine Frage, die sich für die anderen Teilchen des Standardmodells in der Art nicht stellt. Damit verknüpft ist die Frage, ob ihre im Vergleich zu den anderen Teilchen sehr geringe Masse nicht durch die Wechselwirkung mit dem Higgsfeld sondern auf andere Weise zu Stande kommt. In diesem Fall würde die Neutrinomasse ein Fenster zu Physik jenseits des Standardmodells bieten. Aufgrund ihrer Häufigkeit, ihrer geringen Wahrscheinlichkeit mit anderen Teilchen zu wechselwirken und ihrer endlichen Masse haben Neutrinos die Strukturbildung im Universum beeinflusst. Die absolute Massenskala von Neutrinos ist also für sehr unterschiedliche Bereiche der Physik von großm Interesse und hierin liegen der erhebliche Aufwand begründet, der derzeit zu ihrer Bestimmung unternommen wird - bereits eine Verbesserung der oberen Grenze wäre ein wichtiger Beitrag und deutlicher Fortschritt für die Kosmologie und Teilchenphysik.

Während mehrere Methoden zur Bestimmung der Neutrinomasse verfolgt werden, ist die hochpräzise Elektronenspektroskopie des Tritium-β-Spektrums diejenige, die sich durch die aktuell größte Sensitivität bei gleichzeitiger Modellunabhängigkeit auszeichnet. Weder die Natur der Neutrinomasse noch kosmologische Modelle beeinflussen das Ergebnis bei dieser Art der Bestimmung. Das Karlsruher Tritium Neutrino Experiment (KATRIN) treibt diese Methode an ihre technologische Grenze. Ziel des am Tritiumlabor Karlsruhe (TLK) am Campus Nord des Karlsruher Instituts für Technologie (KIT) befindlichen Experimentes ist die Neutrinomasse mit einer Sensitivität von 200 meV (90 % C.L.) zu messen. Diese wird durch eine fensterlose gasförmigen molekularen Tritiumquelle mit hoher Luminosität und ein großes hochauflösendes integrierendes Spektrometer nach MAC-E-Filter-Prinzip ermöglicht.

Die beim β-Zerfall des Tritium emittierten Elektronen werden aus der Quelle über

eine Länge von 70 m durch ein System von supraleitenden Solenoiden zum Detektor geführt. Das Spektrometer fungiert hierbei durch sein jeweils eingestelltes Retardierungspotential als Hochpassfilter für die Energie der Elektronen. Die Detektionswahrscheinlichkeit eines Signalelektrons gegebener Energie hängt hierbei von einer Vielzahl von Effekten und Parametern ab. Hierzu zählen unter anderem Energieverluste der Elektronen durch Streuung oder Synchrotronstrahlung und die durch elektrische und magnetische Felder bestimmten Filtereigenschaften des Spektrometers. Für eine genaue Bestimmung der Neutrinomasse ist es unerlässlich, dass diese Detektionswahrscheinlichkeit, die Antwortfunktion des Experiments und ihre Abhängigkeiten genau bekannt sind.

Entscheidend für das Erreichen der um einen Faktor 10 besseren Sensitivität im Vergleich zu Vorgängerexperimenten ist eine Reduktion der statistischen und systematischen Messunsicherheiten um den Faktor 100, da die tatsächliche Observable das Quadrat der Neutrinomasse ist. Unter der Vielzahl von zu berücksichtigenden experimentellen Effekten ist für die statistische Messunsicherheit – bei gleicher Luminosität – die Untergrundrate ausschlaggebend. Hier stellte sich jedoch bereits bei den ersten Messungen mit dem Hauptspektrometer heraus, dass der Untergrund wesentlich höher als erwartet war. Gemessene Raten von der Größenordnung 1 cps verfehlen das Designziel einer Rate von weniger als 10^{-2} cps um ein vielfaches. Dementsprechend war die Suche nach der Ursache des erhöhten Untergrunds von hoher Priorität bei den Testmessungen mit der Spektrometer-Detektor-Sektion. Auf der Seite der systematischen Messungenauigkeit ist einer der größten Effekte die Streuung der Signalelektronen in der Quelle. In Konsequenz sind diese beiden Effekte, die Elektronenstreuung in der Quelle und der Untergrund der Fokus dieser Arbeit. Für beide wurden verbesserte Modelle entwickelt. Im Fall der Elektronenstreuung an Wasserstoffmolekülen wurde dies durch die geeignete Kombination und extrapolation verfügbarer Daten erreicht. Im Fall des Untergrundes, der bei KATRIN vor allem im Haupspektrometer entsteht, konnten im Rahmen dieser Arbeit durch eine Vielzahl von Messungen alle bisher aus vergleichbaren Spektrometern bekannten Untergrundprozesse ausgeschlossen werden. Nach langer Suche konnten als Ursache durch α-Aktivität im Spektrometer gesputterte hochangeregte Rydbergatome identifiziert werden die im Vakuum durch thermische Strahlung ionisiert werden. Einzig durch diesen Prozess ist es möglich alle beobachteten Eigenschaften des Untergrundes auf einmal zu erklären. Die Berechnung und Simulation dieses Prozesses von den α-Zerfällen im Stahl der Apparatur, über das Sputtering oberflächennaher Atome, ihre Anregung in hohe Rydberg-Zustände hin zu ihrer Ionisation durch thermische Strahlung oder lokale elektrische Felder stellen den Kern dieser Arbeit dar. Mit ihrer Hilfe lassen sich Vorhersagen für die räumliche Verteilung des Untergrundes, seine zeitliche Struktur, seine Temperaturabhängigkeit und seine Reaktion auf das elektrische Feld an der Tankoberfläche ableiten. Diese Eigenschaften konnten auch in Messungen bestimmt werden. Deren Ergebnisse sind im Einklang mit den Berechnungen und ein konkurrierendes Modell konnte bisher nicht entwickelt werden. Es ist festzustellen das der Untergrund nur durch das Entfernen der ohnehin geringen Aktivität durch z.B. erneute Elektropolitur des Spektrometers völlig zu beseitigen wäre. Der Aufwand hierfür ist jedoch prohibitiv hoch und von ungewissem Erfolg. Daher wird die Unterdrückung der Untergrundrate

durch ein höheres Magnetfeld untersucht. Diese Methode ist in Verbindung mit einer optimierten Messzeitverteilung ausreichend um einen drastischen Verlust an Sensitivität auf die Neutrinomasse zu verhindern, wenn die dadurch erhöhte systematische Unsicherheit unter Kontrolle bleibt.

Aktuell befindet sich das Experiment in einer Phase umfangreicher Inbetriebnahmemessungen, bei denen eine Vielzahl von Eigenschaften des Apparats in situ bestimmt werden die für eine erfolgreiche Auswertung der folgenden Neutrinomassemessungen unabdingbar sind. In diesem Rahmen werden sich die hier entwickelten Modelle weiter bewähren müssen.

Introduction and Objectives

Within particle physics and cosmology neutrinos play a special role: Though they are by numbers the most frequent (known) particles in the universe, their basic properties are least known. On the one hand this concerns their masses for which until today only an upper bound of $\approx 2\mathrm{eV/c^2}$ is known – despite the unambiguous evidence for non-zero neutrino masses given by the observation of neutrino oscillations. On the other hand also the question if they are Majorana particles and as such their own anti-particles is open – a question which does not arise in the same way for the other particles of the Standard Model. Related to this is the question whether their very small masses compared to the other particles are not generated via interaction with the Higgs field but through a different mechanism. In this case the neutrino mass would offer a window to physics beyond the Standard Model. Because of their high abundance, their small interaction probability and their non-zero masses neutrinos influenced the structure formation in the Universe. The absolute mass scale of neutrinos is therefore of high interest for different branches of physics and therein lies the cause for the considerable effort that is undertaken to determine it. An improvement of the upper bound on the neutrino mass would already be an important contribution for cosmology and particle physics.

While several methods of neutrino mass determination are pursued at present the high precision electron spectroscopy of the tritium β spectrum is the one with the largest sensitivity which is also model independent. Neither the nature of the neutrino mass nor cosmological models influence the results of this method as it depends on kinematical properties of the neutrinos alone. The Karlsruhe Tritium Neutrino experiment (KATRIN) pushes this approach to the technological limit. Situated at the Tritium Laboratory Karlsruhe (TLK) at the Campus North of the Karlsruhe Institute of Technology (KIT) its target is to determine the neutrino mass with a sensitivity of 200 meV (90 % C.L.). This is made possibly through the use of a windowless gaseous molecular Tritium source combined with a large high resolution integrating spectrometer that is built according to the MAC-E-filter principle.

The electrons emitted from the β-decay of Tritium are guided from the source to the detector over a length of 70 m by means of a system of superconducting magnets. The Main Spectrometer functions as a high pass filter for the electrons, allowing only those to be transmitted that have energies equivalent to the retarding potential. Thereby an

integrated electron spectrum is measured. The detection probability of a signal electron with given energy depends on many effects and parameters. Thus it includes energy losses of the electrons by scattering or synchrotron radiation and the filter properties of the spectrometer that are governed by its electric and magnetic fields. For a precise determination of the neutrino mass an exact knowledge of this detection probability, which is the response function of the experiment and its dependencies, is mandatory.

For achieving a factor of 10 better sensitivity in comparison to previous experiments it is necessary to reduce statistical and systematic uncertainties by a factor of 100 as the observable is the squared neutrino mass m_ν^2. Among the various effects that influence the statistical uncertainty the background rate is the most dominant one at a given luminosity. Already the first measurements with the Main Spectrometer showed that the background was significantly higher than anticipated. Rates of the order of 1 cps exceeded the design limit of 10^{-2} cps by far. In consequence the search for the root cause of the elevated background was a high priority during the test measurements with the Main Spectrometer.

For the systematic uncertainty on the other hand one of the largest effects is the scattering of signal electrons inside the source. Consequently, these two effects, electron scattering in the source and background electrons from the Main Spectrometer are the focus of this work. For both models were developed. For the electron scattering this was achieved by combination and extrapolation of existing data. For the background which is almost entirely created within the Main Spectrometer all background processes known from similar spectrometers were excluded. After a long search the ionization of highly excited Rydberg atoms created by sputtering caused by α activity within the spectrometer was identified as cause of the background. Only this process is at present capable of reproducing all observed behavior simultaneously. The calculation and simulation of this process, starting from the α-decays within the steel of the apparatus to the sputtering of surface atoms caused by it, to the excitation of the sputtered atoms into high Rydberg states, their decay processes and finally to their ionization by thermal radiation or local electric fields is the core part of this thesis. With this model it is possible to make predictions about the spatial distribution, the time structure, the temperature dependence and the dependence on local electric fields of the background. These properties were also measured during the commissioning campaign of the spectrometer. The results are in agreement with the calculations and a competitive model could so far not be devised. As a consequence it has to be stated that the background could only be completely avoided if the anyway low activity in the spectrometer is removed, e.g. by electro polishing. However, the effort required for this is prohibitively large and success is not guaranteed. Therefore the suppression of the background rate by an increased magnetic field is studied. This method, together with an optimized measurement time distribution proves sufficient to ensure a good neutrino mass sensitivity of KATRIN, provided the increased systematic effects created by this stay under control.

Currently the experiment is in a phase of extensive commissioning measurements in which various properties and parameters of the apparatus, whose knowledge is mandatory for a successful analysis of the following neutrino mass measurements are deter-

mined in-situ. Within these, the models developed here will have to continue to prove themselves useful.

Outline

In chapter 1 a brief introduction to the history of neutrinos, the phenomenology of neutrino flavor oscillations and approaches for the determination of the absolute neutrino mass scale will be given.

In chapter 2 the principle of the KATRIN experiment and its setup are presented.

In chapter 3 the KASPER software package used in this thesis is discussed and new modules and modifications are presented.

In chapter 4 approaches to a description of scattering energy losses in the gaseous source of KATRIN are discussed and a model is worked out from literature results.

In chapter 5 measurement results from the test measurements with the Main Spectrometer are presented and analyzed. It is shown that they exclude the known background processes as dominant source. As a novel process the sputtering of Rydberg atoms following α-decays is introduced and modeled. The thereby predicted properties of the background are in agreement with the measurements. The consequences of the background for the neutrino mass measurement are discussed.

In chapter 6 the results presented here are recapitulated and an outlook is given.

Contents

CHAPTER 1

Neutrino Physics

The KATRIN experiment is targeted to measure the effective mass of the electron anti-neutrino with a sensitivity of $m_{\bar{\nu_e}} < 200$ meV (90% C.L.) by means of precision spectroscopy of tritium β-decay near its endpoint at 18.6 keV. In this chapter a brief overview of the history of neutrino physics is given in section 1.1. The properties of neutrinos and their role in the Standard Model (SM) are discussed in 1.2, while section 1.3 elaborates on the phenomenon of neutrino oscillations and the implied non-zero neutrino masses. Finally, an overview of different experimental approaches to determine the neutrino mass is given in 1.4.

1.1 Discovery of the neutrino

The neutrino was first proposed in 1930 by Wolfgang Pauli in a famous letter [1] as a solution to a problem that was discovered by James Chadwick in 1914 [2]. Chadwick had observed that the β-energy spectrum of the isotope radium was continuous, as displayed in figure 1.1 from a similar measurement by Scott [3], and not discrete as previously known for α- and γ-spectra. A continuous β-spectrum cannot be explained by a two-body decay in a way that preserves momentum- and energy conservation.

As a possible resolution, Pauli postulated a very light, electrically neutral spin 1/2 particle to be emitted in addition to the β-particle. With the new particle, initially called *neutron* by Pauli, the β-decay kinematics is modified to a three-body-decay where the reaction products share the decay energy and thus continuous spectra are expected.

$$n \rightarrow p + e^{-} + \bar{\nu_e} \tag{1.1}$$

The neutron as part of the atomic nucleus was discovered in 1932 by Chadwick [4]. In 1934 Enrico Fermi formulated a theory of the nuclear beta decay [5] and renamed Paulis

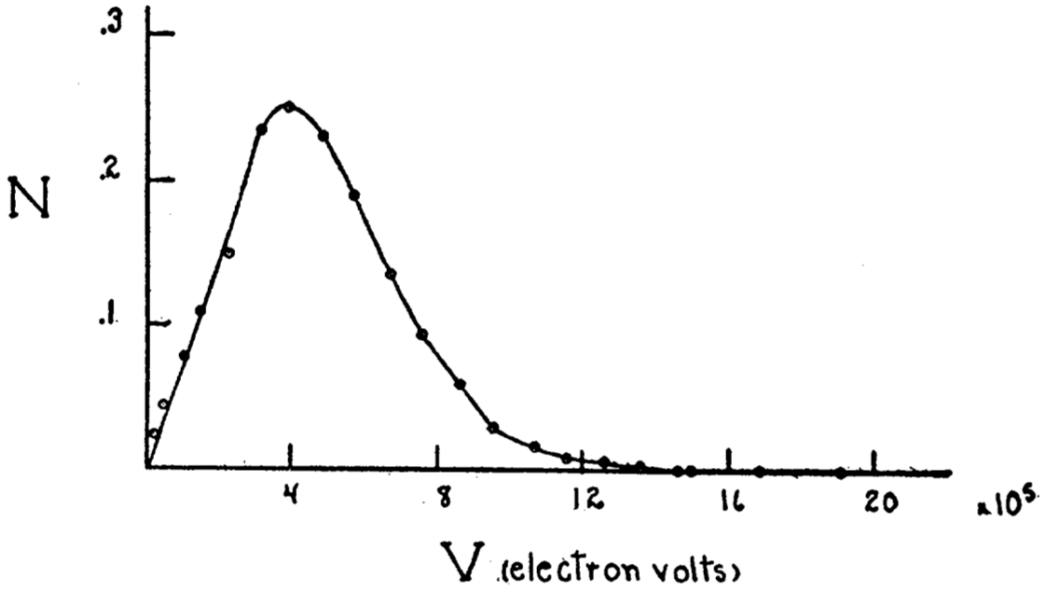

Figure 1.1: The β-spectrum turned out to be continuous. Original image taken from [3]

particle *neutrino*. There a point like interaction is assumed. The cross sections derived from Fermi's theory are valid till today at low energies.

Today we know that the weak force is not a point-interaction, but mediated by heavy W^+-, W^- and Z-bosons leading to corrections for higher energies. The cross section for the inverse β-decay

$$\bar{\nu} + n \rightarrow p + e^- \tag{1.2}$$

was first calculated by Bethe and Peierls in 1934 [6] to be of the order of $\sigma < 10^{-44}$ cm^2. Due to the extremely small cross section and the resulting small interaction rates, the "ghost particle" was directly discovered only 26 years later in 1956 by Fred Reines and Clyde Cowan [7, 8] in their famous series of *Poltergeist experiments* near the Savannah River nuclear power plant.

In these experiments, the inverse beta decay reaction on the free protons in water was used to detect electron anti-neutrinos from nuclear fission with a flux of $\approx 10^{13}$ cm^{-2}s^{-1}. "Herr Auge", one of their earlier detectors, was eventually made up of two tanks filled with 200 liters of cadmium chloride solution each and three liquid scintillation counters of 1400 liters. An inverse β-decay reaction results in the emission of a positron and a neutron. When the positron annihilates with an electron in the target two monoenergetic 511 keV photons headed in opposite directions are produced. But even despite this distinct signature, previous experiments struggled to find the neutrino as they suffered from a large background by cosmic rays.

In their final stage apparatus, cadmium was used to capture the emitted neutron after its moderation in the surrounding water. This excites the nucleus, leading to a γ-decay

with energies in the 3-11 MeV range. Eventually these were also detected, allowing for coincidence discrimination and thereby suppressing background signals drastically. This allowed them to detect about three neutrino events per hour, resulting in a measured cross section of $(1.2^{+0.7}_{-0.4}) \cdot 10^{-43}$ cm^2 for the inverse beta decay (eq. 1.2), a value compatible with the prediction within 5%, though carrying a much larger uncertainty. About four decades later, in 1995, Reines received the Nobel prize for this breakthrough, also in the name of Cowan, who passed away in 1974. The muon neutrino, ν_μ, was discovered in 1962 by Ledermann, Steinberger and Schwartz at the AGS at Brookhaven National Laboratory [9]. They used a spark chamber made of 10 t aluminum to investigate pion decay reactions

$$\pi^+ \to \mu^+ + \nu_\mu \qquad \pi^- \to \mu^- + \bar{\nu}_\mu \tag{1.3}$$

and observed that the neutrinos from the pion beam did not cause electronic showers in the detector material. Instead, they observed muon-like events, thereby showing that the neutrinos from the muon beam were different from the electron (anti-)neutrinos. The existence of a third neutrino, the ν_τ, was predicted [10] after the discovery of the τ lepton in 1975. In 2001, the tau neutrino was finally observed in the DONUT experiment at Fermilab [11]. There, particle showers of a 800 GeV proton beam hitting a tungsten target contained a small fraction of D_s-mesons, and their decay into τ-leptons that again decay producing ν_τ.

A massive shielding was used to remove almost all particles but ν_τ from the beam, while a combination of lead emulsion and stainless steel was used as detector material for the ν_τ. The DONUT experiment was designed to detect the charged-current interactions of ν_τ by observing only tau leptons being created at the interaction points.

Since the typical decay length of the τ is only 2 mm at the ν_τ energies produced in the beam, it was very challenging to identify the signature of the tau lepton: A track with a sudden kink that results from a decay with a large transverse momentum and the neutrino remaining "invisible". An indirect observation, indicating a third neutrino flavor however was made earlier in 1989 by the experiments at the LEP collider at CERN [12, 13]. Within the standard model the Z^0 boson decays into all neutral fermions with approximately the same probability. Therefore the total decay width Γ_{Z^0} is sensitive to the number of light neutrino species N_ν:

$$\Gamma_{Z^0} = N_\nu \Gamma_\nu + 3\Gamma_{ee} + \Gamma_{had.} \tag{1.4}$$

For example the ALEPH experiment found $N_\nu = 3.3 \pm 0.3$, in agreement with the theoretical expectation by the Standard Model predicting three light left-handed neutrinos. A combination of all LEP experiments ALEPH, DELPHI, L3 and OPAL together with the results of SLC gives the PDG value $N_\nu = 2.9840 \pm 0.0082$ [14]

1.2 Neutrinos in the Standard Model

The Standard Model of particle physics is a highly successful, yet incomplete, description of nature. It describes all known fundamental particles and their interactions - except

for gravity - in the framework of quantum field theories and stems from the principle of gauge invariance. Most of the structure of the theory is strictly derived once a gauge group is fixed. A complete treatment is found in the standard literature, e.g. [15], which this section is based on. The Standard Model's Lie group is

$$SU(3)_c \times SU(2)_L \times U(1)_{Y_w} \tag{1.5}$$

and results in a predominantly strongly interacting $SU(3)_c$ sector as described by QCD and an only electro-weakly interacting $SU(2)_L \times U(1)_{Y_w}$ sector which is described by the Glashow-Weinberg-Salam-Model [16–18]. Thus particles are classified according to their participation in these interactions.

The only known interaction not described by the Standard Model is gravity, for its quantisation is a difficult and largely unsolved problem. Several approaches such as String theory, Loop Quantum Gravity and Asymptotic Safety exist [19–21], neither of which has been tested experimentally, mostly because up to now they are incomplete or lack predictive power.

Apart from gauge symmetries and those related to spacetime, e.g. the SO(3,1) group of special relativity, which are continuous, there are discrete symmetries in the Standard Model that are more intricate.

In the SM and its extensions, fundamental particles are described as point-like objects without internal substructure. Different kinds of particles can be distinguished by their quantum numbers only, while there are no means to distinguish one particle of a certain kind from another of the same kind. That is if we change the world by only exchanging two particles of the same kind it makes no difference in the outcome of measurements. This constraint allows two possibilities for the behavior of the system's wave function under this change.

It can either stay the same, or pick up a minus sign. In both cases all observables remain unchanged. This fundamental symmetry in quantum mechanics allows us to classify particles into the two categories of fermions (anti-symmetric, pick up a minus sign) and bosons (symmetric). This property is directly linked to the intrinsic angular momentum of the particle by the spin-statistics theorem [22, 23]: particles with integer spin are bosons, particles with half-integer spin are fermions.

With these tools at hand we can describe the particle content of the Standard Model seen in figure 1.2: It embodies three generations of fermions grouped into the electro-weakly interacting leptons and the strongly (and electro-weakly) interacting quarks. Each generation consists of two quarks and two leptons, with each couple forming an isospin doublet that transforms under the $SU(2)$ group.

The quarks are the only particles participating in all four interactions including gravity. They are also special because they carry fractional values of the elementary charge e: $+\frac{2}{3}$e for up-type quarks (up, charm, top) and $-\frac{1}{3}$e for down-type quarks (down, strange, bottom). However, due to the effect of color confinement, experimentally observable particles carry integer multiples of e.

When attempting to separate quarks from each other, the strong interaction potential increases and new quarks are created out of the vacuum by the potential energy of the

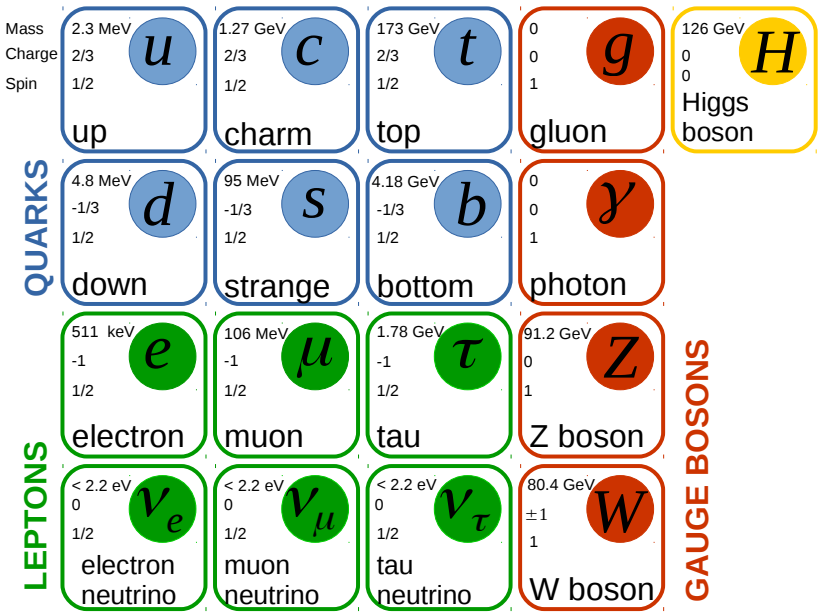

Figure 1.2: Particles of the standard model, adapted from [24]

gluon field created by the color charge. To a macroscopic observer only color-neutral and integer electric charge states are visible.

The interactions are mediated by bosons: The electroweak interaction is carried by the $W^{\pm}$, Z bosons and photons, the strong interaction by gluons. A strict gauge symmetry however would forbid these particles to be massive with a simple mass term in their Lagrangian. This problem is solved within the Standard Model by the Higgs mechanism [25, 26] of dynamical symmetry breaking. This approach is based on the models and observations in solid state physics, where the ground state of a system (e.g. a crystal) is often found to be less symmetric than the corresponding Lagrangian.

In this scenario the observed particle content is interpreted as low-energy excitations of the vacuum forming a ground state with lower symmetry within the high-energy symmetric theory. This part of the Standard Model was the last to be confirmed when in 2012 the Higgs boson was finally discovered at the LHC [27, 28]. Although this neutral scalar particle, an excitation of the Higgs background field that is understood to generate the particle masses in a gauge-invariant way, is the only accessible hint to the high-energy theory so far, its discovery is a major confirmation after decades of search.

In this picture Neutrinos are neutral leptons, being the isospin partners of the electron, muon and tau as displayed in table 1.1. They carry no electric charge and only

interact weakly, implying parity and CP violation. Within the Standard Model, neutrinos are assumed to be massless based on observations of β-spectra and Goldhaber's 1958 measurement of the neutrino helicity [29]. Helicity is defined as the normalized projection of the particle spin $\vec{\sigma}$ onto its momentum $\vec{p}$:

$$h = \frac{\vec{\sigma} \cdot \vec{p}}{|\vec{p}|} \tag{1.6}$$

Goldhaber found neutrinos to have a helicity of -1. If the neutrino's helicity is indeed always negative and the anti-neutrino's always positive, they have to travel at the speed of light. Otherwise reference frames could be found in which the momentum, but not the spin, is reversed and therefore the helicity would flip. Traveling at light speed consequently implies massless neutrinos. This asymmetry between ν_L and $\bar{\nu}_R$ is different from what is observed for the other fermions. There, the charge conjugation operation C transforms a fermion into its anti-particle $Cf_{L/R} = \bar{f}_{L/R}$, not affecting handedness. This fails with neutrinos, as the ν_R and $\bar{\nu}_L$ states appear to be missing in nature. The two observed states however transform into each other under CP transformation $CP\nu_L = \bar{\nu}_R$. Two explanations to this puzzle are widely discussed.

Ettore Majorana showed that massive neutral particles can have a two-component spinor description [30]. In this case the neutrino and antineutrino would be their own antiparticles, i.e. $C\nu_L = \nu_L$ and $C\bar{\nu}_R = \bar{\nu}_R$. The neutrino would be a *Majorana particle*. The other possibility is that the "missing" states actually do exist, but because they only interact gravitationally or by neutrino mixing, they have not been observed so far. In this case the neutrino would be a Dirac particle like the other fermions.

In both cases the neutrino would be massive, as actually indicated by the observation of neutrino oscillations. In a strict interpretation this observation implies new physics beyond the Standard Model.

1.3 Neutrino mass and oscillations

For a long time, the discrepancy between the expected and the actually observed number of neutrinos coming from the sun had puzzled physicists. Neutrino oscillations turned out to be the solution to this longstanding problem, revealing the massive nature of

Generation			Electric	Lepton	Interaction
1	2	3	charge	number	
e^-	μ^-	τ^-	-1	$+1$	electromagnetic, weak
ν_e	ν_μ	ν_τ	0	$+1$	weak
e^+	μ^+	τ^+	$+1$	-1	electromagnetic, weak
$\bar{\nu}_e$	$\bar{\nu}_\mu$	$\bar{\nu}_\tau$	0	-1	weak

Table 1.1: Leptons of the Standard Model

neutrinos. This section will cover both historical and theoretical aspects of neutrino oscillations and discuss the implications for the neutrino mass quest.

1.3.1 The solar neutrino puzzle

As can be seen in figure 1.3 one of the main neutrino sources available on Earth are the nuclear reactions fueling the sun. In terms of neutrino flux density the sun is a strong source.

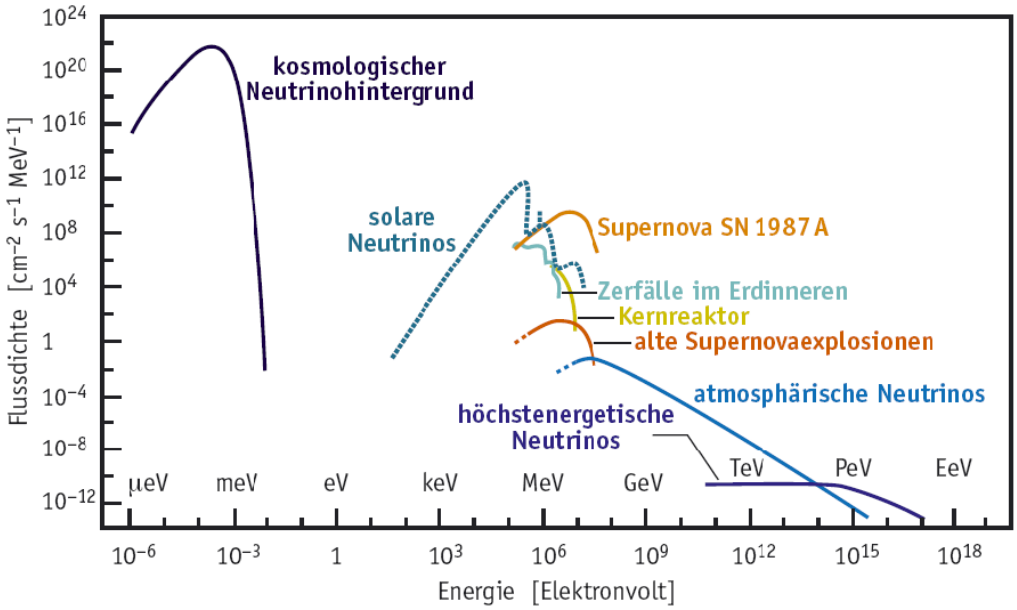

Figure 1.3: Shown are the flux densities of different neutrino sources in units of $\mathrm{cm}^{-2}\mathrm{s}^{-1}\mathrm{MeV}^{-1}$. Solar neutrinos provide a total (integrated) flux of about $6 \cdot 10^{10}$ $\mathrm{cm}^{-2}\mathrm{s}^{-1}$ at the earth. Due to its close distance the sun is an even stronger source than the spectacular SN 1987 A supernova from which the Kamiokande, IMB and Baksan experiments recorded a neutrino burst over 10 s [31]. This was a distant event, however, as the supernova happened in the nearby Large Magellanic Cloud, at a distance of 51.47 kpc (167885 Ly). Image taken from [32]

The dominant process contributing to the sun's neutrino spectrum is the pp-chain starting with the reaction

$$p + p \rightarrow d + e^{+} + \nu_e \tag{1.7}$$

This reaction accounts for about 85% of the solar neutrino flux. In contrast to earth-based neutrino sources like nuclear reactors the sun produces only ν_e and no $\bar{\nu}_e$. In heavier stars the otherwise sub-dominant CNO-cycle becomes important.

The solar neutrino puzzle came up when the Homestake [34, 35] experiment measured the neutrino flux from the sun to be significantly lower then expected from the Standard Solar Model (SSM). To detect solar neutrinos R. Davis et al. developed a radiochemical

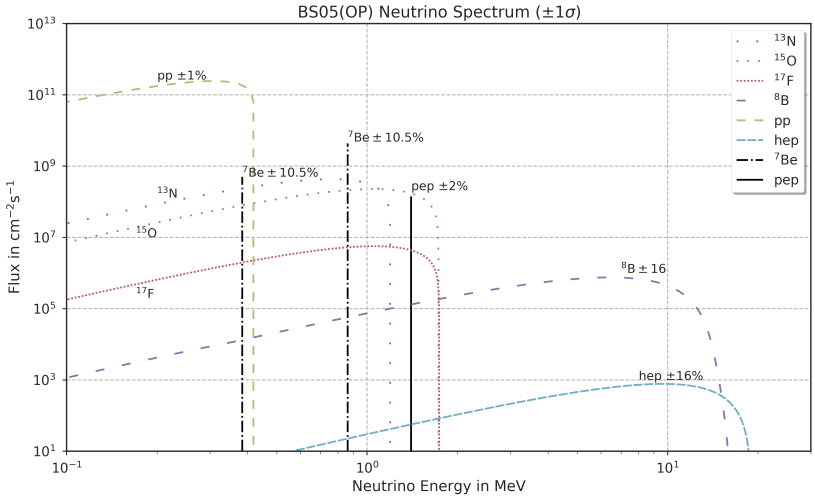

Figure 1.4: Solar neutrino spectrum. Displayed are neutrino fluxes from the pp-chain and the CNO-cycle. Replot of the predicted fluxes of the BS05(OP) solar model from Table 2 in [33]

detection technique based on chlorine in a tank filled with 600 t perchloroethylene using the reaction

$$\nu_e + {}^{37}\mathrm{Cl} \rightarrow {}^{37}\mathrm{Ar} + e^- \tag{1.8}$$

After a measurement interval of about 30 days they separated the small number of produced argon atoms from the detector material. These argon atoms react via electron capture back to excited states of ^{37}Cl. Their de-excitation by emission of Auger electrons then was measured by proportional counters. The neutrino deficit established by Homestake was confirmed by other experiments like GALLEX [36], GNO [37], SAGE [38] and Kamiokande [39].

While the deficit was at first widely attributed to uncertainties in the SSM and its predictions, a different possibility was pointed out by B. Pontecorvo and V. Gribov [40]: The electron neutrinos generated in the sun could change their flavor during the travel to earth.

To finally resolve this problem the Sudbury Neutrino Observatory (SNO) was built. Its target was to detect all three neutrino flavors ν_e, ν_μ and ν_τ making use of an acrylic sphere filled with 1000 t of pure heavy water, surrounded by photo multipliers situated in a depth of 2000 m in a Canadian mine. In the deuterium nuclei of heavy water (D_2O) the neutrinos can interact via charged current (CC) and neutral current (NC) reactions and also undergo elastic scattering (ES):

$$\nu_x + e^- \rightarrow \nu_x + e^- \quad \text{ES} \tag{1.9}$$

$$\nu_e + d \rightarrow p + p + e^- \quad \text{CC, for } \nu_e \text{ only} \tag{1.10}$$

$$\nu_x + d \rightarrow p + n + \nu_x \quad \text{NC} \tag{1.11}$$

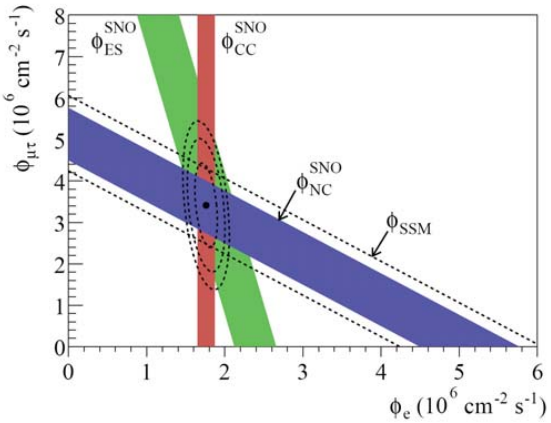

Figure 1.5: The solar neutrino fluxes from ^{8}B as measured by SNO. Plotted is the neutrino flux from μ and τ flavors $\phi_{\mu\tau}$ over the electron neutrino flux ϕ_e. The solid bands represent the 1σ measurements of CC and NC fluxes. While the dashed line indicates the predictions of the SSM, the NC flux measures the total flux and is in good agreement with the predictions [42].

Due to the distinct signals produced by these reactions they could be discriminated and, by this the total neutrino flux and the electron neutrino flux were measured separately. After this phase I measurement multiple checks of the fluxes were performed, including the loading of the detector with salt water (phase 2) and ^{3}He (phase 3) to look for neutron capture with increased sensitivity.

The SNO experiment showed that the total neutrino flux is in good agreement with the predictions of the SSM, whereas the electron neutrino flux is substantially lower by about a factor of three. This established neutrino flavor transformations as the solution to the solar neutrino puzzle [41].

1.3.2 Theoretical description

Within the Standard Model, neutrino flavor changing effects can not be explained. This led Pontecorvo and Gribov [40] to consider massive neutrinos. By introducing a unitary matrix translating between the flavor eigenstates $|\nu_f\rangle$ and the mass eigenstates $|\nu_{m_i}\rangle$:

$$|\nu_{m_i}\rangle = \sum_{f=e,\mu,\tau} U_{fm_i} |\nu_f\rangle \qquad |\nu_f\rangle = \sum_{i=1,2,3} U^*_{fm_i} |\nu_{m_i}\rangle \tag{1.12}$$

The matrix U_{fm_i} is called the **P**ontecorvo-**M**aki-**N**akagawa-**S**akata matrix and is similar to the CKM-matrix in the quark sector. There, Cabibbo was the first to explain (quark-) flavor mixing with, at that time, one mixing angle [43]. A usual parameterization now makes use of the three mixing angles θ_{ij} with $c_{ij} = \cos(\theta_{ij})$, $s_{ij} = \sin(\theta_{ij})$, two complex Majorana phases α_i that appear if neutrinos are Majorana particles, and a complex CP-violating Dirac phase δ. The PMNS matrix then reads:

$$U_{\text{PMNS}} = \begin{pmatrix} 1 & 0 & 0 \\ 0 & c_{23} & s_{23} \\ 0 & -s_{23} & c_{23} \end{pmatrix} \begin{pmatrix} c_{13} & 0 & s_{13}e^{-i\delta} \\ 0 & 1 & 0 \\ -s_{13}e^{i\delta} & 0 & c_{13} \end{pmatrix} \begin{pmatrix} c_{12} & s_{12} & 0 \\ -s_{12} & c_{12} & 0 \\ 0 & 0 & 1 \end{pmatrix} \begin{pmatrix} e^{i\alpha_1/2} & 0 & 0 \\ 0 & e^{i\alpha_2/2} & 0 \\ 0 & 0 & 1 \end{pmatrix}$$

If a neutrino of flavor α is generated at $t = 0$, the value of interest is the *transition probability* P.

Note that since neutrinos interact exclusively weakly, they are always produced in a flavor eigenstate. A flavor eigenstate is a superposition of mass eigenstates:

$$|\nu(t=0)\rangle = |\nu_\alpha\rangle = U^*_{\alpha m_1} |\nu_{m_1}\rangle + U^*_{\alpha m_2} |m_2\rangle + U^*_{\alpha m_2} |m_2\rangle \tag{1.13}$$

The mass eigenstates are the eigenstates of the Hamiltonian and determine the propagation of the neutrino. The time evolution operator in this case is

$$T = \sum_{i=1,2,3} \exp(-i/\hbar t E_i) |\nu_{m_i}\rangle \langle \nu_{m_i}| \tag{1.14}$$

with $E_i = \sqrt{p^2 + m_i^2}$. The state $|\nu_\alpha\rangle$ at $t = 0$ evolves to

$$|\nu(t)\rangle = T |\nu_\alpha\rangle = \sum_{i=1,2,3} U^*_{\alpha m_i} \exp(-i/\hbar t E_i) |\nu_{m_i}\rangle \tag{1.15}$$

which is not necessarily a flavor eigenstate. The transition probability to a different flavor β is then

$$\begin{aligned} P_{\nu_\alpha \to \nu_\beta}(t) &= |\langle \nu_\beta | \nu_f(t) \rangle|^2 = |A(t)|^2 = |\sum_{i=1,2,3} U^*_{\alpha m_i} \exp(-i/\hbar t E_i) U_{\alpha m_i}|^2 \\ &= \sum_{i,j} U^*_{\alpha i} U_{\beta i} U_{\alpha j} U^*_{\beta j} \exp(-i/\hbar (E_i - E_j) t) \end{aligned} \tag{1.16}$$

With the ultra-relativistic approximation $v \approx c$, $L \approx ct$, which is possible due to the exceedingly low neutrino masses, we can rewrite the neutrino energy to

$$E_i = E + \frac{m_i^2 c^4}{2E} \tag{1.17}$$

with $E \approx cp$. The transition probability can then be formulated depending on the distance L traveled by the neutrino and its energy E, which are both parameters accessible in experiments:

$$P_{\nu_\alpha \to \nu_\beta}(L/E) = \sum_{i,j} U^*_{\alpha i} U_{\beta i} U_{\alpha j} U^*_{\beta j} \exp\left(-i/\hbar \frac{\Delta m_{ij}^2 c^3 L}{2E}\right) \tag{1.18}$$

with $\Delta m_{ij}^2 = m_i^2 - m_j^2$. This immediately shows that oscillation experiments are sensitive to the differences in the neutrino mass spectrum only, but not to the overall mass scale

of the neutrino sector. The transition probability is governed by the mass splittings and the mixing parameters of the PMNS matrix.

A further approximation can be made due to the smallness of θ_{13} which has been determined only in 2012 [44–46]. This leads basically to a decoupling of ν_τ and the formula can be simplified to the 2ν case

$$P_{\nu_e \leftrightarrow \nu_\mu}(L/E) = \sin^2(2\Theta) \sin^2\left(\frac{\Delta m^2 c^3 L}{4\hbar E}\right). \tag{1.19}$$

In this form it gets clear that the mixing angle Θ determines the amplitude of the oscillation, while the mass splitting Δm^2 controls the frequency. The typical length L_{osc} associated with this oscillation is then

$$L_{\text{osc}} = \frac{4\pi\hbar E}{\Delta m^2 c^3}. \tag{1.20}$$

1.3.3 Oscillation Parameters

With the introduction of the PMNS-matrix, the Standard Model is extended by at least another 6 parameters that have to be determined experimentally, namely the three mixing angles θ_{12}, θ_{23}, θ_{13} and the three squared mass splittings Δm^2_{12}, Δm^2_{23}, Δm^2_{13}. Furthermore, up to three CP-violating complex phases have to be added depending on the nature of the neutrino.

So far there exists no generally accepted, comprehensive theory of lepton (or equivalently quark-) flavor changing that could reduce this number of parameters. Additionally, the prospects to discover new physics beyond the Standard Model has fueled neutrino physics in the last two decades.

To investigate neutrino oscillations, experiments have used a variety of sources, such as the sun, cosmic particle showers, nuclear reactors and accelerators. Oscillation studies come in two categories: as appearance or disappearance experiments. They either investigate if the neutrino flux of a certain flavor turns out to be smaller than predicted without oscillations (e.g. SNO) or they aim to detect a flavor not expected from the examined source (e.g. OPERA).

As can be seen in figure 1.6, it is very important to tune the L/E ratio of an experiment carefully to achieve a good sensitivity for the parameter of interest. At a given energy the oscillation frequency gets large for $L \gg L_{\text{osc}}$ and only averaged transition (or survival) probabilities are measurable, while at $L \ll L_{\text{osc}}$ there barely is any oscillation. The energy of the neutrino beam however is not easy to control. Only accelerator experiments have a certain handle on this, so once the source is determined the distance L of the detectors needs to be chosen accordingly.

A great success has been achieved in recent oscillation experiments via the detection of anti-neutrino disappearance at several reactor neutrino experiments and the measurement of the corresponding mixing angle θ_{13}. In early 2012, Double Chooz, Daya Bay

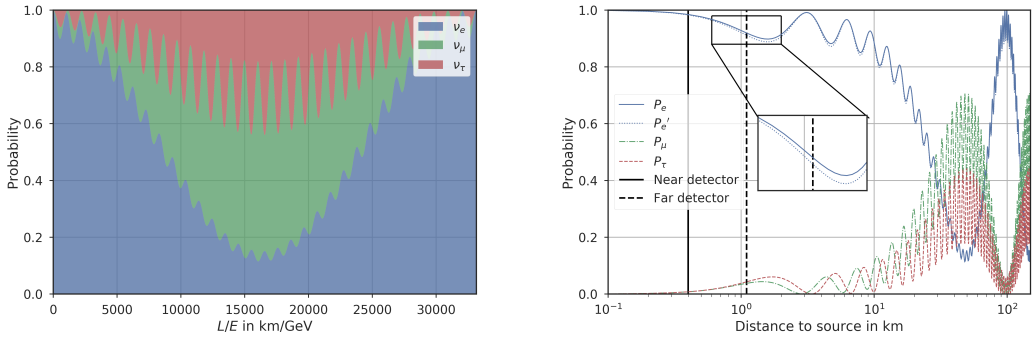

Figure 1.6: Left: Composition of an initial electron neutrino as function of L/E calculated from formula 1.18 with the parameters in table 1.2. **Right**: Example of the theoretically expected oscillation probability for 3 MeV electron neutrinos over the distance with an assumed mixing angle of $\theta_{13} = 10°$ (which is close to the value measured by e.g. Double Chooz). The black lines correspond to the source distances of the near- and far-detectors of Double Chooz. In comparison $P_e{}'$ is calculated with a 5% higher θ_{13}. The difference is small and in practice only measurable by the ν_e disappearance within the first oscillation minimum. Therefore the placement of near and far detector are crucial.

and RENO announced their results:

$$\text{DoubleChooz} : \sin^2(2\theta_{13}) = 0.109 \pm 0.030(\text{stat.}) \pm 0.025(\text{syst.}) \quad (1.21)$$

$$\text{DayaBay} : \sin^2(2\theta_{13}) = 0.089 \pm 0.010(\text{stat.}) \pm 0.005(\text{syst.}) \quad (1.22)$$

$$\text{RENO} : \sin^2(2\theta_{13}) = 0.113 \pm 0.013(\text{stat.}) \pm 0.019(\text{syst.}) \quad (1.23)$$

These very similar experiments work with a two-detector concept, with one detector placed close to the fission reactor (300-500 m) and one further away (1-1.6 km). The near detector determines the total flux, produced by the source, while the far detector detects the disappearance of electron anti-neutrinos.

These experiments are based on the detection principle established by the Poltergeist experiments: the delayed coincidence of an inverse β-decay reaction consisting of a positron signal followed by neutron capture. They profit from the development of advanced scintillators, larger detectors and carefully chosen places for the far detectors to reduce background.

Their results are in good agreement with each other and with previous results from T2K [47], MINOS [48] and CHOOZ [49] that had lower significance. The other mixing angles and mass splittings have already been measured, except for the sign of Δm_{23}.

Pure oscillation experiments are only sensitive to $|\Delta m^2|$, however the sign of Δ_{12} is known from solar neutrinos. Because solar neutrinos travel through the dense sun they experience the so called MSW-effect [50, 51], an effect resulting from propagation through matter, which is sensitive to the sign of the mass splitting. A global best fit of the remaining oscillation parameters is shown in table 1.2:

Parameter	best-fit	3σ
$\Delta m^2_{21}\,[10^{-5}\,\mathrm{eV}^2]$	7.37	6.93 - 7.96
$\Delta m^2_{31(32)}\,[10^{-3}\,\mathrm{eV}^2]$	2.56 (2.54)	2.45-2.69 (2.42-2.66)
$\sin^2\theta_{12}$	0.297	0.250-0.354
$\sin^2\theta_{23},\ \Delta m^2_{31(32)} > 0$	0.425	0.381-0.615
$\sin^2\theta_{23},\ \Delta m^2_{31(32)} < 0$	0.589	0.384-0.636
$\sin^2\theta_{13},\ \Delta m^2_{31(32)} > 0$	0.0215	0.0190-0.0240
$\sin^2\theta_{13},\ \Delta m^2_{31(32)} < 0$	0.0216	0.0190-0.0242
δ/π	1.38 (1.31)	$2\sigma:\ 1.0-1.9$ $(2\sigma:\ (.92-1.88))$

Table 1.2: Measured parameters of the PMNS Matrix from the PDG [14]

1.3.4 Models of neutrino mass

In the Standard Model, there is no mechanism for neutrino masses. The observation of neutrino oscillations together with the very small upper limits on the masses themselves (factor $> 10^5$ smaller than e^-) are hints to physics beyond the SM. Especially the smallness relative to the masses of other particles in the SM led to the assumption that the neutrino masses might be generated by a mechanism different from the standard Higgs mechanism. A popular alternative is the See-Saw mechanism which will be briefly layed out in its simplest version. Full treatment can be found in the literature this section is based on, e.g. [53].

To account for a neutrino mass in the SM Lagrangian analogously to the other leptons, terms in the form of

$$L^{\mathrm{D}}_{\mathrm{mass}} = -\frac{1}{2}\sum_{\alpha,\beta}\bar{\nu}_{\beta\mathrm{L}} M^{\mathrm{D}}_{\alpha\beta}\nu_{\alpha\mathrm{R}} + h.c. \tag{1.24}$$

can be introduced, thereby completing the neutrino's Dirac Lagrangian. It is summed over all flavors with L, R denoting the chirality of the fields, that is the part that is projected out by $(1\pm\gamma^5)/2$. We see immediately that this requires also the introduction of right handed neutrino fields ν_R that are not part of the SM. These new ν_{R} states would not take part in the weak interaction and therefore are called sterile. In this scenario the Higgs mechanism could be invoked to generate the mass terms in a gauge invariant way. This is unappealing due to the extreme fine-tuning og the Yukawa coupling of $\sim 10^{-13}$ needed in this scenari.o

Another possibility was brought up by E. Majorana. It is possible to construct a mass term without referring to the right handed field ν_R. Instead its role is played by $C\nu_L$

$$L^{\mathrm{M,L}}_{\mathrm{mass}} = -\frac{1}{2}\sum_{\alpha,\beta}\bar{\nu}_{\beta\mathrm{L}} M^{\mathrm{D}}_{\alpha\beta}\nu^{C}_{\alpha\mathrm{L}} + h.c. \tag{1.25}$$

This term causes lepton number violation, e.g. in neutrinoless double beta decay, and implies that a Majorana neutrino is its own anti-particle.

It is also possible to invoke both mass terms and add also a Majorana term for the right handed neutrino. When collecting all these terms in a Dirac-Majorana term

$$L^{D+M} = L^D + L^{M,L} + L^{M,R} \tag{1.26}$$

with the neutrino fields combined in the vector

$$N_{\mathrm{L}} = \begin{pmatrix} \nu_{\mathrm{L}} \\ (\nu_{\mathrm{R}})^C \end{pmatrix} \tag{1.27}$$

the mass term can be written as

$$L^{D+M} = -\frac{1}{2} N_{\mathrm{L}} M N_{\mathrm{L}}. \tag{1.28}$$

Here M denotes the mass matrix (for a single neutrino now for simplicity)

$$M = \begin{pmatrix} m_{\mathrm{L}} & m_{\mathrm{D}} \\ m_{\mathrm{D}} & m_{\mathrm{R}} \end{pmatrix}. \tag{1.29}$$

The eigenvalues of this matrix determine the physical neutrino masses observed. In the simplest form of the See-Saw mechanism $m_{\mathrm{L}} = 0$ and $m_{\mathrm{D}} \ll m_{\mathrm{R}}$ is assumed. In this case the diagonalization of the matrix gives

$$m_1 \approx \frac{m_{\mathrm{D}}^2}{m_{\mathrm{R}}} \qquad m_2 \approx m_{\mathrm{R}}. \tag{1.30}$$

One very small mass m_1 and a rather large mass m_2 is found, naturally giving rise to the small neutrino mass. The heavy state consists mostly of ν_{R} and therefore can be called sterile.

1.4 Measurements of the neutrino mass

Since oscillation experiments can only measure squared mass splittings, further measurements are needed to determine the absolute neutrino masses. Indirect methods include observations of the large-scale structure of the universe discussed in section 1.4.1 and searches for neutrinoless double beta decay in section 1.4.2. Both methods however are heavily model-dependent.

Direct neutrino mass measurements on the other hand purely rely on the kinematics of neutrinos. There are in principle two methods to achieve this. Either by measuring the time-of-flight of the massive neutrino precise enough to tell its velocity apart from c - see section 1.4.3, or by examining the shape of spectra of weak decays. This is done either by studying electron capture or single beta decay. Electron Capture (EC) is studied mainly with bolometers using the isotope Holmium 163. Previously also Rhenium 187 was investigated with bolometers, but this isotope is difficult when developing high-resolution bolometers. The β-decay of tritium has for a long time been studied with electrostatic spectrometers. A recent approach is to use cyclotron radiation emission spectroscopy to study tritium β-decay. Until today only upper limits on the absolute neutrino mass scale are known.

1.4.1 Cosmological measurements

Neutrinos play an important role in cosmology. Their exclusively weak interaction and small masses imply that they contribute to the Hot Dark Matter (HDM) component in the Universe. Due to their predicted vast abundance of 336 neutrinos per cubic centimeter left from the Big Bang, the so-called cosmic neutrino background ($C\nu B$) does give a measurable contribution to the matter-energy density in the cosmos in spite of small neutrino masses, see fig. 1.7. While relic neutrinos have not been detected directly, indirect evidences exist.

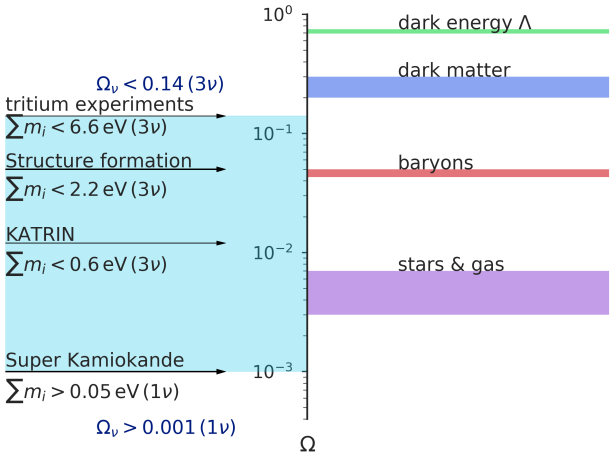

Figure 1.7: Relative contributions to the matter-energy densitiy of the universe from different sources and experimental bounds on the neutrino mass density. KATRIN aims to improve the sensitivity of previous tritium experiments by one order of magnitude. Figure adapted from [54].

Due to their low mass, neutrinos as HDM do not contribute to dark matter, which is dominated by a non-realtivistic Cold Dark Matter (CDM) component. The currently prevailing model of the universe is the ΛCDM model. It describes the universe today as being dominated by the cosmological constant Λ and CDM. Both are not understood on a fundamental level. The cosmological constant is only described in the classical Einstein equation [55–58]

$$R_{\mu\nu} - \frac{1}{2} g_{\mu\nu} R + \Lambda g_{\mu\nu} = \frac{8\pi G}{c^4} T_{\mu\nu}. \tag{1.31}$$

However, it is often regarded residual energy of vacuum fluctuations of the other quantum fields, similar to the zero-point energy $\hbar\omega/2$ of a harmonic oscillator. A particular problem with this interpretation is the smallness of the cosmological constant, which cannot be explained within the SM. This is one motivation for supersymmetry. A full understanding of the cosmological constant may in the end require quantum gravity.

While there are many indirect pieces of evidence for CDM in the universe, e.g. galactic rotational curves [59], weak lensing [60] and the Bullet Cluster [61, 62], no direct

evidence for its particle nature has been found yet. Many experiments search for Dark Matter candidates, the weakly interacting massive particles (WIMPs), predicted by different theories. Examples of WIMP candidates are e.g. the lightest supersymmetric particles.

The ΛCDM model points to an inflationary big-bang cosmology, to be consistent with the cosmic microwave background (CMB)[63], that has been measured with high precision by satellite experiments such as COBE [64], WMAP [65] and Planck [66, 67].

Due to their small mass and weak interaction, neutrinos are able to travel through the universe unperturbed on cosmological scales, which is called free-streaming. They have decoupled from the remaining matter about 1 s after the Big Bang, when they were still highly relativistic, with energies on the order of 1 MeV. Consequently, they have suppressed to some extent the formation of structures on scales below their free-streaming length. In fig. 1.8 the influence of neutrino mass on this process can be seen.

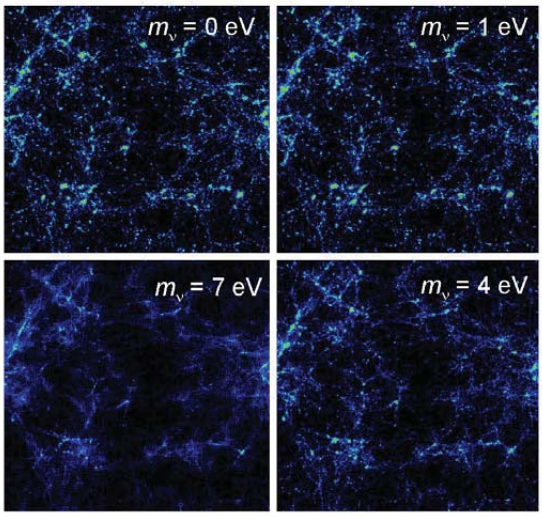

Figure 1.8: Influence on the neutrino mass on the structure formation in the universe. Larger neutrino masses lead to stronger 'wash out' of the small scale structures. Figure from [54].

The matter distribution of the universe (see fig. 1.7) is accessible in experiments measuring the CMB, galaxy surveys and the Lyman-alpha-forest. In cosmology only the sum of the neutrino masses can be accessed. A recent combined analysis of cosmological data gives [68]:

$$\sum_i m_{\nu_i} \leq 0.51 \text{ eV (90\% C.L.)}. \tag{1.32}$$

However, this upper bound is strongly model-dependent [69]. More conservative bounds exist and large variations are common, depending on which model and data set are used.

1.4.2 Neutrinoless double beta decay

Double beta decay is a rare second order weak process. It can only be observed if single β-decays of an even-even nucleus to the neighboring odd-odd-nucleus are forbidden by energy conservation. In the nucleus, two β^- decays happen simultaneously

$$ {}^{A}_{Z}X_N \rightarrow {}^{A}_{Z+2}X^{2+}_{N-2} + 2e^- + 2\bar{\nu}_e. \tag{1.33} $$

Being a second order-process the resulting decay rates are low and typical half-lives are very long. The first observation of a $\beta\beta$-process was in 1987 for the isotope ^{82}Se [70] after it was first proposed for ^{76}Ge in 1935 [71]. Today $2\nu\beta\beta$-decays are known to occur for a total of 12 isotopes out of the 60 for which it would in principle be possible. If neutrinos are indeed their own anti-particles, another process is possible, the neutrinoless double beta decay ($0\nu\beta\beta$). The process of $0\nu\beta\beta$ decay was proposed by G. Racah [72] and W. Furry [73] following Majoranas work [30]. Instead of emitting two neutrinos in the final state, a 'virtual' neutrino is exchanged, flipping from an outgoing anti neutrino at one vertex to an incoming neutrino at the other vertex, as seen in fig. 1.9.

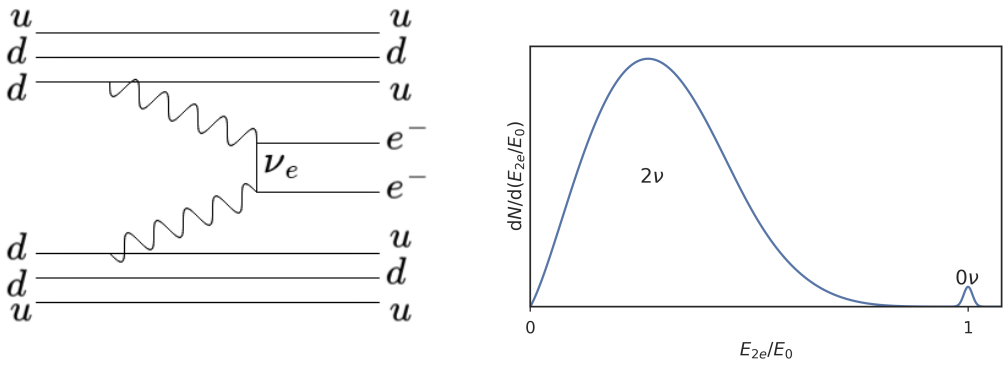

Figure 1.9: Left: Feynman diagram for neutrinoless double beta decay. Two neutrons decay simultaneously emitting two electrons. The neutrino is shared, which is only possible if it is its own antiparticle. **Right** Schematic spectrum for the summed energy of both emitted electrons in double beta decay. In case of a neutrinoless double beta decay the full decay energy is transferred to the electrons creating a monoenergetic line above the Q-Value E_0 at $E_0 + m_\nu c^2$. In practice the energy resolution in experiments does not allow to resolve the shift above the endpoint. Here the size of the peak is vastly exaggerated for visibility.

This is only possible for massive Majorana neutrinos. In contrast to single beta decay and ordinary double beta decay, the summed energy spectrum of the emitted electrons in $0\nu\beta\beta$ reactions is discrete and sharply peaked, since the virtual neutrino can not carry away energy or momentum. This process violates lepton number conservation by two units and would indicate physics beyond the SM. In principle loops of new particles coupling to the neutrino could also contribute to the process, and consequently to the neutrino mass. Therefore, the actual Dirac- and Majorana masses extracted from these

measurements are highly model-dependent. From the observation of neutrinoless double beta decay, a Majorana neutrino mass can be deduced:

$$m_{\beta\beta} = \left| \sum_i U_{ei}^2 m_{\nu_i} \right| = \frac{1}{G^{0\nu} |M^{0\nu}|^2 \tau_{1/2}^{0\nu}}. \tag{1.34}$$

Here $\tau_{1/2}^{0\nu}$ is the measured half-life of the decay, $M^{0\nu}$ the nuclear matrix element for the transition and $G^{0\nu}$ denotes the phase space factor. One important aspect is that unlike single beta decay measurements, neutrinoless double beta decay is sensitive to the *coherent* sum of the neutrino mass eigenstates. Due to the Majorana nature of the neutrino in this case, the Majorana phases come into play and allow for cancellation in this sum. The deduced mass is therefore also model dependent. The Heidelberg-Moscow collaboration published a result claiming an observation and a corresponding neutrino mass $m_{\beta\beta} \approx 0.4$ eV[74], which is not accepted in general, due to its disputed analysis method. Many experiments e.g. CUORE, GERDA and EXO are currently searching for the $0\nu\beta\beta$ decay using different isotopes and different experimental setups to test the claim from Heidelberg-Moscow. Recently, the GERDA collaboration has published improved phase II results, which do not support the earlier observations [75].

1.4.3 Time-of-flight measurements

Since neutrinos are massive particles, they must move slower than the speed of light. Their time-of-flight over a distance d will therefore be larger than the time-of-flight of a photon d/c. Due to the very small neutrino mass, also the difference in time-of-flight is extremely small. In order to detect this a very long baseline d and, consequently, a very strong source and suitable neutrino detectors are necessary.

A "long" baseline in this case necessitates astronomical scales. Possible sources then are core-collapse supernovae, which are intense neutrino-sources. Their intensity would suffice for a measurement on the eV-scale if one happens to be observed in our cosmic neighborhood. Such an event however would be of much broader interest than "only" neutrino physics. An early warning system SNEWS that includes several neutrino detectors and telescopes has been set up [76]. In case of a close-by SN, the neutrinos would arrive hours before the photons. A trigger from the neutrino detectors would therefore help to alert optical telescopes and direct them to the right portion of the sky.

Such an observation of a cosmic neutrinos coincident with a supernova has so far only been made once in case of the supernova SN1987A in the Large Magellanic Cloud. From the relative arrival times of photons and neutrinos an upper limit of $m_\nu < 5.7\,\mathrm{eV}$ (95%C.L.) was derived [77]. While time-of-flight measurements are also possible with long baseline experiments using neutrino beams from accelerators like MINOS or OPERA [78], their sensitivity is not nearly comparable: MINOS reported a (zero-compatible) deviation from the speed of light of $(v/c-1) = (1.0 \pm 1.1) \times 10^{-6}$ [79] and OPERA $(v/c-1) = (2.7 \pm 3.1(\mathrm{stat.})^{+3.4}_{-3.3}(\mathrm{sys.})) \times 10^{-6}$ [80]. An early analysis of SN1987A however gives the much lower limit $|v/c-1| \leq 2 \times 10^{-9}$ [81].

Concludingly, only close-by supernovae allow for time-of-flight measurements useful in neutrino mass determination. These events however are exceedingly rare and the supernova models that predict the neutrino emission over time are at present not precise enough to allow for sensitivities comparable to limits from cosmological or direct neutrino mass measurements on weak nuclear decays [82].

1.4.4 Nuclear decay kinematics

Two types of weak decays are used for direct neutrino mass measurements: electron capture (EC) and single beta-decay.

Electron capture

In electron capture, a shell electron is captured by a proton in the nucleus to produce a neutron, leaving a hole in the shell. In the process, an electron neutrino is emitted and the atom is left in an excited state:

$$\begin{aligned} {}^{A}_{Z}X_N &\rightarrow {}^{A}_{Z-1}X^{*}_{N+1} + \nu_e \\ &\rightarrow {}^{A}_{Z-1}X_{N+1} + E_{EC} \end{aligned} \tag{1.35}$$

The total decay energy is distributed between the neutrino and the excited state of the daughter atom. A calorimetric measurement of the subsequent de-excitation of the atom therefore also yields information about the neutrino mass. The de-excitationmay happen via radiative or non-radiative transitions. In a radiative transitions an outer shell electron with binding energy E_1 moves to the vacant state of the captured electron with binding energy E_0 and the remaining energy $E_\gamma = E_0 - E_1$ is emitted as X-ray. In non-radiative transitions the energy is instead transferred to a weakly bound electron that is emitted as *Auger electron* or, if the replacing and the emitted electron came from the same shell, *Coster-Kronig-electron*. Frequently a single transition is not sufficient for the excited atom to reach the ground state and instead a cascade of several transitions is triggered. In order to gain sensitivity it is necessary to measure the complete excitation energy E_{EC}, otherwise a random width spoils the result. This can be achieved by calorimetric measurements where the source is included in the detector and a rise of temperature is measured. This process is studied primarily in the electron capture of ${}^{163}_{67}\mathbf{Ho}_{96}$

$$\begin{aligned} {}^{163}_{67}\mathbf{Ho}_{96} &\rightarrow {}^{163}_{66}\mathbf{Dy}^{*}_{97} + \nu_e \\ &\rightarrow {}^{163}_{66}\mathbf{Dy}_{97} + E_{EC}. \end{aligned} \tag{1.36}$$

The theoretical spectrum of E_{EC}, first described in [83], has a differential rate

$$\begin{aligned} \frac{\mathrm{d}\Gamma}{\mathrm{d}E_{EC}} &= C(Q_{EC} - E_{E_C})\sqrt{(Q_{EC} - E_{EC})^2 - m_\nu^2} \\ &\times \sum_H \phi_H^2(0) B_H \frac{\Gamma_H}{2\pi} \frac{1}{(E_{EC} - E_H)^2 + \Gamma_H^2/4}, \end{aligned} \tag{1.37}$$

with C absorbing the nuclear matrix element and the Fermi coupling, m_ν the effective electron neutrino mass. For each electronic level H a lorentzian line at energy E_H with width Γ_H contributes to the spectrum, where the relative amplitudes are given by the probability to find the electron at the nucleus in the origin $\phi_H^2(0)$. B_H then are exchange- and overlap corrections.

β^- decay

The β^- decay is a weak nuclear decay. It converts a neutron into a proton, an electron and an anti electron-neutrino.

$$ {}^A_Z X_N \rightarrow {}^A_{Z+1} X_{N-1} + e^- + \bar{\nu}_e. \tag{1.38} $$

On a fundamental level, a down-type quark converts to an up-type quark via emission of a W boson. The W boson then mediates between the first and second vertex, where an electron and an electron-anti-neutrino couple to it as depicted in the Feynman diagram in fig. 1.10. Neutrino, electron and nucleus share the decay energy. The nuclear recoil

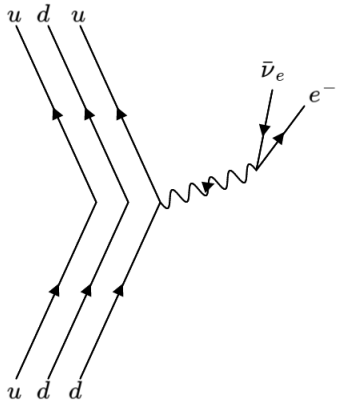

Figure 1.10: Feynman diagram of the β^- decay

can be largely neglected due to the much larger nuclear mass compared to the values of the electron and the neutrino. Since a fraction of the decay energy is needed to create the neutrino with its mass, the electron's spectral shape is influenced by the neutrino mass. Fermi's theory [5] gives for the energy spectrum

$$ \frac{dN}{dE} = C \cdot F(E,Z) p_e (E_e + m_e c^2)(E_0 - E_e) \sqrt{(E_0 - E_e)^2 - m^2_{\nu_e,\mathrm{eff}}} \tag{1.39} $$

$$ C = \frac{G_F}{2\pi^3} \cos^2 \Theta_C |M|^2. \tag{1.40} $$

Here E_e, p_e ,m_e denote the electron energy, momentum and mass, E_0 the endpoint energy and $F(E,Z)$ the Fermi factor that accommodates the electron's interaction with

the Coulomb potential of the nucleus. Other parameters are G_F, the Fermi constant, Θ_C, the Cabibbo mixing angle [43] between up- and down-quark states, and $|M|^2$, the nuclear matrix element. The main influence of the neutrino mass on the spectral shape originates from the phase space factor, since the Fermi function and the nuclear mass element are independent of $m_{\nu_e,\mathrm{eff}}$. In super-allowed decay processes the nuclear matrix element is also energy independent, simplifying the relation. Theoretically, highly sensitive experiments could resolve even the individual mass eigenstates in

$$m^2_{\nu_e,\mathrm{eff}} = \sum_i |U_{ei}|^2 m^2_{\nu_i}. \tag{1.41}$$

However by current means of technology this is not achievable due to the tiny mass splittings and the resolution achieved in spectroscopic experiments. While in principle the neutrino mass could be determined from the energy difference between the measured end of the spectrum and the theoretical endpoint E_0 for a vanishing neutrino mass, this is not feasible because the endpoint is not known precisely enough and the experimental sensitivity is limited by the background rate in the region of vanishing count rates. Instead, the mass is deduced from the relative shape of the spectrum near the endpoint. There, the neutrinos are not ultra-relativistic anymore and the neutrino mass influences the spectral shape.

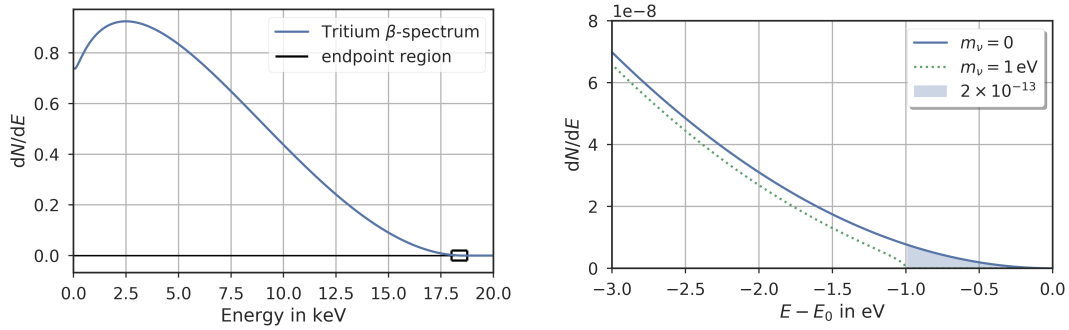

Figure 1.11: Left: Electron energy spectrum of tritium β-decay. **Right**: The neutrino mass manifests itself only in a narrow region close to the endpoint. Only a fraction of 2×10^{-13} of all decays yield electrons with energies in the last eV. This challenges neutrino mass measurements with the requirement of a high resolution spectral scan in a region of very low count rates.

1.4.5 Bolometric experiments

One approach to the neutrino mass pushed forward by several groups is the measurement of the β-spectrum using cryogenic micro-calorimeters. In this type of experiment the source simultaneously serves as the detector. After a beta decay a rise of temperature in the detector is measured by thermistors adjacent to it. The main benefit of this approach is the entire energy is deposited in the detector and thus can be measured. A drawback is that always the complete spectrum has to be measured simultaneously,

resulting in pile-up effects if the total decay activity is not kept sufficiently small, which limits the statistical sensitivity. Therefore it is important for these experiments to select a β-emitter with a low endpoint energy, where a larger fraction of the spectrum is close to the endpoint. Rhenium is a suitable β-emitter with the second-lowest known β-endpoint of 2.67 keV. The disadvantage is its exceedingly long half life of $T_{1/2} = 10^{10}y$, so large amounts of Rhenium are needed to provide sufficient activity for a neutrino mass measurement. Due to potential pile up effects this activity can not be put in one single detector, but an array of many small detectors has to be build. This approach was taken by the MIBETA experiment which found an upper bound on the neutrino mass of [84]:

$$m_{\bar{\nu}_e} \leq 15 \text{ eV (90\% C.L.)}. \tag{1.42}$$

As Rhenium is not an ideal calorimeter the groups previously involved are pursuing the measurement of the electron capture in ^{163}**Ho** instead. Holmium has a similarly low Q-value of $Q_{EC} = (2.555 \pm 0.016)\,\text{keV}$ but a much more favorable half-live of 4570 y, which will help with supplying a sufficient activity. Three collaborations are working towards a neutrino mass measurement with ^{163}**Ho**: ECHo [85], Holmes [86] an NuMecs [87]. They continue to use metallic micro-calorimeters (ECHo) or use transition edge sensors (Holmes, NuMecs).

1.4.6 Tritium experiments

Project 8

A recent alternative approach is to measure the Tritium beta spectrum by cyclotron radiation emission spectroscopy as proposed in [88]. The β electrons, when emitted in a magnetic field B, gyrate with their cyclotron frequency ω_c as

$$\omega_c = \frac{\omega_0}{\gamma} = \frac{qB}{m_e c^2 + E}. \tag{1.43}$$

There ω_0 is the unshifted cyclotron frequency, γ is the relativistic Lorentz factor, q the charge, m_e the electron mass and E the kinetic energy of the electron. For β electrons near the endpoint of 18.6 keV this results in a cyclotron frequency of about $f_c \cong 27\,\text{GHz}$. With suitable detectors the emitted radiation can be detected, though this is challenging due to the feeble power emitted in the range of femto watts. The Project 8 collaboration, nevertheless has achieved to detect the relativistic cyclotron radiation of single electrons [89] and is aiming to develop an atomic tritium source in the future [90].

Electromagnetic spectrometers

The strongest model independent and direct bounds on the neutrino mass have been set by the Mainz and Troitsk tritium experiments.

$$\text{Mainz} \quad : \quad m_{\nu_e} \leq 2.3 \text{ eV (95\% C.L.) [91]} \tag{1.44}$$

$$\text{Troitsk} \quad : \quad m_{\nu_e} \leq 2.05 \text{ eV (95\% C.L.) [92]} \tag{1.45}$$

by analyzing the tritium beta-decay (here in its atomic form[1]):

$$ {}^{3}_{1}\mathrm{T} \rightarrow {}^{3}_{2}\mathrm{He} + \mathrm{e}^{-} + \bar{\nu}_e \tag{1.46} $$

Tritium has a variety of benefits as β^--emitter for neutrino mass measurements, this is layed out in 2.2.1. Both Mainz and Troitsk made use of an electrostatic spectrometer and setup of the kind that the KATRIN experiment will take to its limits. Therefore the KATRIN experiment stands in the long tradition of tritium beta decay experiments [93–97].

[1]Note however that molecular tritium was (is) used in this type of experiments, including KATRIN

CHAPTER 2

The KATRIN Experiment

The **Ka**rlsruhe **Tri**tium **N**eutrino experiment [54] is targeted to perform a model independent measurement of the effective mass of the electron anti-neutrino, $m_{\bar{\nu}_e}$, with a design sensitivity of 200 meV (90% C.L.). The 70 m long apparatus, which is currently being commissioned [98] at KIT Campus North near Karlsruhe (Germany), is the successor to previous tritium neutrino experiments in Mainz [91, 99] and Troitsk [100, 101]. It stands in a long tradition of tritium β-decay measurements probing the neutrino mass scale [94–97]. Similar to these predecessors KATRIN will measure the shape of the tritium β-spectrum close to the endpoint of $E_0 \approx 18.6$ keV, however with unprecedented precision employing a large spectrometer of the MAC-E-filter type[1]. KATRIN uses a **W**indowless **G**aseous **T**ritium **S**ource (WGTS) that was recently commissioned at the Tritium Laboratory Karlsruhe (TLK), the only place in Europe with the necessary license to process and handle the required 40 g/day of molecular tritium in a closed loop in order to deliver a luminosity $> 10^{11}$ Bq for the KATRIN experiment. To improve the sensitivity on m_ν by one order of magnitude, as compared to predecessor experiments, KATRIN needs to improve on statistical and systematic uncertainties by two orders, as the shape of the tritium β-spectrum depends on the variable m_ν^2. This chapter gives an introduction to the basic measurement principle in section 2.1, a detailed description of the experimental setup and its different components in section 2.2 and a discussion on the experimental sensitivity and discovery potential in section 2.3.

2.1 Measurement Principle

As previously discussed, the neutrino mass can be extracted from the shape of the T β-spectrum close to its endpoint. Due to the very low signal rates in this region -

[1] **M**agnetic **A**diabatic **C**ollimation with **E**lectrostatic filter

only a fraction of 10^{-13} of all decays occurs within the last 1 eV of the spectrum - a high luminosity source and spectrometer are required. The source has to deliver as many signal electrons as possible while the spectrometer has to analyze a large fraction to provide sufficient statistics. Furthermore, a sharp energy resolution is needed for a precise analysis of the spectral shape. These requirements are met by the MAC-E-Filter principle that acts as a high-pass-filter for electrons with an energy eU, where e denotes the elementary charge and U the filter electric potential. The filtered (integral) spectrum will then be counted with a detector at different retarding potentials providing an *integral* measurement.

2.1.1 MAC-E filter

The MAC-E-Filter principle was first proposed by Picard et al. in 1992 [102]. A schematic drawing is displayed in figure 2.1. All of the different spectrometers (pre-, main- and monitor-spectrometer) in the KATRIN setup are built according to this principle. It works as a high pass filter for electrons through a combination of an axial-symmetric magnetic field and a retarding potential U_0 within the spectrometer. The magnetic field adiabatically collimates the electrons parallel to the electric field, which filters out all electrons with longitudinal energies below qU_0. The retarding potential acts as filter of electron momenta along the beamline, the z-axis, and can therefore only analyze the kinetic energy stemming from the Z-momentum $E_\parallel = \frac{p_z^2}{2m}$ at maximum potential. Ideally the kinetic energy

$$E_{\text{kin}} = E_\parallel + E_\perp \tag{2.1}$$

at the maximum of the retarding potential consists of $E_\parallel$ only with $E_\perp = 0$. The degree to which this ideal condition is not fulfilled will define the energy resolution of the spectrometer. The guiding magnetic field is generated by two solenoids on the beam axis at the entrance and exit of the spectrometer. Due to the Lorentz-force charged particles will be guided adiabatically on a cyclotron motion around the field lines. The particle's first adiabatic invariant

$$\gamma\mu = \frac{\gamma + 1}{2} \cdot \frac{E_\perp}{B} \tag{2.2}$$

is, to a high degree, conserved, with the relativistic Lorentz factor γ and the magnetic moment of the particle μ. Thus, in the non-relativistic regime, the orbital magnetic moment $\mu = E_\perp/B$ is conserved. Since the magnetic field strength drops by a factor of ∼20000 from the center of the solenoids to the mid of the spectrometer, $E_\perp$ is reduced accordingly. Consequently, the minimum of the magnetic field strength and the maximum of the retarding potential need to coincide at the center of the spectrometer. This requirement is called *transmission condition*, and the 2d surface of the spectrometer where it is fulfilled is called *analyzing plane*. An electron with zero longitudinal kinetic energy at the analyzing plane will not be transmitted but is reflected back to the source where it is absorbed. The electron energy can thus be determined except for the

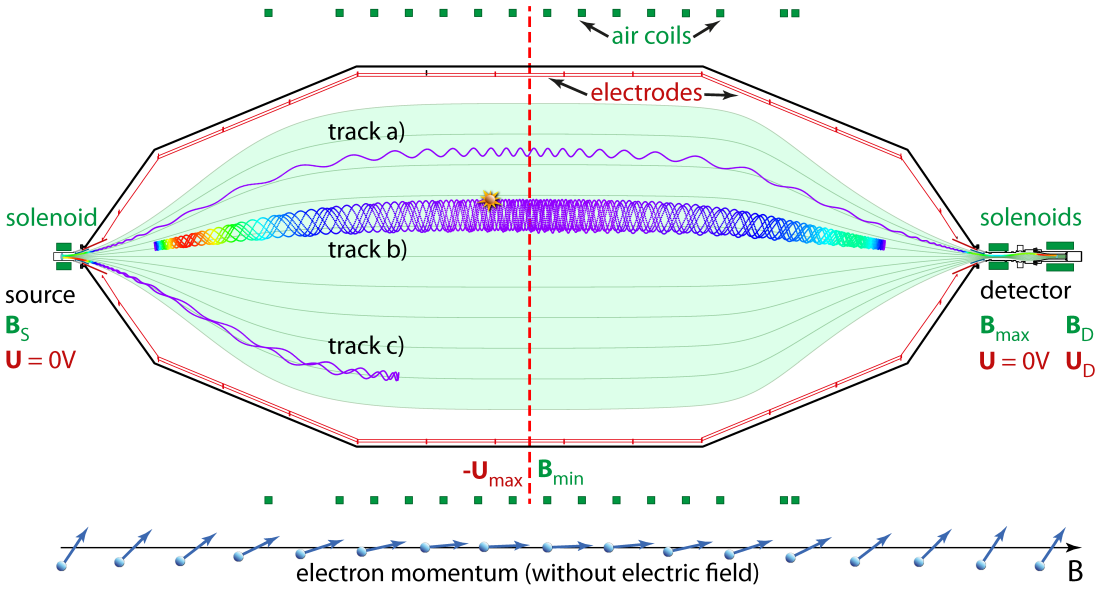

Figure 2.1: Scheme of the MAC-E-Filter. The three possible classes of electron trajectories are: a) Transmission from the source to the detector, b) magnetic storage of electrons created *inside* the spectrometer, c) Reflection of low energy electrons back to the source.

small fraction which remains in the transversal energy component. This is due to the fact that the magnetic field in the analyzing plane cannot be reduced to zero. From the conservation of μ we obtain

$$\frac{\Delta E}{E} = \frac{B_{\mathrm{min}}}{B_{\mathrm{max}}}. \tag{2.3}$$

At the tritium endpoint energy $E = 18.6$ keV, an analyzing magnetic field strength $B_{\mathrm{min}} = 3 \times 10^{-4}$ T together with a maximal field strength $B_{\mathrm{max}} = 6$ T, an energy resolution $\Delta E = 0.93$ eV is obtained, which corresponds the electron energy interval inaccessible by the MAC-E filter. Because this very good energy resolution requires a large decrease of the magnetic field, the flux tube has to widen substantially – necessitating the enormous dimensions of the KATRIN main spectrometer. In addition to the potential barrier there is the effect of *magnetic reflection* [103]: When electrons move along the magnetic field lines to a higher magnetic field, the perpendicular component of electron momenta is increased. Once a polar angle of 90° is reached the electron is magnetically reflected. The maximal accepted starting angle in the KATRIN source is given by

$$\theta_{\mathrm{max}} = \arcsin\left(\sqrt{\frac{B_{\mathrm{S}}}{B_{\mathrm{max}}}}\right) = 50.77° \tag{2.4}$$

for $B_{\mathrm{S}} = 3.6$ T (denoting the starting magnetic field strength) and $B_{\mathrm{max}} = 6$ T. This particular value is a design choice: in principle the angular acceptance of a MAC-E-filter

can read up to 2π. However, electrons with a large polar angle are less favorable in the neutrino mass analysis because of their larger path length in the WGTS and hence scattering probability in the source. Due to the corresponding larger energy losses, they would contribute significantly to the systematic uncertainty of the measurement.

2.1.2 Transmission function

All effects influencing the transmission of electrons through the spectrometers manifest themselves in the *transmission function*. In its simplest form it gives the transmission probability depending on the electron starting energy and the retarding potential. Similary, the *response function* take into account also effects from the source. The transmission function is highly sensitive to the interplay of electric and magnetic fields and can be resolved in many different ways, introducing angular, radial and further dependencies. In the ideal case it would yield a Heavyside function: only electrons above the energy threshold are transmitted. Using the assumptions of adiabacity, i.e. a conservation of the orbital magnetic moment, and an isotropic angular distribution for the source, the transmission function can be derived analytically. With the magnetic field strength at the source B_S, the electron start energy E, the analyzing potential U_0, electron charge q, maximal (pinch) magnetic field strength B_max and magnetic field in the analyzing plane B_A the transmission function can be written as:

$$T(E, qU) = \begin{cases} 0 & \text{if } E - qU_0 < 0 \\ \dfrac{1-\sqrt{1-\frac{E-qU}{E}\cdot\frac{B_\mathrm{S}}{B_\mathrm{A}}}}{1-\sqrt{1-\frac{B_\mathrm{S}}{B_\mathrm{max}}}} & \text{if } 0 < E - qU < \Delta E \\ 1 & \text{if } \Delta E < E - qU \end{cases} \tag{2.5}$$

The transmission probability strongly depends on the electron's starting angular distribution. Electrons at higher starting polar angles require more energy to be transmitted, as their transformation of $p_\perp$ into $p_{||}$ is less efficient.

2.1.3 Response function

As discussed above, the probability for electron transmission through the spectrometer is given by the transmission function T. This information, however, is not sufficient to determine the tritium β-spectrum from a measurement, since scattering in the source is completely unaccounted for. For design values of the column density ρd only about 40% of all decay electrons at the 18.6 keV endpoint will reach the spectrometer without undergoing inelastic scattering off the tritium molecules in the WGTS. This is why the *response function* of the experiment needs to be considered (see fig. 2.2, right). It is a convolution of the source and spectrometer properties reflecting the transmission properties of the spectrometer section and the scattering probabilities in the source. The scattering is characterized by the (normalized) energy loss function

$$f(\Delta E) = \frac{1}{\sigma_\mathrm{tot}} \frac{d\sigma}{d(\Delta E)}. \tag{2.6}$$

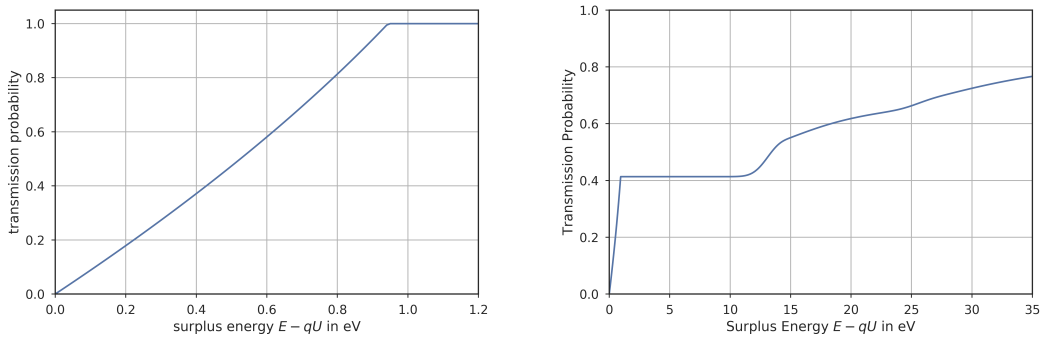

Figure 2.2: Left: Transmission function for electrons propagating along the beam line, emitted by an isotropic source. This transmission function is already normalized to $P = 1$ at large surplus energies, taking into account magnetic reflection for starting angles above 50.1°. **Right**: KATRIN response function at reference values for the magnetic field B and tritium column density ρd: $B_{\mathrm{S}} = 3.6\ T$, $B_{\mathrm{min}} = 3 \cdot 10^{-4}\ T$, $\rho d = 3 \cdot 10^{17}\ \mathrm{cm}^{-2}$. The two bumps indicate the thresholds of one-fold and two-fold inelastic scattering. Below 10 eV the response function coincides with the transmission function since this is the minimum energy loss for inelastic scattering on tritium. Minor changes to the shape originate from the altered angular distribution.

.

with ΔE being the energy loss and σ_{tot} the total scattering cross section. The energy loss function also features an angular dependence. However this fact is negligible for small energy losses of electrons within the analysis range of 30 eV below the endpoint. The response function can be obtained by convoluting the transmission function with the electron energy loss probability distribution $f(\epsilon)$:

$$R(E, qU) = \int_0^{E-qU} T(E - \epsilon, qU) \cdot \left(\bar{P}_0 \delta(\epsilon) + \bar{P}_1 f(\epsilon) + \bar{P}_2 (f \otimes f)(\epsilon) + \dots \right) d\epsilon \qquad (2.7)$$

Here P_n is the probability of n-fold scattering. For the case of no scattering the energy loss distribution is a δ function, for one scattering it is $f(\epsilon)$ and in the case of two or more scatterings it is the n-fold convolution of $f(\epsilon)$ with itself. The general shape of the response function is shown in figure 2.2. The energy loss function found in the literature is not known precisely enough for a theoretical determination of the response function. Therefore it will be determined in a separate measurement before the dedicated tritium measurements. This will be done using mono-energetic electrons provided by the rear section (see 2.3.2). Since there exist radial as well as azimuthal inhomogeneities in the experiment, the response function needs to be determined over the whole cross section of the source. Radial dependencies are introduced by the density profile of the WGTS, azimuthal ones by violations of the rotational symmetry (e.g. disturbances of the magnetic field by remanent magnetization of the steel or the earth magnetic field).

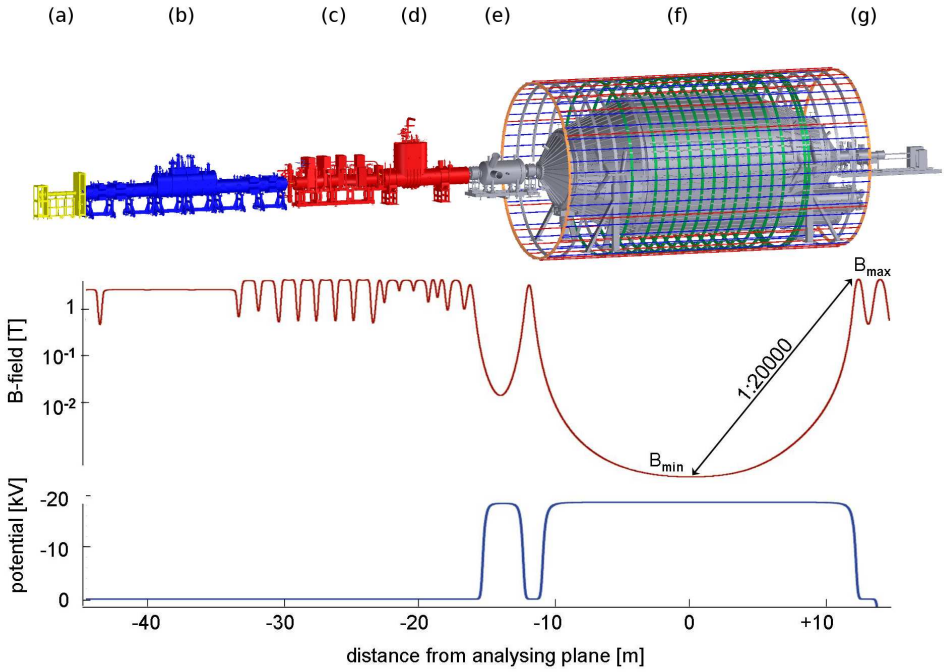

Figure 2.3: The 70 m long KATRIN experimental setup, together with the magnetic field and electric potential along the Z-axis. In different colors: **a)** the rear section (yellow) for monitoring the source potential, **b)** the WGTS (blue) acting as high luminosity tritium source, **c)** the **D**ifferntial **P**umping **Section** and **d)** the **C**ryogenic **P**umping **S**ection (both red) to suppress inflow of tritium into the spectrometers, the Spectrometer-Detector-Section (SDS grey) consisting of **e)** the pre spectrometer for filtering out the low-energy part of the β-spectrum, **f)** the main spectrometer for high resolution analysis of the β-spectrum and **g)** the focal plane detector for counting the transmitted electrons. Figure from [104]

2.2 Experimental Setup

KATRIN combines an extremely stable high-luminosity molecular tritium source with a variable and precise MAC-E-filter. By counting the transmitted electrons at various retarding potentials an integrated β-decay spectrum can be recorded. Figure 2.3 displays a schematic drawing of the experimental setup with its different subsections: the source, transport section, spectrometers and detector.

2.2.1 Tritium source

KATRIN employs a **W**indowless **G**aseous **T**ritium **S**ource[105], where molecular tritium decays according to

$$^{3}_{1}\mathrm{H} \rightarrow ^{3}_{2}\mathrm{He} + \mathrm{e}^{-} + \bar{\nu_e} \tag{2.8}$$

Figure 2.4: CAD drawing of the WGTS including the DPS-1F and DPS-1R on seperate stands.

The hydrogen isotope tritium as β-source has a number of advantages for measuring the neutrino mass:

- Tritium has a comparably **low endpoint of 18.6 keV**. Since the total activity of the source scales as $\Gamma \propto Q_0^4$ and the relative fraction of electrons in the vicinity of the endpoint as $\Gamma \propto Q_0^{-3}$ a moderate dependence of the rate in the region of interest on Q_0 results.
- ${}^3_1T$ **has a short half life of only 12.3 a.** This ensures a high rate per mol, allowing to operate at low source densities of a gaseous source. This is a great benefit for systematic uncertainties due to scattering effects of the electrons in the source.
- The transition ${}^3_1\mathrm{H} \rightarrow {}^3_2 He$ **is a super-allowed β-decay** between mirror nuclei. As a consequence, the transition matrix element is easy to compute, energy independent and rather large.
- ${}^3_1\mathrm{H}$ **has the lowest possible Z value** and thus a simple electronic structure. This is advantageous for the computation of the final state spectrum and scattering processes, both very important for the understanding of source systematics. Also the resulting cross section for inelastic scattering is small in the multi-keV region.

Besides providing a high luminosity, the KATRIN source needs to feature very low and well understood systematic uncertainties. The WGTS will reach an activity of $\sim 10^{11}$ Bq by injecting cold (27° K) high purity ($\geq 95\%$) tritium gas in the center of the 10 m long, 90 mm diameter stainless steel beam tube. Tritium molecules will diffuse, from their point of injection in the center of the WGTS to both ends, resulting in an overall column density of $\rho d = 5 \cdot 10^{17}$ cm^{-2}. At each end of the WGTS, a 3 m long pumping section (DPS-1F, DPS-1R) will pump out the tritium gas with TMP's

and re-inject it in the closed tritium (inner) loop [106] for purification. This measure already reduces the tritium flow from the source to the adjacent sections by two orders of magnitude.

Because the column density defines the overall source luminosity it has to be known very precisely, where deviations of 0.1% or lower can be tolerated. This in turn leads to stringent requirements for the source temperature. Consequently, the allowed fluctuations have to stay below $\Delta T \leq 30$ mK. The required cooling will be provided by a two phase neon system that has already was tested at the WGTS demonstrator [107, 108] and actually outperformed this bound [109]. Recent commissioning tests with the final cryostat have reached a comparable performance [110].

The temperature regime of 27° K is required to minimize the tritium throughput and suppress the formation of molecular clusters. On the other hand it minimizes Doppler shifts that broaden the β-spectrum and contribute to the systematic uncertainty of the spectrum. It is the lowest possible temperature without the tritium molecules starting to cluster, which again would raise the systematics.

Further systematic uncertainties include fluctuations of the tritium purity and the final state distribution of the $^3HeT^*$ daughter molecules. The final state distribution arises from rotational, vibrational and electronic excitations that modify the β-electrons energy. Precise calculations of the final state distribution are needed to account for this [111]. To correct for changes in the tritium purity the Laser Raman system LARA [112, 113] is operated at TLK will provides a fast determination of the isotopic composition of the tritium gas by Raman spectroscopy.

In the WGTS the decay electrons are guided by a 3.6 T magnetic field created by several superconducting solenoids around the beam tube. It forms a magnetic flux tube of 229 Tcm^2 over the whole source cross section. However, only an inner flux tube of 191 Tcm^2 (corresponding to 3.3 T, the magnetic flux at the detector) will be analyzed since in the outer parts scattering processes at the walls can occur which disturb the measurement. The electrons thus travel to both ends of the WGTS, leaving either towards the transport section or the rear section. So half the activity can be later on analyzed in the spectrometer section - the true acceptance, however is lower, taking into account the higher magnetic field in the pinch magnet of the spectrometer and the resulting acceptance angle of 50.77°.

2.2.2 Rear section

The Rear Section (see fig. 2.5), situated at the back end of the DPS1-R, will serve several purposes:

- monitoring the source activity by **B**eta **I**nduced **X**-ray **S**pectroscopy BIXS [114]
- defining the source potential via the Rear Wall in case of plasma conditions,
- measuring the column density with an high intensity electron gun,
- mapping the KATRIN response function and energy loss distribution across the whole flux tube using the electron gun.

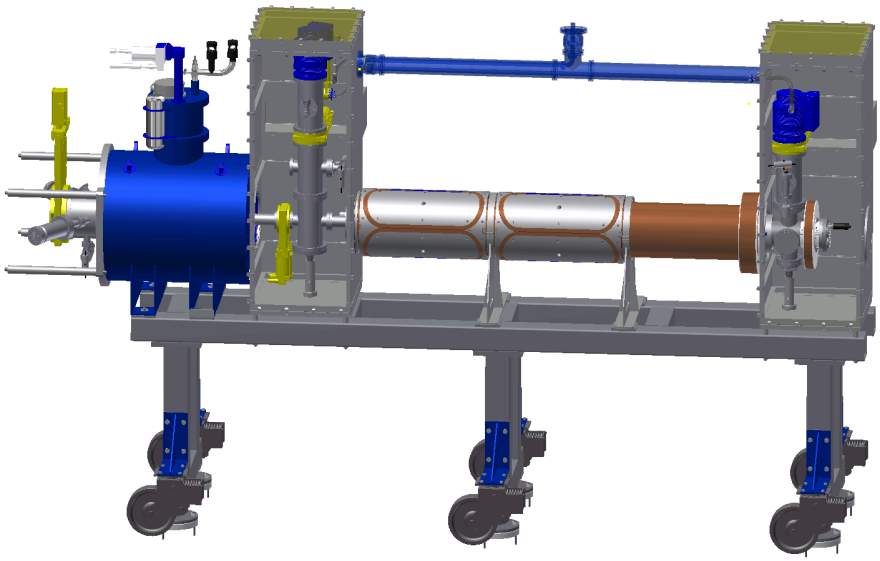

Figure 2.5: Technical design of the Rear Section.

The potential will be set by the Rear Wall that also functions as target for the BIXS. Through a small central hole in the Rear Wall electrons from the electron gun will be allowed to enter the beam tube. They can be used to measure the response function, while photo-electrons from UV-illumination of the rear wall keep the tritium plasma quasi-neutral. A full scan of the flux tube in the WGTS will be possible with the use of additional magnetic dipoles there for deflection. These measurements will be done repeatedly and allow a close monitoring of the source parameters, which is very important to control systematic effects [105].

2.2.3 Transport section

The transport section consists of two subsystems: the **D**ifferential **P**umping **S**ection (DPS) and the **C**ryogenic **P**umping **S**ection (CPS). Both have the same general purpose, a reduction of the tritium flow from the source to the spectrometers by 14 orders of magnitude and an adiabatic guidance of the electrons to the spectrometer section.

A small tritium inflow to the main spectrometer would lead to a significant increase in background, severely hampering the KATRIN sensitivity. A partial pressure of less than 10^{-20} mbar [115] in the main spectrometer is required to keep this background lower than 10^{-3} cps [116].

Differential Pumping Section

The DPS (see fig. 2.6) will reduce the tritium flow by five orders of magnitude. For this purpose it uses four large Turbo Molecular Pumps (TMPs) housed in pump ports between the five superconducting solenoids that create the guiding magnetic field in

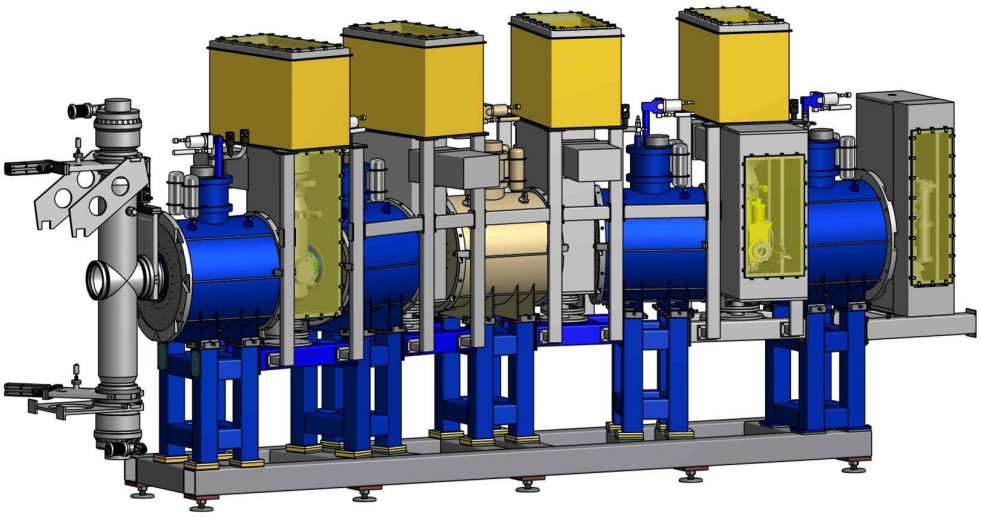

Figure 2.6: DPS with its five solenoids for adiabatic guidance of the electrons in a magnetic field of up to 5.5 T. Four TMPs are used for tritium retention.

the beam tubes. These run through the warm bores of the solenoids and are, as the solenoids, tilted by 20° with respect to each other. This prevents a direct line of sight between source and spectrometer section, avoiding the molecular beaming effect [117]. The DPS is instrumented with extra units to measure and remove ions from the flux tube as these are neither pumped by the TMPs nor blocked by the tilting because they follow the field lines. The ion content will be determined with an FT-ICR [118, 119] (Fourier Transform Ion Cyclotron Resonance) unit: ions are caught in a Penning trap and their cyclotron frequency is measured. As they circle around in the trap, the periodically induced charge on a close electrode is measured. A Fourier transform of the signal gives the charge/mass spectrum. Ion removal is done - similar to methods used in the spectrometers - by an electric dipole field. The resulting $\vec{E} \times \vec{B}$-drift moves the ions to the wall over the course of several passes. To that end, special electrodes are integrated into the system [120, 121]. This large effort is necessary, because the β-decay in the source creates a large number of various ion species. The decay products ${}^{3}_{2}\mathrm{HeT}^{+}$ can dissociate and combine with other hydrogen isotopologues in the source.

Cryogenic Pumping Section

The tritium flow at the end of the DPS cannot be reduced further with TMPs, so an additional (passive) pumping section is needed, now based on the principle of cryosorption: The **C**ryogenic **P**umping **S**ection (CPS), shown in fig. 2.7. It reduces the tritium flow towards the spectrometers by seven orders of magnitude at least [117, 122], so that the overall tritium retention from the WGTS to the spectrometer section will be a factor of 10^{14}. The inner surfaces of the beam tubes of the CPS are held at 3 K

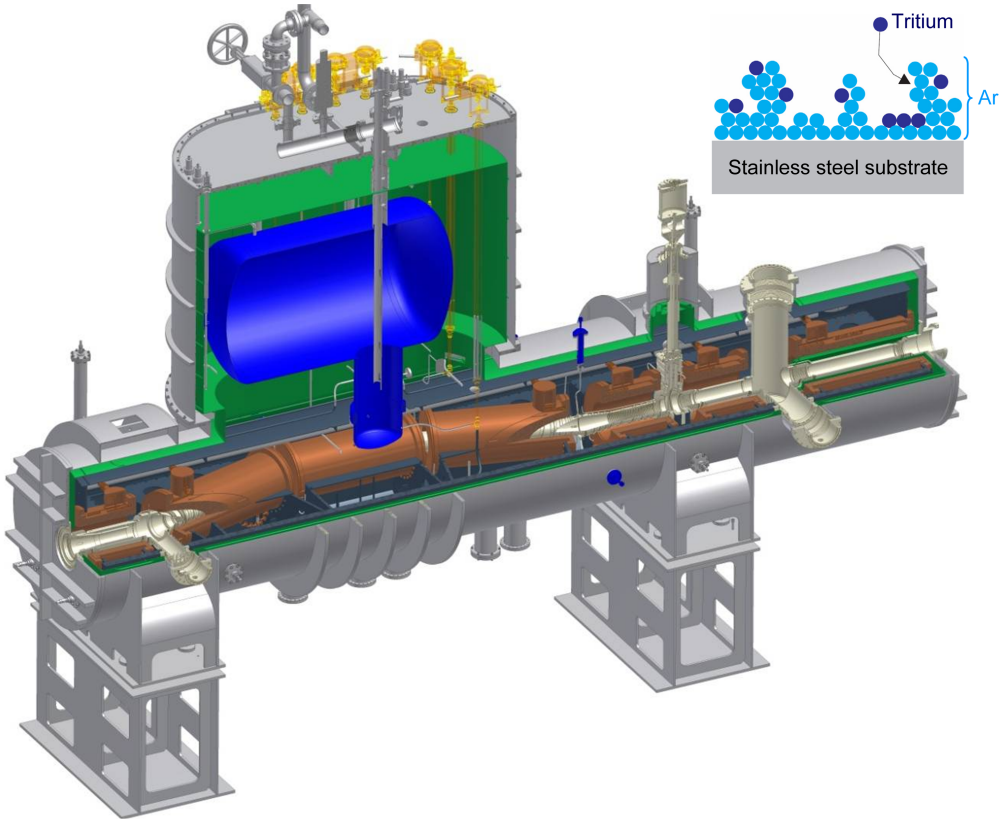

Figure 2.7: Cryogenic Pumping Section. The bulge on the top houses the liquid helium reservoir (blue) surrounded by the liquid nitrogen heat shield and reservoir (green). The beamtube (brown) follows the magnetic chicane designed to block tritium ions. Image taken from [115]

and are covered by argon frost. This strongly enlarges the total inner surfaces and thus enhances the pumping characteristics. Any tritium or hydrogen molecule that hits the wall will stick to it. Like the DPS the cryostat uses tilted beam tubes to prevent molecular beaming. A total of seven superconducting solenoids creates the magnetic guiding field for signal electrons.

2.2.4 Spectrometer section

The KATRIN experiment uses altogether three spectrometers, all built according to the MAC-E-Filter principle layed out in section 2.1.1. Whilst the pre- and main spectrometer are set up in line with the source and the detector to filter the β-decay signal electrons, the monitor spectrometer resides in a separate building. Its purpose is to monitor the high voltage of the main spectrometer. All three spectrometers are described in the following.

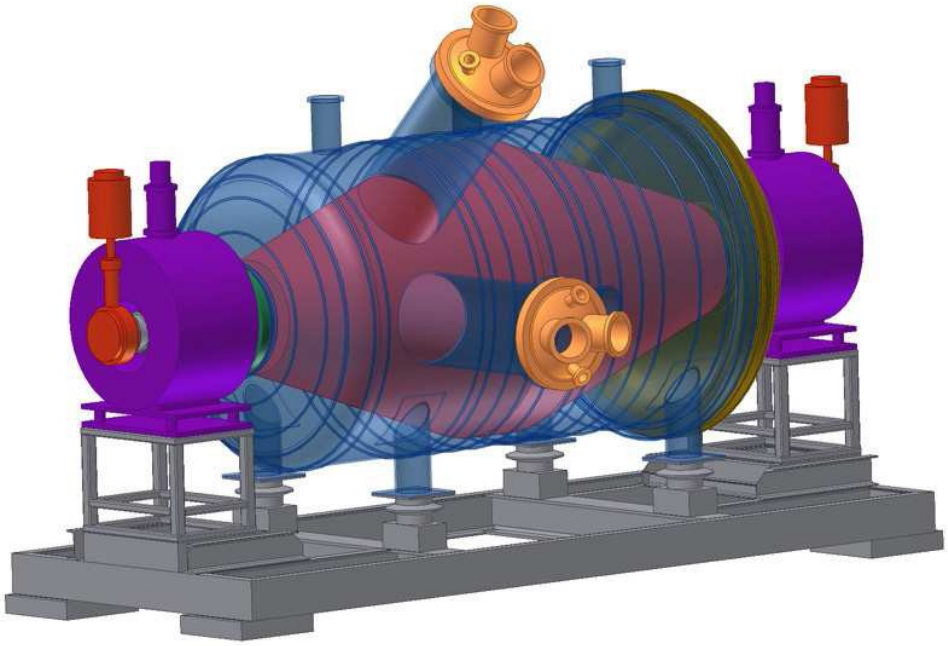

Figure 2.8: The pre-spectrometer vessel (blue), with the two solenoids (purple), and the inner electrode system (red).

Pre-spectrometer

The pre-spectrometer (see fig. 2.8) is set up to pre-filter the low-energy part of the β-spectrum that contains no information about the neutrino mass, as the effect of the neutrino mass only is visible in the last few electron volt below the endpoint. It is located between the CPS and the main spectrometer. Its two solenoids achieve a maximum magnetic field in the solenoids of 4.5 T and its inner electrode operates at a retarding potential of -18.3 kV. In this setting the electron flow into the main spectrometer is reduced by a factor of 10^7 [123]. The pre-spectrometer was used initially to test techniques later incorporated in the main spectrometer and for research into background generation mechanisms of MAC-E-filters. This includes methods of active (magnetic pulse [124], electric dipole [125], ECR [126]) and passive (cryo-baffles) background reduction [127]. Most importantly, the radon isotopes ^{219}Rn and ^{220}Rn) emanating from the steel of the vessel as well as from the getter pumps were identified as a significant source of background and suitable design decisions for the Main Spectrometer could be made.

Main Spectrometer

The Main Spectrometer poses a particular technical and engineering challenge due to its enormous dimensions. With a length of 23.6 m and a diameter of 10 m, its total volume amounts to 1250 m^3, not including the LFCS and EMCS air coil systems surrounding it

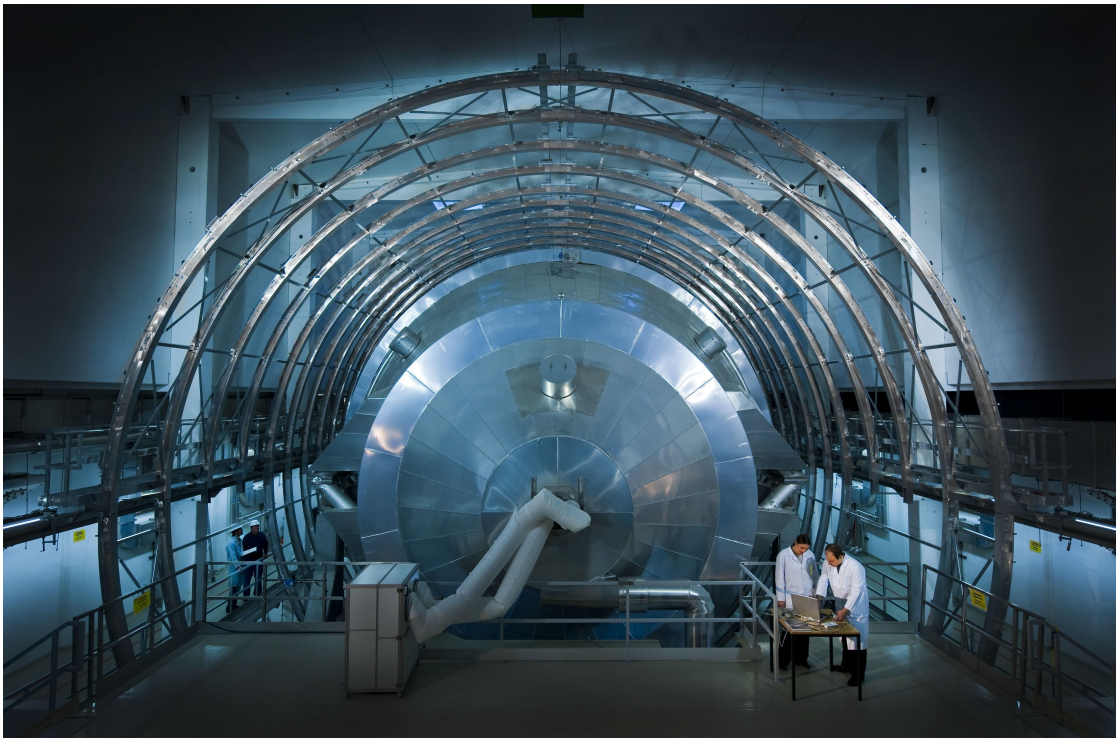

Figure 2.9: The KATRIN main spectrometer surrounded by the air coil system. (photo: KIT)

(see fig. 2.9).

The scale of the spectrometer is directly connected to the required energy resolution. Since the resolution depends on the ratio of $\frac{B_{\text{min}}}{B_{\text{max}}}$, the magnetic field has to drop by a factor of 20000 from the pinch magnet to the analyzing plane. This leads to a drastic widening of the flux tube.

The magnetic guiding field is created in part by 4 solenoids: the 2 pre-spectrometer solenoids PS1 and PS2, the pinch solenoid PCH, capable of B-fields up to 6 T, and the detector magnet DET, responsible for the precise imaging of the flux tube onto the detector. In addition a large air coil system [128], consisting of 14 coils surrounding the vessel, is needed to fine tune the magnetic field in the analyzing plane where the design magnetic field is as low as $\sim$ 300 μT. Therefore, the influence of the earth magnetic field, with a total field strength of 48 μT cannot be neglected. Consequently, an Earth Magnetic Field Compensation System (EMCS) was implemented [129].

In contrast to the Mainz and Troitsk experiments, the vessel of the Main as well as the Pre-spectrometer is put on HV and an inner electrode system is used to fine shape the retarding potential. In case of the main spectrometer, this electrode system is nearly massless: it consists of 24000 thin (200-300 μm) wires organized in 248 modules in a double layer configuration [130, 131]. It is designed to create a high precision and very homogeneous potential in the spectrometer volume as well as to shield the volume from background electrons originating from the wall that are induced by cosmic rays

[132, 133]. The screening is achieved by running the two layers of wires on different potentials where only the inner wire layer is set to the full analyzing potential.

Besides the electromagnetic field the most challenging demand on the main spectrometer is to achieve an ultra high vacuum (UHV) of $< 10^{-11}$ mbar in a volume of $1250\,\mathrm{m}^3$. This is necessary to ensure that the signal electrons are not perturbed by scattering off residual gas on the one hand. On the other hand, it suppresses an important mechanism of background generation: cascades of secondary electrons are induced when stored electrons scatter off residual gas molecules and ionize them. The vacuum system consists of 6 cascaded TMPs (Leybold MAG-W-2800) and 7 km of non-evaporable getter (NEG) strips SAES St707. The TMPs pump out all gases including hydrogen with a pumping speed of $\geq 10^4\ \ell/\mathrm{s}$. For hydrogen, the dominant gas in the main spectrometer, however, the passive NEG pump is much more powerful with a pumping speed of $10^6\ \ell/\mathrm{s}$ [134–137].

Over the course of this thesis the commissioning of the Main spectrometer from outbaking, alignment, background studies to first transmission measurements with an angular resolved e-gun as source took place. This was an important step towards the completion of the KATRIN experiment. The background studies and measurements of the main spectrometer form an important part of this thesis and will be reported on in chapter 5.

Monitor spectrometer

The monitor spectrometer is the former spectrometer of the Mainz experiment, that is now housed close to the KATRIN beamline in a separate building. The distance between the beam lines is so that it minimizes the influence of stray fields on the transmission properties of the main spectrometer. Its purpose is to monitor the HV of the Main Spectrometer. Since the retarding potential defines the energy threshold of the transmission, this parameter has to be known very precisely and stabilized at the ppm level to reach the design sensitivity. The monitor spectrometer's retarding potential is fed by the same voltage as the MS. It uses a quench condensed krypton source as nuclear standard. By a continuous measurement of the $^{83\mathrm{m}}$Kr conversion lines, small shifts of the lines will indicate fluctuations of the HV [138–141]. The monitor spectrometer is equipped with a silicon PIN-diode detector, an EMCS as well as four air coils. It is operational and taking data since 2012 [142, 143].

The voltage will independently be measured with the help of precision HV dividers developed in cooperation with the Physikalisch-Technische Bundesanstalt in Braunschweig [144]. These are stable on the ppm level and give an output voltage of less than 10 V suitable for state-of-the-art precision volt meters [145].

2.2.5 Focal plane detector

The **F**ocal **P**lane **D**etector (FPD) is situated at the downstream end of the main beam line (see fig. 2.11). It consists of a 90 mm diameter 148 pixel silicon PIN-diode wafer to count the small number of electrons ($\sim 10^{-2}$ cps) typically transmitted through

Figure 2.10: Picture of the operational monitor spectrometer which is the repurposed setup of the Mainz experiment. It has two solenoids and three aircoils. (photo: M. Erhard [140])

the spectrometers. These small rates put high demands on the detector efficiency and intrinsic background rate. To achieve a low background of less than 10^{-2} cps, passive measures such as lead shielding and careful material selection aiming at a low intrinsic radioactivity have been taken and are supported by an active muon veto system. A post acceleration electrode is installed and allows to shift the signal by up to 10 keV into a region of lower background and higher signal amplitude. The detector has a moderate energy resolution of 2 keV (FWHM) at 18.6 keV to discriminate between background and signal electrons. It is equipped with two sources for energy calibration, an ^{241}Am γ-source and a UV-illuminated titanium disk for electrons of energies up to 25 keV [146].

2.3 Neutrino mass sensitivity

As the KATRINs experiment targeted sensitivity to measure the effective anti-neutrino mass $m_{\bar{\nu_e}}$ is $m_\nu \leq 200$ meV (90%C.L.) the KATRIN uncertainty budget may not exceed a value of

$$\sigma_{\text{abs}} = \sqrt{\sigma_{\text{sys}}^2 + \sigma_{\text{stat}}^2} \leq 0.025 \text{ eV}^2. \tag{2.9}$$

To extract the neutrino mass from the measured rates a comparison with theoretically expected rates needs to be done. Since KATRIN measures a convolution of the differential energy spectrum $\frac{dN}{dE}$ with its response function R, the expected signal rate is

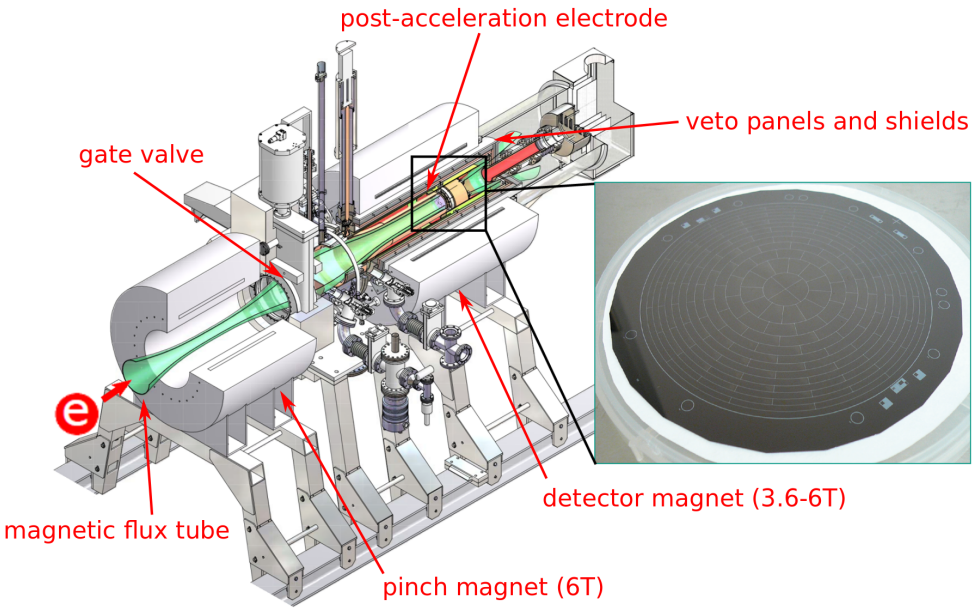

Figure 2.11: Scheme of the FPD system and a picture of the detector wafer before integration. Image taken from [147]

calculated according to

$$N_s(qU, E_0, m_\nu) = N_{\text{tot}} \cdot t_U \cdot \int_0^{E_0} dE R(E, qU) \frac{dN}{dE}(E_0, m_\nu) \tag{2.10}$$

where N_{tot} is the number of tritium nuclei in the source and t_U the measuring time at the potential U. Taking into account a constant background N_b with a signal-to-noise ratio R_s/R_b we obtain

$$N_{\text{model}}(qU, E_0, m_\nu, R_s, R_b) = R_s N_s(qU, E_0, m_\nu) + R_b N_b \tag{2.11}$$

To extract the neutrino mass, the free parameters E_0, m_ν, R_s and R_b have to be fitted as well.

2.3.1 Statistical uncertainty

The design value of the statistical uncertainty is $\sigma_{stat} = 0.018$ eV^2. This corresponds to a pure measurement time of three years which results in five calendar years runtime including maintenance and calibration. A low background rate is key to achieving a good statistical uncertainty. Not only the rate, but also possible time- and energy-dependencies have a big influence on the statistical uncertainty. Also, depending on the background the measurement time distribution for the different retarding potentials needs to be optimized, to push the statistical uncertainty as low as possible. While close to the endpoint the sensitivity to the neutrino mass is largest, the very low count rates

there also require low background rates. Further away from the endpoint, the signal rates are larger, but the influence of the neutrino mass gets significantly lower, enforcing longer measurement times for the same sensitivity. Also, systematic uncertainties due to scattering of the signal electrons gets bigger further away from the endpoint.

Multiple possible sources of backgrounds have to be under control in the KATRIN experiment:

- **Detector background**: due to the keV-scale energy resolution of the detector, events around the endpoint region contribute to the background. However a post-acceleration electrode is installed to shift the region-of-interest (ROI) to regions of lower intrinsic background, if necessary.

  Cosmic particles hit the detector and deposit energy in the wafer and its surroundings, thereby creating background events. A muon veto system is in place to filter out most of the μ-induced activity from the data set.

  Nuclear decays can occur due to residual radio-active nuclei in the detector. To prevent this the detector materials were selected very carefully.

  High-energy photons can originate from natural radioactivity in the surrounding.

- **Spectrometer background**: Since all electrons that reach the detector from the inside of the spectrometer are accelerated by the analyzing potential, any low energetic electron is pushed to the investigated energy and presents potentially dangerous background.

  Secondary electrons from cosmic particles or gamma radiation can hit the spectrometer vessel, and especially the inner electrodes. Electrons from the vessel are predominantly shielded by the axial symmetric magnetic field, and to a lesser extent by the 200 V potential difference between vessel and inner electrode (IE). Low-energy electrons from the IE, however, also are accelerated into the ROI.

  Field emission due to imperfect surfaces at the IE would also produce low-energy electrons similar to cosmic rays. Much care was taken to prevent this in the design and construction of the inner electrode system.

  Radioactive decays (from the α-active radon) in the volume of the main spectrometer create electrons that are stored in the magnetic bottle inherent to the field configuration of the spectrometer, and escape randomly onto the detector. Tritium β-decays play no role due to the transport section that suppresses the tritium flow by 14 orders of magnitude. An important source are radon isotopes emanating from the material of the getter pump (^{219}Rn) or the walls (^{220}Rn).[104, 148–151]

  Stored particles can cool down by ionizing the residual gas in the spectrometer and to create secondaries, which can themselves be stored.

  Penning traps store particles locally and can generate huge background rates through Penning discharges. They have to be avoided by careful electromagnetic

design.

2.3.2 Systematic uncertainty

The systematic uncertainty of the KATRIN experiment on the (squared) neutrino mass is aimed to stay below $\sigma_{\text{sys}} \leq 0.017$ eV. To achieve this, the key parameters like the retarding voltage and source activity have to be controlled thoroughly. Systematic effects that have to be taken care of are [54, 152, 153]

- Radiative corrections to the theoretical beta spectrum
- Corrections to the spectrum from the final state distribution of the helium daughter molecules
- Corrections to the spectrum from nuclear recoil
- Corrections to the spectrum from Doppler-broadening due to the thermal and bulk motion of the tritium molecules
- Scattering of signal electrons in the WGTS (or transport section)
- Synchrotron losses of signal electrons during the transport
- Variations in the source activity. These will be monitored by the Rear Wall BIXS system and the LARA-system and also kept small by the temperature and injection stability of the WGTS
- Variations of the retarding potential. These will be monitored by the monitor spectrometer.
- Non-Poissonian variations of the background rate.
- Any non-adiabatic effects of electrons.

CHAPTER 3

Simulation Software: The KASPER Package

Computer simulations are a necessary tool for detailed investigations in any modern experiment. At KATRIN they are used to investigate e.g. the spectroscopic properties of the MAC-E-Filter, the expected tritium β-spectra, electron scattering in the source, electron or ion transport, background generation from radon decays or cosmic muons. All aspects of KATRIN are covered by simulations to ensure a precise understanding of all effects that have an influence on the neutrino mass measurement.

In this chapter an overview of the KASPER software package is given. It is developed in collaboration between UNC, MIT, University of Münster and KIT and integrates different algorithms needed for field computations, particle tracking, scattering, source- and detector simulations into a unified suite that is easily extendable and configurable via XML. The KASPER software package includes the particle tracking program KASSIOPEIA [124, 154–156], the electric and magnetic field computation framework KEMField [125, 157, 158], the near time analysis software BEANS, the geometry tool KGeoBag [155], the database access module KALI [152] the source simulation SSC [153] and the fitting toolkit KaFit [152]. A brief introduction into electric and magnetic field computations with KEMField is given in sect. 3.2 and the zonal harmonic expansion is discussed. The KASSIOPEIA program is discussed in sect. 3.3 since it is used later on to investigate background generation in the main spectrometer. Detailed discussions of these tools have been given in the respective publications and theses. Here new contributions will be the focus. A large structural change was the unification of the various toolboxes together with the introduction of a single uniform commandline interface for all applications within KASPER. Beyond that the physical models of electron hydrogen scattering to be discussed in chapter 4 and Rydberg interactions in chapter 5 were integrated into KASSIOPEIA. Single additions include

- a tool to generate the region of convergence of KEMField's zonal harmonic expansion as a geometrical object within KASSIOPEIA so it can be used to confine the

simulation to the region where the field computation is fast.

- an extension to provide truly particle-state dependend configuration, KSModifier.
- An event generator for the electron emission of ^{210}Pb decays.
- many bugfixes and small changes not mentioned further.

3.1 General Design Principles

KASSIOPEIA established the XML Format for configuration files within KASPER. Soon KaFit and SSC made use of it too, but used their own commandline tools and toolbox systems. KEMField on the other hand remained by itself unintegrated from the XML System. Only within KASSIOPEIA that interface was provided, which was disadvantageous because it created a close coupling between the two programs. At the core of this framework is the Toolbox, which stores and manages all the different objects that are created during the process of configuration. Now it is implemented as a (C++) singleton class that stores shared pointers to the objects in two hashmaps, once by their unique (user-given) name and once by a tag which may point to a set of several objects. Previously these were different classes for KaFit, SSC and KASSIOPEIA using different data structures, providing different functions for object retrieval, which hindered development of new tools that use parts of all programs and complicated the already existing interoperation. Wrapper code for KEMField existed multiple times because it did not adhere to that system. Through extensive refactoring of the existing code these were unified and the XML system extended to KEMField.

3.2 KEMField

KEMfield [125, 157] is the field computation module integrated into the KASPER package. It can operate with three dimensional geometries, exploit axial symmetry, provides support for MPI and GPUs (via OpenCL). Geometry input is possible through KGeoBag in XML input files or legacy plain text files for compatibility. However, KEMField provides by far the most advanced and comfortable framework for field computations within KASPER, integrating all of the functions of the earlier field codes. What so far is not implemented in KEMField are the Biot-Savart and magnetic dipole methods needed for precise calculations of the EMCS-Field and the inhomogeneities induced by magnetic materials.

3.2.1 Electric field computation

KEMField performs electric field computation using the **B**oundary **E**lement **M**ethod (BEM[159, 160]). The following linear equation is to be solved

$$U_i = \sum_j C_{ij}\sigma_j, \tag{3.1}$$

where U_i is the voltage applied to an electrode, σ_i the charge density that results from this voltage and C_{ij} is the Coulomb matrix element representing the influence of the electrode j on the electrode i. The Coulomb matrix contains purely geometrical information and its elements are computed according to

$$C_{ij} = C_i(\vec{r}_j) = \frac{1}{4\pi\epsilon_0} \int_{S_j} \frac{1}{\vec{r}_i - \vec{r}_S} d^2 r_S, \tag{3.2}$$

where the integral runs over the surface of the jth electrode element. This covers only the time-independent static case. To solve the Coulomb matrix KEMField provides several methods:

- Gauss elimination
- LU-method
- Robin Hood method [161]

These are built to make use of parallel computing. The Robin Hood algorithm has a better scaling behavior than the first two for which the computing time grows as N^2, with N denoting the number of elements. This especially gets important for the full three dimensional model of the main spectrometer which has about 4 million elements. After the charge densities are computed usually the electric field and/or potential has to be evaluated for further computations e.g. within particle tracking. For this purpose KEMField provides a method based on zonal harmonic expansion and direct summing of the subelement contributions. Furthermore, a spherical multipole expansion for fast field evaluation in fully three dimensional geometries is being tested.

The direct method sums up the contributions of each element to the potential at a certain point. Generally, the subelements can be treated as point charges. Only close to the electrodes expressions depending on the geometry of the subelements have to be used. However, for triangles and rectangles corresponding analytical formulas exist and are being used. This is also true for the computation of the electric field. Only if the analytical evaluation fails the electric field is computed by numerical derivation.

The zonal harmonic expansion (ZHE) is based on Legendre polynomials. The expansion coefficients are computed at certain source points on the symmetry axis. After this time consuming process is done once, the field can be evaluated very fast. This method, however, relies on the axial symmetry of the setup. Since this is a good approximation for many applications in the KATRIN setup, it is widely used. The ZHE is based on the following representation of the potential

$$\Phi_{\text{cen}}(r,z) = \sum_{n=0}^{\infty} \Phi_n^{\text{cen}}|_{z_0} \left(\frac{\rho}{\rho_{\text{cen}}}\right)^n P_n(\cos(\theta)) \tag{3.3}$$

$$\Phi_{\text{rem}}(r,z) = \sum_{n=0}^{\infty} \Phi_n^{\text{rem}}|_{z_0} \left(\frac{\rho}{\rho_{\text{rem}}}\right)^{-(n+1)} P_n(\cos(\theta)) \tag{3.4}$$

$$\tag{3.5}$$

where ρ is the distance to the source point and $\rho_{\mathrm{cen/rem}} = \sqrt{(z - z_0)^2 + r^2}$. The Φ_n are the source coefficients that have to be computed. These two expansions differ in their convergence behavior. While the central expansion only converges inside a convergence radius r_c, the remote expansion does so outside of such an radius.

3.2.2 Magnetic field computation

The KATRIN experiment has numerous coils and solenoids to precisely shape the magnetic field that guides the signal electrons along. Their degree of adiabaticity and the precision of the energy analysis in the main spectrometer depend on a model of the magnetic fields, which is built using KEMField. In general, the magnetic field generated by a current is described by the Biot-Savart law:

$$\mathbf{B} = \frac{\mu_0}{4\pi} \int_C \frac{I d\vec{\mathbf{l}} \times \vec{\mathbf{r}}}{|\mathbf{r}|^3} \tag{3.6}$$

The contour integral runs over the path C of the current I and $\vec{r}$ points from the line segment $d\vec{\mathbf{l}}$ to the position the field is calculated at. In case of coils with thousands of windings, this integral would be very slow to compute numerically, so analytic methods are used in KEMField instead. These are based on elliptic integrals which can be used to compute the field at any point. Since the computation of the elliptic integrals is still rather slow (field computation accounts for a majority of the computing time needed), and since the coils are, at least locally, axially symmetric, again a zonal harmonic expansion is used. In a last step, the fields of the separate coils are superimposed to yield the total magnetic field of the configuration.

3.3 KASSIOPEIA

The KASSIOPEIA package is built to simulate particle trajectories in the whole KATRIN setup. It is configured via XML files and provides a wide range of possibilities to generate, track and stop particles. Particle interactions are included, e.g. electron scattering on residual hydrogen atoms or energy deposition in the detector (handled by the KESS[162] module). KASSIOPEIA makes use KEMField and further methods to calculate the electric and magnetic fields needed to determine the trajectories.

3.3.1 Tracking methods

KASSIOPEIA offers multiple methods to track particles in magnetic and electric fields. Particle trajectories are calculated with the help of different Runge-Kutta algorithms that can be selected to solve the user defined Ordinary Differential equation ODE. The default choice is an embedded Runge Kutta algorithm of 8th/6th order with internal error estimation. To define the particle's trajectory, different trajectory types can be selected for propagation. The simplest trajectory is a straight line, which can be directly generated from the particle's initial velocity without the need for the Runge-Kutta algorithm. To follow a certain magnetic field line, a so-called "magnetic trajectory" is

computed using the Runge-Kutta algorithm to adjust the particle momentum to point in the direction of the magnetic field. With this tool magnetic field settings can be visualized by field lines. Furthermore there one can choose to track charged particles in the fields using the exact Lorentz equation, or an adiabatic approximation. In both cases a term to include the effect of synchrotron radiation can be switched on. In addition to these different possibilities of trajectory calculation, there exist several algorithms for step size control to choose from. Besides setting a simple fixed step size either in length or in time, also one of the following precision criteria can be chosen. With an *energy* step size control, a step is accepted if the energy violation of the step is below a user-defined level, typically of the order of 10^{-13} relative error. Furthermore since the curvature of the trajectory is largely controlled by the strength of the magnetic field, an adaptive *cyclotron* step size control is possible. In this case, the cyclotron period $T = 2\pi\frac{m_0\gamma}{qB}$ is subdivided into a fixed number of steps. If this number is chosen to be smaller than one, a single step spans more than one cyclotron period. If several step size controls are active at the same time, the step gets re-evaluated till the strongest criterion is met.

Exact tracking

Exact tracking uses the Runge-Kutta ODE solver to solve the exact Lorentz equation

$$\vec{F}_L = q(\vec{E} + \vec{v} \times \vec{B}). \tag{3.7}$$

Since the ODE-solver only solves systems of first order ODEs, this needs to be reformulated to

$$\frac{d\vec{r}}{dt} = \frac{\vec{p}}{\gamma m} \tag{3.8}$$

$$\frac{d\vec{p}}{dt} = q(\vec{E}(\vec{r},t) + \frac{\vec{p} \times \vec{B}(\vec{r},t)}{\gamma m}) \tag{3.9}$$

This is the propagation term.

Since the electrons from the source perform cyclotron motions around the guiding magnetic field lines, thereby describing strongly curved trajectories, they emit synchrotron radiation. Synchrotron radiation was first discovered in a synchrotron accelerator at General Electric [163] and is a dreadful effect in high energy particle physicis. It is emitted coherently over the whole electro-magnetic frequency band whenever a charged particle describes a curved trajectory. Due to this effect, modern HEP particle accelerators and storage rings are forced to take the enormous sizes of an LHC to achieve low synchrotron losses and high energies by minimizing the curvature of the particle's path. Within the KATRIN experiment synchrotron losses of the signal electrons are a systematic effect that has to be taken into account.

In KASSIOPEIA synchrotron radiation is dealt with on a classical level as a term added to the ODE. This so called Abraham-Lorentz-Dirac[164] force has raised a lot of debate in the past since, in a theoretical understanding, it is highly problematic, seemingly violating causality and energy conservation in special situations. On the one

hand, for a particle at rest exponential runaway-solutions exist. On the other hand, for a time-dependent external force causality is violated: The particle starts acceleration before the force acts. There exists, however, a quantum description[165] that avoids these fallacies. Nevertheless, this topic still is worked on today [166–168]. Fortunately, these controversial situations do not occur in the case of KASSIOPEIA simulations, allowing an application of this method. The relativistic version of the (classical) force term, first proposed by Dirac[164] is

$$F_\mu^{\mathrm{rad}} = \frac{\mu_o q^2}{6\pi mc}\left[\frac{d^2 p_\mu}{d\tau^2} - \frac{p_\mu}{m^2c^2}\left(\frac{dp_\nu}{d\tau}\frac{dp^\nu}{d\tau}\right)\right]. \tag{3.10}$$

The corresponding radiation power is

$$P = \frac{\mu_0 q^2 a^2 \gamma^6}{6\pi c}. \tag{3.11}$$

For our purpose, this has to be reformulated into a system of first order ODEs. This was done for KASSIOPEIA [155]

$$\frac{d\vec{r}}{dt} = 0 \tag{3.12}$$

$$\frac{d\vec{p}}{dt} = -\frac{\mu_0}{6\pi c}\frac{q^4\vec{p}}{mp^2}(\gamma\xi_1 + \gamma^2\xi_2 + \gamma^3\xi_3) \tag{3.13}$$

with

$$\xi_1 = E_T^2 + B_V^2\frac{p^2}{m^2} \tag{3.14}$$

$$\xi_2 = 2E_U B_V \frac{p}{m} \tag{3.15}$$

$$\xi_3 = E_U^2 + E_V^2 \tag{3.16}$$

where **T**, **U** and **V** span an orthonormalized frame in which $\vec{T} \parallel \vec{p}$, $\vec{U} \parallel \vec{p}\times\vec{B}$ and $\vec{V} = \vec{T}\times\vec{U}$. Due to the generally low electric but strong magnetic fields the first two terms dominate the synchrotron losses in KATRIN. This term is expensive to compute and can be switched on if necessary for the simulation.

Adiabatic tracking

The electron transport in the KATRIN experiment is designed to be adiabatic to a very high degree, so that electron energies can be analyzed properly. This property is also used for tracking making use of the adiabatic approximation. It is valid if the particle's trajectory can be split up in two components, one following the magnetic field lines, and one describing cyclotron motions around this field lines (*gyration*). Within KASSIOPEIA, multiple choices exist for the degree of detail that is modeled in this motion.

Furthermore it is possible to take into account $\vec{E} \times \vec{B}$ and $\nabla\vec{B} \times \vec{B}$ drift terms that perturb the motion in radial or azimuthal direction. The advantage of the adiabatic method is that it allows for much larger step sizes, jumping over several cyclotron motions of the particle, making the simulation much faster.

The adiabatic method is based on the conservation of the first adiabatic invariant, the orbital magnetic moment of the particle

$$\frac{d}{dt}(\gamma\mu) = 0. \tag{3.17}$$

It is given by

$$\gamma\mu = \frac{p_\perp^2}{2mB_c} \tag{3.18}$$

and proportional to the magnetic flux enclosed by the particle's trajectory, with $p_\perp$ the momentum orthogonal to the direction of the magnetic field and B_c the magnetic field at the guiding center position. An adiabatic motion is only possible if the magnetic field does not change significantly within one cyclotron period. From this we get

$$0 = \frac{d}{dt}\left(\frac{p_\perp^2}{2mB_c}\right) \tag{3.19}$$

$$0 = \frac{p_\perp \dot{p}_\perp}{mB_c} - \frac{p_\perp^2}{2mB_c^2}\frac{dB_c}{dt}. \tag{3.20}$$

The time derivative of the magnetic field can be expressed by use of the chain rule

$$\frac{dB_c}{dt} = \left(\vec{\nabla}B_c\frac{\vec{B_c}}{B_c}\right)\frac{p_\parallel}{\gamma m} = \nabla_\parallel B_c. \tag{3.21}$$

With this we can get $\dot{p}_\perp$

$$\dot{p}_\perp = \frac{p_\perp p_\parallel}{2\gamma m B_c}\nabla_\parallel B_c \tag{3.22}$$

The other first order derivatives of the system then are

$$\dot{\vec{r}_c} = \frac{p_\parallel}{m\gamma}\frac{\vec{B_c}}{B_c} \tag{3.23}$$

$$\dot{\phi} = \frac{qB_c}{m\gamma} \tag{3.24}$$

$$\dot{p}_\parallel = -\frac{p_\perp^2}{2m\gamma B_c}\nabla_\parallel B_c + qE_\parallel \tag{3.25}$$

With the adiabatic method it is also possible to account for synchrotron radiation. This is particularly important for simulations investigating electron transport through the whole KATRIN system because this would take too long and provide only poor statistics

with the exact method. In this case, only contributions coming from $\dot{p}_\perp$ are considered. Other influences on the radiated power P can be neglected, taking only the first term in 3.13 into account, yielding

$$P = \frac{\mu_0}{6\pi c}\frac{q^4}{m^4}B_c^2 p_\perp^2. \tag{3.26}$$

As only $p_\perp$ gets affected, we can also write, using $P = dE/dt$:

$$P = \frac{p_\perp \dot{p}_\perp}{m\gamma} \tag{3.27}$$

With 3.27 and 3.26 we can conclude

$$\dot{p}_\perp = \frac{\mu_0}{6\pi c}\frac{q^4}{m^3}B_c^2 p_\perp \gamma. \tag{3.28}$$

This is the term that has to be added to the ODE system to accommodate for synchrotron radiation in the adiabatic approach.

3.3.2 Added Extensions and Modifications

All modules added and changes made over the course of this work to KASPER and KASSIOPEIA in particular are already publicly available, see [154].

Dynamic Simulation reconfiguration

Kassiopeia gives the user a wide range of choice when building a simulation. So far however all changes of configuration that could occur (such as a change of the equation governing the motion) were tied to the Geometry used in the simulation and so far static. Sometimes such changes are warranted by dynamical properties. Below a certain energy of the particle for example some processes might be negligible while others gain importance. Such a possibility may also be desirable for convenient analysis. If for example an electron is reflected by the fields of the spectrometer it could be that the user would like to analyze the trajectory upto the reflection separately from the path afterwards. While this track splitting was long possible with explicitly predefined static surfaces, so far it was impossible with such an implicit surface that depends on the path of the particle within the given fields. For this the KSModifier class was introduced. If used within the configuration it allows to execute arbitrary code after or before every integration step. As example modules exist KSModEnergyTrajectorySwitch (written by the author) and KSModSplitOnTurn (written by J. Behrens). KSModEnergyTrajectorySwitch takes two KSTrajectory objects and switches from the default one to the triggered one if a total energy threshold is crossed from above by the particle in question. This can e.g. be used to switch from an exact integration of the Lorentz equation to the adiabatic approximation. KSModSplitOnTurn detects turns of the particle momentum with respect to the magnetic field and splits the path into two parts at each one. The user can specify this to happen at turns where either the dot product of particle momentum and magnetic

field changes from positive to negative ("forward"), the other way round ("backward") or in both cases ("both") by setting the "direction" option.

Listing 3.1: KSModifier configurations

```
<ksmod_energy_trajectory_switch
name="trajectory_switch"
default_trajectory="exact"
trigger_trajectory="adiabatic"
trigger_energy="1.96e4"/>

<ksmod_split_on_turn
        name="split"
        direction="forward"/>
```

Zonal Harmonic Boundary

One common issue in KASSIOPEIA simulations was that the very fast zonal harmonics method for (electric) field computations has a convergence radius that ends close to the electrodes. Within the KATRIN main spectrometer for example the zone of convergence reaches from the central axis towards a few cm before the inner electrode. When an electron reaches a part of the spectrometer where the ZHE does not converge, KEMField falls back to a direct computation of the field, which is much slower. While this behavior is correct, for many purposes it is not desired. Often only a very small fraction of the electrons reach this region in space, and if they do they are unlikely to reach the detector or contribute other noteworthy effects. For these cases where electrons very close to the electrodes can be safely excluded from the simulation a new module, the "root_zh_painter" was written. This module can be used with any Kassiopeia simulation that employs KEMFields Zonal Harmonic Expansion to calculate the electric field. Given these it probes the radius of convergence along the symmetry axis and creates a representation of the Geometry within KGeoBag that can later on be used as boundary in the simulation. The user may choose to terminate electrons that cross the generated (explicit or implicit) surface and come close to the electrode and or use a better performing approximation of the electric field there.

The calculation of the geometric boundary works by checking for points of a grid in the z-r plane if the ZHE converges or not. It starts on the symmetry axis (z) at $r = 0$ and steps to bigger r until finally the convergence breaks down. The range of the grid and the stepping have to be given by the user. As a result the rotational surface of the last points of convergence can be written out as KGeoBag XML configuration file and displayed in a ROOT plot.

The options for this module are shown in Listing 3.2. By "x_axis" and "y_axis" the plane to plot is chosen. With "electric_field" the field object to test is selected. "z_min", "z_max", "r_min" and "r_max" specify the range of the grid that is scanned while "r_steps" and "z_steps" the number of points along the respective axis. "file" allows to name an output file to which the resulting geometry is written if "write" is true. By

"geometry_type" this can either be a surface or a volume. With "radial_safety_margin" the geometry can be additionally shrinked if at some points the field calculation becomes unstable earlier.

Listing 3.2: Zonal harmonics painter configuration

```
<root_zh_painter
        name="root_zh_painter"
        x_axis="z"
        y_axis="x"
        electric_field="field_name"
        z_min="-12."
        z_max="12."
        r_min="0"
        r_max="6."
        r_steps="{1e4}"
        z_steps="{2.4e3}"
        file="output.xml"
        geometry_type="volume"
        write="true"
        radial_safety_margin="0.01"
/>
```

Hydrogen Scattering

Also before this work electron scattering on hydrogen molecules was implemented within KASSIOPEIA and successfully used as discussed in [104]. The new, more detailed model developed later in chapter 4 is new in so far as it is also suitable for neutrino mass analysis. The previous Monte Carlo model had large deviations from the model in [92], which became apparent in [156] was further studied in [169] (supervised by the author) and finally led to the new model presented in chapter 4.

^{210}Pb Beta decay

In [170] a ^{210}Pb electron event generator was used in order to simulate the effect of the ^{210}Pb β-decays and the following emission of conversion and Auger electrons within the steel of the main spectrometer and to estimate the arrival probability of the 30 keV conversion electrons at the detector. This was used there to give an estimate of the ^{210}Pb activity within the main spectrometer. That estimate is used later on in chapter 5. The event generator as cited in [170] was developed within this work. The electron emission spectrum of the decay consists of two concurrent beta spectra which are calculated using equation 1.39 with endpoints E_0 at 17 keV and 63 keV respectively. For this existing routines within KASSIOPEIA were used. After the β-decay the ^{210}Bi nucleus may be in an excited state that can emit conversion electrons. In that case further electrons from the shell may be emitted in relaxation processes. This is modelled using the algorithms used for radon decays, developed and described in detail in chapter 7 within [104]. The relevant decay probabilities and energies were gathered from NuDat [171], the shell

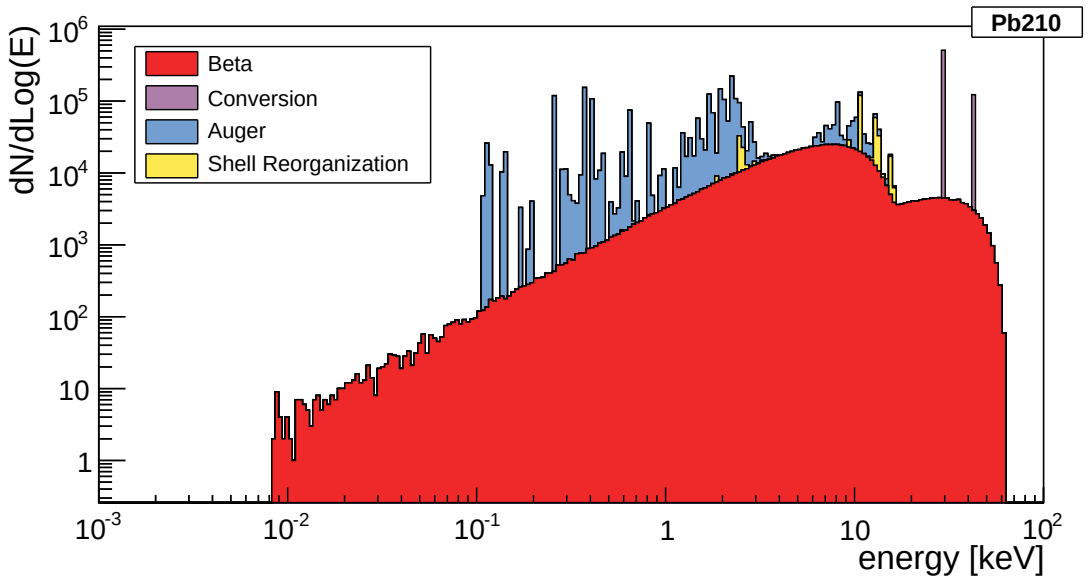

Figure 3.1: Energy spectrum of electrons from a ^{210}Pb decay.

energy levels and transition probabilites from [172, 173]. The resulting electron energy spectrum and multiplicity distribution are shown in fig. 3.1 and 3.2. The module can be used within a KASSIOPEIA XML configuration file simply by using the following tag within the particle generator configuration:

```
<energy_lead_event do_conversion="true" do_auger="true"/>
```

The list of options is short. The module allows to selectively disable the generation of conversion and auger electrons if for some reason they should be studied separately.

Rydberg Physics

The Interactions of Rydberg atoms with a thermal radiation field that are in detail discussed in chapter 5 have been integrated into KASSIOPEIA. In order to use this interaction in an XML configuration file the listing below can be used. A target particle ID "target_pid" can be given so that only a certain species of particles within the simulation is subject to the Rydberg transitions. The "temperature" option sets the temperature of the BBR-Radiation to be used within the calculations. BBR-Transitions between neighboring states, spontaneous decays and ionization reactions can be used independently if necessary.

```
<ksint_decay_calculator_spontaneous
        name="spon"
        target_pid="11"
/>
<ksint_decay_calculator_bbr_transition
```

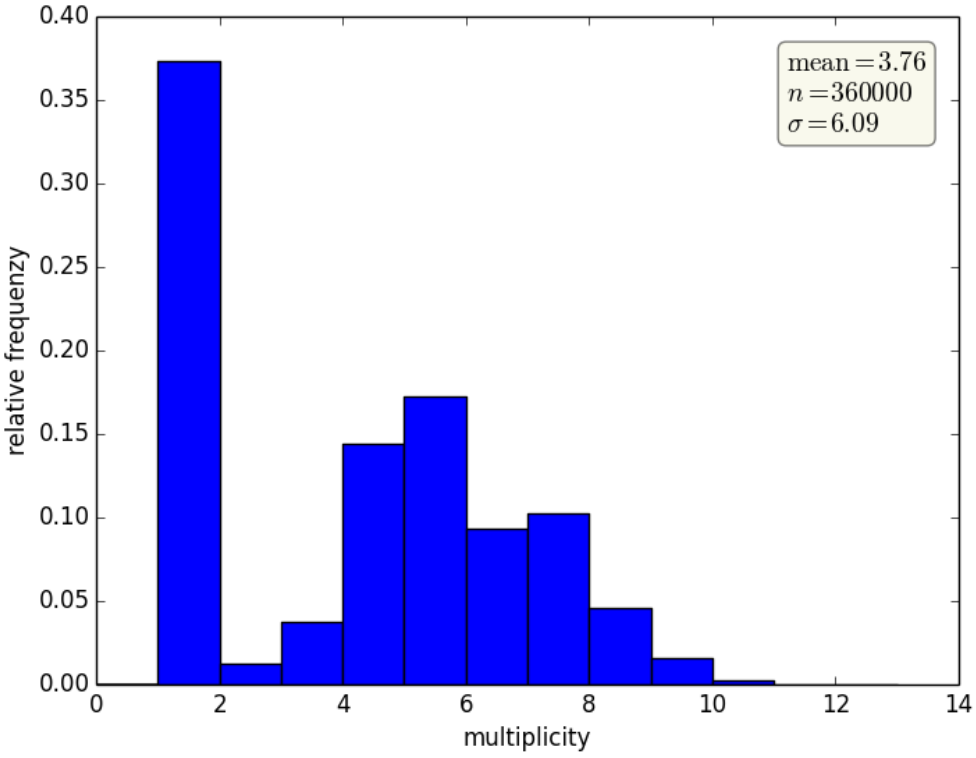

Figure 3.2: Electron multiplicity distribution of ^{210}Pb decays

```
        name="bbr"
        target_pid="11"
        temperature="[Temperature]"
/>

<ksint_decay name="rydberg"
        calculator="bbr"
        calculator="spon">
        <decayionisation
                name="decay"
                temperature="[Temperature]"
                target_pid="11"/>
</ksint_decay>
```

3.4 SSC

The Source and Spectrum Calculation (SSC) [153] module of KASPER computes integrated tritium decay spectra as measured by KATRIN. It provides the model function of the experiment, namely N_{th} from eq. 2.11:

$$N_{th}(qU, E_0, m_\nu, R_s, R_b) = R_s N_s(qU, E_0, m_\nu) + R_b N_b \tag{3.29}$$

To accomplish this it calculates theoretical differential spectra including various corrections and models the response function of the apparatus taking into account the electromagnetic and gasdynamic properties of the source section, which determine the mapping of the flux of electrons onto the pixels of the silicon detector.

It is noteworthy that this is not done using Monte Carlo simulations as provided by the KASSIOPEIA module. From the differential spectrum to the detection efficiency everything is calculated analytically in multiple foldings, which sometimes are carried out numerically. The difference is important since the objective of SSC is to provide the fit function for the KATRIN experiment, which needs to be computed many times for a single fit. However, the analytical computation of the expected count rates is by orders of magnitude faster than a particle tracking Monte Carlo simulation.

The key challenge in SSC is to take into account the 3-d profiles of all the parameters that influence the electron emission in the source. These are the gas density $\rho(\vec{x})$, and thus temperature $T(\vec{x})$ and gas velocity $\vec{v}(\vec{x})$, but also the magnetic field $\vec{B}(\vec{x})$ and an eventual plasma potential $U(\vec{x})$. For this the three dimensional solution of the Boltzmann equation is needed which includes gas dynamics from the hydrodynamical regime at high pressure near the gas inlet, to the free-molecular regime at low pressure at the pumping ports. This model then is evaluated for discrete parts of the source volume separately. This voxelization slices the WGTS in equidistant parts in z direction, while the ϕ, r slicing matches the pattern of the detector pixels. The resulting beta spectra of the voxels, weighted by the density, and each one with its own transmission function, source strength, source magnetic field, scattering probability etc. are summed up to yield the total spectrum. This way inhomogeneities of the tritium gas are taken into account.

A lot of code is shared between SSC and the other modules: Tritium spectra computed by SSC can be used as input for a particle tracking simulation with KASSIOPEIA. Vice versa detailed Monte Carlo simulations of the transmission with KASSIOPEIA have been used to model an accurate analytical description of the transmission function [156], which is used by SSC as input to compute the integrated β spectrum.

The first version of SSC was written by two former doctoral students at KIT, W. Käfer and M. Hötzel as part of their theses [111, 174]. Since then, the code has undergone intensive refactoring by M. Kleesiek [152].

3.5 KaFit

KaFits final purpose is to perform the neutrino mass fit once the measurement is done. Beside this it is used to study the sensitivity of KATRIN and the systematic effects that influence it. For this KaFit implements the necessary statistical and auxiliary tools and integrates with the model of the experiment implemented in SSC as well as the data access library KaLi. It was first written by M. Kleesiek and is described extensively in [152]. In order to estimate the neutrino mass from a measurement (or a simulation) the difference between the data and the model prediction needs to be minimized. This is done by maximizing the Likelihood function L or approximated by minimizing $\chi^2 = -2 \log L$ which for KATRIN is

$$\chi^2(m_\nu^2, E_0, R_s, R_b) = \sum_i \sum_j \left(\frac{N^j_{\mathrm{meas}}(qU_i) - N_{\mathrm{th}}(qU_i, m_\nu^2, E_0, R_s, R_b)}{\sigma_{\mathrm{th}^j(U_i)}} \right)^2 \tag{3.30}$$

with N_{th} from eq. 2.11. In order to find the global minimum of χ^2 the squared neutrino mass m_ν^2 and the nuisance parameters, namely the endpoint E_0, the signal amplitude R_s and the background rate R_b have to be varied. For this minimization task KaFit offers several minimizers such as MINUIT from the ROOT package or Markov Chain Monte Carlo (MCMC) algorithms. It allows for Bayesian as well as frequentist methods to construct a confidence or credible interval for the neutrino mass best fit.

For this purpose it includes several models of geometry-dependent background and provides the logic to define a run interval strategy in conjunction with a given total measurement time distribution. In this way the code can be used to predict the expected event count on each pixel of the detector for various configurations, and to simulate a complete set of KATRIN data taking runs.

The neutrino mass sensitivity of the KATRIN Experiment is studied by determining the variance of the neutrino mass estimator which is given by the best fit result obtained from fitting the spectral shape. KaFit provides two methods to calculate this variance: An ensemble test using a Monte Carlo simulation on the one hand and the width derived from the shape of the profiled likelihood around its minimum on the other. By introducing differences between the models used for generating and fitting the data systematic effects can be studied - these generally result in a mean shift of the neutrino mass fit result.

For the ensemble test a repeated simulation of the experiment with the null-hypothesis $m_\nu^2 = 0$ as Monte Carlo truth is carried out by generating random numbers according to a Poissonian distribution with the calculated expected mean rates for the tritium signal and background separately. The spectrum model is then repeatedly fitted to the Monte Carlo data and the distribution of m_ν^2 fit results (and those of the nuissance parameters) can be studied.

For the profile likelihood method the likelihood ratio $\lambda = \frac{L(m_\nu^2)}{L(\hat{m}_\nu^2)}$ is calculated for different values of m_ν^2, while the nuisance parameters are profiled. Within KaFit this is done by MINOS, a part of the ROOT package. This method allows to estimate shifts of the neutrino mass best fit as well as confidence intervals without a Monte Carlo simulation. An increase of $-\log\lambda$ by 0.5 from the minimum yields the $1\,\sigma$ confidence interval as shown in figure 3.3

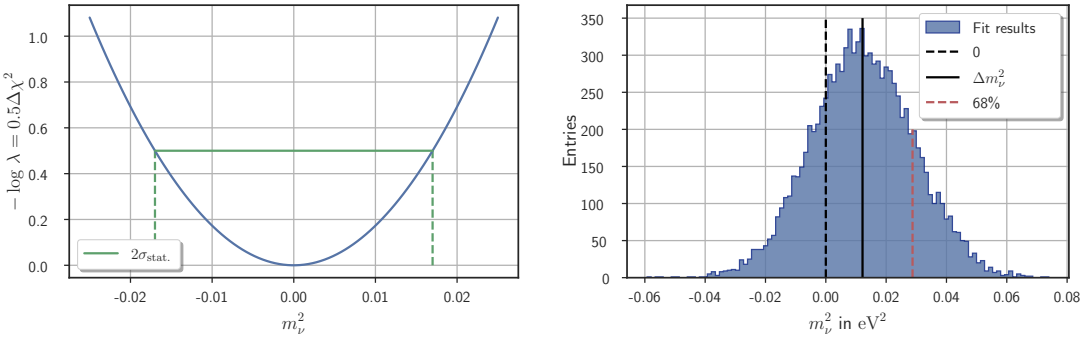

Figure 3.3: Left: Profiled Likelihood of KATRIN from MINOS. For a single fit result where the model is compared against itself the resulting χ^2 values are shown in dependency of m_ν^2, while the nuisance parameters are profiled. An increase of $-\log\lambda$ by 0.5 from the minimum yields the $1\,\sigma$ confidence interval. **Right**: Ensemble test of the neutrino mass measurement. The (square root of the) variance of the distribution of the 10000 fit results yields the 1σ statistical uncertainty of m_ν^2. Here for the fitting of the spectra a magnetic field and thereby transmission function different from the Monte Carlo model was assumed. This results in a shift of the mean fit result. This way systematic effects can be estimated .

CHAPTER 4

Modeling of electron impact scattering on molecular hydrogen and electron energy losses in the WGTS

An accurate description of electron impact scattering on the isotopologues of H_2 is of paramount importance for the KATRIN experiment. Beta electrons from the tritium decay may scatter within the gaseous tritium source of KATRIN before they reach the spectrometer where they are filtered according to their energy. The energy losses that occur within these source scatterings distort the shape of the measured β-decay spectrum from its initial form. These are the largest electron energy losses within the experiment. Given the design gas density, only about 30% of the electrons within the last 70 eV below the tritium endpoint leave the source unscattered. Inelastic energy losses amount to 10 eV and more, depending on the type and multiplicity of interactions. This is large compared to the neutrino mass sensitivity of 200 meV. Therefore the probability and the distribution of these energy losses must be known precisely in order to describe the measured spectrum and retain information about the neutrino mass from the unperturbed spectrum. Within this chapter the KATRIN response function, introduced in section 2.1.3, is discussed in section 4.1. In this function the description of energy losses from scattering enter the model of the experiment in the form of n-fold scattering probabilities and the single-scattering energy loss function. In [175] a proposal was made to recover these from a dedicated measurement with an electron gun using a deconvolution method. This approach is re-evaluated in section 4.2 and it is found that the measurement time needed for an acceptable reconstruction of the energy loss function was underestimated. In section 4.3 processes in electron impact scattering on hydrogen and the relevant sources are discussed. Another way to model the energy loss function using literature results is presented in section 4.4. This work is compared to measurements of the Troitsk Experiment and J. Geiger in section 4.5. However, the uncertainties that come with the input parameters of the model are in part too large for KATRIN. This and the required limits on the model will be explored in section 4.5.4. Regardless of

what approach is chosen in the end: KATRIN can not purely rely on existing data. It is imperative for the experiment to measure the energy loss in-situ with a precision electron source – an effort that is well under way at present. While the model developed here is not accurate enough for the design sensitivity, it is suitable to assess the requirements on the precision of the various model parameters. It could also serve as a starting point and be improved by using it as a fit model in coming measurements. Ultimately an effort for a theoretical precision calculation is desirable. Molecular hydrogen is the simplest existing molecule and a similar approach is successfully pursued with regard to the more sophisticated calculation of the final state distribution of the tritium β-decay products [176–178].

4.1 Description of Energy Loss in the WGTS

In the following the formalism of the KATRIN response function is briefly introduced according to [156] with the focus on the energy loss function $f(\epsilon)$ and the s-fold scattering probabilities P_s. Then the experimental strategy presented in [175] to measure the energy loss function in KATRIN in-situ. How to unfold it from the measurement data is discussed in section 4.2. Afterwards this approach is re-evaulated. When calculating the rates to expect for a given retarding potential, energy losses by scattering must be taken into account as they shuffle electrons towards lower energies and reshape the spectrum. This is done within the response function, which encodes all experimental effects within the KATRIN experiment.

4.1.1 Response function

The response function relates the measured rate at the detector $\dot{N}(qU)$ with the unperturbed energy spectrum of the electrons emitted within the source $\frac{d\dot{N}}{dE}$. Thereby it must encompass all effects on the analysed electrons by KATRIN from source to spectrometer. The response function $R(E, qU)$ is the response to an isotropic source of electrons with energy E and gives the fraction of electrons that are counted at the detector for a given retarding voltage U

$$\dot{N}(qU) = N_T \epsilon_{\mathrm{det}} \frac{\Omega}{4\pi} \int_{qU}^{E_0} \frac{d\dot{N}}{dE} \cdot R(E, qU) \mathrm{d}E. \tag{4.1}$$

It can be calculated as

$$R(E, qU) = \int_0^{E-qU} T(E-\epsilon, qU) \cdot \left(\bar{P}_0 \delta(\epsilon) + \bar{P}_1 f(\epsilon) + \bar{P}_2 (f \otimes f)(\epsilon) + \dots \right) \mathrm{d}\epsilon, \tag{4.2}$$

with the transmission function $T(E-\epsilon, qU)$, the probabilities $\overline{P_i}$ for for i-fold scattering and the energy loss function $f(\epsilon)$. The symbol $\otimes$ denotes a folding integral

$$(f \otimes f)(\epsilon) = \int_0^{E/2} f(\epsilon - \epsilon') f(\epsilon') \mathrm{d}\epsilon'. \tag{4.3}$$

The energy loss function $f(\epsilon)$ is the probability distribution of all possible energy losses ϵ that can occur in a scattering event. It can be expressed by the differential scattering cross section, normalized by the total scattering cross section:

$$f(\epsilon) = \frac{1}{\sigma_{\text{tot}}^{\text{inel}}} \frac{d\sigma}{d\epsilon}. \tag{4.4}$$

Each inelastic scattering successively adds a more broadened version of the spectrum shifted down by 10 eV – the minimum scattering energy. The key signature of a non-vanishing neutrino mass – a change in the slope of the spectrum – does not appear outside this energy window due to its smallness. When fitting the spectral shape and extracting the neutrino mass, a precise knowledge of the slope and amplitude even away from the endpoint as well as the endpoint itself are necessary. Therefore, the response function must be known very precisely further into the spectrum and with it the shape of the energy loss function.

4.1.2 Scattering probabilities

The scattering probabilities are generally small and independent. They are calculated from a Poisson distribution

$$P_s(z,\theta) = \frac{(\lambda(z,\theta) \cdot \sigma_{\text{tot}}^{\text{inel}})^s}{s!} \cdot e^{-\lambda(z,\theta)\cdot\sigma_{\text{tot}}^{\text{inel}}} \tag{4.5}$$

and depend on the inelastic scattering cross section $\sigma_{\text{tot}}^{\text{inel}}$ and the gas density distribution in the source. Here, λ is the effective column density that an electron starting from a position z with polar angle θ has to traverse

$$\lambda(z,\theta) = \frac{1}{\cos(\theta)} \int_{z'=z}^{L/2} \rho(z')dz', \tag{4.6}$$

with $\rho(z)$ being the local gas density along the source tube which ranges from $z = -L/2$ to $z = +L/2$. So for an electron that starts at z only the gas column downstream contributes to the scattering, neglecting backscattering. The factor $1/\cos(\theta)$ originates in the cyclotron motion of the electron. Electrons with helical trajectories that possess a larger polar angle towards the magnetic field thus require an accordingly longer flightpath through the gas filled source tube and therefore have a higher scattering probability. To calculate the average scattering probability first the angular dependency needs to be integrated over, weighted with the angular distribution $\omega(\theta)$

$$\bar{P}_s(z) = \int_{\theta=0}^{2\pi} \omega(\theta) \cdot P_s(z,\theta)d\theta. \tag{4.7}$$

Using an isotropic angular distribution $\omega(\theta) = \sin(\theta)$ this gives

$$\bar{P}_s(z) = \frac{1}{1-\cos(\theta_{\text{max}})} \int_{\theta=0}^{\theta_{\text{max}}} \sin(\theta) \cdot P_s(z,\theta)d\theta. \tag{4.8}$$

With $\theta_{\max}$ being the maximal angle θ with which electrons are transmitted through the main spectrometer. Integrating the result weighted with the local gas density then gives the overall average scattering probability which enters the response function in equation 4.2

$$\bar{P}_s = \frac{1}{\rho d} \int_{-L/2}^{L/2} \rho(z) \cdot \bar{P}_s(z) dz. \tag{4.9}$$

4.1.3 Transmission function

The transmission function describes the properties of the spectrometer and the angular distribution of the transmitted electrons. It is the probability of transmission for an electron with energy E_S when the spectrometer is operated at a retarding potential U_A. The probabilistic notion rises from the ignorance of the polar angle θ_S of an individual electron. With a given polar angle θ_S with respect to the magnetic field the energy required for an electron to arrive at the detector is

$$E_{\mathrm{tr}} = \frac{q(U_A - U_S)}{1 - \sin^2(\theta_S) \cdot \frac{B_A(\gamma_S+1)}{B_S(\gamma_A+1)}} \tag{4.10}$$

So the transmission function is simply a Heaviside step function

$$T(U_A) = \Theta(E_S - E_{\mathrm{tr}}). \tag{4.11}$$

It is convenient to include the angular distribution within this description. Given an isotropic angular distribution ω of the electrons

$$\omega(\theta) = \sin(\theta), \tag{4.12}$$

the transmission function is

$$\begin{aligned} T(E_S) &= \int_0^{\theta_{\mathrm{tr}}(E_S)} d\theta \omega(\theta) \\ &= 1 - \cos\left(\theta_{\mathrm{tr}}(E_S)\right), \end{aligned} \tag{4.13}$$

with the transmission angle $\theta_{\mathrm{tr}}(E_S)$

$$\theta_{\mathrm{tr}}(E_S) = \arcsin\left(\sqrt{\frac{E_S - qU}{E_S} \cdot \frac{B_S}{B_A}}\right). \tag{4.14}$$

Using the relation $\cos(\arcsin(\sqrt{x})) = \sqrt{1-x}$, the transmission function can be written as

$$T(E_S, qU) = 1 - \sqrt{1 - \frac{E_S - qU}{E_S} \cdot \frac{B_S}{B_A}}. \tag{4.15}$$

Handling cases where the root or the result becomes negative the function can be extended for definition over all retarding voltages U

$$T(E_S, qU) = \begin{cases} 0 & E_S - qU < 0 \\ 1 - \sqrt{1 - \frac{E_S - qU}{E_S} \cdot \frac{B_S}{B_A}} & 0 \leq E_S - qU \leq \frac{B_A}{B_S} E_S \\ 1 & E_S - qU > \frac{B_A}{B_S} E_S \end{cases} . \tag{4.16}$$

4.2 Experimental strategies to obtain the Energy Loss function

In [175] Hannen et al. evaluated deconvolution methods to obtain the energy loss function without the use of inputs by scattering models purely from measurement data with the KATRIN experimental setup. For this a special measurement has to be conducted where the response of the apparatus to a (quasi-) mono-energetic electron source is measured at different column densities of gas within the source section. From this data the energy loss function can in principle be recovered. The authors evaluated various methods for the unfolding procedure which is the critical part of the analysis. The most promising was Singular Value Decomposition (SVD) which will be further investigated here. They evaluated these methods by making Monte Carlo toy simulations of the KATRIN experiment using the unfolded energy loss function within the fitting of the neutrino mass but the original model for the generation of the toy data. From the distribution of the fitted results for m_ν^2 they determined an average shift of the squared neutrino mass by $\mu = (5.3 \pm 0.5) \cdot 10^{-3}\,\mathrm{eV}^2$ for the SVD Method. By this they could show that unfolding methods can in principle provide an energy loss function suitable for use in KATRIN. Since then their code was incorporated into the KASPER framework. While much work went into the development and testing of the defolding procedures, the sensitivity study remained cursory: Only a *single* toy model Monte Carlo of the energy loss measurement was performed which resulted in a *single* unfolded energy loss function per tested method with which then the ensemble tests were conducted.

This approach seemed reasonable because they used a large statistic for the energy loss toy measurement: at each retarding potential 10^7 electrons were simulated. However, to bring the method to application more scrutiny is necessary. It needs to be shown that it is likely for a deconvoluted energy loss function to result in a low neutrino mass shift. That is, that the method is robust against the variation in the e-gun measurement that remains, despite the high statistics.

In order to incorporate variations of the deconvoluted energy loss function into the sensitivity study it is necessary to include the e-gun toy measurement in the ensemble test instead of performing the ensemble test on the tritium spectrum alone while keeping the energy loss model fixed.

This more rigorous approach here will reveal that despite the high statistics the unfolded energy loss functions can vary strongly from one toy measurement to another and with them the associated neutrino mass shifts.

4.2.1 Deconvolution method

Below the deconvolution approach is briefly introduced following [175]. The n-fold scattering functions are defined as

$$\begin{aligned}
\epsilon_0(E_S) &= T_e(E_S) \\
\epsilon_1(E_S) &= T_e(E_S) \otimes f(\Delta E) \\
\epsilon_2(E_S) &= T_e(E_S) \otimes f(\Delta E) \otimes f(\Delta E) \\
\epsilon_3(E_S) &= T_e(E_S) \otimes f(\Delta E) \otimes f(\Delta E) \otimes f(\Delta E), \\
&\vdots
\end{aligned} \tag{4.17}$$

with T_e denoting the transmission function for a monoenergetic highly collimated electron source (e-gun). Using these, the response function can be reformulated and the equation split into one part including these scattering functions, and one part being independent of them:

$$\begin{aligned}
R(E_S) &= \sum_{i=0}^{n} P_i \cdot \epsilon_i(E_S) \\
R(E_S) - P_0 \cdot T(E_S) &= \sum_{i=1}^{n} P_i \cdot \epsilon_i(E_S).
\end{aligned} \tag{4.18}$$

The idea is to reconstruct the parameters ϵ_i from a measurement of the terms on the left side using an electron gun with a good angular and energy resolution and calculated scattering probabilities P_i. In order to incorporate n-fold scattering n independent measurements are needed which can be achieved by varying the column density and by this the scattering probabilities. Together they give a linear equation system

$$\vec{R} - \vec{P_0} \cdot T_e(E_S) = \boldsymbol{P} \cdot \vec{\epsilon} \tag{4.19}$$

with

$$\boldsymbol{P} = \begin{pmatrix} P_1^a & P_2^a & P_3^a \\ P_1^b & P_2^b & P_3^b \\ P_1^c & P_2^c & P_3^c \end{pmatrix}, \ \vec{R} = \begin{pmatrix} R_a \\ R_b \\ R_c \end{pmatrix}, \ \vec{P_0} = \begin{pmatrix} P_0^a \\ P_0^b \\ P_0^c \end{pmatrix}, \text{ and } \vec{\epsilon} = \begin{pmatrix} \epsilon_1 \\ \epsilon_2 \\ \epsilon_3 \end{pmatrix} \tag{4.20}$$

in this case for three column densities a, b, c. Inverting the linear equation the scattering functions can be obtained:

$$\vec{\epsilon} = \boldsymbol{P}^{-1} \cdot \left(\vec{R} - \vec{P_0} \cdot T_e(E_S) \right). \tag{4.21}$$

This equation system can be solved with standard methods. Within the KEloss[1] package this task is done with the Gauss-Jordan algorithm implemented in ROOT. For a

[1]The package developed by the authors in [175] and used therein

measurement of the response function with N points the scattering function turns from its integral definition

$$\vec{\epsilon}(E_S) = T_e(E_S) \otimes f(\Delta E) = \int_0^{E/2} T_e(E_S - \Delta E) f(\Delta E) d\Delta E \tag{4.22}$$

into a discrete sum

$$\epsilon_1(E - qU_i) = \sum_{J=0}^{N-1} T_e(E - qU_i - \Delta E_j) f(\Delta E_j) \tag{4.23}$$

which can, again, be formulated as a linear equation now of dimension N

$$\vec{\epsilon_1} = \boldsymbol{T_e} \cdot \vec{f} \tag{4.24}$$

with $\boldsymbol{T_e}$ defined as the $N \times N$ matrix

$$\boldsymbol{T_e} = \begin{pmatrix} T_0 & 0 & & \dots & 0 \\ T_1 & T_0 & 0 & \dots & 0 \\ T_2 & T_1 & T_0 \quad 0 & \dots & 0 \\ T_{N-1} & T_{N-2} & T_{N-3} & \dots & T_0 \end{pmatrix} \quad \text{with } T_i = T_e(E - qU_i) \tag{4.25}$$

To obtain the energy loss function $\vec{f}$, the linear equation must be solved and thereby $\boldsymbol{T_e}$ inverted. This however proves to be difficult because the matrix $\boldsymbol{T_e}$ is close to singular. For this purpose, Singular Value Decomposition according to [179] was used in KEloss and compared to Bi-CGSTAB [180] from the Meep [181] package.

4.2.2 Re-evaluation of the deconvolution procedure

The deconvolution approach recapitulated above was introduced and studied in [175] as a potential source of systematic uncertainty for a neutrino mass measurement using the ensemble test method. This was done by dicing a single toy Monte Carlo of the e-gun measurement resulting in a single deconvoluted energy loss function that was then ensembletested against the input model for a systematic shift of the neutrino mass fit result. This was done using the model and fitting routines built into the KEloss Package. The reported result of the conducted ensemble test was a mean shift of $\mu = (5.3 \pm 0.5) \cdot 10^{-3}\,\mathrm{eV}^2$. This value is valid for that particular energy loss function, deconvoluted with the SVD Method and an $w_{thr} = 0.3\%$ damping. This showed that the method works and is indeed in principle applicable to KATRIN. However, in order to estimate the performance of this method in general it needs to be run over a random set of e-gun-simulations and for each of those the neutrino mass shift must be estimated and only then an average be taken. What needs to be assessed for a reliable sensitivity result is how randomness in the e-gun measurement affects the neutrino mass analysis in general.

To investigate this, we start by repeating the simulation of [175] a 1000 times. As a result it is found that the unfolded energy loss functions vary strongly from one e-gun

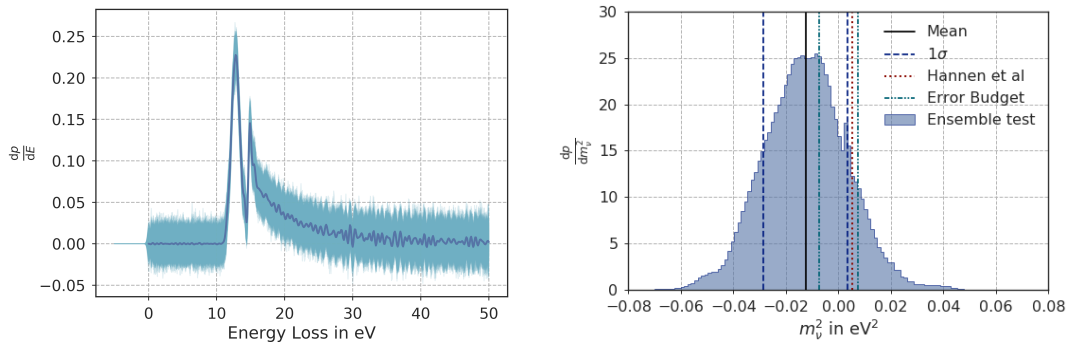

Figure 4.1: Left: Results of the deconvolution with the proposed SVD Method. For this a total of 1000 e-gun toy measurements each with 10^7 electrons per measurement point with a 0.1 V stepping were simulated and deconvoluted. The dark blue line is the point-wise mean of all results, the light blue shading indicates the maximal spread over all simulations. Despite the high statistic in the toy measurement input, the deconvoluted energy loss function varies strongly. **Right**: For each deconvoluted energy loss function an ensemble test of 1000 KATRIN experiments was simulated. The histogram contains the combined 10^6 fit results.

simulation to another despite their high statistic. This shows that the SVD method is very sensitive to experimental noise. Given a distribution of simulation results it is possible to ask how probable it is to find the reported shift within a single simulation: Out of 1000 simulated deconvoluted energy loss functions 14 showed an absolute neutrino mass shift of $\mu = 5.3 \cdot 10^{-3}\,\mathrm{eV}^2$ or smaller. The average shift over all energy loss functions is $\mu = (-12.5 \pm 3.1) \cdot 10^{-3}\,\mathrm{eV}^2$ and thus not only significantly higher than the previously reported value $\mu = 5.3 \cdot 10^{-3}\,\mathrm{eV}^2$ but close to the overall systematic uncertainty budget of $17 \cdot 10^{-3}\,\mathrm{eV}^2$, which is unacceptable. It follows that the method requires a significantly higher statistic than expected in the measurement of the response function - even if the the rate is purely Poissonian, as assumed in the simulation. This can be obtained by either prolonging the measurement time or with a higher rate of the electron gun. With the already assumed performance of 25 kcps resulting in 10 days measurement time this is a challenge for the electron gun because the higher rate must not come at the cost of larger spreads in energy (0.2 eV assumed in [175]) or angular distribution. Much higher rates would also need improvements of the detector to resolve pile-up. Another drawback of this method is that the only way to quantify uncertainties of the deconvoluted energy loss function is the Monte Carlo method presented here. All measurement points are independent and therefore also all points of the model resulting in the same amount of parameters that need to be accommodated. In the following we investigate the scattering of electrons of hydrogen in more detail.

4.3 Electron Impact scattering

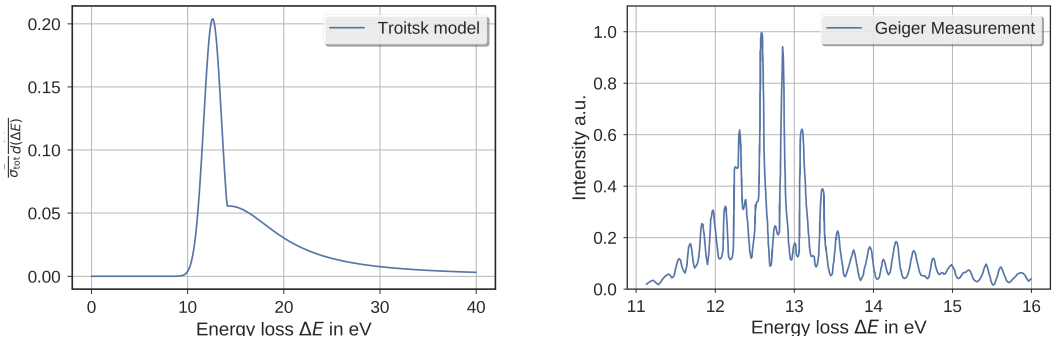

Figure 4.2: Results of the Troitsk model (left) and the electron scattering measurements by J. Geiger (right). The latter reproduces the data of fig. 4 in [182].

Electron scattering off hydrogen molecules has been studied in great detail with electrons in the energy range below 1 keV [183]. However, at the energies around the tritium endpoint comparably few detailed measurements have been published. The situation is even more difficult for measurements with the isotope tritium. For the modelling work in this thesis we resort to cross sections of molecular hydrogen. Mass effects within the spectrum are observed in vibrational and rotational excitations and use of this is made within KATRIN to measure the composition of the tritium gas [184, 185]. For inelastic scattering these are usually neglected in two ways: Only scattering off the ground state is considered, and possible rotational final states are not resolved. Elastic scattering, which in principle contributes too, was shown to be not relevant [153, 156]. As sketched in section 2.1.3, two quantities describing the energy loss in the source will enter the final neutrino mass analysis: the total inelastic cross section σ_{tot} and the energy loss function $\frac{1}{\sigma_{\mathrm{tot}}}\frac{d\sigma}{d\epsilon}$. While the former is simply a number, the latter is a complicated function, that enters the analysis directly but also in its self-convolutions. Therefore it is essential to assign proper uncertainties to the model and propagate them to the final neutrino mass result. While it is technically possible to treat these as two completely independent quantities in the analysis they are of course not truly independent: $\sigma_{\mathrm{tot}} = \int_0^\infty \mathrm{d}\epsilon \frac{d\sigma}{d\epsilon}$. This will be used as a basis consistency check of our model.

Most related to the issue at hand is the joint study by the predecessor experiments in Mainz and Troitsk [186]. The model used there is too coarse for the purposes of KATRIN. It was suitable for the measurements back then since the resolution of the smaller spectrometers used at the time were lower and the overall error budget bigger. Another measurement very close to the conditions at KATRIN is the 1964 measurement by J. Geiger [182], which was studying the scattering of a 25 keV electron beam by sparse hydrogen gas. A comparison of the two works, shown in figure 4.2, visualises the step KATRIN needs to take in terms of resolution of the energy loss model. In absence of other suitable material we will compare the results of the model developed here with

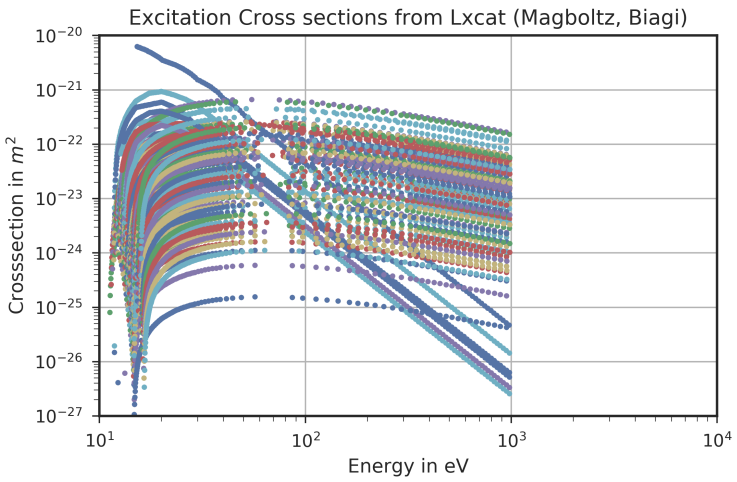

Figure 4.3: Excitation cross section data retrieved from [187] for 90 different states - all are unlabeled here. As with many more sources, this data ends at 1 keV which makes extrapolation necessary. Two populations are visible: one with fast decreasing cross sections towards higher energies with approximate power law-scaling and one only slowly varying.

these works.

Figure 2 in [183] and figure 4.3 - which displays data retrieved from [187] - can be used to illustrate how detailed state-resolved cross section data tends to be available at lower energies, but not at the tritium endpoint.

Note that the Troitsk model on the left in figure 4.2 displays an actual probability distribution while the Geiger measurement on the right shows measured intensities in arbitrary units. A further important difference is that the Troitsk model was fitted to a measurement in which very large scattering angles were accepted (which is very much the virtue of a MAC-E-Filter), while Geiger worked with highly collimated electron beams at 25 keV ($\theta < 3 \cdot 10^{-4}$) (rather than 18.6 keV) to achieve the good energy resolution (40 meV FWHM) and also restricted the scattered electrons to such a narrow window. The Troitsk model consists of a single Gaussian peak accounting for the excitations and a Lorentzian tail modelling the ionisation. The measurement of Geiger shows that the spectrum of molecular hydrogen is far more complicated. Yet it cannot be directly used, as ionisation is largely unaccounted for due to the limitation to small angles and the small energy window. The long tail towards high energy losses from ionisation shifts the mean energy loss and must be accounted for in KATRIN.

The model implemented in the following will extrapolate upon the Magboltz data using the expressions of [188] to fit the data.

4.3.1 Elastic Scattering

While elastic scattering is not relevant to the neutrino mass analysis, it does affect storage times of electrons within the main spectrometer[104, 126]. Since it is an reaction described in Kassiopeia [154], it shall be briefly mentioned here for completeness. The used total cross section for elastic scattering is

$$\sigma_{\mathrm{tot}}^{\mathrm{el}} = \frac{\pi}{k_0^2}(4.2106 - 2/k_0^2) \tag{4.26}$$

in atomic units and is taken from [189]. Around the tritium endpoint it is smaller than the cross section for inelastic scattering by an order of magnitude:

$$\sigma_{\mathrm{tot}}^{\mathrm{el}} = 0.29 \cdot 10^{-22}\,\mathrm{m}^2 \tag{4.27}$$

The corresponding median scattering angle is $\theta_{el} = 2.1^\circ$ [156]. The energy loss due to elastic scattering is given by the relation

$$\Delta E = 2\frac{m_e}{M_{T_2}}E(1 - \cos(\theta)) \tag{4.28}$$

For an angular distribution as given by [189] the median energy loss amounts to $\Delta E = 4.0\,\mathrm{meV}$. The systematic error on m_ν^2 from neglecting the elastic-scattering component is small ($1.1 \cdot 10^{-3}\,\mathrm{eV}^2$ [156]) and therefore it will not be considered further here.

4.3.2 Inelastic Scattering

Two types of inelastic scattering processes are considered in the following: ionisation and excitation scattering. From [188] a theoretical description of the total inelastic cross section is given as

$$\sigma_{\mathrm{tot}}^{\mathrm{inel}} = \frac{4\pi a_0^2 R}{T}\left[1.5482 \cdot \ln\left(\frac{T}{R}\right) + (2.2212 \pm 0.0434)\right]. \tag{4.29}$$

with a_0 denoting the Bohr radius, R the Rydberg constant and T the kinetic energy of the incoming electron. This amounts to a value of

$$\sigma_{\mathrm{tot}}^{\mathrm{inel}} = (3.45 \pm 0.0112) \cdot 10^{-22}\,\mathrm{m}^2 \tag{4.30}$$

around the tritium endpoint of 18575 eV, which agrees with the value of $(3.40 \pm 0.07) \cdot 10^{-22}\,\mathrm{m}$ from [186]. In a later paper by Liu, another parameterization is given [189]:

$$\sigma_{\mathrm{tot}}^{\mathrm{inel}} = \frac{4\pi a_0^2}{k_0^2}\left[1.5487\ln(k_0^2) + 2.4036 + \gamma_{\mathrm{tot}}/k_0^2\right] \tag{4.31}$$

which yields

$$\sigma_{\mathrm{tot}}^{\mathrm{inel}} = 3.498 \cdot 10^{-22}\,\mathrm{m}^2 \tag{4.32}$$

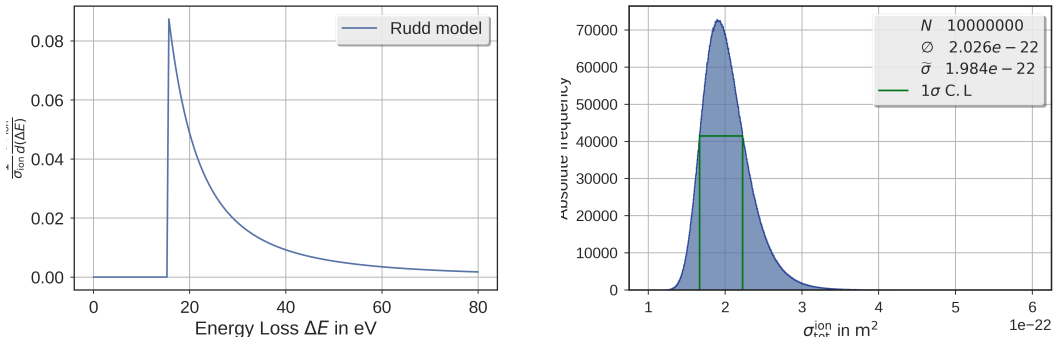

Figure 4.4: Left: Ionisation energy loss spectrum in the Rudd model for low energies. **Right**: The confidence interval for the ionisation cross section of the Rudd model was constructed as equal probability density interval from a Monte Carlo simulation.

As outlined above, two different processes contribute to inelastic scattering: electronic excitations and ionisation. The former brings a discrete component to the energy loss spectrum, the latter a continuous one. Note that the electronic processes are fast and the intrinsic widths of the lines in the spectrum are negligible within this context. The line widths found in the Geiger measurement are thus explained by the intrinsic width of the electron beam.

4.3.3 Ionisation

For ionisation we rely on two sources: the semi-empirical model by Rudd [190] and again on [188]. Rudd's model yields cross sections at high energies which are significantly too high with respect to the Troitsk measurement and [188]. Therefore it is only used for the energy loss distribution. The total cross section from [188] is

$$\sigma_{\text{tot}}^{\text{ion}} = \frac{4\pi a_0^2 R}{T}\left[(0.71 \pm 0.02)\ln\left(\frac{T}{R}\right) + (1.30 \pm 0.40)\right]. \tag{4.33}$$

This yields a total ionisation cross section of

$$\sigma_{\text{tot}}^{\text{ion}} = (1.66 \pm 0.14) \cdot 10^{-22}\,\text{m}^2 \tag{4.34}$$

at the tritium endpoint. As a result Rudd offers three functions: the total ionisation cross section $\sigma_{\text{ion}}(t)$, the single differential cross section $\sigma(t, w)$ and the double differential cross section $\sigma(t, w, \theta)$

$$\begin{aligned} \sigma_{\text{ion}}(t) &= S \cdot F(t) \cdot g_1(t) && (4.35)\\ \sigma(t, w) &= G_1(t, w)\left[g_B E(t, w) + G_4(t, w) g_b\right] && (4.36)\\ \sigma(t, w, \theta) &= G_1(t, w)\left[f_{BE}(t, w, \theta) + G_4(t, w) f_b(t, w, \theta)\right]. && (4.37) \end{aligned}$$

These are calculated by the set of equations 4.35 - 4.48 with the parameters given in table 4.1.

$$S = 8\pi a_0^2 \frac{R}{I}^2 \tag{4.38}$$

$$F(t) = \left(A_1 \cdot \ln(t) + A_2 + \frac{A_3}{t}\right)/t \tag{4.39}$$

$$g_1(t) = \frac{1-t^{1-n}}{n-1} - \left[\frac{2}{t+1}^{\frac{n}{2}} \cdot \frac{1-t^{1-\frac{n}{2}}}{n-2}\right] \tag{4.40}$$

$$g_{BE}(w,t) = 2\pi G_3 \cdot \left[\tan^{-1}\left(\frac{1-G_2}{G_3}\right) + \tan^{-1}\left(\frac{1+G_2}{G_3}\right)\right] \tag{4.41}$$

$$f_1(w,t) = \frac{1}{(w+1)^n} + \frac{1}{(t-w)^n} - \frac{1}{[(w+1)(t-w)]^{\frac{n}{2}}} \tag{4.42}$$

$$f_b = \frac{1}{1+[(\cos\theta+1)/G_5]^2} \tag{4.43}$$

$$f_{\mathrm{BE}} = \frac{1}{1+[(\cos\theta-G_2)/G_3]^2} \tag{4.44}$$

$$G_1(t,w) = \frac{SF(t)f_1(t,w)}{I(g_{\mathrm{BE}}(t,w)+G_4(t,w)g_b)} \tag{4.45}$$

$$G_2(t,w) = \sqrt{\frac{w+1}{t}} \tag{4.46}$$

$$G_3(t,w) = \beta\sqrt{\frac{1-G_2^2}{w}} \tag{4.47}$$

$$G_4(t,w) = \gamma\frac{(1-\frac{w}{t})^3}{t(w+1} \tag{4.48}$$

Therein θ represents the scattering angle, $t = T/I$ is the kinetic energy in units of the binding energy and $w = W/I$ the kinetic energy of the outgoing primary electron (the outgoing electron with the largest energy) in units of I, the (first) ionisation energy of 15.43 eV. Within Kassiopeia [154] the complete model, including the doubly differential cross section $\sigma(t,w,\theta)$, was implemented as part of this work. Because Monte Carlo simulations of the KATRIN response function by Groh [156] showed that effects of angular changes due to scattering are negligible for neutrino mass analysts they will be not regarded here. The total ionisation cross section within this model yields

$$\sigma_{\mathrm{tot}}^{\mathrm{ion}} = 1.984^{+0.245}_{-0.316} \cdot 10^{-22}\,\mathrm{m}^2 \tag{4.49}$$

The confidence interval for this ionisation cross section was constructed as equal probability density interval making use of a monte carlo simulation. The distribution is shown on the right in 4.4. For this the four input parameters of the model A_1, A_2, A_3 and n which were given with uncertainties (the others do not enter the total cross section) were diced from Gaussian distributions, assuming them to be uncorrelated. The resulting distribution is not normal and not symmetric. Its mean does not coincide with

Table 4.1: Parameters of the ionisation model in [190]. The first four variables were fitted to measurement data. The other four are numerical constants. Helium scattering was implemented in Kassiopeia [154] as well for simulation of stored particles, but is not discussed here.

	Hydrogen	Helium
A_1	0.74 ± 0.02	0.85 ± 0.04
A_2	0.85 ± 0.05	0.36 ± 0.09
A_3	-0.60 ± 0.02	-0.1 ± 0.1
n	2.4 ± 0.2	2.4 ± 0.3
G_5	0.33	0.33
β	0.6	0.60
γ	10	10
g_b	2.9	2.9

the model evaluated at the means of the parameters. This issue does not arise with the median which is therefore chosen as central value. While this result is compatible with the lower value $(1.656 \pm 0.140) \cdot 10^{-22}\,\mathrm{m}^2$ calculated from equation 4.33, it is still much higher and carries a larger uncertainty. The higher value will, when added to the excitation cross section, also be in conflict with the total inelastic cross section of $\sigma_{\mathrm{tot}}^{\mathrm{inel}} = (3.45 \pm 0.0112) \cdot 10^{-22}\,\mathrm{m}^2$ from equation 4.29. Therefore only the singly differential cross section $\sigma(t, w)$ from Rudd will be considered here in the form of a normalized energy loss probability distribution at the tritium endpoint:

$$f_{\mathrm{ion}}(\epsilon) = \frac{1}{\sigma_{\mathrm{tot}}^{\mathrm{ion}}} \frac{d\sigma^{\mathrm{ion}}}{d\epsilon} = \frac{\sigma(t, w)}{\sigma_{\mathrm{tot}}^{\mathrm{ion}}(t)} = \frac{\sigma(E_0/I, (E_0 - \epsilon)/I)}{\sigma_{\mathrm{tot}}^{\mathrm{ion}}(E_0/I)}. \tag{4.50}$$

This function is shown on the left in figure 4.4. Note that the KATRIN analysis window only probes less than 100 eV into the spectrum. However, for the calculation of rates also the fraction of electrons that scatter out of this window due to their exceedingly high energy losses must be accounted for as these processes lead to a lowering of the overall rate.

4.3.4 Excitation

The total excitation cross section from [188] is given by the parameterization

$$\sigma_{\mathrm{tot}}^{\mathrm{exc}} = \frac{4\pi a_0^2 R}{T} \left[(0.80 \pm 0.089) \cdot \ln(T/R) + (0.28 \pm 0.06) \right]. \tag{4.51}$$

This includes both, pure excitation processes and dissociative discrete excitations. In the following we will not differentiate between them, ignoring the fate of the molecule, since we are only interested in the energy loss of electrons. At the tritium endpoint this expression gives

$$\sigma_{\mathrm{tot}}^{\mathrm{exc}}(18575\,\mathrm{eV}) = (1.56 \pm 0.18) \cdot 10^{-22}\,\mathrm{m}^2. \tag{4.52}$$

For the energy loss description, the situation is very different from what was discussed for ionisation: The energy loss spectrum of excitations is discrete, with individual intrinsic line widths which are far too small to be resolved within KATRIN. In order to construct an energy loss function, all the cross sections for all individual excitations are needed. In absence of dedicated data these will be retrieved from extrapolation.

4.4 A new energy loss model

Using the sources discussed above we now construct an energy loss function

$$f(\epsilon) = \frac{1}{\sigma_{\text{tot}}}\frac{d\sigma}{d\epsilon} = p_{\text{exc}}\frac{1}{\sigma_{\text{tot}}^{\text{exc}}}\frac{d\sigma^{\text{exc}}}{d\epsilon} + p_{\text{ion}}\frac{1}{\sigma_{\text{tot}}^{\text{ion}}}\frac{d\sigma^{\text{ion}}}{d\epsilon} \tag{4.53}$$

The first term consists of the discrete excitation lines:

$$\frac{1}{\sigma_{\text{tot}}^{\text{exc}}}\frac{d\sigma^{\text{exc}}}{d\epsilon} = \sum_i p_i \delta(\epsilon - E_i) \tag{4.54}$$

with

$$p_{\text{tot}}^{\text{ion,exc}} = \frac{\sigma_{\text{tot}}^{\text{ion,exc}}}{\sigma_{\text{tot}}}, \tag{4.55}$$

$$p_i = \frac{\sigma_i}{\sigma_{\text{tot}}^{\text{exc}}}, \tag{4.56}$$

$$\sigma_{\text{tot}}^{\text{exc}} = \sum_i p_i. \tag{4.57}$$

Therein σ_i is the cross section for excitation of the molecule into the state of energy E_i and $\delta(\epsilon - E_i)$ is the, up to now arbitrary, line shape. Values for E_i are included in the data from [187]. In order to calculate the missing cross sections σ_i we will split this data into two sets which are then extrapolated differently. For the first subset a simple power-law scaling $f(x) = a \cdot x^b$ is used, which is of sufficient precision. For the second, larger, subset the same form that describes the scaling of the total excitation cross section

$$f(x) = N/x \cdot (a \cdot \ln(x) + b) \tag{4.58}$$

is used with $N = 4\pi a_0^2$ and $x = T/R$. In both cases a and b are the free parameters. The power-law scaling of the first subset is evident from the plot and these cross sections are orders of magnitude smaller at the tritium endpoint than those of the second subset. Therefore it is this second subset that dominates the scaling of expression 4.51. As both fitting expressions are unsuitable to describe high-energy scaling and threshold behaviour simultaneously well only data from 300 eV onwards is regarded for the fit. This unphysical cutoff parameter is a potential source of systematic uncertainty that needs to be accounted for later on. It is important to note that some processes are

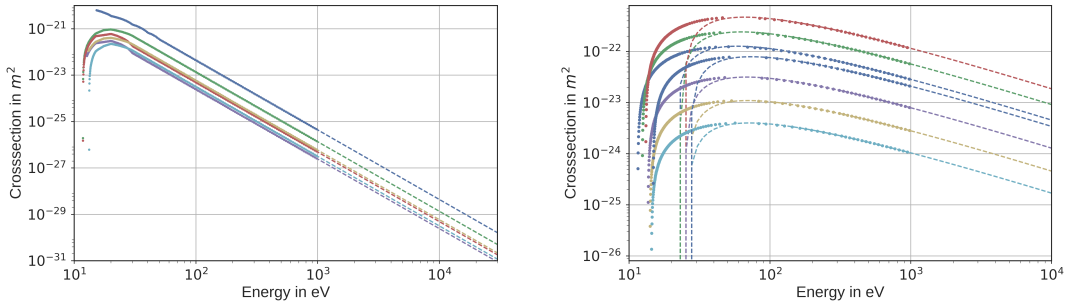

Figure 4.5: Examplary fits for the power law subset (left, complete subset) and the ln-scaling subset (right, only a few curves shown to avoid a too crowded plot). Only data above 300 eV was considered for the fit.

included multiple times in the data set (stand-alone and as part of a multiplet) and the doublings have obviously to be excluded to arrive at the correct results. This and the correct extrapolation methods are the key ingredient that were missed in an earlier bachelor thesis advised by the author [169]. The cross section data in [187] are not available with an uncertainty estimate which makes it difficult to assess the goodness of fit objectively. In figure 4.5, exemplary fits are shown for both subsets. In figure 4.6 a combined histogram of the relative deviations between the fits and all the data points is given. The maximal deviation is 2.5%. The numerical values of the obtained fit parameters are listed in the appendix together with the energies of the excitations, the extrapolated cross sections at the tritium endpoint and their uncertainties calculated from the fits correlation matrices. However, since the cross section data does not come with uncertainties these have to be treated with caution, most likely they are too small. The total excitation cross section calculated this way is

$$\sigma_{\text{tot}}^{\text{exc}} = (1.65 \pm 0.017) \cdot 10^{-22}\,\text{m}^2 \tag{4.59}$$

For the total ionisation cross section we again use a fit to extrapolate from the data in [187]. As fitting function we use the form given in [189]

$$\sigma_{\text{ion}}(T, a, b) = \frac{4\pi a_0^2 R}{T}\left[a \cdot \ln(T/R) + b + \gamma_{\text{tot}} R/T\right] \tag{4.60}$$

again with a and b as free parameters where

$$\gamma_{\text{tot}} = 2\left[-\frac{7}{4} + \ln\left(\frac{IR}{T}\right)\right]. \tag{4.61}$$

The result is displayed in figure 4.7. It gives an extrapolated total ionisation cross section at the tritium endpoint of

$$\sigma_{\text{tot}}^{\text{ion}} = (1.84 \pm 0.015) \cdot 10^{-22}\,\text{m}^2 \tag{4.62}$$

Again the uncertainty obtained from the fit is likely too small.

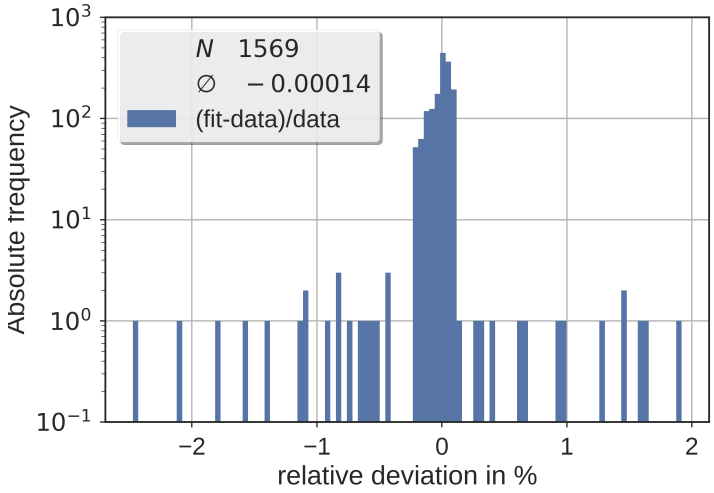

Figure 4.6: Relative deviation between Biagi Data and fitted formulas for all data points of all cross sections above 300 eV

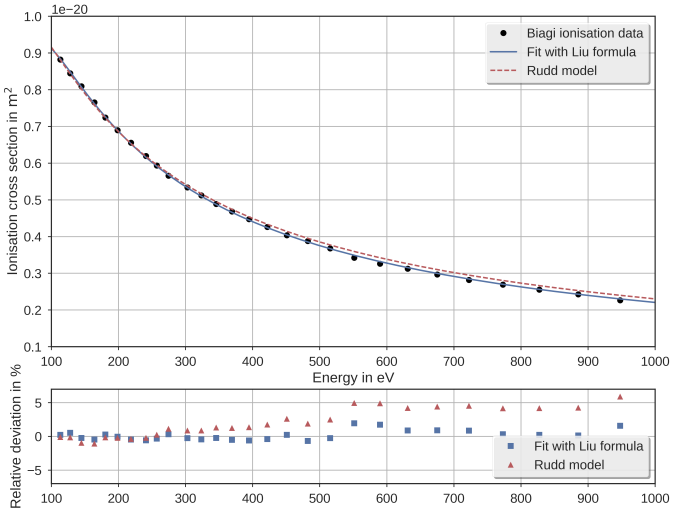

Figure 4.7: Comparison of the Rudd model [190], Biagi data [187] and the fit with equation 4.60. While all three agree at low energies the Rudd model starts to depart from the Biagi cross sections. Since the result by Liu [189] is also considerably smaller, we will stick to the fit performed here.

Line shape and width

By now we have almost all the ingredients together that make up the energy loss model. The remaining question concerns the line shape δ in equation 4.54 and the corresponding line width. For the emission of the β-spectrum the Gaussian Doppler width caused by the thermal motion of the tritium molecules at 30 K the was calculated in [111] to be

$$\sigma_{\mathrm{Th}} = \sqrt{2E_0 k_B T m_e / M_{T_2}} \approx 93\,\mathrm{meV} \tag{4.63}$$

$$W_{\mathrm{FWHM}} = 2\sqrt{2\ln 2} \cdot \sigma_{\mathrm{Th}} = 213\,\mathrm{meV} \tag{4.64}$$

with E_0 being the tritium endpoint energy. For the energy loss spectra, however, the situation is different. The main difference between the energy loss broadening and the β spectrum broadening is that in the scattering case it is the excitation energy of the state that is broadened, while for the β-decay it is the much higher decay energy leading to a larger broadening. The correct approximation of the Doppler width with incident energies far above the excitation energy for zero angle inelastic scattering is, according to Chantry [191]

$$W_{\mathrm{FWHM}} = E^* \sqrt{\frac{11.1}{4} \cdot \frac{m_e}{M_{T_2}} \frac{k_B T}{E_0}} \approx 0.074\,\mathrm{meV} \tag{4.65}$$

where E^* is the excitation energy. However, there is also the derivation by Read [192] which accounts for a small scattering angle:

$$W_{\mathrm{FWHM}}(\theta) = 4\sqrt{\frac{\ln(2) k_B T m_e E}{M_{T_2}}} \tag{4.66}$$

where

$$E = \frac{1}{2} m_e \Delta v^2 = E_i + E_f - 2\sqrt{E_i E_f}\cos(\theta) \tag{4.67}$$

This agrees with the formula of Chantry [191] for $\theta = 0$. For the mean inelastic scattering angle of 0.61° calculated as by Groh [156] a equivalent broadening of

$$W_{\mathrm{FWHM}}(0.61^\circ) = 2.34\,\mathrm{meV} \tag{4.68}$$

is calculated. This corresponds to a Gaussian width $\sigma_{\mathrm{Th}} = 1\,\mathrm{meV}$. The width of the energy loss is thus negligible in comparison to other random widths caused by e.g. high voltage fluctuations (specification 60 mV, current measurements 20 mV). As all other possible broadening effects such as natural broadening, field broadening, pressure broadening are again much smaller, the lines can be treated as being discrete in nature for all practical purposes. This is important, because any unaccounted for random width folded into the measured β spectrum will impose a systematic neutrino mass shift equivalent to $\Delta m_\nu^2 = -2\sigma^2$, see the result from [193] and its derivation in [194] (pp. 21-24) leading to equation 2.32 therein.

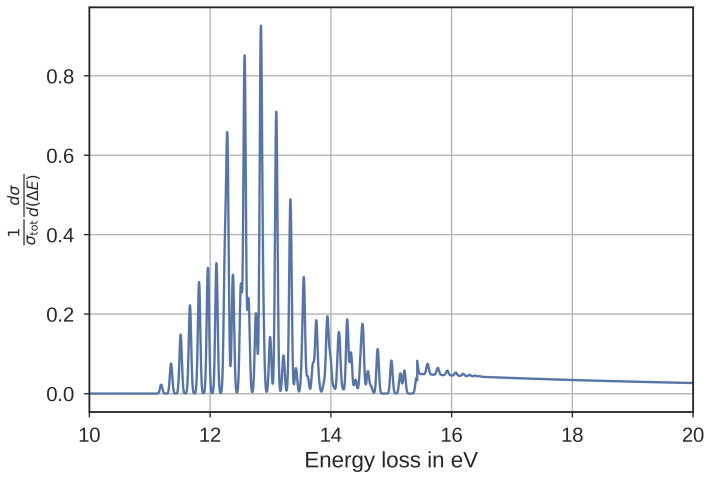

Figure 4.8: Resulting energy loss function. The discrete lines were smoothed with a $\sigma = 20\,\mathrm{meV}$ wide Gaussian for visualization purposes only.

Total inelastic cross section and energy loss distribution

Finally, our total inelastic cross section is given by

$$\sigma_{\mathrm{tot}}^{\mathrm{inel}} = \sigma_{\mathrm{tot}}^{\mathrm{ion}} + \sigma_{\mathrm{tot}}^{\mathrm{exc}} = (3.487 \pm 0.022) \cdot 10^{-22}\,\mathrm{m}^2. \tag{4.69}$$

The energy loss function constructed according to equation 4.53 is plotted in figure 4.8 smoothed with an artificial $\sigma = 20\,\mathrm{meV}$ Gaussian line width for better visualisation. In the following these results will finally be compared to the literature.

4.5 Model Evaluation

We will compare the results of the model constructed here to different available sources in the literature:

- The total cross sections of Liu [188, 189], Troitsk [186] and Rudd [190].
- The energy loss function given by [186]
- The energy loss spectrum from [182]

Afterwards we will study how deviations of the model parameters from their true values would influence the neutrino mass sensitivity of KATRIN when used in analysis.

While the comparison of the scattering cross sections is straight forward, the Troitsk model includes 6 parameters and a model assumption, which makes a direct comparison difficult: all lines are treated together, while here we explicitly deal with them separately.

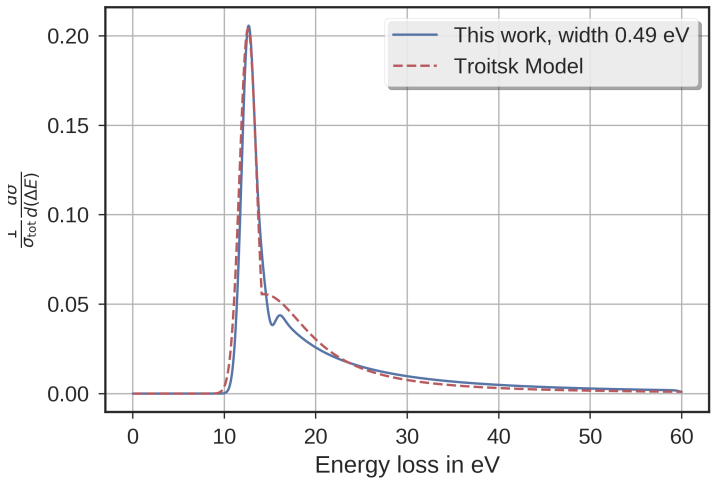

Figure 4.9: Comparison between the Troitsk model and the calculated energy loss function.

With the not normalized energy loss spectrum of [182] comparison is also difficult. Ultimately the meaningful way to compare two models of energy loss for KATRIN is to evaluate the neutrino mass shift

4.5.1 Total cross sections

In table 4.2, the different total cross sections at the tritium endpoint calculated from the aforementioned sources are listed. Obviously, there is a certain tension between the ionisation cross sections from Rudd and Liu. The value calculated from extrapolation falls between these and is consistent with both. The last line shows what the model in this work achieves: It is exactly normalized. The individual cross sections of all the excitations and the ionisation process sum up to the total cross section. While the results from Liu are still consistent with each other this is not the case there. This property is necessary in order to construct a meaningful energy loss spectrum.

Table 4.2: Comparison of the different total electron impact scattering cross sections on $H_2(T_2)$ from the literature and those obtained here by fitting the data from [187].

Unit ($10^{-22}\,\mathrm{m}^2$)	Liu 73 [188]	Liu 87 [189]	Rudd [190]	Troitsk [186]	This work
$\sigma_{\mathrm{tot}}^{\mathrm{inel}}$	3.45 ± 0.01	3.498		3.4 ± 0.07	3.487 ± 0.022
$\sigma_{\mathrm{tot}}^{\mathrm{ion}}$	1.66 ± 0.14		$1.984^{+0.245}_{-0.316}$		1.840 ± 0.015
$\sigma_{\mathrm{tot}}^{\mathrm{exc}}$	1.56 ± 0.18				1.647 ± 0.017
$\sigma_{\mathrm{tot}}^{\mathrm{exc}} + \sigma_{\mathrm{tot}}^{\mathrm{ion}}$	3.22 ± 0.23	-	-	-	3.487 ± 0.022

4.5.2 Comparison of the model against the Troitsk results

The energy loss model of the Troitsk experiment is given by [186]

$$f(\epsilon) = \begin{cases} A_1 \cdot e^{-2\frac{\epsilon-\epsilon_1}{w_1}^2} & \epsilon < \epsilon_c \\ A_2 \cdot \frac{w_2^2}{w_2^2+4(\epsilon-\epsilon_2)^2} & \epsilon > \epsilon_c \end{cases} \tag{4.70}$$

with fitted parameters given in table 4.3.

This model is considered here because it was used in a previous tritium-based neutrino mass experiment with a gaseous source very similar to KATRIN. This means the energy range under scrutiny is the same for the kinetic impact energy as well as for the energy loss. The function was used in fitting transmission measurement data taken with the Troitsk setup and a monochromatic electron source. It was instrumental in the extraction of the final result of the Troitsk measurement of an upper limit on the neutrino mass of $m_e \leq 2.05\,\mathrm{eV}$ (95%C.L.).

A direct numerical point-by-point comparison between the Troitsk model and the one developed here makes little sense due to the completely different shapes of the distributions. This stems from the much higher resolution of the new model. Certain statistical properties however are expected to be consistent within uncertainties between the two distributions. This way of comparison was chosen in [186] as well for the results of different measurements. Values of interest are the mean energy loss $\bar{\epsilon}$ and the most probable value ϵ_1. These were found to be $\bar{\epsilon} = (29.9 \pm 1)\,\mathrm{eV}$ and $\epsilon_1 = (12.6 \pm 0.3)\,\mathrm{eV}$ for gaseous T_2, well in agreement with predictions for gaseous H_2 as seen in Table 4 in [186]. The new model is compatible with these findings and yields $\bar{\epsilon} = 29.98\,\mathrm{eV}$ and $\epsilon_1 = 12.66\,\mathrm{eV}$. Furthermore, it is possible to fold a Gaussian into the new model and compare the broadened energy loss function directly with the Troitsk form. This is shown in figure 4.9. In order to derive comparable results, the calculated energy loss spectrum was convolved with a Gaussian of width $\sigma = 0.49\,\mathrm{eV}$. chosen to best match the results of the Troitsk model. While the excitation peak is reproduced, the ionisation tail differs severely between the models. It should be noted that the Troitsk model suffers a problem: The Lorentzian tail is naturally normed on the interval $(0, \infty)$ which would in principle allow - of course unphysical - infinite energy losses. This makes the model results ultimately dependent on an artificial cutoff at large energy losses. Rudd's model avoids this because the energy loss function is symmetric with respect to the kinetic energies of the two electrons in the final state. Therefore it is defined only within the interval between the binding energy and the incident energy minus the binding energy. This forces the tail into a different shape than within the Troitsk model.

4.5.3 Comparison of the model against measurement results by J. Geiger

The measurement by Geiger [182] also is nontrivial to compare against our results. Apart from mentioning the peak of the distribution at $\Delta E = 12.6\,\mathrm{eV}$ no other value describing directly the energy loss distribution is given. While we can easily adapt

Table 4.3: Parameters of the Troitsk model

A_1	0.204 ± 0.001
w_1	1.85 ± 0.02
ϵ_1	12.6
A_2	0.0556 ± 0.0003
w_2	12.5 ± 0.1
ϵ_2	14.3 ± 0.02
ϵ_c	14.09

our model to 25 keV incident energy, as used in that measurement instead of 18.6 keV, the possible effect of the narrow allowed scattering angle on the peak ratios cannot be estimated without prior knowledge of the full double differential cross section for each line. The same is to be said about ionisation. While a double differential cross section for ionisation is given in equation 4.37, it is not helpful without knowing how it compares to those of the excitation lines. In the Geiger measurement the ionisation threshold is not visible. Furthermore, the measurement data itself is probably lost - from the paper we have retrieved the figure 4. and digitized the plotted line by hand, which of course presents another source of error. The plot does not give a probability distribution but an intensity spectrum in arbitrary units and we do not know the background rate in that measurement. That being said, a comparison between the Geiger measurement, scaled arbitrarily, and the energy loss model developed here - with an artificial Gaussian line width of 40 meV FWHM, matching the reported resolution of the measurement - is shown in figure 4.10.

4.5.4 Evaluation of Uncertainties in the Energy Loss model

Within the context of the neutrino mass analysis of KATRIN the most meaningful way to quantify the uncertainty of the energy loss model is by estimating the average shift of the m_ν^2 fit result caused by a deviation between estimated and true value of an input parameter. Under the assumption that the developed model is close to an exact description of electron energy losses by scattering off hydrogen the influence of small deviations of the model input parameters from their true values on the neutrino mass fit result can be studied. This was done using the profile likelihood method as explained in and the results are shown in table 4.4. For each parameter neutrino mass shifts caused by higher (lower) true values are listed right next to the largest tolerable relative deviation of that parameter - for which a maximal allowed squared neutrino mass shift of less then $2.5 \times 10^{-3}\,\mathrm{eV}^2$ is assumed. This amounts to 1% of the KATRIN total systematic uncertainty budget. Finally, the present uncertainties on the parameters are given if they are known. The associated neutrino mass shifts for the known uncertainties are calculated conservatively and take the uncertainty as actual deviation. Parameters A_1 through I stem from Rudd's model of ionisation.

The inelastic scattering cross section as well as the energy loss distribution both

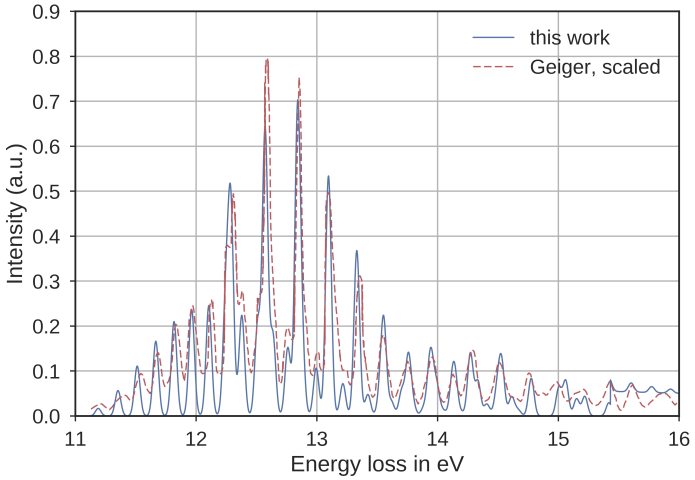

Figure 4.10: Comparison between the Geiger measurement and the energy loss function calculated here. Superficially they are similar, but in the details they differ. The line positions mostly agree, though there seems to be a systematic shift visible at low energies. The peak heights are similar for high and low energies, but the two highest peaks are not matched.

depend on the kinetic energy of the impacting electron E_{kin} and have generally been taken as constant so far [54], completely ignoring the energy dependence of the scattering model over the 70 eV measurement interval of KATRIN. Here the neutrino mass shift assigned to the parameter E_{kin} conservatively estimates this systematic effect by assuming a 70 eV deviation for *all* measured (and scattered) electrons. This is of course in principle avoidable though a running energy loss model is presently not implemented within the KATRIN Model SSC. Naturally, no meaningful uncertainty is assigned to this parameter.

The set of parameters E_i and σ_i are the energies of the individual excitation and their cross sections. For E_i the tolerable deviation and its associated shift refer to the highest probability excitation line being displaced. For σ_i it is the deviation of the largest excitation cross section. For these parameters no reliable uncertainty could be determined.

The requirements on the individual parameters are so tight because a change in most of them causes a change in the normalisation of the energy loss function. Then even a seemingly local deviation in a single excitation spreads out over the energy loss distribution and influences the measured spectrum over the entire energy range. If, for example, a single excitation cross section would change, the total inelastic cross section would, too. Then the weighted contribution of the ionisation is affected as well. As result, the whole tail towards high energies is enhanced or suppressed.

The total systematic uncertainty of the whole model amounts to $2.57 \cdot 10^{-3}\,\mathrm{eV}^2$ if the requirements are fulfilled and the running of the energy loss model is properly incorporated into the spectrum calculation - assuming quadratic summation and thus

Parameter	Value	Upper Tolerance(rel)	$\Delta m^2\,\mathrm{eV}^2$	Lower Tolerance(rel)	$\Delta m^2\,\mathrm{eV}^2$	known (abs)	known (rel)	$\Delta m^2\,\mathrm{eV}^2$
A_1	0.74	1.e-3	6.4e-4	1.e-3	6.5e-4	±0.02	2.7e-2	1.7e-2
A_2	0.87	1.e-2	1.0e-3	1.e-2	1.0e-3	±0.05	5.7e-2	6.1e-3
A_3	-0.6	3.e-1	3.4e-6	3.e-1	4.4e-5	±0.05	8.3e-2	0.
n	2.40	1.e-3	1.5e-3	1.e-3	1.6e-3	±0.02	8.3e-3	1.3e-2
I	15.43 eV	1.e-3	8.3e-4	1.e-3	1.4e-4	–	–	–
E_{kin}	18575 eV	Irr	Irr	-70 eV	2.5e-3	–	–	–
E_i	–	1.e-3	2.5e-4	1.e-3	2.5e-4	?	–	–
σ_i	–	2.e-2	1.6e-3	2.e-2	1.6e-3	?	–	–

Table 4.4: Model requirements. For each parameter neutrino mass shifts caused by higher (lower) true values were calculated using the Profile Likelihood method provided by KaFit, see sec. 3.5. A maximal allowed squared neutrino mass shift of less then $2.5 \cdot 10^{-3}\,\mathrm{eV}^2$ is assumed, which increases the systematic uncertainty by 1% when added in quadrature to the standard budget of $0.017\,\mathrm{eV}^2$

no correlations between the parameters.

4.6 Conclusion

In this chapter we were led to the construction of an improved model to describe electron impact scattering off molecular hydrogen and tritium, since we found that a previously proposed method of measurement suffers from a high sensitivity to experimental noise and as a result has a high demand of measurement time. The uncertainties of the constructed model stem from the literature results it was built upon and are still not sufficient for the purpose of the ultimate neutrino mass analysis. It is essential that the model is improved upon either by measurement or theoretical calculations.

CHAPTER 5

Measurement and Simulation of Neutral Particle Background

Within [170] the present understanding of stored particle background was discussed. This mechanism is, however, at the current stage not the dominating source of background at the KATRIN Main spectrometer. Within this chapter known background processes will be excluded as main contributions and a novel mechanism by which surface α-activity creates background within the flux tube of the spectrometer will be presented, simulated and compared to measurements. At first the measured characteristics of the spectrometer background will be presented in sect. 5.1. Then in sect. 5.2 known background processes will be excluded, partially by dedicated measurements. The principles of the new background model will be outlined in sect. 5.3. The simulation methods and results of the model will be presented in sect. 5.4. Afterwards possibilities for background mitigation and consequences of the background for the KATRIN experiment will be discussed in section sect. 5.5, followed by the conclusion in sect. 5.6.

Naturally, this chapter is deeply intertwined with chapter 6 of [170] as it starts from there, recapitulates the findings, and then sets out to go beyond it for building and testing the background model. The most important turn is that the topics of ^{210}Pb induced background and neutral particle (Rydberg) background which were treated separately there are indeed connected by an α-decay chain and the sputtering caused by it.

5.1 Characteristics of the remaining Main Spectrometer Background

In the following the main characteristics of the residual background coming from the KATRIN main spectrometer will be discussed. In particular, this comprises its distribution in volume and time as well as the dependence on the voltage settings of the spectrometer. For this we partly rely on results from [170] as indicated. However, novel

dedicated measurements were carried out. Finally we show how the background was actively increased by artifically contaminating the spectrometer with the short lived decay chain of ^{222}**Rn**.

5.1.1 Spatial background profile

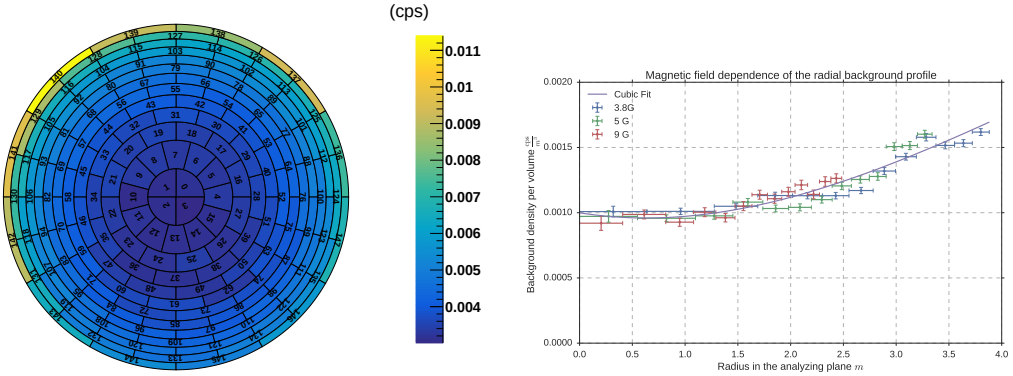

Figure 5.1: Left: Schematic mapping of the focal plane detector wafer. Pixels are colored according to the raw absolute spectrometer background rate they measure. Background increases from the the center towards the outer rings. **Right**: Radial background profiles for different magnetic fields. The rates for each detector ring have been normalized by the volume of the fluxtube that is imaged on to it. The data are consistent with a fixed spacial background density which is imaged differently on to the detector by different magnetic field settings. The absolute magnetic field strength it self does not have a direct influence on the background creating processes

The first feature of the residual background to be observed during the SDS commissioning measurements was the distribution of the rate over the 148 pixels of the detector wafer. As can be seen in figure 5.1 the rate is distributed over the whole wafer with an increase of (raw) rate per pixel by a factor of about 3 towards the outer rings. However, if measurements for different magnetic fields are combined a different picture emerges. Higher magnetic fields reduce the total background rate in the same manner as they shrink the volume from which electrons can reach the detector. In figure 5.1 the radial profile was normalized to the volume imaged onto the detector for different magnetic field settings. Furthermore, we do not use the radius of the pixel boundaries at the site of the detector is on the x-axis but the radius of the field line in the analyzing plane which hits the pixel boundary. This radius is dependent on the magnetic field. The rate density per volume still sees a small increase towards the outside, which however is of a more modest factor of 1.5 - Apparently the rate is nearly homogeneous distributed in volume. The data is consistent with the hypothesis that the rate density per volume is not affected by the absolute value of the magnetic field. Only the size of the volume from which electrons are guided to the detector is changed and, accordingly, the rate.

It is emphasized here that this implies a background density that is constant in the otherwise empty (up to a residual pressure of 10^{-10} mbar) space of the main spectrometer

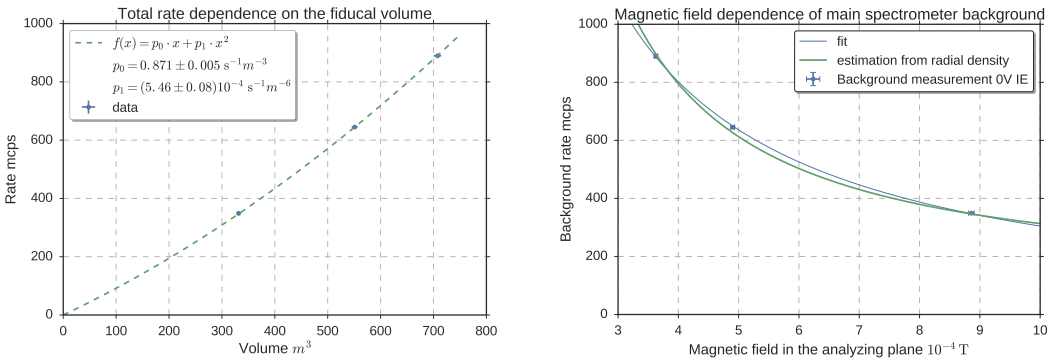

Figure 5.2: Left: The background rate scales nearly linearly with the volume. A small quadratic term is needed due to the increase of background density towards larger radii. **Right**: Modeling the dependence of the background rate as a function of the applied analyzing magnetic field.

vessel. Any process to create these free electrons that relies on the rare residual gas atoms would be heavily suppressed. Together with the fact that the background volume density is higher towards the outside this hints at processes on the vessel walls as origin. In the following we will build a spatial model of the background in order to give a rough estimate of the expected background rate for arbitrary (but sensible) analyzing magnetic field strengths. This will be useful later on for studying the trade off in neutrino mass sensitivity to make when choosing the optimal magnetic field configuration. While higher magnetic fields reduce the background, they introduce a higher systematic uncertainty, as layed out in [195].

5.1.2 Background time structure

To investigate the time structure of the background we reanalyze the data set of the Christmas Measurements as in [170], yielding essentially the same results: The background is largely Poissonian distributed - in contrast to the previously observed and eliminated Radon background. However a so far unnoticed sub-percent contribution of correlated events coming from the main spectrometer does exist and is shown in figure 5.4. These coincident events feature interarrival times of less than 100 μs which is much shorter than the 0.2 s time scale of radon events observed at *elevated pressure* ($\approx 10^{-8}$mbar), in which case the larger residual pressure is necessary to shorten the storage times of the electrons, for otherwise the time scale of their correlation would be too large and therefore no event structure could be observed. These measurements were done at a nominal pressure of 10^{-10} mbar where storage times are expected to be longer than in the case of elevated pressure. The observed correlation time scale is therefore too short for stored electrons on the one hand but too long for atomic or nuclear physics to be dominant. However, this range does fit to the time scale of flight time differences of low energy electrons within the main spectrometer as measured in [158] (Fig. 8.8 on

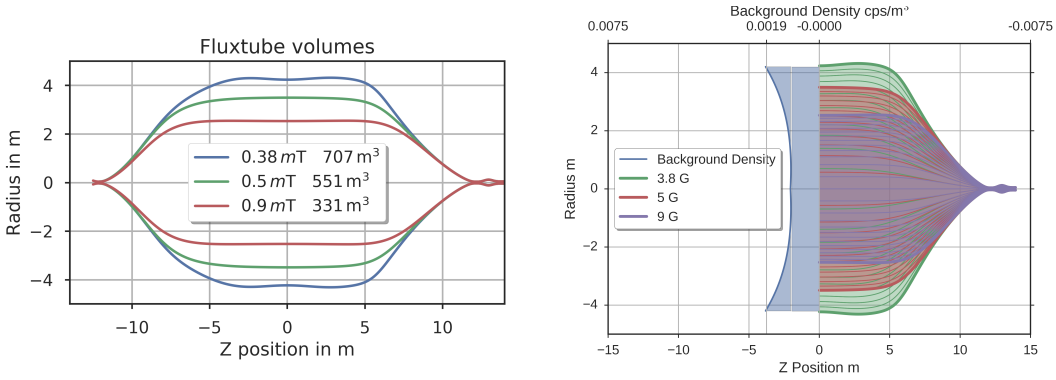

Figure 5.3: Left: Outer field lines of the different air coil settings simulated with Kassiopeia and the enclosed volume. As the magnetic flux is constant, $BA = const.$, and stronger analyzing fields only affect the central, approximately cylindrical volume, the volumes are expected to scale roughly like $V \propto \frac{1}{B} + const.$ **Right**: Scheme to illustrate how the fixed background density (blue) is mapped on to the detector by different magnetic flux tubes

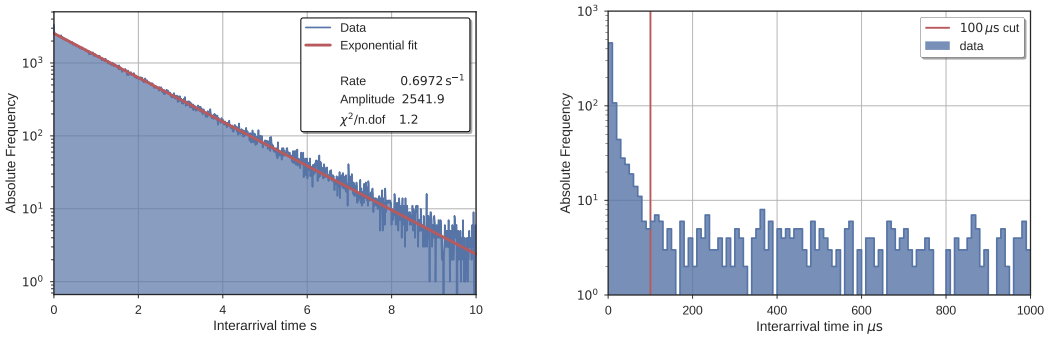

Figure 5.4: As visible on the left, the background is largely Poissonian. However on short time scales below 100 μs a non-Poissonian contribution is present. These are 730 events which amounts to 1.99 ± 0.07‰ of all events.

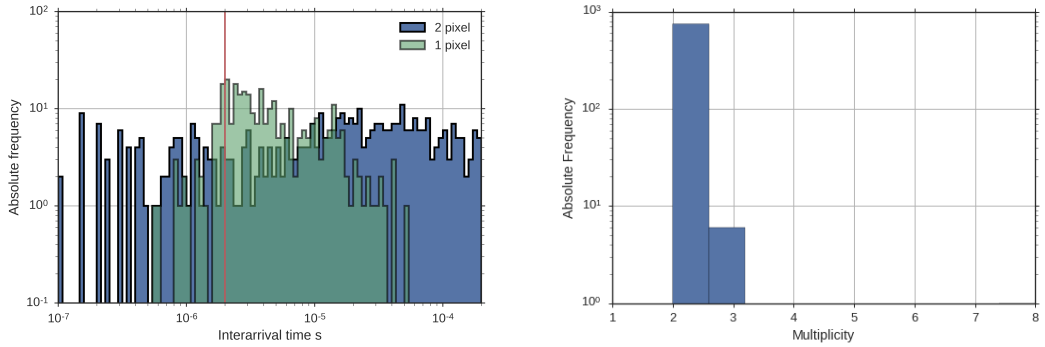

Figure 5.5: Left: Interarrival Times of clusters with multiplicity 2 divided into populations of one pixel hits and two pixel hits. The red line at 2 μs indicates the multi-pixel cut that is applied in general to filter out genuine detector background. Right: overall Multiplicity distribution. The majority of clusters consist of two events, with in total five clusters of three events.

p207). A closer inspection of these correlated events is shown and described in figure 5.5.

5.1.3 Vessel potential dependence

The background rate depends smoothly on the overall vessel potential. The dependence of the spectrometer background is shown in figure 5.6. At low retarding voltages only a small residual background is measured. It significantly increases with higher voltages of several hundred volts and then reaches a plateau above 10 kV. The behavior can be described by a empirical functional dependence $R_{\mathrm{bg}}(U_0)$:

$$R_{\mathrm{bg}}(U_0) = p_0 \cdot e^{p_1/(U_0+p_2)}. \tag{5.1}$$

This however is not unique to the residual background. A measurement conducted by F. Fränkle is shown also in figure 5.6. There the background was artificially increased by attaching a radon source to the main spectrometer. As a result, the background was dominated by stored electrons, yet the same type of functional dependence is found again, albeit with different parameters.

5.1.4 Inner electrode screening potential dependence

The observed background rate strongly depends on the potential applied between the vessel wall and the inner wire electrode. This fact alone hints at the materials of the vessel wall, inner electrode, and holding structure as origin of the background as the resulting electric fields are strongest in that region. Together with the spatial distribution of the background, which features higher rates per pixel towards the outside of the flux tube, this is very suggestive.

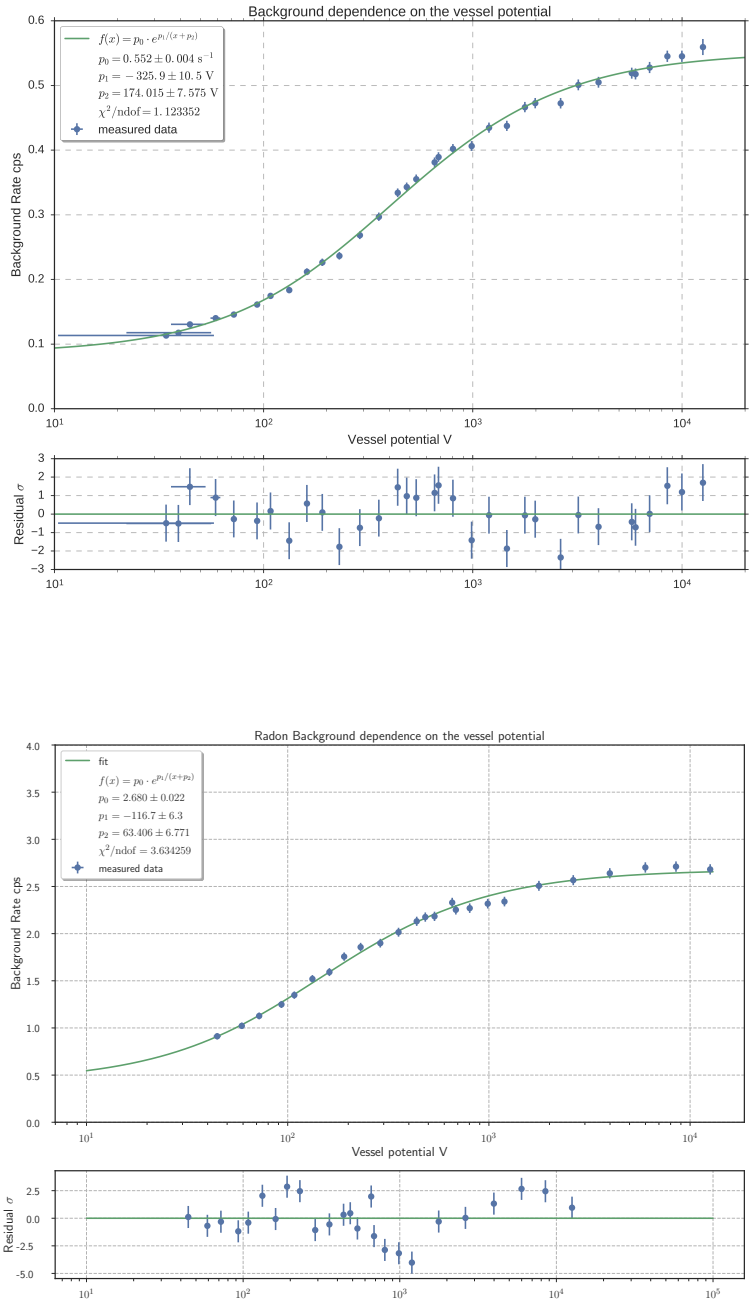

Figure 5.6: Top: Dependence of the total background rate on the vessel potential of the main spectrometer. Measurement taken *after* bake out. **Bottom:** a similar measurement taken by F. Fränkle with an artificial Radon source attached to the main spectrometer. The same type of functional dependence of the background rate on the vessel potential is found. The deviations are larger because the Poissonian uncertainty estimate for the rate does not capture the full variance of the rate.

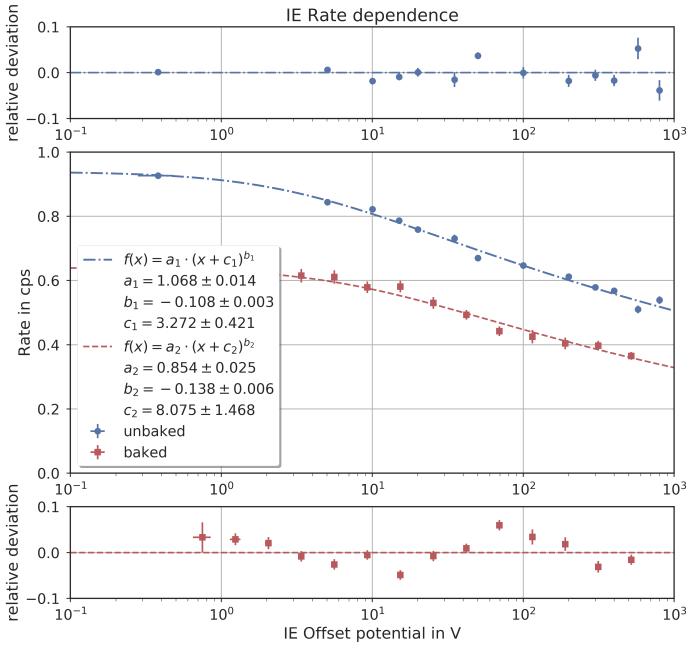

Figure 5.7: Dependence of the background rate on the offset potential between the vessel wall and the inner wire electrodes, before and after bakeout. The dashed/dotted lines are fits with a broken power law of the form $f(x) = a \cdot (x + c)^b$

What is even more striking, is that this spacial profile of the background does not change significantly with higher voltages, only the total rate (see fig. 5.8). After the measurement conducted in [170] with an *unbaked* spectrometer, another dedicated and more detailed measurement was conducted after baking. It was found that the outbaking of the spectrometer vessel significantly reduces the background. This is consistent with the idea of the background origin being located at the vessel wall and inner electrode structure. The creation process then depends on the surface conditions of the material. These are changed by the thermal cycle: The H_2O monolayer on the surface is removed completely or in significant parts. The data is presented in fig. 5.7 together with fits of a broken power law. It can be seen that as for the spatial profile the reaction of the background to increasing inner electrode potential is not changed by outbaking the spectrometer.

5.1.5 Temperature Dependence

Within the SDS-II measurement campaign the dependence of the background rate on the temperature of the main spectrometer vessel was studied with a dedicated measurement. For this the oil heating system of the spectrometer was used. Over the course of several days the spectrometer vessel was heated from an ambient temperature of about 19 °C

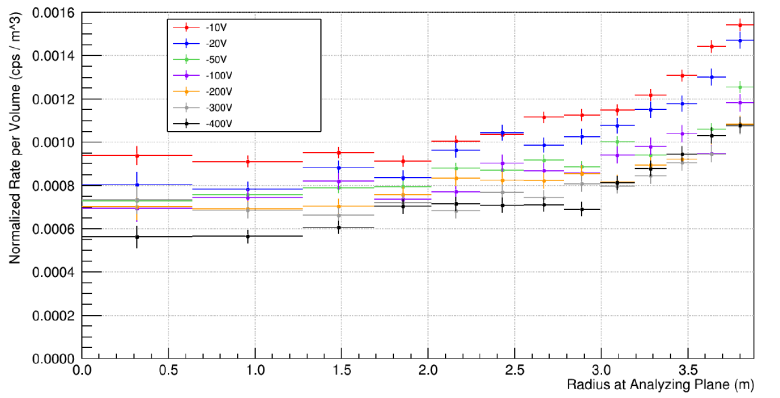

Figure 5.8: Radial background profiles for different inner electrode offset potentials. While the total rate decreases with higher voltage, the radial distribution is not influenced.

up to about 43 °C and back down while the FPD monitored the background rate, see fig. 5.9. Four different electro-magnetic settings were cycled through. Here the symmetric default setting is examined as it yields the highest statistics. From the regression of the measurement a relative increase of background by $(6.8 \pm 0.6)\%$ between minimum and maximum temperature is observed.

5.1.6 Artificial ^{220}Rn contamination of the Main Spectrometer

In order to test whether the residual main spectrometer background is caused by the ^{210}Pb contamination found by [170] a dedicated measurement was performed in December 2016: the main spectrometer was artificially contaminated using the short-lived isotope ^{220}Rn. In contrast to the natural occurring ^{222}Rn all decay products in this chain are also short-lived and thus pose no risk of long-term contamination. Furthermore this chain was chosen as it closely resembles the long-lived ^{222}Rn chain in decay types, decay energies, masses and the generated ^{212}Pb has a significantly longer half life than the rest of the chain (10.64 h in comparison to the order of seconds or at most an hour in the case of ^{212}Bi). That, analogously to the ^{210}Pb case, means a ^{212}Pb-contamination can be built up, which is expected to be deposited in the same way. If the residual background observed is caused by the ^{210}Pb-contamination it is to be expected that the artificial ^{212}Pb-contamination creates additional background which shares all the key characteristics observed so far, but decays with the half live of ^{212}Pb, see figure 5.10.

5.2 Exclusion of known background processes

In the following the arguments excluding the previously known and studied background processes will be briefly recounted.

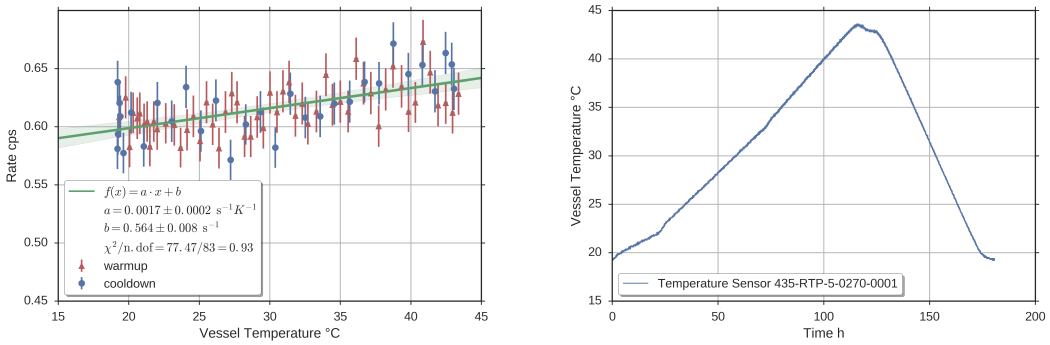

Figure 5.9: Left: A small dependence of the background rate on the temperature of the Main Spectrometer vessel can be established. Each data point represents the mean rate of a 1000 second run with the same settings while the temperature was changed very slowly. **Right**: Thermal cycle imposed on the main spectrometer over the course of several days. The safety of the 200 μm thick wires of the inner electrode prohibits a steeper temperature gradient.

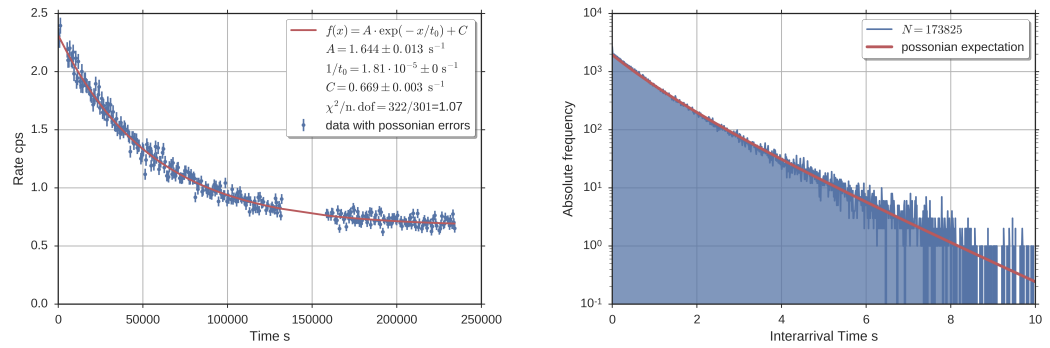

Figure 5.10: Left: Rate of the main spectrometer background after the artificial radon contamination calculated in 500 second time bins. The exponential fit was carried out with time constant fixed to the value corresponding the ^{212}Pb half life time. In between data is omitted due to a failure of the high voltage. **Right**: Inter arrival time distribution of the events in the contamination measurement. Due to the time dependence of the rate deviations from a purely exponential distribution are visible. The decaying rate is all it takes to account for the non-Poissonian behavior. In red the expected time distribution is plotted which subsumes an exponential distribution for every time bin shown on the left.

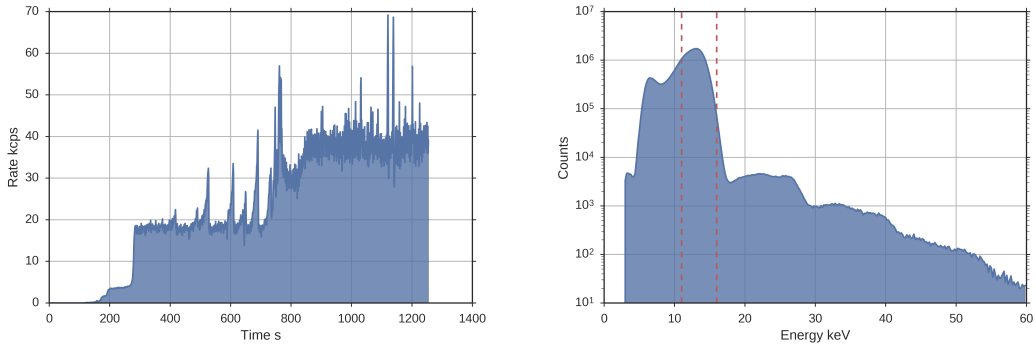

Figure 5.11: Left: development of a Penning discharge. **Right**: Associated energy spectrum. The dashed lines indicate the region of interest studied for the rate graph.

Penning Discharges

Penning traps are widely known as useful precision instruments. Within the context of MAC-E-Filter background characteristics however any field configuration that features a dip in electrostatic potential along a magnetic field line corresponds to a Penning trap, which is of concern. Resulting discharges that can occur when such conditions are present are a long-known possible source of background in MAC-E-Filters [126, 196]. During the design and construction of the KATRIN main spectrometer high precautions were taken to avoid Penning traps [131, 197, 198]. From the Penning-trap background behaviour observed in the early test measurements at the KATRIN prespectrometer it can easily be stated that this mechanism does not fit the observations at the KATRIN main spectrometer. The observed rate of the order of 0.5-0.7 cps - depending on operational parameters - is much lower than the kcps observed during a typical Penning trap discharge. Also, the rate produced by Penning traps depends strongly on the pressure. In [170] (section 6.2.5) only a weak dependence on this parameter was found. Also the smooth dependence on the vessel potential is contrary to typical discharge behavior: discharges typically ignite above a certain threshold voltage. This value may also depend on the magnetic field strength of the trap. As no such behavior is observed, Penning traps can safely be excluded. However, it is still possible to deliberately create them by switching the polarity of the Anti-Penning-Electrode. This electrode, sitting at the entrance and exit of the spectrometer, was specifically designed to avoid Penning discharges in these regions of strong electric and magnetic fields. This was done and genuine discharge behavior with exceedingly high rates and strongly fluctuating backgrounds could be observed as displayed in figure 5.11.

5.2.1 Stored Particles and nuclear decays

In [170] it was shown conclusively that the remaining background rate (i.e. during operation of the LN2 baffles) is not dominated by stored particles. While the work focused on the Radon background this result extends to possible stored electrons originating from

^{210}Pb β-decay or conversion processes following from it. In further works countermeasures against stored particles were established [104, 126].They were successfully tested, but interestingly, they did not affect the remaining background [124, 125].

This appears to be a contradictory situation: On one hand it was shown that the observed background characteristics can be produced by contamination of the spectrometer. On the other hand the non-observation of clustered events by [170] forbids the only know efficient process of fast dissipation of the decay energy into low energy electrons until now.

5.2.2 Muons and γ-radiation

After stored particles in the volume were excluded as dominant contribution for the remaining background the focus shifted towards the study of processes on the surfaces of the main spectrometer. The main idea was that secondary electrons from the wall drift into the flux tube and finally reach the detector. Two possible culprits for secondary electron production were intensively studied: muons and environmental gamma radiation.

Background production by muons was intensively studied in [199] and [200]. In [170] their correlation with the spectrometer background in standard configurations was studied and thereby muons could be dismissed as primary background source.

A detailed study of gamma rays as background source is under way by other authors in the collaboration in parallel [201] but we will briefly report the main finding also here as it is an essential piece to the background puzzle: Within the SDS-II Measurement campaign a 53.3 MBq ^{60}Co Source was brought to the KATRIN main spectrometer hall and used to actively produce secondary electrons in the spectrometer. Despite placing the strong source close to the spectrometer walls no change in background rate was observed in the standard measurement configuration. However, when guiding the electrons from the walls to the detector vie the so called asymmetric field setup the additional rate created by the source was easily observed. This implies that the non-observation of a rate increase within the standard configuration not only strongly disfavors gamma radiation as source of the remaining background. Moreover it also strongly disfavors any low energy secondary electrons from the wall, created by whichever process. This is consistent with the observation of a constant radial background profile for differing analyzing magnetic fields, as stated earlier in section 5.1.1. If low energy electrons from the vessel wall and electrodes were to constitute the observed background the density would be expected to decrease, also in the center, with higher magnetic fields due to a larger shielding effect.

5.2.3 UV Discharge on insulator surfaces

Over the course of excluding possible background scenarios a new mechanism was considered: That of a partial discharge occurring at the ceramic insulators at the exit and entrance of the main spectrometer. Ultraviolet flashovers and glow discharges are known

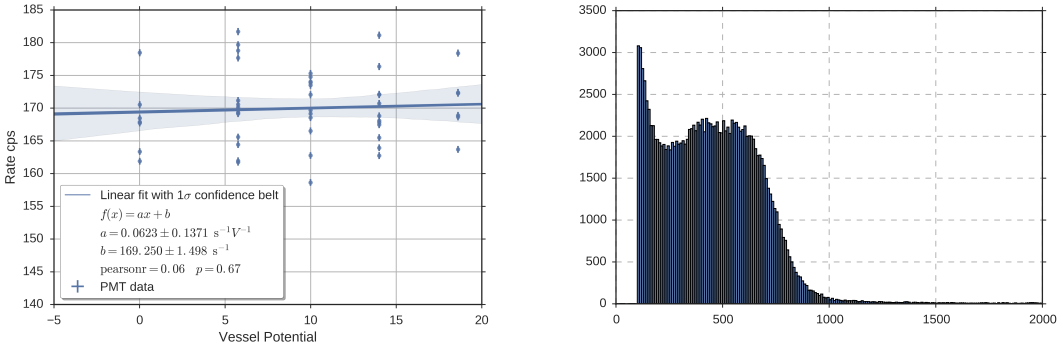

Figure 5.12: Left: No significant dependence of the single photo electron photomultiplier rate can be observed as a function of the vessel potential. Linear regression yields a slope compatible with zero and a correlation of only 6% which has a 67% chance of being spurious. **Right**: ADC Spectrum of the photomultiplier featuring a 1-photo-electron-peak separable from the noise edge. In red the cut used to select the events contributing to the rates in the plot on the left is indicated.

to occur long before a high voltage break down. To investigate this possibility a UV sensitive photomultiplier tube was attached to the entrance port of the main spectrometer, however no support for this hypothesis was found (see fig. 5.12)

5.3 Rydberg state electron transport background model

Since none of the known processes can account for the properties of the residual background observed in the KATRIN Main Spectrometer a new mechanism is needed. From the measurements we extract the main requirements on the mechanism:

1. It needs to provide electrons with extremely low kinetic energies extending to below 1 eV within the flux tube of the spectrometer.

2. Thereby no or very few high energy electrons may be created in order to avoid a strong stored-particle-signature.

3. The spatial distribution of the creation of background electrons in the volume of the flux tube has to be approximately homogeneous.

4. It needs to originate and be caused by the α-chain radioactivity on the vessel surfaces.

5. The messenger-particles between the radioactive decay on the surface and the low-energy electron in the flux tube volume cannot be a charged particle like an electron, as they are properly shielded by the magnetic field.

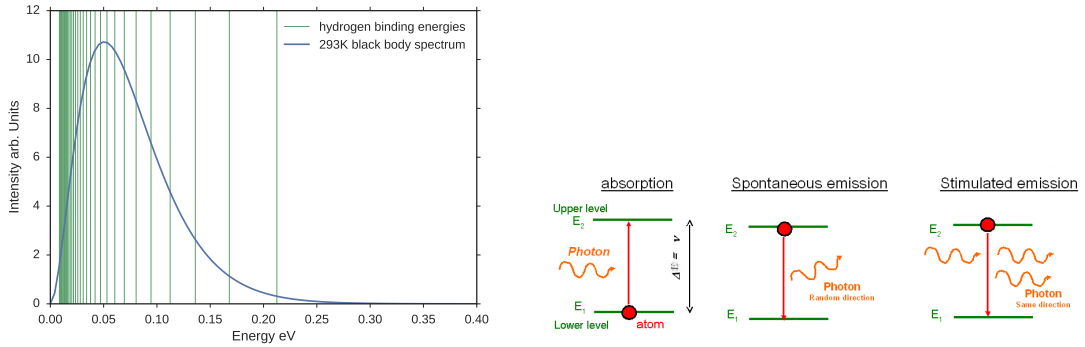

Figure 5.13: Left:Comparison of a room temperature BBR spectrum with the binding energies of hydrogen for the states $n = 8 - 40$. For highly excited states the energy available in thermal photons lies well above their binding energies and can possibly ionize them, thereby creating free electrons with exceedingly low kinetic energies below $\approx 0.3\,\mathrm{eV}$. **Right**: Scheme of atomic interactions with radiation involving two states.

With these constraints in mind it is tentative to look for neutral atomic states that can be ionized or auto-ionized within the flux tube. Given the typical ionization energies of several electron volt for ground-state atoms and the absence of intense light sources in the spectrometer from optical wavelengths up to the ultraviolet, these atomic messengers would need to be in highly excited state. As can be seen from fig. 5.13, room temperature black body radiation (BBR) is in principle sufficiently energetic to ionize highly excited states in hydrogen (or atoms with a hydrogen-like core) from level with $n = 8$. The rates of this process will be discussed in sect. 5.3.5. This is however not the only interaction with radiation such an excited atom can undergo. The processes of spontaneous and stimulated emission as well as absorption displayed in Figure 5.13 will inevitably play a role and their competing rates will be discussed in sect. 5.3.3 and 5.3.4 respectively. Naturally the question emerges how such excited states could be created by radioactive decays, this is discussed in detail in sect. 5.3.1 and 5.3.2. As can be simulated with SRIM [202], recoil nuclei from α-activity within the steel of the main spectrometer can cause bulk atoms to sputter from the vessel surface. From the literature [203] it is known that slow sputtered atoms are in fact efficiently neutralized and often excited, this process is discussed in sect. 5.3.2. Finally, field ionization of the excited states is considered in sect. 5.3.6 since this process – together with enhanced electric fields close to the steel surface – will be responsible for the inner electrode dependence of the background in the proposed model.

5.3.1 Surface sputtering of α-decay recoil nuclei

From [170] it is known that the KATRIN main spectrometer suffers from a ^{210}Pb contamination and in the dedicated radon-contamination measurement in sect. 5.1.6, this surface activity was established as source of the observed residual background. Addition-

Recoil Nucleus	Q Value (MeV)	Recoil Energy (keV)
^{218}Po	5.590	101
^{214}Pb	6.115	110
^{210}Pb	7.833	146
^{206}Pb	5.407	103

Table 5.1: Relevant recoil nuclei in the ^{222}Rn Decay Chain shown in figure 5.14. Decays upward of ^{222}Rn $\rightarrow^{218}$ Po need not be considered for contamination by ambient air. The other decays downward have similar energies but only branching probabilities of less than a percent and are neglected. The Q Values are available at NuDat. The recoil energy can be calculated classically and nonrelativistic using momentum conservation: $E_r = \frac{E_Q}{m_r/m_\alpha+1}$.

ally, measurements of secondary electrons from the main spectrometer vessel wall show that recoil nuclei from alpha decays are explanted and reimplanted [204]. In [170] only the Beta-emission of ^{210}Pb was studied as source of background and in [204] only the secondary electron creation associated with the recoil nucleus was studied. Within this section the atom sputtering effects of the radioactive decays within the surface layers are studied using the SRIM simluation package[202]. **S**topping **R**ange of **I**ons in **M**atter is a widely-used Monte Carlo software package that is renowned for its use in studying ion implantation, but also allows to calculate sputter yields. It employs a binary collision approach. The aim is to calculate the sputter yield and velocity distribution of the atoms sputtered from alpha decays. As will be seen, the main cause of sputtering is associated with the heavy recoil nuclei, whereas the alpha particles predominantly lose energy in the material by ionization. The results of this calculation will enter as input into the background model, affecting the background rates and characteristics. To calculate the sputter yield of an alpha decay of a ^{210}**Po** atom implanted into the steel of the KATRIN main spectrometer, via the up-chain alpha decay of ^{214}**Po** using SRIM several input data are needed:

- the energies of the recoil nuclei,
- a model of the steel surface,
- the implantation profile of ^{210}**Pb** nuclei within this surface.

The energies of the relevant recoil nuclei are listed in table 5.1. For the study here, only the 110 keV ^{214}**Pb** nucleus is relevant. The first step of the calculation is to simulate the implantation of ^{214}**Pb** nuclei into the surface, from this the implantation profile is determined. While this was already carried out in [170] a different surface model was used. In [170] a raw stainless steel surface with a composition predefined in SRIM was used. As we are interested in sputtering we take care to match the actual composition of stainless steel in the main spectrometer. Either a mono layer of water or hydrogen is assumed as surface deposition to model the conditions of an unbaked or baked spectrometer respectively. Additionally a chromium oxide passivation layer is included. The composition information has been taken from the UNISOR data sheet for their

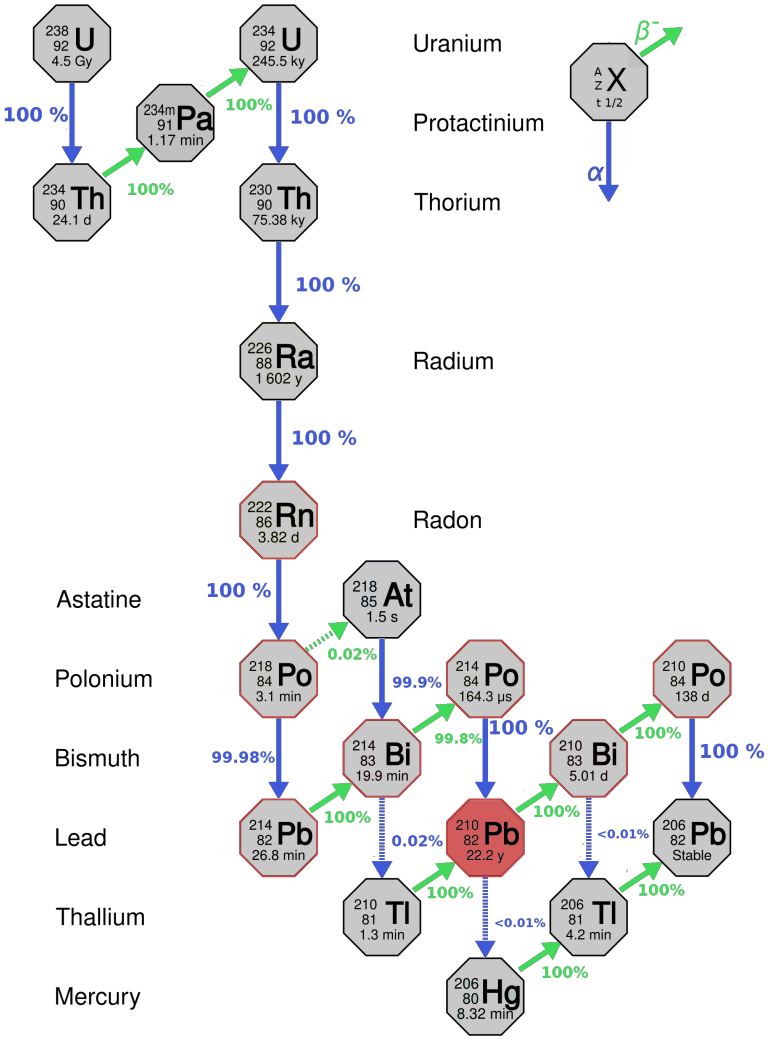

Figure 5.14: Decay chain of ^{238}**U** which produces the naturally occuring ^{222}**Rn** present in ambient air. Marked in red is the dominant decay chain. Side chains have probabilites far below a percent. As ^{210}**Pb** has a rather long half life time of 22 years it could accumulate in the spectrometer walls. Based on fig. 5.7 in [170] and [205]

Layer Number	Layer Name	Width (Å)	Density (g/cm3)	H	Cr	O	Fe	Cr %	Fe	Ni	Mo
1	Water	3	1	66.6	0	33.3	0	0	0	0	0
1	Hydrogen	1	1.25	100	0	0	0	0	0	0	0
2	**CrO_2Fe**	30	3.80	0	30	60	10	0	0	0	0
3	Stainless Steel	967	7.94	0	0	0	0	15.9	69.5	12.2	2.34

Table 5.2: Surface Model

W1.4492 stainless steel. The steel was treated according to DIN 17440/09.96. While no measurement on the surface condition and passivation layer of the main spectrometer is available we refer to [206], where chromium oxide (**CrO_2Fe**) layers of 3-5 nm depth were found to be common for stainless steel. In table 5.2 the composition and width of the surface layers that were used are given. Of course, the true surface conditions inside the main spectrometer may differ somewhat from this rather schematic model in terms of surface deposition as well as geometry. However an in-situ measurement of the properties of the large main spectrometer inner surface is not feasible. Thus only generic simulation results can be expected from these generic input data. We will see that these generic results suffice to explain the various measurements. In fig. 5.15 the result of simulating 10000 146 keV ^{210}**Pb** nuclei impinging isotropically on the vessel surface is shown. About 88% are implanted in a mean depth of 12 nm, similar to the results found by Harms. The remaining 12% are scattered back. Unfortunately, implantation is an efficient process to deposit activity within the main spectrometer. For the calculation of the sputter

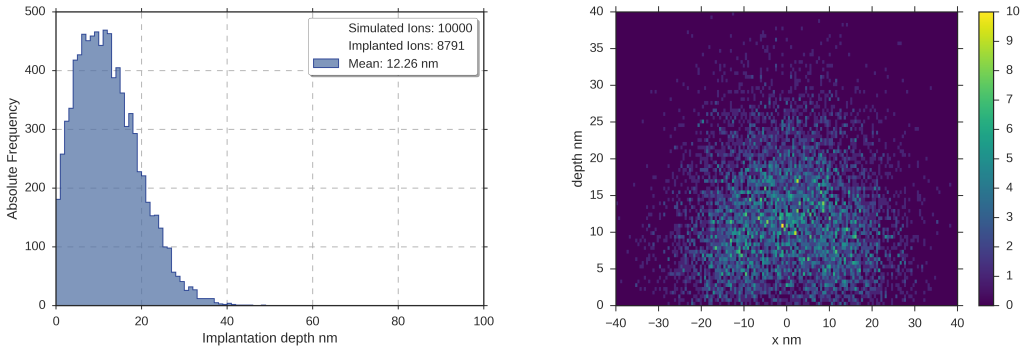

Figure 5.15: Implantation depth profile of ^{210}Pb nuclei with 146 keV kinetic energy into stainless steel as simulated with SRIM. **Left**: Essentially the same profile and mean implantation depth of 12 nm as found in [170]. **Right**: 2-d histogram for a more visual impression of the implantation profile. The color indicates the total number of implanted nuclei in a bin with a bin width of 0.5 nm. The nuclei are set up by SRIM to hit the material at the point of origin.

yield the emerging 103 keV ^{206}Pb nuclei from the α-decay chain are started from the final implantation positions, again assuming an isotropic momentum distribution. It is also important to not only include the sputter yield of the explantation process, but

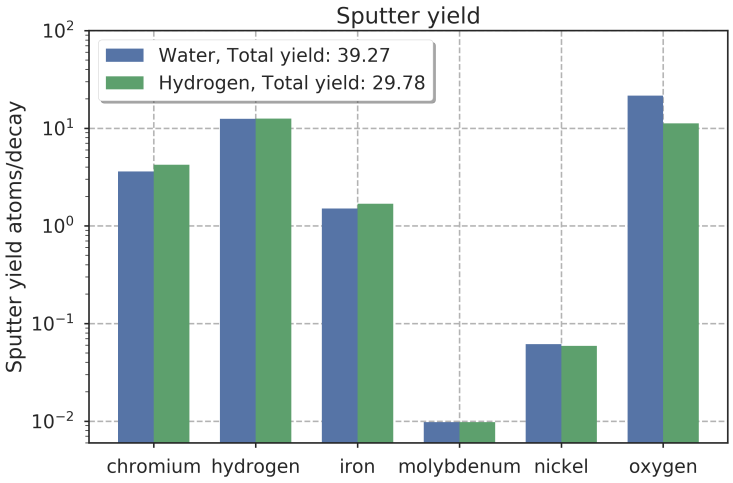

Figure 5.16: Sputter yields per atom species durign explantation and reimplantation of 103 keV ^{206}**Pb** nuclei born in the bulk material by alpha decay. The surface is covered by a mono layer of water and hydrogen, respectively. The comparison shows that removing the water by outbaking the spectrometer significantly reduces the sputter yield.

also to calculate the yield due to reimplantation after the ^{206}Pb nucleus crossed the evacuated main spectrometer. This is achieved by using SRIMs output as starting input and repeating the simulation. The resulting sputter yields are shown in figure 5.16. The most abundant species are hydrogen and oxygen. With a surface layer of water the total sputter yield is about 25% higher compared to the yield with a surface layer of hydrogen. The increase stems mainly from the oxygen atoms in the water because they are more often scattered due to higher cross sections compared to hydrogen. This implies that if sputtered atoms are indeed the source of background, removing the water content of the system should significantly reduce the background. Apart from providing a sputter yield SRIM also outputs the kinetic energies of the sputtered atoms. These are shown per sputtered species in figure 5.17. While the median energy of all sputtered atoms is 12 eV, the spectrum is very hard with a percent of the atoms having kinetic energies above 10 keV up to the primary energy. The sputter yields of the nuclei, on the other hand, are rather high with 30-40 sputtered atoms per decay on average. The corresponding multiplicity spectra are hard, with up to 200 atoms for a single α-decay. The atomic composition, energy distribution and multiplicities obtained here will be directly used in the background simulation detailed later. The simulation was also carried out for the 5 MeV alpha particles produced in the initial decay, there the total sputter yield is 5.2×10^{-3} atoms per decay, which is negligible compared to the large yields of recoil nuclei.

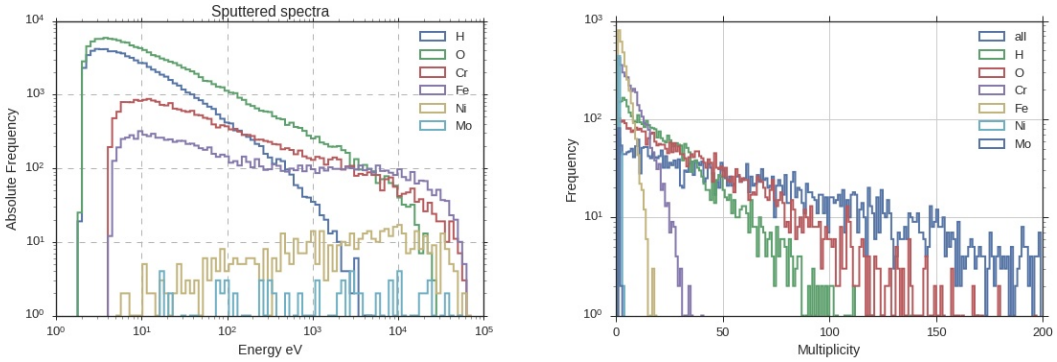

Figure 5.17: Left: Energy spectra of the various atom species sputtered off the stainless steel surface by the recoiling 103 keV ^{206}**Pb** daughter nucleus following the α-decay of ^{210}**Po**. For this investigation recoil nuclei starting isotropically from their point of implantation were simulated with SRIM. The spectra are rather hard ranging from a few eV up to a $\approx 1\%$ contribution close to the primary energy. The median energy over all species is ≈ 12 eV. **Right**: Multiplicity spectra per species for sputtering events following the ^{210}**Po** decay. High multiplicities are common, and can imprint a time structure on the resulting background.

5.3.2 Excitation of sputtered atoms

Alpha decays of implanted ^{210}**Pb** thus cause neutral atoms to sputter off the surface. In the following we are interested in the electronic state of these atoms. High velocity neutral atoms (in the ground state) can in principle scatter off residual gas and thereby cause ionization to release electrons. However, as there is a very good vacuum of $\propto 10^{-10}$ mbar this process is very unlikely. Far more important are highly excited states, where ionization can be caused by room-temperature thermal radiation, as discussed later in section 5.3.5. In fact, it is known that a large fraction of sputtered atoms emerges from the solid in excited states [207–209]. We will discuss processes that affect these excitations in the following. To model the background it is crucial to get an understanding of the distribution of excited states, as we will see in the following subsections. We thus focus on sputtered atoms which contain a sizeable fraction which exhibit complicated electronic configurations. Beyond the surface conditions, also the electronic band structure inside the solid plays a role. As a result, a complete and accurate treatment is not feasible for the purpose of this work. Instead we will rely on universal properties of highly excited Rydberg atoms in simulating the background.

While SRIM allowed us to simulate the collision cascade of the recoil nuclei, it does not keep track of the electronic shell configuration in these atoms. Naturally one would expect that a lot of the sputtered atoms to be ionized and excited by the same collisions that sputter them off the solid. However, aside from inelastic scattering there are also charge exchange reactions with the bulk material, once an atom or ion is closely above the surface. These are schematically shown in figure 5.18 and effectively neutralize sputtered atoms. The mechanism is called resonant neutralization and relies on resonant tunneling of electrons between the solid and the ion.

The cross sections for exciting an atom into a Rydberg state n in general scale as n^{-3}. This can be understood by recounting that the value of $|\psi_{n00}(0)|^2$ - the probability to find the electron of a hydrogen atom at the origin - scales this way. If an electron is now excited from the ground state into a high n state, the atom jumps from the size of about 1 angström to having the electron in a large orbit. As the orbital radius scales as n^2, for Rydberg states from $n = 10$ the radius is over a hundred times larger than in the ground state. Approximately, if the electron jumps from a position very close to the nucleus to a large radius, it is expected that the probability of this process scales as the overlap between these two states: the probability to find the electron at the site of the nucleus when it is in the highly excited state n. This line of argument was given by Gallagher [210]. Two facts about this argument are important to notice. First, it works regardless of the excitation mechanism, be it scatterings by electrons, charge exchange reactions or photons that provide the energy for the electron. Second, and most importantly, it applies to all *neutral* Rydberg atoms, regardless of their atomic number. Any neutral Rydberg atom can, to a good degree, be thought of as being a heavier hydrogen atom. The reason for this is obvious: a neutral Rydberg atom has a single electron in a highly excited state far away from the ionic core, so it is mostly insensitive to the details of the other electrons in the lower states. It only sees a nucleus with atomic number $Z = 1$ with a different mass. This approximation allows us to understand all Rydberg states and spectra in terms of the well known and simple hydrogen wave functions. For the purpose of this study we will fully rely on this approach as it makes feasible a unified treatment of all the sputtered atoms: Only a different atomic mass needs to be accounted for. This is also relevant for the following sections that discuss the interactions of Rydberg atoms with radiation: No complicated spectra need to be accounted for and the rates for various transitions are essentially identical for all species.

5.3.3 Spontaneous Decay

Excited states of a hydrogen (or hydrogen-like) atom have a finite lifetime as they decay into the ground state by emission of photons. The rates of these decays can be calculated analytically and are fundamental as they govern also the rates of stimulated emission and excitation by a radiation field, as first shown by Einstein and Ehrenfest [211]. In order to calculate how many background events can be produced per Rydberg atom starting on the vessel surface, we need to account for all channels through which a Rydberg state can be depopulated. Due to the vacuum of 10^{-10} mbar inside the KATRIN main spectrometer collisions with other atoms are very unlikely. Radiative transitions however can happen, and even be stimulated by the thermal photon bath radiated from the room-temperature surroundings. Due to the exceedingly small binding energy of Rydberg states with high principal quantum number n of $E_n = \frac{1}{n^2} \cdot 13.6$ eV, even ionization is possible as we will see. Based on the expressions for the rates of spontaneous decay derived here, we later on describe the other processes using the Einstein-relations. The following derivation follows [212] and references therein, however we will recapitulate it

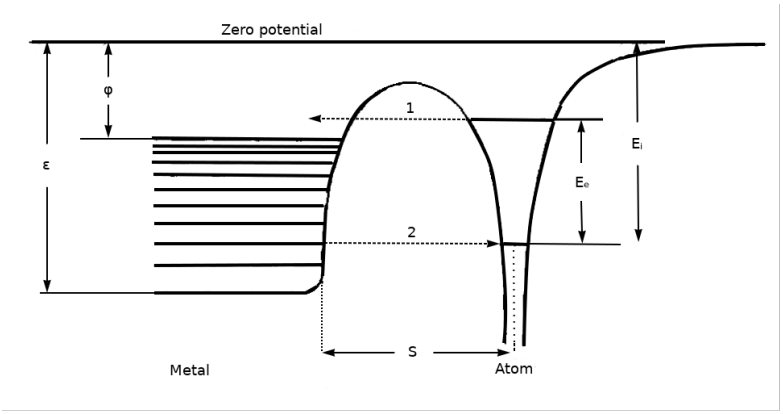

Figure 5.18: Scheme of charge exchange processes near metal surfaces. ϕ is the work function, ϵ is the energy of the bottom of the conduction band and S the distance. E_i and E_e are the ionisation energy and the excitation energy of the atom. Process 1 is resonance ionisation, where an electron tunnels from a bound state in the atom to the solid. The reverse process (2) is resonant neutralization. Notice that highly excited Rydberg states are found only far above the Fermi level. Neutralization processes therefore have to fill lower states. Figure adapted from [203]

for the sake of completeness. Following the literature we use atomic units:

$$e = m_e = \hbar = 1, \quad h = 2\pi, \quad 4\pi\varepsilon_0 = 1 \tag{5.2}$$

$$\alpha \approx 1/137, \quad c = 1/\alpha \approx 137. \tag{5.3}$$

In these definitions, the Hartree E_h is the unit of energy and the Bohr radius a_0 the unit of length:

$$E_h = \alpha^2 m_e c^2 \approxeq 27.2 \text{ eV}, \tag{5.4}$$

$$a_0 = \hbar/(m_e c\alpha) \approxeq 0.053 \text{ nm}. \tag{5.5}$$

Assuming a 1-electron atom to be in a state n, the fundamental probability per unit time to make a transition into the state n' and emitting a photon of frequency $\omega_{nn'} = (E_n - E_{n'})$ with polarization direction x and wave vector $\mathbf{k}$ is given by:

$$P_{n,n'}(\mathbf{k}, x)d\Omega = \frac{\alpha^3}{2\pi}\,\omega_{nn'}\,|D^{\mathbf{k}x}_{nn'}|^2 d\Omega \tag{5.6}$$

$$\tag{5.7}$$

where the matrix element $D^{\mathbf{k}x}_{nn'}$ is

$$D^{\mathbf{k}x}_{nn'} = \int \psi^*_{n'}(x,\tau)e^{i\mathbf{k}\cdot\mathbf{r}}\frac{\partial\psi_n(x,\tau)}{\partial x}d\tau. \tag{5.8}$$

$$\tag{5.9}$$

Within the dipole approximation it is assumed that

$$e^{i\mathbf{k}_\gamma \mathbf{r}} \approx 1, \quad k_\gamma = \frac{2\pi}{\lambda}, \quad \lambda >> 2\pi r \tag{5.10}$$

so the matrix element reduces to the x component of the vector $\mathbf{D_{nn'}}$

$$\mathbf{D_{nn'}} = \int \psi^*_{n'} \nabla \psi_n d\tau \tag{5.11}$$

$$\tag{5.12}$$

which is simply the matrix element of the momentum operator $\mathbf{p} = -i\hbar\nabla$.
Using the commutator relation $[\mathbf{r}, \mathbf{H}] = i\mathbf{p}$ for the central potential and $[\mathbf{r}, \mathbf{H}]_{nn'} = (E_n - E_{n'})\mathbf{r_{nn'}}$ it follows that $\mathbf{p_{nn'}} = -i\omega_{nn'}\mathbf{r_{nn'}}$ and therefore

$$\mathbf{D_{nn'}} = \omega_{nn'} \int \psi^*_{n'} \mathbf{r} \psi_n d\tau \tag{5.13}$$

Substituting this back into eq. 5.6 we arrive at

$$P_{nn'}(\Omega, \mathbf{x}) d\Omega = \frac{\alpha^3}{2\pi} \omega^3_{nn'} (\mathbf{e_x} \cdot \mathbf{r_{nn'}})^2 d\Omega \tag{5.14}$$

where

$$\mathbf{r_{nn'}} = \int \psi^*_{n'} \mathbf{r} \psi_n d\tau. \tag{5.15}$$

To calculate actual rates from this general result the wave functions ψ_{nlm} for the hydrogen atom are needed. The static Schrödinger equation for the $\frac{1}{r}$ potential

$$\frac{1}{2} \triangle \psi + \left(E + \frac{1}{r} \right) \psi = 0 \tag{5.16}$$

can be solved by separation of variables in spherical coordinates with a wave function

$$\psi_{nlm}(r, \theta, \phi) = \frac{1}{\sqrt{2\pi}} R_{nl}(r) Y_{lm}(\theta) e^{im\phi} \tag{5.17}$$

where the $Y_{lm}(\theta)$ are the Legendre functions and

$$R_{nl}(r) = \sqrt{\frac{4(n-l-1)!}{n^4(n+l)!}} e^{-\rho/2} \rho^l L^{2l+1}_{n-l-1}(\rho) \tag{5.18}$$

$$\rho = 2r/n \tag{5.19}$$

are the normalized radial wave functions, with the Laguerre polynomials recursively defined by

$$L^m_0(x) = 1 \tag{5.20}$$

$$L^m_1(x) = 1 + m - x \tag{5.21}$$

$$L^m_n(x) = \frac{2n - 1 + m - x}{n} L^m_{n-1}(x) - \frac{n - 1 + m}{n} L^m_{n-2}(x). \tag{5.22}$$

Using these wave functions the integral $\mathbf{r_{nn'}}$ in equation 5.15 is solved componentwise with $z = r\cos\theta$ using the linear combinations

$$x + iy = r\sin\theta e^{i\phi} \quad \text{and} \quad x - iy = r\sin\theta e^{-i\phi}. \tag{5.23}$$

The integral for the z-component then reads

$$z_{n\,l\,m}^{n'\,l'\,m'} = \int \psi_{n'l'm'}\, r\cos\theta\, \psi_{nlm} d\tau = \int_0^\infty r^2 dr R_{n'l'}(r) R_{nl}(r) \cdot r \times \tag{5.24}$$
$$\times \int_0^\pi Y_{l'm'}(\theta) Y_{lm}(\theta) \cos\theta \sin\theta d\theta \times \int_0^{2\pi} \frac{1}{2\pi} e^{i(m-m')\phi} d\phi.$$

The integral over ϕ yields a delta function

$$\int_0^{2\pi} \frac{1}{2\pi} e^{i(m-m')\phi} d\phi = \delta_{mm'} \tag{5.25}$$

and leads to the selection rule $\Delta m = 0$ for photons polarized in z-direction. Making use of the relation

$$Y_{lm}\cos\theta = \sqrt{\frac{(l+1)^2 - m^2}{(2l+3)(2l+1)}} Y_{l+1,m} + \sqrt{\frac{l^2 - m^2}{(2l+1)(2l-1)}} Y_{l-1,m} \tag{5.26}$$

and the orthogonality relation for the Legendre functions

$$\int Y_{l'm} Y_{lm} \sin\theta d\theta = \delta_{ll'} \tag{5.27}$$

we obtain accordingly the selection rule $\Delta l = \pm 1$. The integral reduces to

$$z_{n\,l\,m}^{n'\,l'\,m'} = R_{nl}^{n'l'} \times \begin{cases} \sqrt{\frac{(l+1)^2-m^2}{(2l+3)(2l+1)}}, & l' = l+1 \\ \sqrt{\frac{l^2-m^2}{(2l+1)(2l-1)}}, & l' = l-1 \\ 0, & \Delta l \neq 1 \end{cases} \tag{5.28}$$

where

$$R_{nl}^{n'l'} = \int R_{n'l'}(r) R_{nl}(r) r^3 dr. \tag{5.29}$$

The integral for $x \pm iy = r\sin\theta e^{\pm i\phi}$ is then

$$(x \pm iy)_{n\,l\,m}^{n'\,l'\,m'} = R_{nl}^{n'l'} \int_0^\pi Y_{l'm'}(\theta) Y_{lm}(\theta) \sin^2\theta d\theta \int_0^{2\pi} \frac{1}{2\pi} e^{i(m\pm1-m')\phi} d\phi \tag{5.30}$$

yielding

$$(x+iy)^{n'\,l'\,m'}_{n\,l\,m} = R^{n'l'}_{nl} \times \begin{cases} \sqrt{\frac{(l+m+2)(l+m-1)}{(2l+3)(2l+1)}}, & l' = l+1 \wedge m' = m+1 \\ -\sqrt{\frac{(l-m)(l-m-1)}{(2l+1)(2l-1)}}, & l' = l-1 \wedge m' = m+1 \\ 0, & \text{else} \end{cases} \tag{5.31}$$

and

$$(x-iy)^{n'\,l'\,m'}_{n\,l\,m} = R^{n'l'}_{nl} \times \begin{cases} -\sqrt{\frac{(l-m+2)(l-m+1)}{(2l+3)(2l+1)}}, & l' = l+1 \wedge m' = m-1 \\ \sqrt{\frac{(l+m)(l+m-1)}{(2l+1)(2l-1)}}, & l' = l-1 \wedge m' = m-1 \\ 0, & \text{else.} \end{cases} \tag{5.32}$$

Summing these components up gives an m-independent result

$$\begin{aligned} \sum_{m'} |\mathbf{r}^{\mathbf{n'\,l+1\,m'}}_{\mathbf{n\,l\,m}}|^2 &= |z^{n'l+1m}_{nlm}|^2 + |x^{n'l+1m+1}_{nlm}|^2 + |x^{n'l+1m-1}_{nlm}|^2 + \\ &\quad + |y^{n'l+1m+1}_{nlm}|^2 + |y^{n'l+1m-1}_{nlm}|^2 \\ &= \frac{(R^{n'l+1}_{nl})^2}{(2l+3)(2l+1)} \cdot \Big[(l+1)^2 - m^2 + \frac{1}{2}(l+m+2)(l+m+1) \\ &\quad + \frac{1}{2}(l-m+2)(l-m+1) \Big] \\ &= \frac{l+1}{2l+1} \cdot (R^{n'l-1}_{nl})^2 \end{aligned} \tag{5.33}$$

and

$$|\mathbf{r}^{\mathbf{n',l-1,m'}}_{\mathbf{nlm}}|^2 = \frac{l}{2l+1} \cdot (R^{n',l-1}_{nl})^2 \tag{5.34}$$

respectively. Both can be subsumed as

$$\begin{aligned} |\mathbf{r}^{\mathbf{n'l\pm1m'}}_{\mathbf{nlm}}|^2 &= \frac{l_{\max}}{2l+1} \cdot (R^{n'l-1}_{nl})^2 \\ l_{\max} &= \max(l, l') \end{aligned} \tag{5.35}$$

The transition rate is then:

$$P^{\text{sp}}_{nl\to n',l\pm1} = \frac{4\alpha^3 \omega^3_{nn'} l_{\max}}{3(2l+1)} |\mathcal{R}_{nl\to n',l\pm1}|^2. \tag{5.36}$$

What remains to be solved is the radial integral $R_{nl}^{n'l-1}$. The result of this, derived by Gordon [213], is

$$\begin{aligned} R_{nl}^{n'l-1} &= \int_0^\infty R_{nl} R_{n'l-1} r^3 dr \qquad (5.37) \\ &= \frac{(-1)^{n'-l}}{4(2l-1)!}\sqrt{\frac{(n+l)!(n'+l-1)!}{(n-l-1)!(n'-l)!}} \times \frac{(4nn')^{l+1}(n-n')^{n+n'-2l-2}}{(n+n')^{n+n'}} \\ &\times \left[F\left(-n_r, -n_r', 2l, -\tfrac{4nn'}{(n-n')^2}\right) - \left(\tfrac{n-n'}{n+n'}\right)^2 F\left(-n_r-2, -n_r', 2l, -\tfrac{4nn'}{(n-n')^2}\right)\right] \end{aligned}$$

where

$$F(a,b,c;x) = \sum_{k=0}^{\infty} \frac{(a)_k (b)_k}{(c)_k k!} x^k \qquad (5.38)$$

is the hypergeometric function, $n_r = n - l - 1$ and $n_r' = n' - l$ the radial quantum numbers and $(a)_k$ the Pochhammer symbol defined by:

$$(a)_0 = 1 \qquad (5.39)$$

$$k > 0: \quad (a)_k = \prod_{i=0}^{k-1} (a+i) \qquad (5.40)$$

By now all results necessary to calculate the decay rates for a state $|n,l\rangle$ are at hand. However, as can be spotted in eq. 5.37 many factors of order $n!$ appear in the formula. Since we are interested in states of possibly very high $n \approx 100$ it is important for the implementation to consider the numerical stability of this expression. A method to calculate the hypergeometric functions in a way suitable for up to $n = 1000$ was presented in [214] in (2004), which is made use of here. It is essential to avoid computing the series 5.38 directly and instead rely on the recurrance relation

$$(a-c)F(a-1) = a(1-x)\left[F(a) - F(a+1)\right] + (a+bx-c)F(a) \qquad (5.41)$$

where

$$F(a) = F(a,b,c;x) \qquad (5.42)$$

with

$$F(0) = 1, \quad F(-1) = 1 - \frac{b}{c}x \qquad (5.43)$$

as starting values for the recursion. In this way large cancelling factorials are avoided, so no problems with numerical stability occur. From the definition of the hypergeometric function 5.38 it is clear that it is symmetrical with respect to a and b: $F(a,b,c,x) = F(b,a,c,x)$. Therefore 5.41 can also be used for b. As $a = -n_r$ (or $-n_r - 2$) and $b = -n_r'$ are negative integers these relations suffice completely to calculate the hypergeometric function for all values required from 5.37 for all possible transitions. Since there are only simple arithmetic operations used in 5.41 and less then $2n$ recursions are needed to arrive at the result, this method is also fast compared to numerical integration. The resulting

n	l	Eq. 5.46	Q.M. results [215]	this work	base 10 exponent
50	49	2.861	2.861	2.860	1
50	40	1.915	1.907	1.906	1
50	30	1.086	1.065	1.065	1
50	20	4.904	4.697	4.695	0
50	10	1.284	1.195	1.194	0
50	1	2.335	2.300	2.299	-2
30	29	2.194	2.195	2.194	0
30	20	1.059	1.046	1.045	0
30	10	2.775	2.637	2.636	-1
30	1	5.045	4.975	4.973	-3
10	9	8.408	8.420	8.415	-3
10	5	2.803	2.746	2.744	-3
10	1	1.868	1.864	1.863	-4
3	2	1.513	1.547	1.546	-5
3	1	5.045	5.271	5.268	-6
2	1	1.495	1.596	1.595	-6

Table 5.3: Rates of spontaneous decay for different Rydberg states in milliseconds - to be multiplied by powers of ten with the exponent given in the last column common to all.

rates agree with semiclassical approaches for high n shown in [215] as well as the exact result shown there. In Table 5.3 rates for selected states are shown in comparison with values tabulated in [215]. For high n the values are in good agreement with the simple semiclassical result for the lifetime τ_{nl}^{sp}

$$\tau_{nl}^{\mathrm{sp}} \approx \tau_0 n^3 l(l+1) \tag{5.44}$$

with

$$\tau_0 = 9.3 \cdot 10^{-11}\ \mathrm{s}. \tag{5.45}$$

The lifetime τ relates to the calculated rates as

$$\tau_{nl}^{\mathrm{sp}} = 1/P_{nl}^{\mathrm{sp}} \tag{5.46}$$

with P_{nl}^{sp} being the sum of the rates of all possible spontaneous decays

$$P_{nl}^{\mathrm{sp}} = \sum_{n'=1}^{n-1} \{P_{nl\to n',l-1}^{\mathrm{sp}} + P_{nl\to n',l+1}^{\mathrm{sp}}\} \tag{5.47}$$

5.3.4 Thermal black body radiation stimulated transitions

Apart from spontaneous decay, transitions can also be stimulated by external radiation. In the absence of other sources, the field present within the KATRIN main spectrometer is the thermal BBR emitted by the steel vessel at room temperature.

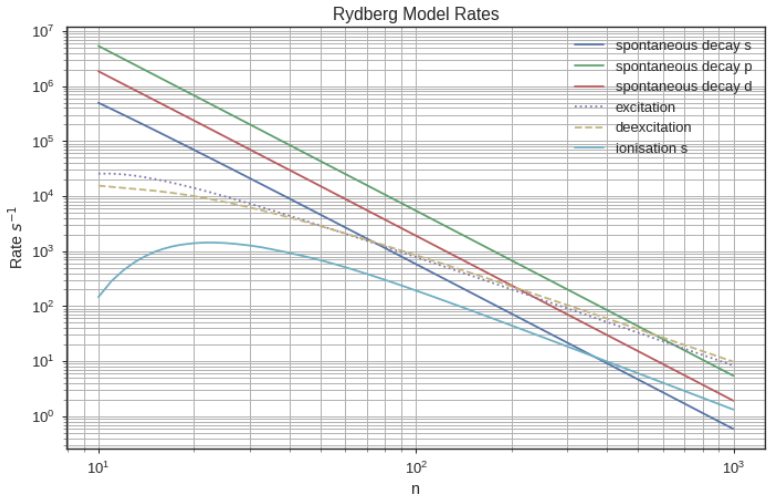

Figure 5.19: Rates for the different processes of the Rydberg atoms as function of the principal quantum number n as calculated by the methods shown in this chapter. "excitation" and "deexcitation" stand for the sum of BBR-stimulated transitions into higher (lower) Rydberg states as described in the next section. The rate of decay into the ground state depends strongly on the angular momentum l and is here shown for the $l = 0, 1, 2$ (s,p,d) states.

The spectral photon density of the thermal radiation is:

$$n_\gamma(\omega) = \frac{\omega^2}{\pi^2 c^3} \frac{1}{\exp[\omega/(kT)] - 1} \tag{5.48}$$

The rates of stimulated emission and absorption are governed by the same bound-bound matrix elements $|\mathcal{R}_{nl\to n',l\pm1}|^2$ which also govern the spontaneous decay together with the spectral photon density n_γ:

$$P^{\mathrm{BBR}}_{nl\to n',l\pm1} = \frac{4}{3}\alpha^3\omega^3_{nn'} \cdot \frac{l_{max}}{2l+1} \cdot \frac{|\mathcal{R}_{nl\to n',l\pm1}|^2}{\exp[\omega_{nn'}/(kT)] - 1} \tag{5.49}$$

However, when we consider states with very high n the electric field of the nucleus at the position of the electron diminishes as these states occupy space further away from the nucleus. The average field E_H that acts upon the electron scales as

$$|\mathbf{E}_H| = \frac{1}{r^2} \sim \frac{1}{n^4} \tag{5.50}$$

whereas the peak electric field strength of the thermal radiation is

$$|\mathbf{E}_{BBR}|^2 = \frac{8\pi^3 (kT)^4 \alpha^3}{15}. \tag{5.51}$$

Comparing these it results that

$$|\mathbf{E}_{BBR}| > |\mathbf{E}_H| \qquad \text{for} \qquad n > 140. \tag{5.52}$$

Therefore the assumption made within the dipole approximation in 5.3.3 is not valid anymore. In these very highly excited states, however, the semiclassical approximation for spontaneous transitions from equation 5.44 is known to work well and is in good agreement with the results from the matrix element $|\mathcal{R}_{nl\to n',l\pm1}|^2$. By the Einstein-Ehrenfest relations this then must also hold true for induced transitions. We therefore may use the result anyway.

5.3.5 Photoionisation by thermal black body radiation

Finally we are interested in the ionization of Rydberg atoms by room-temperature BBR. This is the process that will ionize the highly excited states in the vacuum of the main spectrometer and create free electrons with very small kinetic energy that then travel towards the detector. The process

$$H^* + \gamma \to H^+ + e^- \tag{5.53}$$

however is more complicated than the spontaneous decay and radiation-induced transitions between bound states as it involves the free states ψ_f of the electron which are not contained in the basis that the bound states span and orthogonality is not given anymore. The ionization probability is the integral of the cross section σ_{nl}^{ion} times the photon number density n_γ

$$P_{nl}^{\text{ion}} = c \int_{1/(2n^2)}^{\infty} d\omega\, \sigma_{nl}^{ion}(\omega)\, n_\gamma(\omega) \tag{5.54}$$

starting from the ionization threshold $\frac{1}{2n^2}$ and where

$$\omega = \frac{1}{2n^2} + E_{\text{kin}}. \tag{5.55}$$

The ionization cross section depends now on the bound-free matrix elements as

$$\sigma_{nl}^{ion}(\omega) = \frac{4\pi^2\alpha\omega}{3(2l+1)} \left[l\mathcal{R}^2_{nl\to E,l-1} + (l+1)\mathcal{R}^2_{nl\to E,l+1} \right]. \tag{5.56}$$

with the bound-free matrix element

$$\mathcal{R}_{nl\to E,l\pm1} = \int_0^{\infty} dr \cdot r^3 R_{nl}(r) R_{E,l\pm1}(r). \tag{5.57}$$

The radial free electron eigenfunctions $R_{El}(r)$ are normalized such that

$$\int_0^{\infty} R_{El}(r) R_{E'l}(r) dr = \pi\delta(E - E') \tag{5.58}$$

and are $R_{El} = R_{kl}/k$ with

$$R_{kl}(\rho) = \sqrt{\frac{\pi}{2(1-e^{-2\pi/k})}\prod_{s=0}^{l}(1+s^2k^2)}\frac{(2\rho)^{l+1}}{(2l+1)!}e^{ik\rho}\,{}_1F_1(l+1-i/k;2l+1;-2ik\rho). \tag{5.59}$$

The matrix element was also solved by Gordon [213]

$$\begin{aligned}\mathcal{R}_{nl\to E,l\pm1} &= \sqrt{\frac{(n+l)!}{(n-l-1)!(1-e^{-2\pi/k})}\Pi_{s=0}^{l'}(1+s^2k^2)} \\ &\times \left(\frac{4n}{1+n^2k^2}\right)^{(l_<+1)}\frac{\exp[-\frac{2}{k}\arctan(nk)]}{4n^2(2l\pm1)!}Y_\pm\end{aligned} \tag{5.60}$$

where

$$\begin{aligned}Y_+ &= i\eta\left(\frac{n-i\eta}{n+i\eta}\right)^{n-l}\left[{}_2F_1\left(l+1-n,l-i\eta;2l+2;\frac{-4ni\eta}{(n-i\eta)^2}\right)\right. \\ &- \left.\left(\frac{n+i\eta}{n-i\eta}\right)^2{}_2F_1\left(l+1-n,l+1-i\eta;2l+2;\frac{-4ni\eta}{(n-i\eta)^2}\right)\right]\end{aligned} \tag{5.61}$$

and

$$\begin{aligned}Y_- &= \left(\frac{n-i\eta}{n+i\eta}\right)^{n-l-1}\left[{}_2F_1\left(l+1-n,l-i\eta;2l;\frac{-4ni\eta}{(n-i\eta)^2}\right)\right. \\ &- \left.\left(\frac{n+i\eta}{n-i\eta}\right)^2{}_2F_1\left(l+1-n,l-i\eta;2l;\frac{-4ni\eta}{(n-i\eta)^2}\right)\right]\end{aligned} \tag{5.62}$$

with $\eta = 1/k$ and $k^2 = E$. As with the bound-bound matrix element these expressions are hard to compute due to large factorials and cancellation. Therefore, again, a recurrence relation is used. Burgess [216] gives 2 sets of equations but only the first one is useable in the present context as calculations up to high n are needed. With these we can then calculate $\sigma_{nl}^{ion}(\omega)$ and, together with the BBR spectrum, the photo ionization spectra shown in 5.20. Electrons from Rydberg photo-ionization at room temperature thus have very low kinetic energies below 0.15 eV. This is below the energy resolution of $\Delta E = 0.95\,\text{eV}$ of the KATRIN main spectrometer, so it is guaranteed that they are not magnetically stored.

5.3.6 Field Ionization

The last process we need to examine for the proposed background model is field ionization. Highly excited hydrogenic atoms are not stable within an external electric field. This is caused by the resulting non-monotonic radial potential which allows the electron to tunnel from a bound into a free state or simply because it can already classically escape the potential well and there is no bound state of that energy anymore. In figure

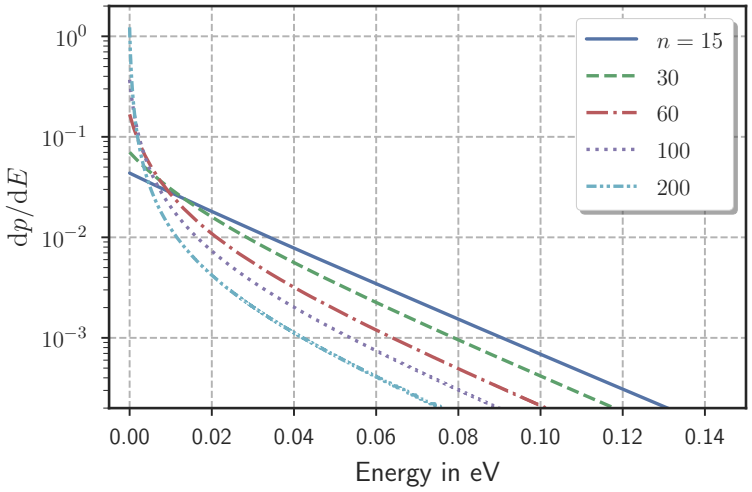

Figure 5.20: Energy spectrum of electrons emitted from BBR Photo-ionisation for varying n and $l = 1$ at $293\,K$

5.21 this is shown schematicly. There are two regimes where field ionization happens: classically the disturbed potential of the atom

$$V = -\frac{1}{r} + Ez \tag{5.63}$$

has a saddle point at $z = -1/\sqrt{E}$. There the potential yields the value $V = -2\sqrt{E}$. If an atom enters a field E, previously bound states above this threshold become free and are ionized. Comparing this with the - undisturbed - energy levels of hydrogen $E_n = 1/n^2$ yields a critical field of

$$E_c = \frac{1}{16n^4}, \tag{5.64}$$

given in atomic units. This is a very simple approach which not only ignores tunneling but also the Stark effect. Additionally there is an m dependence [210] (p.84). For states with $m \neq 0$ electrons are centrifugally kept away from the z-axis and therefore the threshold field for ionisatzon is higher by

$$\frac{\Delta E_c}{E_c} = \frac{|m|\sqrt{W}}{\sqrt{2}}. \tag{5.65}$$

The tunneling rate decreases exponentially when the energy of the state drops below the classical ionization threshold. The dependence of the field ionization rate on the electric field in the tunneling regime below the critical field was calculated by Lanczos [217]. Here, however, it is neglected.

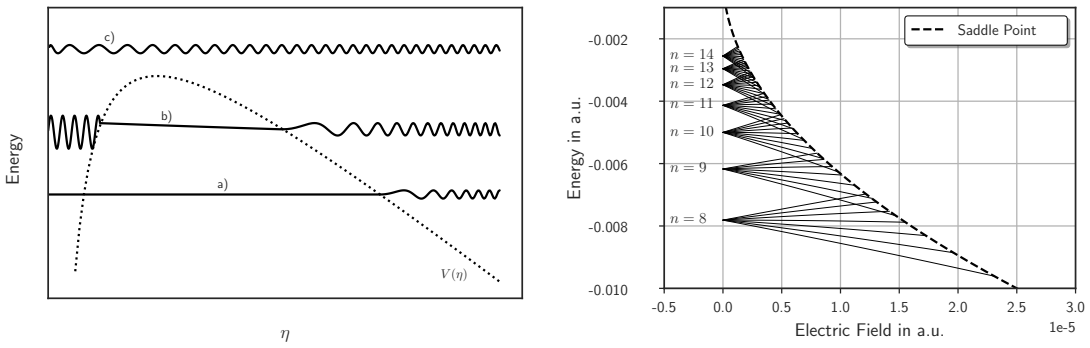

Figure 5.21: Left: Scheme of wave functions within the $1/r$ potential of an atom which is superimposed by an external linear potential resulting in $V(\eta)$. a) The energy is below the peak of the potential but away from a resonance of the inner well, representing either a bound state inside or a free state outside the well which are unconnected to each other. b) This scenario represents field ionization by tunneling: The two classically allowed regions inside and outside the well are connected by a non-vanishing wave functions and the transmission probability is finite as well. c) A completely free state. A single state of the atom at a fixed energy can move from scenario a) through b) to c) when the electric field is increased successively. **Right**: Shown are the energies of the Stark splitted $m = 1$ states of hydrogen from $n = 8$ to $n = 14$ including up to second order corrections according to equation 5.76 in their dependence of the electric field, both given in atomic units. The dashed line gives the value of the potential at the saddle point, states that lie above are classically ionized.

For a discussion of the Stark effect the hydrogen atom levels need to be treated in an external electric field. The following results are from [210], but can also be found in [212] in a similar form. The hydrogen atom in a constant external field remains a separable problem if treated in parabolic coordinates, which are defined as

$$\begin{aligned} \xi &= r + z = r(1 + \cos\theta) \\ \eta &= r - z = r(1 - \cos\theta) \\ \phi &= \tan^{-1} y/x, \end{aligned} \tag{5.66}$$

and

$$\begin{aligned} x &= \sqrt{\xi\eta}\cos\phi \\ y &= \sqrt{\xi\eta}\sin\phi \\ z &= (\xi - \eta)/2 \\ r &= (\xi + \eta)/2. \end{aligned} \tag{5.67}$$

Using these the Schrödinger equation reads

$$\left[-\frac{\nabla^2}{2} - \frac{2}{\xi + \eta} + \frac{E(\xi - \eta)}{2}\right]\psi = W\psi. \tag{5.68}$$

where the Nabla operator in parabolic coordinates is defined as

$$\nabla^2 = \frac{4}{\xi + \eta}\frac{\partial}{\partial\xi}\left(\xi\frac{\partial}{\partial\xi}\right) + \frac{4}{\xi + \eta}\frac{\partial}{\partial\eta}\left(\eta\frac{\partial}{\partial\eta}\right) + \frac{1}{\xi\eta}\frac{\partial^2}{\partial\phi^2}. \tag{5.69}$$

Making the ansatz for ψ to be separable

$$\psi(\xi, \eta, \phi) = u_1(\xi)u_2(\eta)e^{im\phi} \tag{5.70}$$

the Schrödinger equation parts into two equations

$$\frac{d}{d\xi}\left(\xi\frac{du_1}{d\xi}\right) + \left(\frac{W\xi}{2} + Z_1 - \frac{m^2}{4\xi} - \frac{E\xi^2}{4}\right)u_1 = 0 \tag{5.71}$$

$$\frac{d}{d\eta}\left(\eta\frac{du_1}{d\eta}\right) + \left(\frac{W\eta}{2} + Z_2 - \frac{m^2}{\eta} - \frac{E\eta^2}{4}\right)u_2 = 0 \tag{5.72}$$

$$Z_1 + Z_2 = 1 \tag{5.73}$$

connected by the constants Z_1 and Z_2. The parabolic wavefunctions that solve these at zero field acquire two new quantum numbers n_1 and n_2 in addition to n and m. These are non-negative and count the number of nodes in u_1 and u_2 respectively. They are connected to n and m as

$$n = n_1 + n_2 + |m| + 1 \tag{5.74}$$

and to the constants $Z_{1,2}$ by

$$Z_{1,2} = \frac{1}{n}\left(n_{1,2} + \frac{|m|+1}{2}\right). \tag{5.75}$$

The second order energies are

$$W_{nn_1n_2m} = \frac{-1}{2n^2} + \frac{3En}{2}(n_1 - n_2) - \frac{E^2}{16}n^4\left[17n^2 - 3(n_1-n_2)^2 - 9m^2 + 19\right]. \tag{5.76}$$

The states $|nn_1n_2m\rangle$ can be expanded to the usual $|nlm\rangle$ states as

$$|nn_1n_2m\rangle = \sum_l |nlm\rangle \langle nlm|nn_1n_2m\rangle \tag{5.77}$$

given the Wigner-3J symbols

$$\langle nlm|nn_1n_2m\rangle = (-1)^{(1-n+m+n_1-n_2)/2+l}\sqrt{2l+1} \times \begin{pmatrix} \frac{n-1}{2} & \frac{n-1}{2} & l \\ \frac{m+n_1-n_2}{2} & \frac{m-n_1+n_2}{2} & -m \end{pmatrix}. \tag{5.78}$$

From equation 5.76 we see that the energy eigenvalues depend on the difference of the parabolic quantum numbers $n_1 - n_2$. The first order term $\frac{3En}{2}(n_1 - n_2)$ is linear and therefore symmetric around zero for red- and blue-shifted states. Only the second order term introduces asymmetric shifts. However, the asymmetric contribution is negligible overall. Only for the circular states with $m = n - 1$ and $n_1 - n_2 = 0$ the first order correction vanishes and the second order becomes dominant. In figure 5.21 the splitting of the states $n = 8$ to $n = 14$ with increasing electric field is shown.

5.4 Background Simulation

Finally, all the previous results will be combined in a simulation of the proposed background process: Atoms at the surface of the main spectrometer vessel are scattered by the recoil nuclei from ^{210}Pb decays and sputtered off into the vacuum. Their outermost electron can occupy a highly excited state just below the ionization threshold. Some of these states are ionized by the electric fields at the surface, some decay into the ground state and finally a fraction will live long enough for the atom to travel into the center of the main spectrometer volume where a small fraction is finally ionized by the thermal BBR emanating from the surroundings at room-temperature. The low energy electrons created after ionization then are magnetically guided to the detector. Thereby they are accelerated by the vessel potential, rendering them indistinguishable from actual signal electrons.

5.4.1 Method

The simulation is done in several steps. At first, the composition and energy distribution of sputtered atoms are simulated following discussions in section 5.3.1. Two more

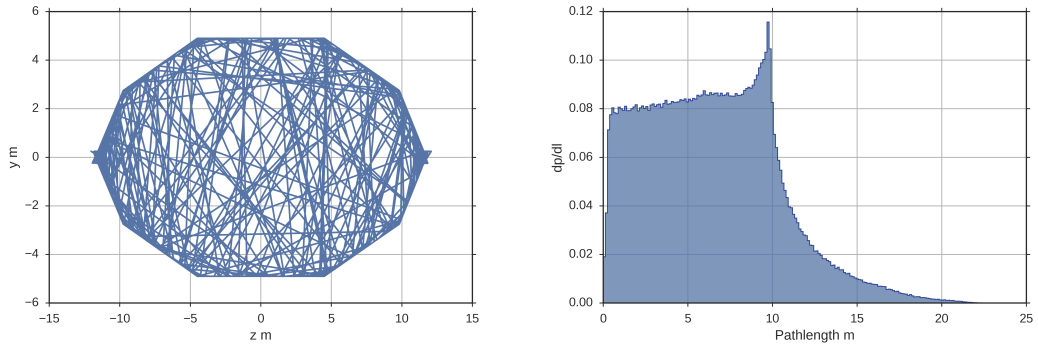

Figure 5.22: Left: Display of a cut through the spectrometer showing a small subset of simulated flight tracks close to the x-plane. **Right**: The resulting distribution of path lengths, the prominent peak at $\approx 10\,\mathrm{m}$ corresponds to the diameter of the central part

ingredients are necessary: The simulation of the decay of the Rydberg states and with it their lifetime distribution, and the path of the atoms through the geometry of the spectrometer. The latter is trivial when making use of Kassiopeia: As we assume to track neutral atoms, they will follow a straight line through the vacuum until they hit a wall. As input for the starting positions we assume a homogeneous distribution of activity on the vessel walls. Finally the momentum distribution is assumed to be isotropic. Running the simulation and stopping the particles upon hitting a part of the spectrometer gives the endpoints of the paths. The result of this is shown in figure 5.22.

The simulation of the time evolution of the Rydberg states is more involved: As argued in section 5.3.2 we will start with a distribution of Rydberg states according to $p(n,l) = \frac{2l+1}{n^2} n^{-3}$. We are interested in the overall ionization probability before hitting a wall and the distribution of ionization times. This is calculated using a Monte Carlo method. The total rate for a Rydberg atom to undergo any of the considered interactions is the sum of the contributing rates, which were calculated previously:

$$R_{\mathrm{tot}} = R_{\mathrm{spon}} + R_{\mathrm{trans}} + R_{\mathrm{ion}} \tag{5.79}$$

For every timestep t_s interaction times t_i are drawn from the exponential distributions with time constants $R_{\mathrm{spon,trans,ion}}$. The fastest reaction is executed, with the particle being set to the interaction point. A spontaneus decay terminates the calculation yielding no electron in contrast to ionization. Transitions between different Rydberg states may happen and affect the interaction rates. By propagating all states a time distribution of ionizations is generated and we get the overall ionization probability. From this distribution, ionization times are drawn for every sputtered atom. If the path length up to ionization exceeds the path length of the atom inside the spectrometer the atom is discarded. The resulting time distributions are shown in fig. 5.23.

Given the ionization times together with the velocity of the atoms and their propagation through the spectrometer it is possible to calculate the distribution of decay points. In general it could be necessary to generate electrons with an isotropic momen-

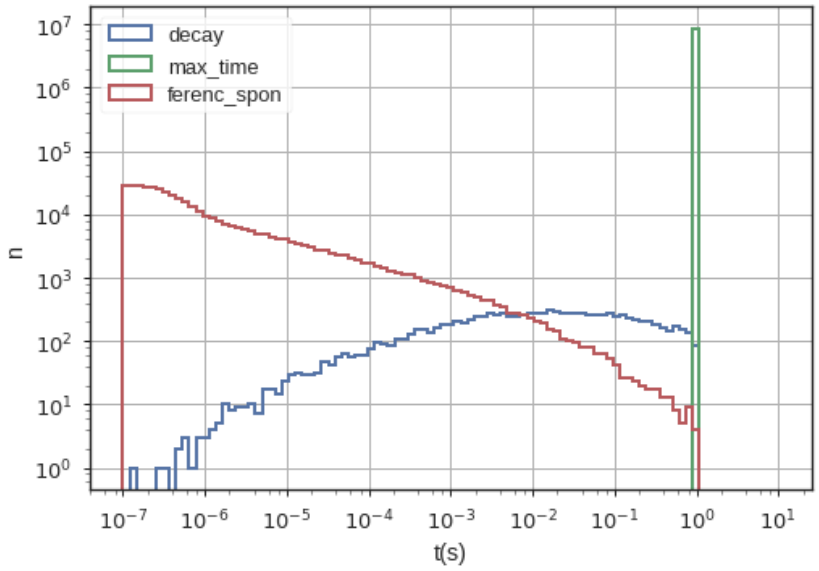

Figure 5.23: Distribution of the simulated final times of the Rydberg atoms. The simulation of an atom ends when it decays to the ground state, when it is ionized or when it surpasses a simulation time of 1 second. As the minimal velocity of the sputtered atoms simulated is still of the order of 3000 m/s, the sampling of larger times becomes increasingly a waste of computation time. The overall ionisation probability – for ionisations to happen before 1 second – is 1.128‰

tum distribution and calculate their trajectories through the electric and magnetic fields until they reach the detector or scatter of residual gas while being magnetically stored. This however is computationally intensive and not necessary in our case. The kinetic energies of the electrons created are in the meV range and well below the energy resolution of the spectrometer, which is the relevant scale for particle storage. Their gyration radii are negligible and they strictly follow the magnetic field lines towards the detector. Furthermore magnetic reflection does not occur. Treating the field as rotationally symmetric, we can calculate the magnetic field lines that hit the borders between the detector pixels and simply count all the ionizations between two of these field lines to get the counts for a detector ring. The transport to the detector is thereby modelled as two geometric cuts: First all the decay events outside of the flux tube are removed and then all events that lie upstream of the analyzing plane, as they do not have sufficient energy to overcome the potential barrier. For both cuts we use a b-spline interpolation [218] over a set of calculated points. For the field line points we use the ones calculated with Kassiopeia and shown in figure 5.24. The analyzing plane is approximated as rotational surface described by a $z - r$ dependence. The analyzing points we use for interpolation have been calculated by S. Groh in [156]. Only for the magnetic field setting "3.8G" a significant deviation of the analyzing plane from $z = 0$ is recognized. After this cut we have the sample of simulated background events and the probability for a sputtered atom to create a background event. We can now start to examine how these depend on

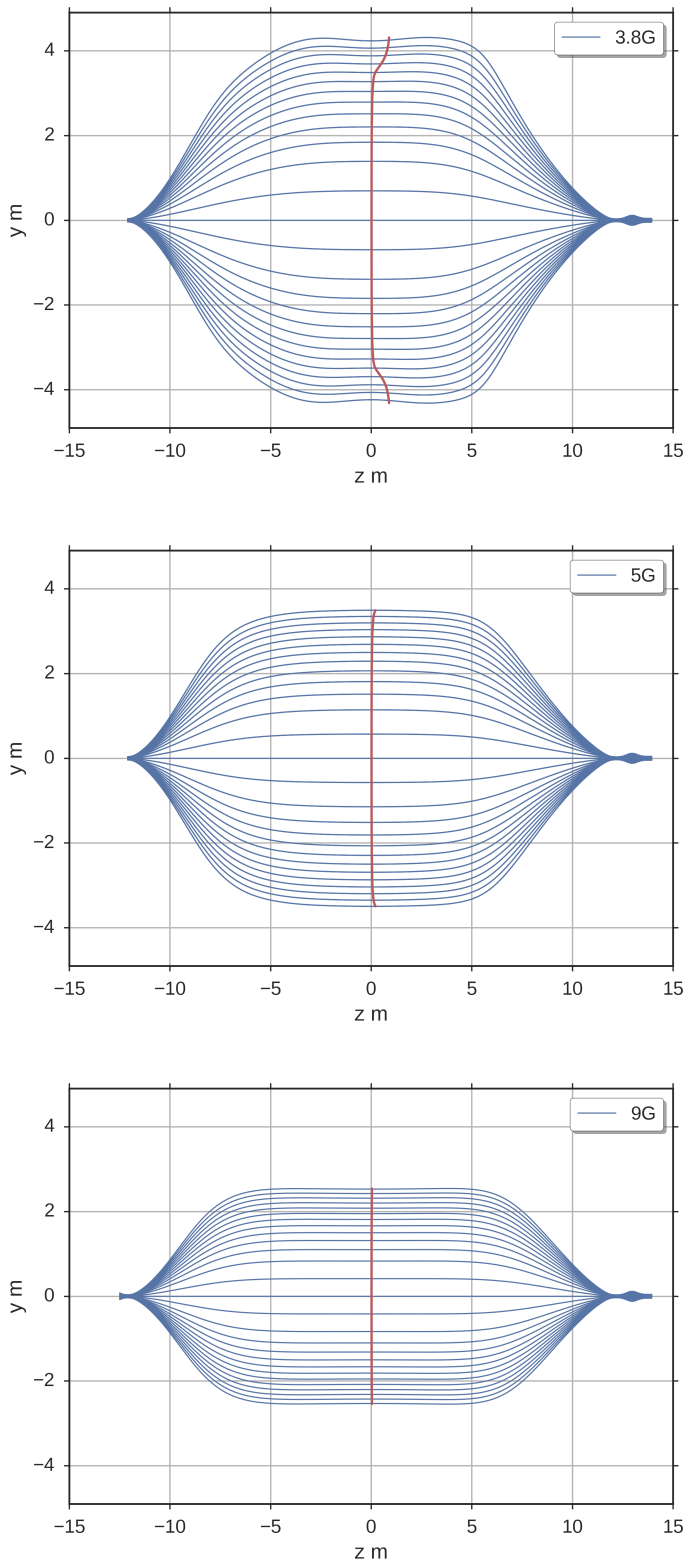

Figure 5.24: Magnetic field lines for the 3.8G, 5G, and 9G Settings and the corresponding analyzing plane. Low-energy electrons created right of the red line and inside the blue fluxtube are guided to the detector

operational parameters and compare the results to the measurements.

5.4.2 Results

Total Rate

The first test our model has to pass is to explain the overall size of the observed background. While there are large uncertainties tied to the model assumptions, further examination would not be necessary if the predicted background rate was orders of magnitude smaller than observed. The predicted rate depends on the amount of ^{210}Pb-activity in the steel. In [170] it was estimated by the simulating the arrival probability of conversion electrons at the detector and measuring their rate to be of the order of $A_{\mathrm{Pb}} = 998 \pm 117\,\mathrm{Bq}$. Using this result we can calculate the background rate by

$$R_{\mathrm{bg}} = A_{\mathrm{Pb}} \cdot Y_{\mathrm{sputter}} \cdot P_{\mathrm{ion}} \cdot P_{\mathrm{det}} \tag{5.80}$$

with Y_{sputter} being the average yield of sputtered atoms per decay, P_{ion} the probability of the Rydberg state to be ionized and P_{det} the probability of this to happen in a region of the spectrometer from where the electron will be transported to the detector. Both, P_{ion} and P_{det} generally depend on the Rydberg state $|n, l\rangle$ and the velocity of the sputtered atom. While this is inherently considered in the simulation, here we only refer to the net quantities based upon the assumed $1/n^3$ statistical state mixture and the velocity distribution from the SRIM simulation. The average sputter yield is $Y_{\mathrm{sputter},H_2O} = 39.27 \pm 0.07\,(\mathrm{stat.})$ for a monolayer of water and $Y_{\mathrm{sputter},H} = 29.78 \pm 0.06\,(\mathrm{stat.})$, the ionisation probability is $P_{\mathrm{ion}} = (1.12 \pm 0.01\,(\mathrm{stat.})) \times 10^{-3}$ and the transport efficiency is $P_{\mathrm{det}} = (1.851 \pm 0.006\,(\mathrm{stat.})) \times 10^{-2}$. Together this results in

$$\begin{aligned} R_{\mathrm{bg},H_2O} &= 812 \pm 77\,\mathrm{mcps}\,(\mathrm{stat.}). \\ R_{\mathrm{bg},H} &= 616 \pm 57\,\mathrm{mcps}\,(\mathrm{stat.}). \end{aligned} \tag{5.81}$$

The largest contribution to the uncertainty in rate stems from the activity, which is not precisely known. The uncertainties for P_{ion},P_{det} and Y_{sputter} are the assigned statistical uncertainties of the simulation efficiencies assuming Poisson statistics. The systematic uncertainty of Y_{sputter} however is much more difficult to quantify as it depends on the unknown surface condition of the spectrometer vessel. The difference in rate between a mono layer of water and a mono layer of hydrogen of $\Delta R = 149\,\mathrm{mcps}$ illustrates the size of the influence - in the following we assume this model assumption to be correct. Larger or lower rates can be related to higher (multi-layer) or lower surface occupation with hydrogen, water or a mixture of both. In principle other atoms, though unlikely, could be thought of as well. The measured rates at 5 V inner electrode voltage within a 3G setting pre and post bake-out however, agree with those calculated above:

$$\begin{aligned} R_{\mathrm{unbaked}} &= 843 \pm 5\,\mathrm{mcps} \\ R_{\mathrm{baked}} &= 611 \pm 7\,\mathrm{mcps} \end{aligned} \tag{5.82}$$

It is observed that by baking the spectrometer the background is reduced to 72.3 ± 0.4(stat.)% while our model predicts 75.6 ± 0.2(stat.)% (the reduced uncertainty stems from the fact that the most uncertain terms cancel out). If established, this could in principle be used to determine the surface occupation within the spectrometer in the future. Here no such effort will be made. For the present purpose it suffices to state that the background rate can be explained by the presented model. For further comparisons the background is assumed to be completely caused by the presented effect. This result is crucial because it definitely shows that this previously unknown background contribution exists and is sizeable in KATRIN: Once we know there is a contamination with α-activity causing sputtering, the excited states and their ionization by thermal radiation are inevitable. Earlier experiments with MAC-E-Filters could not observe this for several reasons. First of all the absolute amount of background by Rydberg atoms is proportional to the volume - which is 1000 times larger in KATRIN compared to other MAC-E-Filter devices. Also the size of the contamination (1 kBq for KATRIN) can be expected to scale with the size of the apparatus. The sensitivity to rare background processes of KATRIN is simply much larger than in predecessor experiments. Furthermore those experiments most likely have avoided much of the contamination KATRIN suffers from because the time between cleaning and electro polishing of the spectrometer inside and the evacuation of the vessel was much shorter than the three years it took to install the wire electrode in the KATRIN main spectrometer using forced ventilation of the vessel. This could only have been prevented if the spectrometer and adjacent clean room had been vented with an artificial radon-free pure nitrogen-oxygen atmosphere for the entire electrode installation phase.

Background time structure

In order to compute the inter-arrival time spectrum a complete particle tracking simulation of the created electrons would be necessary. Instead we will calculate the expected fraction of correlated events which stem from two or more atoms sputtered from the same decay being ionized. The arrival time differences between these electrons will be dominated by flight time differences within the spectrometer. These were studied in detail in [124, 219] and found to be of the order of ... . Together the ionisation probability of $P_{\mathrm{ion}} = (1.12 \pm 0.01) \times 10^{-3}$ and the transport efficiency of $P_{\mathrm{det}} = (1.851 \pm 0.006) \times 10^{-2}$ yield a probability of $p_{\mathrm{bg}} = 2.073 \times 10^{-5}$ for any given sputtered atom to create a background electron. If we have a decay with n sputtered atoms the probability for k background electrons is

$$p(n, k, p_{\mathrm{bg}}) = \binom{n}{k} \cdot p_{\mathrm{bg}}^{k} \cdot (1 - p_{\mathrm{bg}})^{1-k}. \tag{5.83}$$

For decays with n sputtered atoms we can calculate therefore the fraction of correlated background electrons from the same decay by

$$f(n) = \frac{\sum_{k=2}^{n} p(n, k, p_{\mathrm{bg}}) \cdot k}{\sum_{k=0}^{1} p(n, k, p_{\mathrm{bg}}) \cdot k}. \tag{5.84}$$

The number of sputtered atoms per decay however is not a fixed number but of course a distribution which is also a result of the SRIM simulations shown in figure 5.25. For every multiplicity n it yields the probability p_n. When including this in the calculation of the fraction of correlated events it yields

$$f = \sum_{n=2} f(n) \cdot p_n = (1.90 \pm 0.02)‰ \tag{5.85}$$

All of this assumes that ionizations happen independently for every atom. The measured fraction of correlated events in the remaining background is $1.99 \pm 0.07(\text{stat.})‰$ as found in section 5.1.2, a value in good agreement with eq. 5.85.

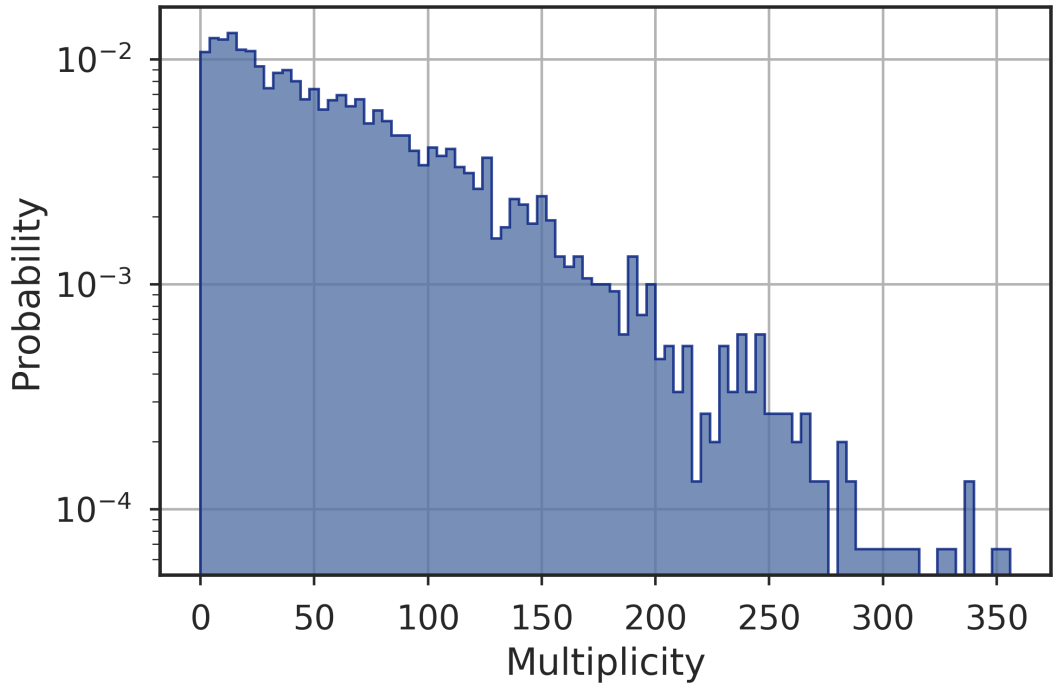

Figure 5.25: Simulated multiplicity spectrum for ^{210}**Pb** decays including all sputtered species.

Spatial Distribution

The measured spatial distribution of the background was discussed in 5.1.1. From the simulation we can obtain corresponding information by projecting all diced points of Rydberg ionization in the spectrometer along the magnetic field lines onto the detector using the magnetic field maps as discussed above. The result is shown in figure 5.26. The radial background distribution is largely reproduced by the simulation. It is worthy to note that starting from the same simulated background sample slightly differing density profiles are predicted for varying magnetic fields as observed in the measurement.

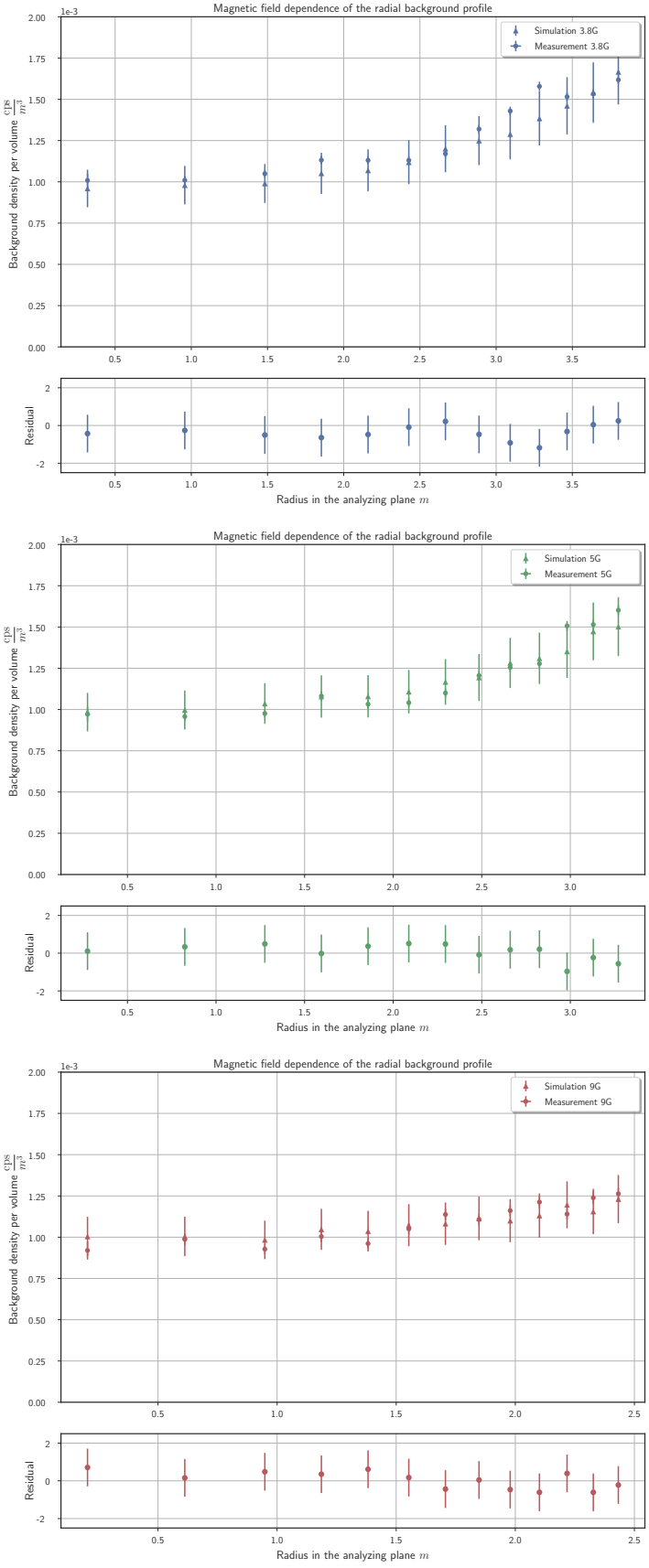

Figure 5.26: Simulated and measured radial profiles for the three different magnetic field settings 3G, 5G, and 9G from top to bottom

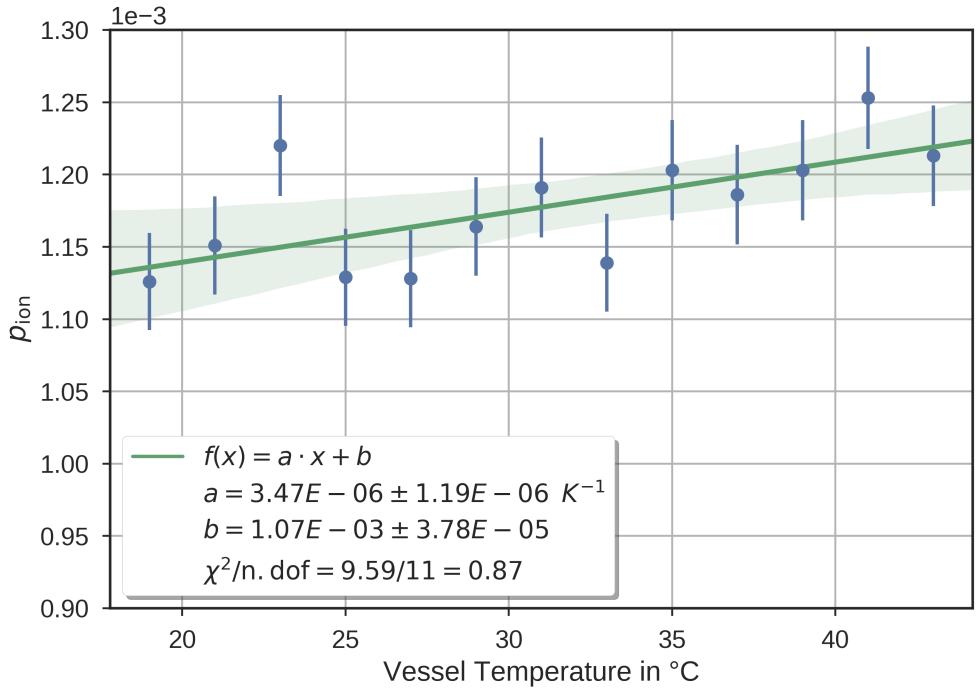

Figure 5.27: Simulation of temperature dependence of the ionisation probability p_{ion}. For this the simulation shown in Figure 5.23 was repeated with varying temperatures from 19 °C to 43 °C and 10^6 simulated Rydberg states per point.

Temperature dependence

The presented background model can be used to predict a dependence of the background rate on the ambient temperature, as observed in section 5.1.5: A higher temperature causes a higher intensity of the thermal radiation as well as a higher-energetic radiation spectrum, both resulting in higher ionization rates, which in turn cause higher background rates. Within the small temperature range that was accessible with the measurement only a linear increase can be expected. The simulation of the ionization probability for Rydberg states was carried out for the temperatures in the range of the measurement and is shown in figure 5.27. As a result it predicts a relative increase of rate by $7.3 \pm 2.1\,\%$ between 19 °C and 43 °C, which is compatible with the measured value $6.8 \pm 0.7\,\%$.

Inner electrode screening potential dependence

In our model the influence of the inner electrode potential on the rate arises from field ionisation of Rydberg atoms near the surfaces. Field ionization destroys the Rydberg states and prevents them from reaching the center of the spectrometer where their spon-

taneous ionization creates background electrons. Electrons from the field ionization are created well outside the flux tube and shielded by the magnetic field. The electric field caused by the screening potential of the inner electrode will be enhanced near microscopic structures of the vessel surface. Also, the energetic recoil ion will cause a surface disruption when be explanted, leading to an enhancement of the local field close to the track and thereby in the vicinity of the sputtered Rydberg atom. This is crucial because the fields in the volume of the order of up to 53 V/cm (a maximal 800 V as retarding voltage of the inner electrode was applied, the distance between the wire electrodes and the vessel wall is 15 cm) would not suffice to cause sizable field ionization and therefore the observed behavior could not be explained by them. The observation of field emission within the main spectrometer in previous measurements by Schwarz [220] already showed the presence of high field enhancements. At that time a field enhancement factor of $\beta = 10^5$ (there called γ, p198) was found. However since then the spectrometer was subjected to several ventings and high voltage conditioning and no field emission was observed anymore. This suggests a lower enhancement factor. The enhancement factor β relates the local electric field to the macroscopic field in the volume.

$$E_{\text{local}} = \beta \cdot E_{\text{vol}}. \tag{5.86}$$

It is understood as a measure of surface roughness. Near microscopic structures on the surface for example edges, peaks or craters with a small curvature radius electric fields are proportionally increased. A local roughness at the position of the implanted radioactivity may not be a mere coincidence. If the deposition mechanism relies on aerosols as discussed in [170], it is unsurprising that these have adhesed preferrably near structures in the surface. A single, fixed enhancement factor is not sufficient to accommodate the data. We assume a broken inverse power law distribution. In order to compare the measured dependence of the background rate on the inner electrode screening potential with the simulation it is necessary to investigate the n-distribution of the simulated background sample. For every Rydberg atom in the sample that decays the first order Stark shifted energy is calculated according to equation 5.76. The corresponding critical field where ionization classically occurs for this Stark state is then

$$E_c = (1 + |m|\sqrt{-E_n/2}) \cdot E_n^2/4. \tag{5.87}$$

The critical field of each state is then compared to the local electric field $\beta \cdot E_{\text{vol.}}$ and only those states with a critical field higher than the local field are accepted into the background sample. As a result the relative reduction of the background $f_R = R_{bg}(U_{\text{IE}}/R_{bg}(U_{\text{IE}} = 0)$ can be calculated. The same is extracted from the measurement presented in sect. 5.1.4. A comparison is shown in fig. 5.28. The field enhancement factor distribution was fitted with an inverse power law of $a = 1.05$ with a median β of 131.5.

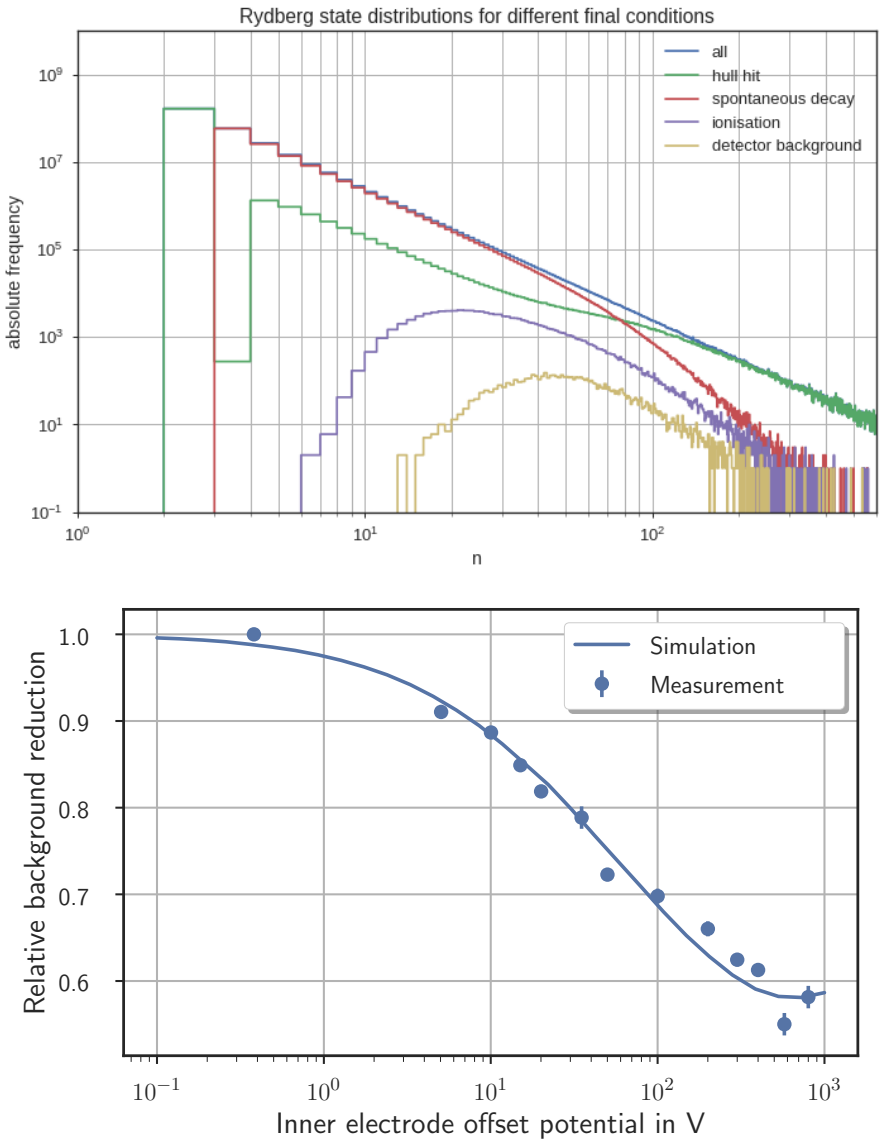

Figure 5.28: Top: Rydberg state distribution for different final states of the Rydberg atom. The envelope ("all", blue) follows $1/n^3$ law discussed earlier. **Bottom**: Comparison of the simulated state distribution and the effective distribution deduced from measurement.

5.5 Consequences and possible background mitigation

5.5.1 Electropolishing

A standard procedure to remove surface contamination from metals is electro-polishing [221]. All inner parts of the KATRIN Spectrometers were subject to this. However, the observation of field emission and field ionization hint towards a local high surface roughness inside the main spectrometer. It may be the result of the long exposure to (HEPA-filtered) ambient air, during the construction period, just as the ^{210}Pb contamination. In fact it is to be expected that the implantation of the contamination is also the cause of the surface roughness.

A re-application of electro-polishing on the inner parts of the spectrometer would be costly and time-consuming as it would necessitate the full dis- and reassembly of the inner wire electrode[1]. This will not be performed before KATRIN starts its long term measurement. We will discuss this in the light of best practices and in case any major extensions of the experiment are considered in the future (e.g. time-of-flight measurements, an atomic tritium source, new detector).

5.5.2 Background reduction

Other neutrino or Dark Matter experiments requiring ultra-low background rates routinely deal with background minimization by fiducialization: For measured events the location in the detector is reconstructed and all events close to the surfaces of the detector are rejected. This method is effective, since radioactive contaminations are harder to prevent on the detector surfaces and then most of the background is situated there. In practice much effort needs to be put in the reconstruction. For KATRIN this standard approach is not possible. The observed background offers no signature, making it inseparable from the signal, because no timing information of the creation of the incident electrons is available. While it would be possible to simply cut away the data on the outer rings of the detector, the loss in signal rate accompanied with the cut would be unfavorable. Moreover while the α-contamination is also at the surface of the spectrometer, the background electrons are created in the volume, although with a small radial decrease towards the center. However, as discussed in section 5.1.1 it is possible to reduce the background by increasing the magnetic field in the spectrometer. This leads to a smaller fluxtube - a smaller "fiducial" volume from where electrons are magnetically guided to the detector. But reducing the background this way comes at the cost of a reduced energy resolution of the spectrometer as this parameter depends only on the ratio of minimal to maximal magnetic field. Even more important, the systematic uncertainties related to the uncertainty of a larger magnetic field is bigger and strongly contributes to the overall systematic uncertainty of the experiment [195]. Another parameter that influences the background rate is the inner electrode screening potential, as discussed in sections 5.1.4 and 5.4.2. Both options change the electromagnetic configuration of the spectrometer and therefore necessitate the careful re-assessment of its

[1] the installation lasted 3 years

transmission characteristics as performed in [124, 156, 195] in order to ensure a correct description within the neutrino mass analysis. In the following the interplay between the systematic effects in the neutrino mass analysis from the magnetic field and the statistical uncertainty from the background rate are studied.

5.5.3 Neutrino mass sensitivity at elevated background levels

The observed background rate in the range of 200-900 mcps - depending on operational parameters - exceeds by far the design value of 10 mcps by far. Until the writing of this work no easy counter-measure against Rydberg-induced background was found, and given its origin in form of a minute environmental contamination of the spectrometer, it is questionable whether there will be one in the near future. This makes the precise measurement of the background even more important to achieve a good neutrino mass sensitivity. As the background depends on surface conditions inside the apparatus, and new conditions may arise this can only performed once the setup is in the final measurement condition, including the full tritium content of the source. The general dependence of KATRIN's neutrino mass sensitivity on the background rate R_{bg} is well known from [54]: it scales proportional to $\propto R_{bg}^{1/6}$ and is further diminished by non-Poissonian contributions [126]. Using the relation between magnetic field and background rate found in section 5.1.1, the resulting neutrino mass sensitivity in dependence of the magnetic field setting was estimated with SSC+KaFit [153]. For this the magnetic field model developed in the thesis of M. Erhard [195] is used. Specifically, the resulting systematic uncertainty of the analyzing magnetic field that is proportional to the absolute magnetic field strength is considered as an additional systematic effect. The deviation between the model in [195] and the measurement close to the analyzing plane is $\Delta B_A = 3.9 \times 10^{-3} \cdot B_A + 1.07 \times 10^{-6}\,T$) and the resulting systematic shift from this is $\Delta m_\nu^2 = \beta_1 \cdot B_A^2 + \beta_2 \cdot B_A$ with $\beta_1 = (-11.4 \pm 1.8) \times 10^{-10}\,\mathrm{eV}^2\mu\mathrm{T}^{-2}$ and $\beta_2 = (7.0 \pm 1.3) \times 10^{-8}\mathrm{eV}^2\mu\mathrm{T}^{-1}$. which was added to the standard KATRIN systematic uncertainty budget of $0.017\,\mathrm{eV}^2$. To estimate the sensitivity, the measurement interval was varied between 30 eV, 45 eV and 60 eV and an optimized measurement time distribution was calculated for each analyzing magnetic field, taking into account the elevated background using the optimization method developed in [152]. The inner electrode offset potential is not varied because higher offsets are expected to be unfavorable due to the increased inhomogeneity of the analyzing potential. The results are shown in figure 5.29. Without any mitigation of the elevated background, the sensitivity would be 363 meV (90% C.L.) instead of the design value of 200 meV. It is found that by combining an optimized scanning strategy with an extended measurement interval and higher analyzing magnetic fields it is possible to recover most of the sensitivity. This assumes that no other additional systematic effects arise, neither by extending the measurement interval nor by increasing the analyzing magnetic field. This crucial assumption relies primarily on the correctness of the energy loss model as discussed in chapter 4, and the magnetic field model of [195]. Conversely any improvement on these matters leaves more room to mitigate the background.

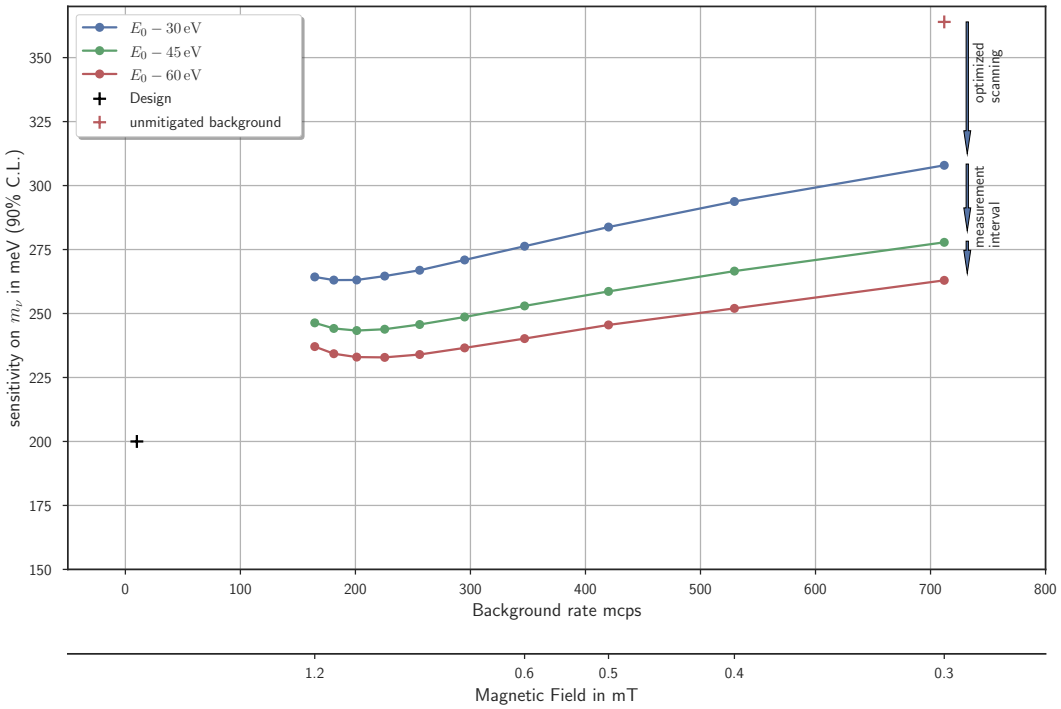

Figure 5.29: KATRIN's neutrino mass sensitivity for 3 years of measurement time and otherwise standard conditions in the light of a background exceeding the design limit. The crosses dots mark the design values (10 mcps background, 200 meV 90%C.L sensitivity lower left, but at 0.38 mT analyzing magnetic field, the second X-Axis does not apply to this data point) and the current status without any countermeasures (711 mcps, 363 meV, upper right). Sensitivity can be regained by increasing the measurement interval, by optimizing the measurement time distribution as shown by [152], and by increasing the magnetic field, thereby reducing the background. Included here is the increasing systematic uncertainty for higher magnetic fields found in [195]. The configuration file and measurement time distribution for this investigation are found in the appendix.

5.5.4 Open questions

Several observations and corresponding simulations were discussed. Yet there are several open issues that shall be addressed briefly:

Excitation Spectra

Only a rudimentary model of the spectra of excited states was used in this work. While this is sufficient for the purpose of this work a full understanding of all processes would be beneficial: By constraining the composition of sputtered atoms and their spectra it could ultimately be possible to revert the line of argument posed here and draw more detailed conclusions about the surface condition of the main spectrometer. This would be useful as the work function and by proxy the analyzing potential is affected by it - a parameter that so far is only accessible by e-gun measurements. If fully understood the measurement of the background could potentially be used as cross validation or an additional method of monitoring the work function. In fact general interesting effects on the excitation spectra were neglected so far: The details of the charge exchange reactions of the sputtered atoms with the bulk material in the vicinity of the surface, and the resulting velocity dependence and the influence of the band structure on the excitation levels of sputtered H and O atoms.

Ion reactions

The reactions of the ionized atoms in the vacuum were not considered here, but indeed could contribute to the background. After Rydberg atoms are photo-ionized, positive ions are left in the flux tube of in the spectrometer. Due to the negative vessel potential they do not reach the detector. Very low energetic ones however could potentially be stored by the magnetic field, all others will hit the vessel walls. Their energies are typically too low to further generate Rydberg states. A fraction of sputtered atoms emitted as charged states will be neutralized at the wall.

Anion production

The hydrogen anion production observed in [220] was not discussed but may be well be related to the sputtering that also creates the Rydberg atoms.

Vessel voltage dependence

So far the vessel voltage dependence of the background rate stands out to be explained.

Kinetic energy spectrum

The kinetic energy spectrum of the photo-ionized electrons was not tested in this thesis. This leaves an open prediction to test the Rydberg hypothesis presented here. For this we refer to the thesis by D. Hilk [125] which backs sub-ev electrons and the ongoing investigations by A. Pollithy [222], which points to eV-scale electrons. In a decisive

measurement any systematic effects on the scale of then of meV or larger must be considered to truly pin down the electron energy spectrum.

5.6 Conclusion

A model of background generation in the KATRIN main spectrometer vacuum through thermal photo ionization of Rydberg atoms which are excited and sputtered following nuclear decays on metal surfaces was developed and its experimental signatures were extracted: A largely Poisson-distributed background of 0.2-0.8 counts per second with a 2‰ coincident contribution, distributed nearly homogeneous in the volume of the spectrometer, with a linear dependence on the temperature of the vessel. This background is reduced throughout the entire vessel if an offset potential is applied to the inner electrode. These signatures agree with the experimental findings within errors. We conclude that the background of the main spectrometer vessel is caused by the 1 kBq contamination of ^{210}**Pb** found previously. As a removal of the activity is a major undertaking only mitigation by an increased magnetic analyzing field that reduces the sensitive volume of the spectrometer was discussed. In combination with a large analysis interval and an optimized scanning strategy the sensitivity of the KATRIN experiment can be retained.

CHAPTER 6

Outlook

Within this work models for inelastic electron scattering on molecular hydrogen and the creation of background electrons within the KATRIN Main Spectrometer by the ionization of highly excited Rydberg atoms sputtered from nuclear decays were built and compared to literature or measurement data. Both describe processes that are of paramount importance for the KATRIN experiment. Energy losses of the β-electrons within the gaseous tritium source are one of the major systematic effects that need a precise description to allow a successful estimation of the neutrino mass from a measurement. The rate of background electrons on the other hand are the largest contribution of statistical uncertainty. Therefore the elevated rate of the order of $\approx 1\,\mathrm{cps}$ found in the measurements with the KATRIN Main Spectrometer which exceeds the design goal of $10^{-2}\,\mathrm{cps}$ by far is of major concern for the experiment.

However, the observed properties of the background could not be explained by processes known from similar spectrometers, in fact it was possible to exclude them as dominant sources. Penning traps in the field configuration cause much higher and fluctuating backgrounds, which are not observed. Stored particles from nuclear decays have a distinct signature when measuring at elevated pressure, which the residual background lacks after radon is removed by the cryogenic baffles. Low energy electrons from the vessel walls of the spectrometer have been shown to be nearly perfectly shielded with the help of a strong γ-source. Only very low energetic electrons that originate within the vacuum of the spectrometer fit all observations simultaneously. This requires a creation mechanism that is probable enough to explain the observed rate. Highly excited neutral Rydberg atoms can traverse the fields of the spectrometer largely unperturbed, until they react with the ambient temperature thermal radiation which suffices to ionize them. Within sputtering processes following α-decays in the steel, sufficient energy is provided to create these atoms abundantly. The sputtering yields, Rydberg state distribution, decay and ionization rates have been calculated. As a result, the absolute rate,

spatial distribution, time structure, temperature dependence and local field dependence of the background can be derived. The results are in agreement with the observations. By intentional contamination of the spectrometer with short-lived α-activity the same background properties were observed at higher rates. This showed that the background is indeed sourced by a minute contamination of the spectrometer. As a result the background can only be completely defeated if this activity is removed from the spectrometer. The required effort for cleaning the spectrometer, e.g. with electro polishing, is exceedingly high and would cause a major delay without guarantee of success. Therefore the suppression of the background by means of an increased analyzing magnetic field was studied. With the higher field the flux tube volume from which electrons within the spectrometer are guided towards the detector is shrinked, and therefore the background rate reduced. This comes at the cost of a lower energy resolution of the spectrometer, which needs to be compensated by optimizing the measurement time distribution accordingly and extending the analysis interval. By analysis of ensemble tests it was shown that this is sufficient to achieve a good neutrino mass sensitivity of $230 - 250\,\mathrm{meV}$, depending on the final magnetic field configuration, provided that the systematic uncertainties of the magnetic field and the scattering in the gaseous source stay within their purported bounds even at higher magnetic field and in the larger analysis interval. This necessitates a good model of the inelastic scattering of the β-electrons, for which a first step was also made in this thesis. From literature results and databases an extrapolation of the excitation and ionization cross sections for electron impact scattering on molecular hydrogen were compiled and compared to other earlier results. By studying the systematic effects of this model on the neutrino mass fit, required bounds on the uncertainties of the models parameters are derived. These are at present not fulfilled for several of them, for others no reliable uncertainties are available. Within the particular energy range of interest for KATRIN of $18.5 - 18.6\,\mathrm{keV}$ accurate data on electron impact scattering on molecular hydrogen is scarce. It is therefore of utmost importance that KATRIN measures the energy loss of electrons by inelastic scattering within the source in-situ. First measurements with an electron gun are being conducted at the moment. Additionally it is stressed that as hydrogen, or tritium for that matter, has the simplest electronic structure of all molecules. It is therefore again stated that an ab-initio calculation of the energy-loss distribution and the cross section, similar to the calculations that exist for the final-state distribution of the $^3\mathrm{HeT}^+$ daughter nuclei after β decay is undertaken.

List of Acronyms

AGS Alternating Gradient Synchrotron

ALEPH Apparatus for LEP physics

BBR Black Body Radiation

BEM Boundary Element Method

BIXS Beta Induced X-ray Spectroscopy

CC Charged Current

CDM Cold dark matter

CERN Conseil Européan pour la Recherche Nucléaire

CKM Cabbibo-Kobayashi-Maskawa

CMB Cosmic Microwave Background

CNO Carbon Nitrogen Oxygen

COBE Cosmic Background Explorer

CP Charge and Parity

CPS Cryogenic Pumping Section

CUORE Cryogenic Underground Observatory for Rare Events

DELPHI Detector with Lepton, Photon and Hadron Identification

DONUT Direct Observation of Nu Tau

DPS Differential Pumping Section

ECR Electron Cyclotron Resonance

EMCS Earth magnetic field compensation system

ES Elastic Scattering

EXO Enriched Xenon Observatory

FT-ICR Fourier Transfrom Ion Cyclotron Resonance

FPD Focal Plane Detector

FWHM Full Width at Half Maximum

GALLEX Gallium Experiment

GERDA Germanium Detector Array

GNO Gallium Neutrino Observatory

GPU Graphics Processing Unit

HDM Hot Dark Matter

IE Inner electrode

KATRIN Karlsruhe Tritium Neutrino Experiment

KIT Karlsruhe Institute of Technology

LARA Laser Raman

LEP Large Electron-Positron Collider

LFCS Low Field Correction System

LHC Large Hadron Collider

MAC-E Magnetic Adiabatic Collimation with Electrostatic

MARE Microcalorimeter Arrays for a Rhenium Experiment

MINOS Main Injector Neutrino Oscillation Search

MIT Massachusetts Institute of Technology

MPI Message Passing Interface

MSW Mikheyev-Smirnov-Wolfenstein

NC Neutral Current

NEG Non-evaporable getter

OPERA Oscillation Project with Emulsion Tracking Apparatus

PDG Particle Data Group

PMNS Pontecorvo-Maki-Nakagawa-Sakata

RENO Reactor Experiment for Neutrino Oscillations

ROI Region of interest

SAGE Soviet American Gallium Experiment

SM Standard Model of particle physics

SDS Spectrometer Detector Section

SLC Stanford Linear Detector

SNEWS Supernova Early Warning System

SNO Sudbury Neutrino Experiment

SRIM The Stopping and Range of Ions in Matter

SSM Standard Solar Model

STS Source Transport Section

T2K Tokai to Kamioka

TLK Tritium Laboratory Karlsruhe

TMP Turbo Molecular Pump

UNC University of North Carolina

UV Ultraviolet

WGTS Windowless Gaseous Tritium Source

WIMP weakly interacting massive particle

WMAP Wilkinson Microwave Anisotropy Probe

XML X Markup Language

Appendix

Below the Kassiopeia configuration file for the calculation of the Rydberg ionisation probability is listed. Call this like :

```
#!/bin/bash
KatrinKassiopeia IonisationProbabiltiy.xml -r seed=14 Temperature=316
↪  tbpath=~/output nev=1000000
```

```
<define name="log_path" value="[tbpath]/log"/>
<define name="output_path" value="[tbpath]/data"/>

<external_define name="Temperature" value="292"/>

<!--  define verbosity level of messages -->
<messages>
    <file path="[log_path]" base="IonizationProbabilityLog-[seed]-[Temperature]K.txt"/>
    <message key="all" terminal="normal" log="warning"/>
    <message key="ks_main" terminal="normal" log="warning"/>
    <message key="ks_run" terminal="normal" log="warning"/>
    <message key="ks_event" terminal="normal" log="warning"/>
    <message key="ks_track" terminal="normal" log="warning"/>
</messages>

<!-- put together geometry -->
<geometry>
        <!--  define a world space, and put spectrometer and detector inside -->
    <cylinder_space name="world_space" z1="-100." z2="100000." r="100."/>

    <space name="world" node="world_space"/>
</geometry>

<kassiopeia>
    <ksgen_generator_composite name="rydberg">
        <pid_fix value="11"/>

        <position_cylindrical_composite>
            <r_fix value="0."/>
            <phi_fix value="0."/>
            <z_fix value="0."/>
        </position_cylindrical_composite>

        <time_composite>
                <time_fix value="0."/>
        </time_composite>

        <n_composite>
            <n_pareto
                value_min="1."
                value_max="{1000.}"
                offset="{0.0}"
                cutoff="1"
                slope="0.5"
            />
        </n_composite>

        <l_statistical/>
```

```
49
50          <energy_composite>
51                 <energy_fix value="1.e-5"/>
52          </energy_composite>
53
54          <direction_spherical_composite>
55              <theta_fix value="0."/>
56              <phi_fix value="0."/>
57          </direction_spherical_composite>
58
59      </ksgen_generator_composite>
60
61       <kstraj_trajectory_linear name="rydberg_tracking" length="40."/>
62
63       <ksint_decay_calculator_glukhov_spontaneous
64           name="glukhov_spon"
65           target_pid="11"
66       />
67       <ksint_decay_calculator_ferenc_spontaneous
68           name="ferenc_spon"
69           target_pid="11"
70       />
71       <ksint_decay_calculator_ferenc_bbr_transition
72           name="ferenc_bbr"
73           target_pid="11"
74           temperature="[Temperature]"
75       />
76
77       <ksint_decay name="glukhov"
78                    calculator="ferenc_bbr"
79                    calculator="ferenc_spon">
80                    <decay_ferenc_ionisation name="decay"
81                                    temperature="[Temperature]"
82                                    target_pid="11"/>
83       </ksint_decay>
84
85
86       <ksnav_space name="nav_space"
87           enter_split="false"
88           exit_split="false"/>
89
90       <ksnav_surface name="nav_surface"
91           transmission_split="false"
92           reflection_split="false"/>
93
94       <ksterm_max_steps name="max_steps" steps="1"/>
95       <ksterm_max_z name="max_z" z="9900."/>
96       <ksterm_max_time name="max_time" time="1."/>
97       <kswrite_root name="write_root"
98           path="[output_path]"
99           base="IonizationProbability-[seed]-[Temperature]K.root"/>
100
101      <ks_component_member name="output_track_initial_particle"
102          field="initial_particle"
103          parent="track"/>
104
105      <ks_component_member
106          name="output_track_final_particle"
107          field="final_particle"
108          parent="track"/>
109
110      <ks_component_member
111          name="terminator_name"
112          field="terminator_name" parent="track"/>
113
114      <ks_component_group name="output_track_world">
115          <component_member name="track_id"
116              field="track_id" parent="track"/>
117          <component_member name="initial_n"
118              field="n" parent="output_track_initial_particle"/>
119          <component_member name="initial_l"
120              field="l" parent="output_track_initial_particle"/>
121          <component_member name="final_n"
122              field="n" parent="output_track_final_particle"/>
123          <component_member name="final_l"
124              field="l" parent="output_track_final_particle"/>
125          <component_member name="initial_kinetic_energy"
126              field="kinetic_energy_ev"
127              parent="output_track_initial_particle"/>
128          <component_member name="final_time"
129              field="time" parent="output_track_final_particle"/>
130          <component_member name="final_position"
131              field="position"
```

```
132             parent="output_track_final_particle"/>
133         <component_member name="terminator_name"
134             field="terminator_name" parent="track"/>
135     </ks_component_group>
136
137     <kswrite_root_condition_terminator name="write_decays"
138                                        parent="terminator_name"
139                                        match_terminator="decay"/>
140
141     <!-- navigation -->
142
143     <ksgeo_space name="space_world" spaces="world">
144
145             <!-- add trajectory -->
146         <command parent="root_trajectory"
147                  field="set_trajectory"
148                  child="rydberg_tracking"/>
149
150         <!-- add terminators -->
151         <command parent="root_terminator"
152                  field="add_terminator"
153                  child="max_z"/>
154
155         <command parent="root_terminator"
156                  field="add_terminator"
157                  child="max_time"/>
158
159         <command parent="root_space_interaction"
160                  field="add_space_interaction"
161                  child="glukhov"/>
162
163         <command parent="write_root"
164                  field="add_track_output"
165                  child="output_track_world" />
166
167     </ksgeo_space>
168
169     <!-- simulation -->
170
171     <ks_simulation
172         run="1"
173         seed="[seed]"
174         events="[nev]"
175         space="space_world"
176         generator="rydberg"
177         space_navigator="nav_space"
178         surface_navigator="nav_surface"
179         writer="write_root"
180     />
181
182 </kassiopeia>
```

Below the Kassiopeia configuration file for the simulation of rydberg paths is listed. call this like

```
#!/bin/bash
$ KatrinKassiopeia AxialMainSpecSimulation_Rydberg-Paths.xml -r
↪  seed=12348 tbpath=~/output nev=1000000
```

```
<define name="log_path" value="[tbpath]/log"/>
<define name="output_path" value="[tbpath]/data"/>
<define name="geometry_path" value="/home/trost/kasper/install/config/TheBag"/>


<external_define name="ac_setting" value="3.8"/>
<!--  define verbosity level of messages -->
<messages>
    <file path="[log_path]" base="AxialMainSpecSimulation-SDS2-Rydberg-Ferenc_hull_only-Log-[ac_setting]g-[seed].txt"/>
    <message key="all" terminal="warning" log="warning"/>
    <message key="ks_main" terminal="normal" log="warning"/>
    <message key="ks_run" terminal="normal" log="warning"/>
    <message key="ks_event" terminal="normal" log="warning"/>
</messages>

<external_define name="ps_1_current" value="104.7"/> <!-- reference value for 4.5 T, is 157 -->
<external_define name="ps_2_current" value="148.6"/> <!-- reference value for 4.5 T, is 157 -->
<external_define name="pinch_magnet_current" value="72.625"/>        <!--87.115 is 6 T-->
<external_define name="detector_magnet_current" value="46.795"/>        <!--56.154 is 3.6 T-->

<!--  include geometry files of magnets and electrodes -->

<include name="[geometry_path]/AxialMainSpec/AxialMainSpecModel.xml"/>
<include name="[geometry_path]/AxialMainSpec/AxialMainSpecHullSurface.xml"/>

<!-- put together geometry -->
<geometry>
        <!--  define a world space, and put spectrometer and detector inside -->
    <cylinder_space name="world_space" z1="-50" z2="50" r="20"/>
     <disk_surface name="disk_surface" z="{0.}" r="{0.2}"/>
    <space name="world" node="world_space">
        <space name="axial_main_spec" tree="axial_main_spec_assembly"/>
        <space name="generation_surface" tree="generator_surface_hull_assembly"/>
         <surface name="exit_disk" node="disk_surface">
            <transformation displacement="{0.} {0.} {12.1835}"/>
        </surface>
        <surface name="entrance_disk" node="disk_surface">
            <transformation displacement="{0.} {0.} {-12.10375}"/>
        </surface>
    </space>

    <mesh name="gen_mesh_main_spec" surfaces="world/generation_surface/#"/>
</geometry>


<kassiopeia>

    <ksgen_generator_composite name="rydberg">
        <pid_fix value="10000"/>

        <position_surface_random surfaces="world/generation_surface/#"/>

        <time_composite>
                <time_fix value="0."/>
        </time_composite>

        <energy_composite>
                <energy_fix value="1."/>
        </energy_composite>


        <direction_surface_composite surfaces="world/generation_surface/#">
                  <theta_fix value="0."/>
            <phi_uniform value_min="0." value_max="360."/>
        </direction_surface_composite>

        <position_surface_adjustment_step length="1.e-3"/>

        <direction_surface_composite surfaces="world/generation_surface/#">
            <theta_spherical angle_min="0." angle_max="89."/>
            <phi_uniform value_min="0." value_max="360."/>
        </direction_surface_composite>
```

```
73
74      </ksgen_generator_composite>
75
76       <kstraj_trajectory_linear name="rydberg_tracking" length="1."/>
77
78       <ksnav_space name="nav_space" enter_split="false" exit_split="false"/>
79       <ksnav_surface name="nav_surface" transmission_split="false" reflection_split="false"/>
80
81       <ksterm_min_z name="term_min_z" z="-12.10375"/>
82       <ksterm_max_z name="term_max_z" z="12.1835"/>
83       <ksterm_death name="term_world_death"/>
84       <ksterm_death name="term_hit"/>
85       <ksterm_mainspec_hull name="term_mainspec_hull" tolerance="0.002" />
86
87
88       <kswrite_root name="write_root"
89           path="[output_path]"
90           base="AxialMainSpecSimulation_SDS-Rydberg-Ferenc_hull_only-[ac_setting]g-[seed].root"/>
91
92
93       <ks_component_member name="output_track_initial_particle" field="initial_particle" parent="track"/>
94       <ks_component_member name="output_track_final_particle" field="final_particle" parent="track"/>
95       <ks_component_member name="initial_time" field="time" parent="output_track_initial_particle"/>
96             <ks_component_member name="final_time" field="time" parent="output_track_final_particle"/>
97       <ks_component_member name="final_speed" field="speed" parent="output_track_final_particle"/>
98       <ks_component_member name="initial_position_vector" field="position" parent="output_track_initial_particle"/>
99       <ks_component_member name="final_position_vector" field="position" parent="output_track_final_particle"/>
100      <ks_component_member name="terminator_name" field="terminator_name" parent="track"/>
101      <ks_component_member name="final_radius" field="perp" parent="final_position_vector"/>
102
103      <ks_component_group name="output_track_world">
104          <component_member name="track_id" field="track_id" parent="track"/>
105          <component_member name="terminator_name" field="terminator_name" parent="track"/>
106          <component_member name="initial_position" field="position" parent="output_track_initial_particle"/>
107          <component_member name="initial_radius" field="perp" parent="initial_position_vector"/>
108          <component_member name="final_position" field="position" parent="output_track_final_particle"/>
109          <component_member name="final_radius" field="perp" parent="final_position_vector"/>
110          <component_math name="track_length" term="(x0-x1)*x2" parent="final_time" parent="initial_time"
             ↪  parent="final_speed"/>
111      </ks_component_group>
112
113      <kswrite_root_condition_terminator name="write_hits" parent="terminator_name" match_terminator="term_hit"/>
114
115      <!-- navigation -->
116
117      <ksgeo_space name="space_world" spaces="world">
118
119          <geo_side name="world_jacket" surfaces="world/jacket">
120              <command parent="root_terminator" field="add_terminator" child="term_world_death"/>
121          </geo_side>
122          <geo_side name="world_top" surfaces="world/top">
123              <command parent="root_terminator" field="add_terminator" child="term_world_death"/>
124          </geo_side>
125          <geo_side name="world_bottom" surfaces="world/bottom">
126              <command parent="root_terminator" field="add_terminator" child="term_world_death"/>
127          </geo_side>
128
129          <geo_surface name="mainspec" surfaces="world/generation_surface/#">
130              <command parent="root_terminator" field="add_terminator" child="term_hit"/>
131          </geo_surface>
132            <!-- add trajectory -->
133          <command parent="root_trajectory" field="set_trajectory" child="rydberg_tracking"/>
134
135          <!-- add terminators -->
136          <command parent="root_terminator" field="add_terminator" child="term_mainspec_hull"/>
137          <command parent="root_terminator" field="add_terminator" child="term_min_z"/>
138          <command parent="root_terminator" field="add_terminator" child="term_max_z"/>
139
140          <command parent="write_root" field="add_track_output" child="output_track_world"/>
141          <command parent="write_root" field="add_track_write_condition" child="write_hits"/>
142
143      </ksgeo_space>
144
145      <!-- simulation -->
146
147      <ks_simulation
148          run="1"
149          seed="[seed]"
150          events="[nev]"
151          space="space_world"
152          generator="rydberg"
153          space_navigator="nav_space"
154          surface_navigator="nav_surface"
```

```
155             writer="write_root"
156         />
157
158     </kassiopeia>
```

Below the TRIM.IN files for use with SRIM describing the used surface model are listed. The first one with a surface layer of hydrogen and the second one with water.

```
==> SRIM-2013.00 This file controls TRIM Calculations.
Ion: Z1 ,  M1,  Energy (keV), Angle,Number,Bragg Corr,AutoSave Number.
     2   4.003        5407       0    1000        1     1000
Cascades(1=No;2=Full;3=Sputt;4-5=Ions;6-7=Neutrons), Random Number Seed, Reminders
                    7                                  0       0
Diskfiles (0=no,1=yes): Ranges, Backscatt, Transmit, Sputtered, Collisions(1=Ion;2=Ion+Recoils), Special EXYZ
     .txt file
                         1       1           3       1               0                                 0
Target material : Number of Elements & Layers
"He␣(21)␣into␣Hydrogen+CrO2Fe+Stainless␣S"       8               3
PlotType (0-5); Plot Depths: Xmin, Xmax(Ang.) [=0 0 for Viewing Full Target]
       5                        0             998
Target Elements:    Z   Mass(amu)
Atom 1 = H =       1   1.008
Atom 2 = Cr =      24  51.996
Atom 3 = O =       8  15.999
Atom 4 = Fe =      26  55.847
Atom 5 = Cr =      24  51.996
Atom 6 = Fe =      26  55.847
Atom 7 = Ni =      28   58.69
Atom 8 = Mo =      42   95.94
Layer   Layer Name /               Width Density      H(1)  Cr(24)    O(8)  Fe(26)  Cr(24)  Fe(26)  Ni(28)
     Mo(42)
Numb.   Description                (Ang) (g/cm3)    Stoich  Stoich  Stoich  Stoich  Stoich  Stoich  Stoich
     Stoich
 1      "Hydrogen"           1  1.25       1       0       0       0       0       0       0       0
 2      "CrO2Fe"            30  3.80218013       0      .3      .6      .1       0       0       0       0
 3      "Stainless␣Steel"            967  7.94044166       0       0       0       0 .159255 .695112 .122196
      .023437
0  Target layer phases (0=Solid, 1=Gas)
0 0 0
Target Compound Corrections (Bragg)
 1   1   1
Individual target atom displacement energies (eV)
      10      25      28      25      25      25      25      25
Individual target atom lattice binding energies (eV)
       3       3       3       3       3       3       3       3
Individual target atom surface binding energies (eV)
       2    4.12       2    4.34    4.12    4.34    4.46    6.83
Stopping Power Version (1=2011, 0=2011)
 0
```

```
==> SRIM-2013.00 This file controls TRIM Calculations.
Ion: Z1 ,  M1,  Energy (keV), Angle,Number,Bragg Corr,AutoSave Number.
    42  97.905         51       0    1000        1     1000
Cascades(1=No;2=Full;3=Sputt;4-5=Ions;6-7=Neutrons), Random Number Seed, Reminders
                    7                                  0       0
Diskfiles (0=no,1=yes): Ranges, Backscatt, Transmit, Sputtered, Collisions(1=Ion;2=Ion+Recoils), Special EXYZ
     .txt file
                         1       1           3       1               0                                 0
Target material : Number of Elements & Layers
"Mo␣(51)␣into␣Water_Liquid␣(ICRU-276)+CrO"       9               3
PlotType (0-5); Plot Depths: Xmin, Xmax(Ang.) [=0 0 for Viewing Full Target]
       5                        0            1000
Target Elements:    Z   Mass(amu)
Atom 1 = H =       1   1.008
Atom 2 = O =       8  15.999
Atom 3 = Cr =      24  51.996
Atom 4 = O =       8  15.999
Atom 5 = Fe =      26  55.847
Atom 6 = Cr =      24  51.996
Atom 7 = Fe =      26  55.847
Atom 8 = Ni =      28   58.69
Atom 9 = Mo =      42   95.94
Layer   Layer Name /               Width Density      H(1)    O(8)  Cr(24)    O(8)  Fe(26)  Cr(24)  Fe(26)
     Ni(28)  Mo(42)
Numb.   Description                (Ang) (g/cm3)    Stoich  Stoich  Stoich  Stoich  Stoich  Stoich  Stoich
     Stoich  Stoich
 1      "Water_Liquid␣(ICRU-276)"           3  1 .666667 .333333       0       0       0       0       0
           0       0
 2      "CrO2Fe"            30  3.80218013       0       0      .3      .6      .1       0       0       0
           0
 3      "Stainless␣Steel"            967  7.94044166       0       0       0       0       0 .159255 .695112
      .122196 .023437
0  Target layer phases (0=Solid, 1=Gas)
0 0 0
Target Compound Corrections (Bragg)
 .94   1   1
Individual target atom displacement energies (eV)
```

```
32        10       28       25       28       25       25       25       25       25
33 Individual target atom lattice binding energies (eV)
34         3        3        3        3        3        3        3        3        3
35 Individual target atom surface binding energies (eV)
36         2        2     4.12        2     4.34     4.12     4.34     4.46     6.83
37 Stopping Power Version (1=2011, 0=2011)
38  0
```

Below python code for the generation of a TRIM.DAT input file to use with SRIM is listed. This allows for the implantation of lead atoms.

```
import numpy as np
import pandas as pd

trimdat = pd.DataFrame()
names = ["Pb210" for i in range(10010)]
trimdat['Name'] = names
trimdat['Atom'] = 82
trimdat['Energy'] = 146000
trimdat['X'] = 0
trimdat['Y'] = 0
trimdat['Z'] = 0
trimdat['Cos(X)'] = np.random.uniform(0.,1.,size=len(trimdat))
lat = np.sqrt(1.-trimdat['Cos(X)']**2)
phi = np.random.uniform(0.,2.*np.pi,size=len(trimdat))
trimdat['Cos(Y)'] = lat*np.sin(phi)
trimdat['Cos(Z)'] = lat*np.cos(phi)
trimdat.to_csv('TRIM.DAT',sep=' ',line_terminator='\r\n',index=False,
        float_format='%.7f',encoding='latin_1')
```

The folllowing python code allows to generate a TRIM.DAT file to use with SRIM taking the final implantation depth from a RANGE_3D.TXT output file of SRIM.

```
import numpy as np
import pandas as pd

ranges = pd.read_table('karge_implant/RANGE_3D.txt',
index_col=0,
delim_whitespace=True,
decimal=",",
skiprows=19,
header=None,
names=['Ion','X','Y','Z'])

trimdat2 = pd.DataFrame()
trimdat2['Name'] = ["Pb_ex" for i in range(len(ranges))]
trimdat2['Atom'] = 82
trimdat2['Energy'] = 102000
trimdat2['X'] = np.array(ranges.X)
trimdat2['Y'] = 0
trimdat2['Z'] = 0
trimdat2['Cos(X)'] = np.random.uniform(-1.,1.,size=len(trimdat2))
lat = np.sqrt(1.-trimdat2['Cos(X)']**2)
```

```
21  phi = np.random.uniform(0.,2.*np.pi,size=len(trimdat2))
22  trimdat2['Cos(Y)'] = lat*np.sin(phi)
23  trimdat2['Cos(Z)'] = lat*np.cos(phi)
24  trimdat2.to_csv('../EXPLANT_TRIM.DAT',sep=' ',line_terminator='\r\n',
25          index=False,float_format='%.7f',encoding='latin_1')
```

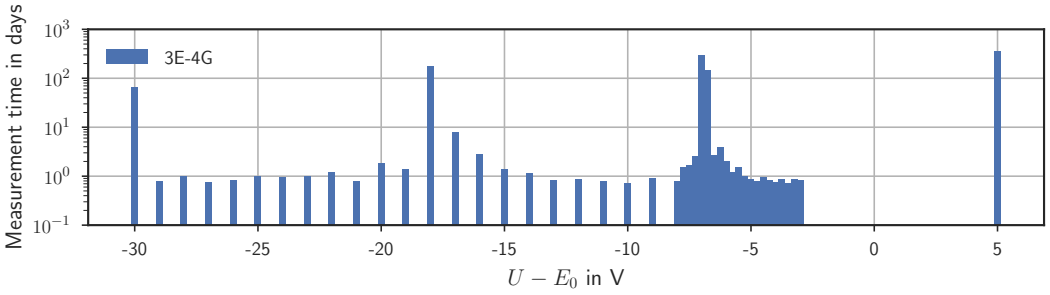
3E-4G
Measurement time in days
10^3
10^2
10^1
10^0
10^{-1}
-30
-25
-20
-15
-10
-5
0
5
$U - E_0$ in V

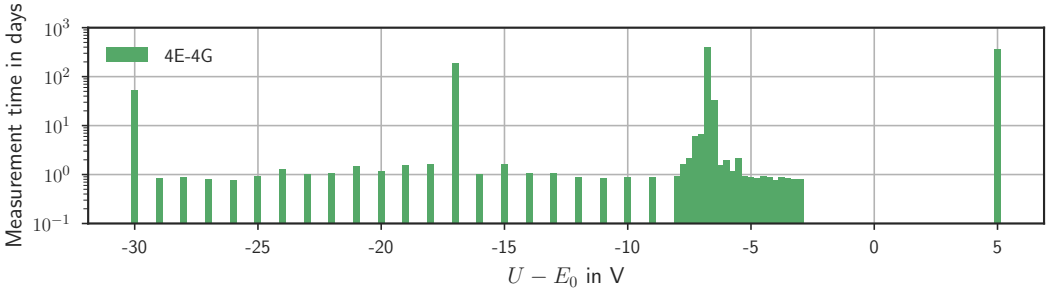
4E-4G
Measurement time in days
10^3
10^2
10^1
10^0
10^{-1}
-30
-25
-20
-15
-10
-5
0
5
$U - E_0$ in V

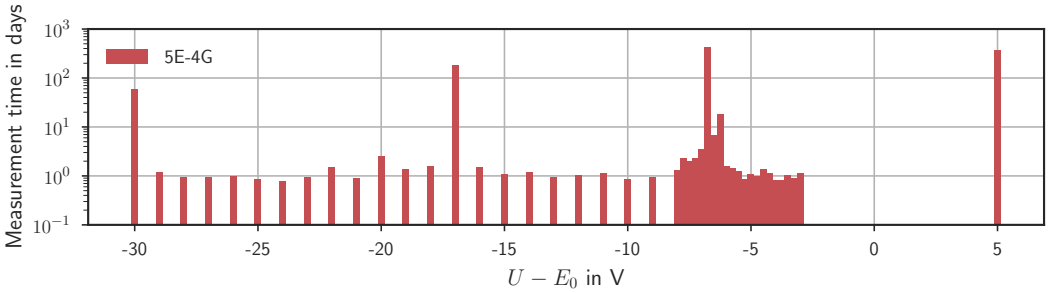
5E-4G
Measurement time in days
10^3
10^2
10^1
10^0
10^{-1}
-30
-25
-20
-15
-10
-5
0
5
$U - E_0$ in V

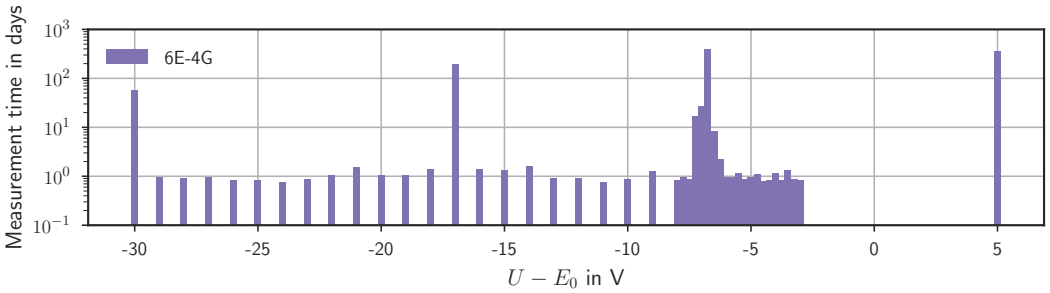
6E-4G
Measurement time in days
10^3
10^2
10^1
10^0
10^{-1}
-30
-25
-20
-15
-10
-5
0
5
$U - E_0$ in V

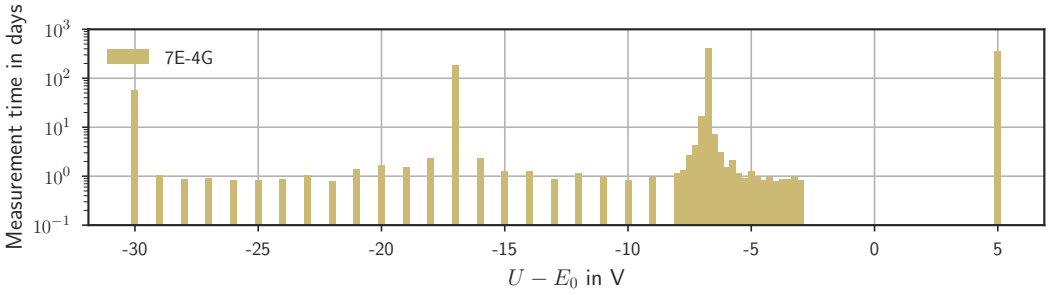
Measurement time in days
7E-4G
10^3
10^2
10^1
10^0
10^{-1}
-30
-25
-20
-15
-10
-5
0
5
$U - E_0$ in V

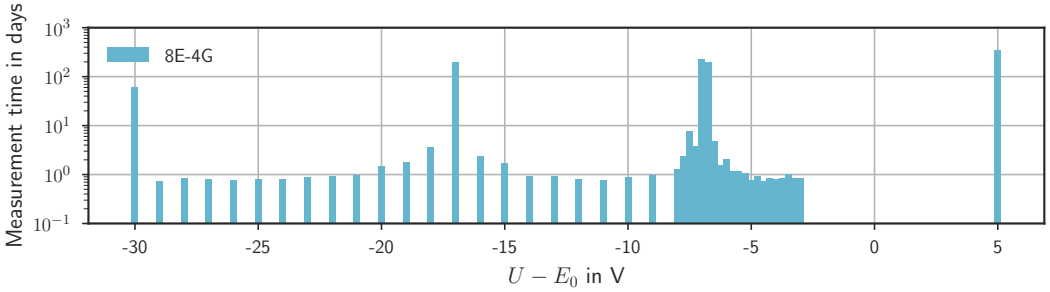
Measurement time in days
8E-4G
10^3
10^2
10^1
10^0
10^{-1}
-30
-25
-20
-15
-10
-5
0
5
$U - E_0$ in V

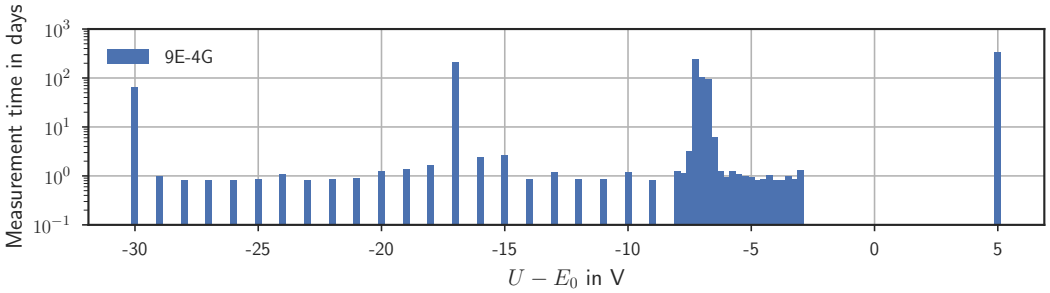
Measurement time in days
9E-4G
10^3
10^2
10^1
10^0
10^{-1}
-30
-25
-20
-15
-10
-5
0
5
$U - E_0$ in V

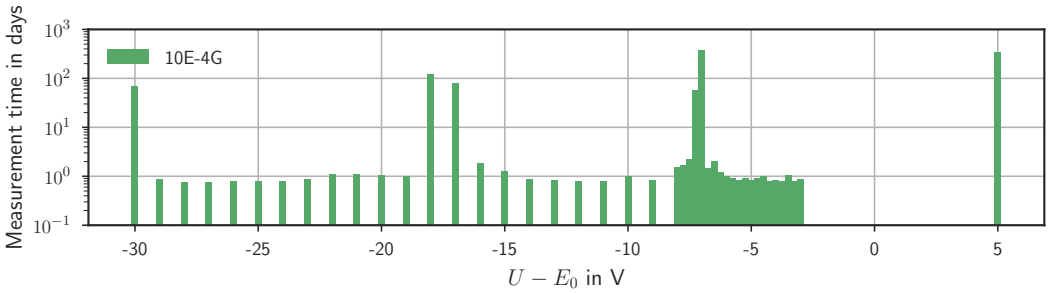
Measurement time in days
10E-4G
10^3
10^2
10^1
10^0
10^{-1}
-30
-25
-20
-15
-10
-5
0
5
$U - E_0$ in V

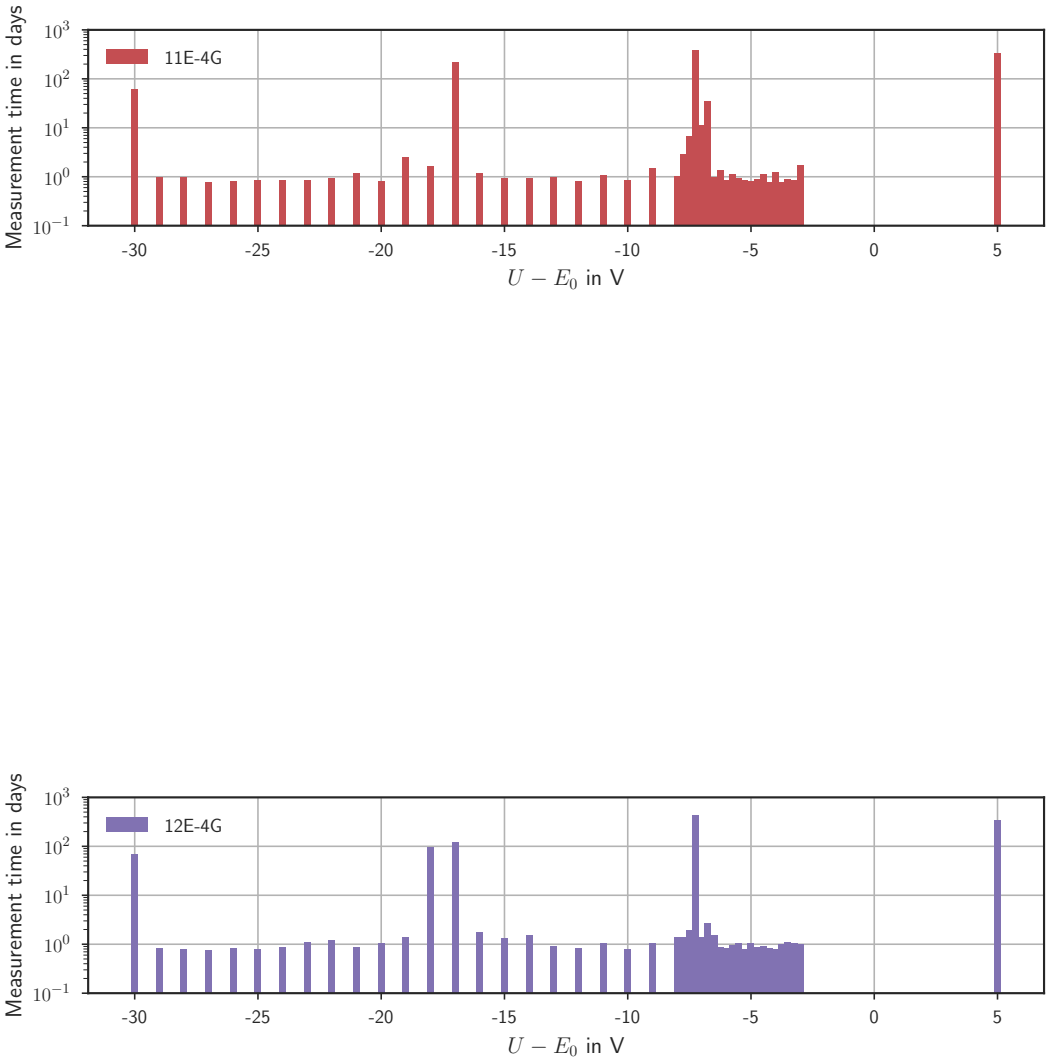

Figure 6.1: Measurement Time distribution

List of Figures

List of Tables

Bibliography

[1] Pauli, W.E.F.: *Offener Brief an die Gruppe der Radioaktiven bei der Gauvereinstagung zu Tübingen (datiert 4. Dez. 1930).* New York, NY : Interscience, 1964 (page 1)

[2] Chadwick, J: Intensitätsverteilung im magnetischen Spectrum der β-Strahlen von Radium B + C. In: *Verhandl. Dtsc. Phys. Ges.* 16 (1914), S. 383 (page 1)

[3] Scott, F. A.: Energy Spectrum of the Beta-Rays of Radium E. In: *Phys. Rev.* 48 (1935), Sep, 391–395. DOI: 10.1103/PhysRev.48.391 (page 1, 2)

[4] Chadwick, James: Possible existence of a neutron. In: *Nature* 129 (1932), Nr. 3252, 312. DOI: 10.1038/129312a0 (page 1)

[5] Fermi, E.: Versuch einer Theorie der β-Strahlen. In: *Zeitschrift für Physik* 88 (1934), Nr. 3–4, S. 161–177. DOI: 10.1007/BF01351864 (page 1, 20)

[6] Bethe, Hans ; Peierls, Rudolph: The "neutrino". In: *Nature* 133 (1934), Nr. 532, 689–690. DOI: 10.1038/133532a0 (page 2)

[7] Reines, F. ; Cowan, C.L.: Detection of the Free Neutrino. In: *Physical Review* 92 (1953), S. 830–831. DOI: 10.1103/PhysRev.92.830 (page 2)

[8] Reines, F. ; Cowan, C. L. ; Harrison, F. B. ; McGuire, A. D. ; Kruse, H. W.: Detection of the Free Antineutrino. In: *Physical Review* 117 (1960), Jan, 159–173. DOI: 10.1103/PhysRev.117.159 (page 2)

[9] Danby, G. ; Gaillard, J-M. ; Goulianos, K. ; Lederman, L. M. ; Mistry, N. ; Schwartz, M. ; Steinberger, J.: Observation of High-Energy Neutrino Reactions and the Existence of Two Kinds of Neutrinos. In: *Phys. Rev. Lett.* 9 (1962), Jul, 36–44. DOI: 10.1103/PhysRevLett.9.36 (page 3)

[10] Perl, M. L. ; Abrams, G. S. ; Boyarski, A. M. et al.: Evidence for Anomalous Lepton Production in $e^+ - e^-$ Annihilation. In: *Phys. Rev. Lett.* 35 (1975), Dec, 1489–1492. DOI: 10.1103/PhysRevLett.35.1489 (page 3)

[11] Kodama, K ; Ushida, N ; Andreopoulos, C ; Saoulidou, N ; Tzanakos, G ; Yager, P ; Baller, B ; Boehnlein, D ; Freeman, W ; Lundberg, B et al.: Observation of tau neutrino interactions. In: *Physics Letters B* 504 (2001), Nr. 3, 218 - 224. DOI: 10.1016/S0370-2693(01)00307-0. – ISSN 0370–2693 (page 3)

[12] Decamp, D ; Deschizeaux, B ; Lees, J-P ; Minard, M-N ; Crespo, JM ; Delfino, M ; Fernandez, E ; Martinez, M ; Miquel, R ; Mir, ML et al.: Determination of the number of light neutrino species. In: *Physics Letters B* 231 (1989), Nr. 4, 519 - 529. DOI: 10.1016/0370-2693(89)90704-1. – ISSN 0370–2693 (page 3)

[13] Decamp, D ; Deschizeaux, B ; Lees, J-P ; Minard, M-N ; Crespo, JM ; Delfino, M ; Fernandez, E ; Martinez, M ; Miquel, R ; Mir, Ll M. et al.: A precise determination of the number of families with light neutrinos and of the Z boson partial widths. In: *Physics Letters B* 235 (1990), Nr. 3, 399 - 411. DOI: 10.1016/0370-2693(90)91984-J. – ISSN 0370–2693 (page 3)

[14] Tanabashi, M: Review of particle physics. In: *Phys. Rev. D* 98 (2018), S. 030001 (page 3, 13, 153)

[15] Peskin, Michael E. ; Schroeder, Daniel V.: *An Introduction to quantum field theory*. Reading, USA: Addison-Wesley, 1995. – ISBN 9780201503975 (page 4)

[16] Glashow, Sheldon L.: Partial-symmetries of weak interactions. In: *Nuclear Physics* 22 (1961), Nr. 4, 579 - 588. DOI: 10.1016/0029-5582(61)90469-2. – ISSN 0029–5582 (page 4)

[17] Weinberg, Steven: A Model of Leptons. In: *Phys. Rev. Lett.* 19 (1967), Nov, 1264–1266. DOI: 10.1103/PhysRevLett.19.1264 (page 4)

[18] Salam, A ; Svartholm, N: Proc. 8th Nobel Symposium. In: *Stockholm, ed. N. Svartholm (Almqvist and Wiksells, Stockholm 1968)* (1968), S. 367 (page 4)

[19] Polchinski, Joseph G.: *String theory*. Cambridge university press, 2003. – ISBN 9780521633048 (page 4)

[20] Rovelli, Carlo: Loop Quantum Gravity. In: *Living Reviews in Relativity* 1 (1998), Nr. 1. DOI: 10.12942/lrr-1998-1 (page 4)

[21] Weinberg, Steven: Ultraviolet divergences in quantum theories of gravitation. In: *General relativity: an Einstein centenary survey* Bd. 1, 1979. – ISBN 0521222850, S. 790–831 (page 4)

[22] Fierz, Markus: Über die relativistische Theorie kräftefreier Teilchen mit beliebigem Spin. In: *Helv. Phys. Acta* 12 (1939), Nr. 3 (page 4)

[23] Pauli, W.: The Connection Between Spin and Statistics. In: *Phys. Rev.* 58 (1940), Oct, 716–722. DOI: 10.1103/PhysRev.58.716 (page 4)

[24] Wikimedia: *Particles of the Standard Model*. `https://commons.wikimedia.org/wiki/File:Standard_Model_of_Elementary_Particles.svg`. Version: 2006 (page 5, 151)

[25] Higgs, Peter W.: Broken Symmetries and the Masses of Gauge Bosons. In: *Phys. Rev. Lett.* 13 (1964), Oct, 508–509. DOI: 10.1103/PhysRevLett.13.508 (page 5)

[26] Englert, F. ; Brout, R.: Broken Symmetry and the Mass of Gauge Vector Mesons. In: *Phys. Rev. Lett.* 13 (1964), Aug, 321–323. DOI: 10.1103/PhysRevLett.13.321 (page 5)

[27] Aad, G ; Abajyan, T ; Abbott, B ; Abdallah, J ; Khalek, S A. ; Abdelalim, AA ; Abdinov, O ; Aben, R ; Abi, B ; Abolins, M et al.: Observation of a new particle in the search for the Standard Model Higgs boson with the ATLAS detector at the LHC. In: *Physics Letters B* 716 (2012), Nr. 1, 1 - 29. DOI: 10.1016/j.physletb.2012.08.020. – ISSN 0370–2693 (page 5)

[28] Chatrchyan, Serguei ; Khachatryan, V ; Sirunyan, AM ; Tumasyan, A ; Adam, W ; Bergauer, T ; Dragicevic, M ; Eroe, J ; Fabjan, C ; Friedl, M et al.: Combined results of searches for the standard model Higgs boson in pp collisions at $\sqrt{(s)} = 7$ TeV. In: *Physics Letters B* 710 (2012), Nr. 1, 26 - 48. DOI: 10.1016/j.physletb.2012.02.064. – ISSN 0370–2693 (page 5)

[29] Goldhaber, M. ; Grodzins, L. ; Sunyar, A. W.: Helicity of Neutrinos. In: *Phys. Rev.* 109 (1958), Feb, 1015–1017. DOI: 10.1103/PhysRev.109.1015 (page 6)

[30] Majorana, Ettore: Teoria simmetrica dell'elettrone e del positrone. In: *Il Nuovo Cimento (1924-1942)* 14 (1937), Nr. 4, 171. DOI: 10.1007/BF02961314. – ISSN 1827–6121 (page 6, 17)

[31] Krivosheina, I. V.: SN 1987 A — Historical View About Registration of the Neutrino Signal with BAKSAN, Kamiokande II, and IMB Detectors. In: Klapdor-Kleingrothaus, Hans V. (Hrsg.): *Beyond the Desert 2003*. Berlin, Heidelberg : Springer Berlin Heidelberg, 2004. – ISBN 978–3–642–18534–2, S. 685–709 (page 7)

[32] Brunner, Jürgen: ANTARES - Astronomie in der Tiefsee. In: *Sterne und Weltraum* (2006). `http://www.astronomie-heute.de/artikel/835876` (page 7)

[33] Bahcall, John N. ; Serenelli, Aldo M. ; Basu, Sarbani: New Solar Opacities, Abundances, Helioseismology, and Neutrino Fluxes. In: *The Astrophysical Journal Letters* 621 (2005), Nr. 1, L85. DOI: 10.1086/428929 (page 8)

[34] Davis, Raymond: A review of the Homestake solar neutrino experiment. In: *Progress in Particle and Nuclear Physics* 32 (1994), 13 - 32. DOI: 10.1016/0146-6410(94)90004-3. – ISSN 0146–6410 (page 7)

[35] Cleveland, B.T. ; Daily, T. ; Davis, R. ; Distel, J. ; Lande, K. ; Lee, C.K. ; Wildenhain, P. ; Ullman, J.: Update on the measurement of the solar neutrino flux with the Homestake chlorine detector. In: *Nuclear Physics B - Proceedings Supplements* 38 (1995), Nr. 1, 47 - 53. DOI: 10.1016/0920-5632(94)00732-B. – ISSN 0920–5632. – Neutrino 94 (page 7)

[36] Hampel, Wolfgang ; Handt, J ; Heusser, G ; Kiko, J ; Kirsten, T ; Laubenstein, M ; Pernicka, E ; Rau, W ; Wojcik, M ; Zakharov, Yu et al.: GALLEX solar neutrino observations: results for GALLEX IV. In: *Physics Letters B* 447 (1999), Nr. 1, 127 - 133. DOI: 10.1016/S0370-2693(98)01579-2. – ISSN 0370–2693 (page 8)

[37] Altmann, Michael ; Balata, M ; Belli, P ; Bellotti, E ; Bernabei, R ; Burkert, E ; Cattadori, C ; Cerulli, R ; Chiarini, M ; Cribier, M et al.: Complete results for five years of GNO solar neutrino observations. In: *Physics Letters B* 616 (2005), Nr. 3, 174 - 190. DOI: 10.1016/j.physletb.2005.04.068. – ISSN 0370–2693 (page 8)

[38] Abdurashitov, JN ; Veretenkin, EP ; Vermul, VM ; Gavrin, VN ; Girin, SV ; Gorbachev, VV ; Gurkina, PP ; Zatsepin, GT ; Ibragimova, TV ; Kalikhov, AV et al.: Solar neutrino flux measurements by the Soviet-American gallium experiment (SAGE) for half the 22-year solar cycle. In: *Journal of Experimental and Theoretical Physics* 95 (2002), Aug, Nr. 2, 181–193. DOI: 10.1134/1.1506424. – ISSN 1090–6509 (page 8)

[39] Fukuda, Y ; Hayakawa, T ; Inoue, K ; Ishihara, K ; Ishino, H ; Joukou, S ; Kajita, T ; Kasuga, S ; Koshio, Y ; Kumita, T et al.: Solar Neutrino Data Covering Solar Cycle 22. In: *Phys. Rev. Lett.* 77 (1996), Aug, 1683–1686. DOI: 10.1103/PhysRevLett.77.1683 (page 8)

[40] Gribov, V. ; Pontecorvo, B.: Neutrino astronomy and lepton charge. In: *Physics Letters B* 28 (1969), Nr. 7, 493 - 496. DOI: 10.1016/0370-2693(69)90525-5. – ISSN 0370–2693 (page 8, 9)

[41] Ahmad, QR ; Allen, RC ; Andersen, TC ; Anglin, JD ; Barton, JC ; Beier, EW ; Bercovitch, M ; Bigu, J ; Biller, SD ; Black, RA et al.: Direct Evidence for Neutrino Flavor Transformation from Neutral-Current Interactions in the Sudbury Neutrino Observatory. In: *Phys. Rev. Lett.* 89 (2002), Jun, 011301. DOI: 10.1103/PhysRevLett.89.011301 (page 9)

[42] Aharmim, B. ; Ahmad, Q. R. ; Ahmed, S. N. et al.: Determination of the ν_e and total ^{8}B solar neutrino fluxes using the Sudbury Neutrino Observatory Phase I data

set. In: *Phys. Rev. C* 75 (2007), Apr, 045502. DOI: 10.1103/PhysRevC.75.045502 (page 9)

[43] Cabibbo, Nicola: Unitary Symmetry and Leptonic Decays. In: *Phys. Rev. Lett.* 10 (1963), Jun, 531–533. DOI: 10.1103/PhysRevLett.10.531 (page 9, 21)

[44] Abe, Y. et al. (Double Chooz Collaboration): Reactor $\overline{\nu}_e$ disappearance in the Double Chooz experiment. In: *Physical Review D* 86 (2012), 052008. DOI: 10.1103/PhysRevD.86.052008 (page 11)

[45] An, F. P. et al. (Daya Bay Collaboration): Observation of Electron-Antineutrino Disappearance at Daya Bay. In: *Physical Review Letters* 108 (2012), 171803. DOI: 10.1103/PhysRevLett.108.171803 (page 11)

[46] Ahn, J. K. et al. (RENO Collaboration): Observation of Reactor Electron Antineutrinos Disappearance in the RENO Experiment. In: *Physical Review Letters* 108 (2012), 191802. DOI: 10.1103/PhysRevLett.108.191802 (page 11)

[47] Abe, K ; Abgrall, N ; Ajima, Y ; Aihara, H ; Albert, JB ; Andreopoulos, C ; Andrieu, B ; Aoki, S ; Araoka, O ; Argyriades, J et al.: Indication of Electron Neutrino Appearance from an Accelerator-Produced Off-Axis Muon Neutrino Beam. In: *Phys. Rev. Lett.* 107 (2011), Jul, 041801. DOI: 10.1103/PhysRevLett.107.041801 (page 12)

[48] Adamson, P ; Auty, DJ ; Ayres, DS ; Backhouse, C ; Barr, G ; Betancourt, M ; Bishai, M ; Blake, A ; Bock, GJ ; Boehnlein, DJ et al.: Improved Search for Muon-Neutrino to Electron-Neutrino Oscillations in MINOS. In: *Phys. Rev. Lett.* 107 (2011), Oct, 181802. DOI: 10.1103/PhysRevLett.107.181802 (page 12)

[49] Apollonio, M ; Baldini, A ; Bemporad, C ; Caffau, E ; Cei, F ; Declais, Y ; De Kerret, H ; Dieterle, B ; Etenko, A ; George, J et al.: Limits on neutrino oscillations from the CHOOZ experiment. In: *Physics Letters B* 466 (1999), Nr. 2, 415 - 430. DOI: 10.1016/S0370-2693(99)01072-2. – ISSN 0370–2693 (page 12)

[50] Wolfenstein, L.: Neutrino oscillations in matter. In: *Phys. Rev. D* 17 (1978), May, 2369–2374. DOI: 10.1103/PhysRevD.17.2369 (page 12)

[51] Mikheyev, S. P. ; Smirnov, A. Y.: Resonant amplification of ν oscillations in matter and solar-neutrino spectroscopy. In: *Il Nuovo Cimento C* 9 (1986), Jan, Nr. 1, 17–26. DOI: 10.1007/BF02508049. – ISSN 0390–5551 (page 12)

[52] Beringer, J. et al. (Particle Data Group): Review of Particle Physics. In: *Physical Review D* 86 (2012), 010001. DOI: 10.1103/PhysRevD.86.010001 (page)

[53] Altarelli, Guido ; Winter, Klaus: *Neutrino Mass*. Springer, 2003 (Springer Tracts in Modern Physics 190). DOI: 10.1007/b13585. – ISBN 978–3–540–40328–9 (page 13)

[54] KATRIN Collaboration: KATRIN design report 2004 / Forschungszentrum, Karlsruhe. Version: 2005. URN: nbn:de:0005-070907. 2005. (Wissenschaftliche Berichte. FZKA). – Forschungsbericht. – ISSN 0947–8620. – 51.54.01; LK 01; Auch: NPI ASCR Rez EXP-01/2005; MS-KP-0501 (page 15, 16, 25, 42, 81, 126)

[55] Einstein, Albert: Die formale Grundlage der allgemeinen Relativitätstheorie. In: *Sitzungsberichte der Königlich Preußischen Akademie der Wissenschaften (Berlin), Seite 1030-1085.* 1 (1914), S. 1030–1085. DOI: 10.1002/3527608958.ch2 (page 15)

[56] Einstein, Albert: Die Feldgleichungen der Gravitation. In: *Sitzungsberichte der Königlich Preußischen Akademie der Wissenschaften (Berlin), Seite 844-847.* 1 (1915), S. 844–847. DOI: 10.1002/3527608958.ch5 (page 15)

[57] Einstein, Albert: Die Grundlage der allgemeinen Relativitätstheorie. In: *Annalen der Physik* 354 (1916), Nr. 7, S. 769–822. DOI: 10.1002/andp.19163540702 (page 15)

[58] Einstein, Albert: Kosmologische betrachtungen zur allgemeinen Relativitätstheorie. In: *Sitzungsberichte der Königlich Preußischen Akademie der Wissenschaften (Berlin), Seite 142-152.* 1 (1917), 142–152. `http://adsabs.harvard.edu/abs/1917SPAW.....142E` (page 15)

[59] Rubin, V. C. ; Ford, W. K. J. ; . Thonnard, N.: Rotational properties of 21 SC galaxies with a large range of luminosities and radii, from NGC 4605 $R = 4$ kpc to UGC 2885 $R = 122$ kpc. In: *APJ* 238 (1980), Juni, S. 471–487. DOI: 10.1086/158003 (page 15)

[60] Fischer, Philippe ; McKay, Timothy A. ; Sheldon, Erin ; Connolly, Andrew ; Stebbins, Albert ; Frieman, Joshua A. ; Jain, Bhuvnesh ; Joffre, Michael ; Johnston, David ; Bernstein, Gary et al.: Weak Lensing with Sloan Digital Sky Survey Commissioning Data: The Galaxy-Mass Correlation Function to 1 h-1 Mpc. In: *The Astronomical Journal* 120 (2000), Nr. 3, 1198. DOI: 10.1086/301540 (page 15)

[61] Markevitch, M ; Randall, S ; Clowe, D ; Gonzalez, A ; Bradac, M: Dark matter and the bullet cluster. In: *36th COSPAR Scientific Assembly* Bd. 36, 2006, 2655 (page 15)

[62] Markevitch, M. ; Gonzalez, A. H. ; Clowe, D. ; Vikhlinin, A. ; Forman, W. ; Jones, C. ; Murray, S. ; Tucker, W.: Direct Constraints on the Dark Matter Self-Interaction Cross Section from the Merging Galaxy Cluster 1E 0657–56. In: *The Astrophysical Journal* 606 (2004), Nr. 2, 819. DOI: 10.1086/383178 (page 15)

[63] Penzias, Arno A. ; Wilson, Robert W.: A Measurement of Excess Antenna Temperature at 4080 Mc/s. In: *The Astrophysical Journal* 142 (1965), S. 419–421. DOI: 10.1086/148307 (page 16)

[64] Wright, EL ; Mather, JC ; Bennett, CL ; Cheng, ES ; Shafer, RA ; Fixsen, DJ ; Eplee Jr, RE ; Isaacman, RB ; Read, SM ; Boggess, NW et al.: Preliminary spectral observations of the Galaxy with a 7 deg beam by the Cosmic Background Explorer (COBE). In: *The Astrophysical Journal* 381 (1991), November, S. 200–209. DOI: 10.1086/170641 (page 16)

[65] Bennett, C. L. ; Larson, D. ; Weiland, J. L. ; Jarosik, N. ; Hinshaw, G. ; Odegard, N. ; Smith, K. M. ; Hill, R. S. ; Gold, B. ; Halpern, M. ; Komatsu, E. ; Nolta, M. R. ; Page, L. ; Spergel, D. N. ; Wollack, E. ; Dunkley, J. ; Kogut, A. ; Limon, M. ; Meyer, S. S. ; Tucker, G. S. ; Wright, E. L.: Nine-year Wilkinson Microwave Anisotropy Probe (WMAP) Observations: Final Maps and Results. In: *The Astrophysical Journal Supplement Series* 208 (2013), Nr. 2, 20. DOI: 10.1088/0067-0049/208/2/20 (page 16)

[66] Planck Collaboration ; Ade, P. A. R. et al.: Planck 2015 results - XIII. Cosmological parameters. In: *Astronomy and Astrophysics* 594 (2016), A13. DOI: 10.1051/0004-6361/201525830 (page 16)

[67] Planck Collaboration ; Aghanim, N. et al.: *Planck 2018 results. VI. Cosmological parameters.* 2018. – arXiv: 1807.06209 (page 16)

[68] Agarwal, Shankar ; Feldman, Hume A.: The effect of massive neutrinos on the matter power spectrum. In: *Monthly Notices of the Royal Astronomical Society* 410 (2011), Nr. 3, 1647-1654. DOI: 10.1111/j.1365-2966.2010.17546.x (page 16)

[69] Hannestad, S.: Neutrino Masses and the Dark Energy Equation of State:Relaxing the Cosmological Neutrino Mass Bound. In: *Phys. Rev. Lett.* 95 (2005), Nov, 221301. DOI: 10.1103/PhysRevLett.95.221301 (page 16)

[70] Elliott, S. R. ; Hahn, A. A. ; Moe, M. K.: Direct evidence for two-neutrino double-beta decay in ^{82}Se. In: *Phys. Rev. Lett.* 59 (1987), Nov, 2020–2023. DOI: 10.1103/PhysRevLett.59.2020 (page 17)

[71] Goeppert-Mayer, M.: Double Beta-Disintegration. In: *Phys. Rev.* 48 (1935), Sep, 512–516. DOI: 10.1103/PhysRev.48.512 (page 17)

[72] Racah, G.: Sulla Simmetria Tra Particelle e Antiparticelle. In: *Il Nuovo Cimento* 14 (1937), Jul, Nr. 7, 322. DOI: 10.1007/BF02961321. – ISSN 1827–6121 (page 17)

[73] Furry, W. H.: On Transition Probabilities in Double Beta-Disintegration. In: *Phys. Rev.* 56 (1939), Dec, 1184–1193. DOI: 10.1103/PhysRev.56.1184 (page 17)

[74] Klapdor-Kleingrothaus, HV ; Dietz, A ; Harney, HL ; Krivosheina, IV: Evidence for neutrinoless double beta decay. In: *Modern Physics Letters A* 16 (2001), Nr. 37, 2409-2420. DOI: 10.1142/S0217732301005825 (page 18)

[75] Agostini, M. ; Bakalyarov, A. M. ; Balata, M. ; Barabanov, I. ; Baudis, L. et al.: Improved Limit on Neutrinoless Double-β Decay of ^{76}Ge from GERDA Phase II. In: *Phys. Rev. Lett.* 120 (2018), Mar, 132503. DOI: 10.1103/PhysRevLett.120.132503 (page 18)

[76] Antonioli, Pietro ; Fienberg, Richard T. ; Fleurot, Fabrice ; Fukuda, Yoshiyuki ; Fulgione, Walter ; Habig, Alec ; Heise, Jaret ; McDonald, Arthur B. ; Mills, Corrinne ; Namba, Toshio ; Robinson, Leif J. ; Scholberg, Kate ; Schwendener, Michael ; Sinnott, Roger W. ; Stacey, Blake ; Suzuki, Yoichiro ; Tafirout, Réda ; Vigorito, Carlo ; Viren, Brett ; Virtue, Clarence ; Zichichi, Antonino: SNEWS: the SuperNova Early Warning System. In: *New Journal of Physics* 6 (2004), Nr. 1, 114. DOI: 10.1088/1367-2630/6/1/114 (page 18)

[77] Loredo, Thomas J. ; Lamb, Donald Q.: Bayesian analysis of neutrinos observed from supernova SN 1987A. In: *Phys. Rev. D* 65 (2002), Feb, 063002. DOI: 10.1103/PhysRevD.65.063002 (page 18)

[78] Acquafredda, R ; Adam, T ; Agafonova, N ; Sanchez, P A. ; Ambrosio, M ; Anokhina, A ; Aoki, S ; Ariga, A ; Ariga, T ; Arrabito, L ; Aufranc, C ; Autiero, D ; Badertscher, A ; Bagulya, A ; Baussan, E ; Bergnoli, A ; Greggio, F B. ; Bertolin, A et al.: The OPERA experiment in the CERN to Gran Sasso neutrino beam. In: *Journal of Instrumentation* 4 (2009), Nr. 04, P04018. DOI: 10.1088/1748-0221/4/04/P04018 (page 18)

[79] Adamson, P. et al.: Measurement of the Velocity of the Neutrino with MINOS. In: *44th Annual Precise Time and Time Interval (PTTI) Systems and Applications Meeting*, 2012, 119–132. – arXiv: 1408.6267 (page 18)

[80] The OPERA collaboration ; Adam, T. ; Agafonova, N. ; Aleksandrov, A. ; Altinok, O. ; Alvarez Sanchez, P. ; Anokhina, A. ; Aoki, S. ; Ariga, A. ; Ariga, T. ; Autiero, D. ; Badertscher, A. ; Ben Dhahbi, A. ; Bertolin, A. et al.: Measurement of the neutrino velocity with the OPERA detector in the CNGS beam. In: *Journal of High Energy Physics* 2012 (2012), Oct, Nr. 10, 93. DOI: 10.1007/JHEP10(2012)093. – ISSN 1029–8479 (page 18)

[81] Longo, Michael J.: Tests of relativity from SN1987A. In: *Phys. Rev. D* 36 (1987), Nov, 3276–3277. DOI: 10.1103/PhysRevD.36.3276 (page 18)

[82] Raffelt, Georg G.: Physics opportunities with supernova neutrinos. In: *Progress in Particle and Nuclear Physics* 64 (2010), Nr. 2, 393 - 399. DOI: 10.1016/j.ppnp.2009.12.057. – ISSN 0146–6410. – Neutrinos in Cosmology, in Astro, Particle and Nuclear Physics (page 19)

[83] Rujula, A. D. ; Lusignoli, M.: Calorimetric measurements of 163holmium decay as tools to determine the electron neutrino mass. In: *Physics Letters B* 118 (1982), Nr. 4, 429 - 434. DOI: 10.1016/0370-2693(82)90218-0. – ISSN 0370–2693 (page 19)

[84] Sisti, M ; Arnaboldi, C ; Brofferio, C ; Ceruti, G ; Cremonesi, O ; Fiorini, E ; Giuliani, A ; Margesin, B ; Martensson, L ; Nucciotti, A et al.: New limits from the Milano neutrino mass experiment with thermal microcalorimeters. In: *Nuclear Instruments and Methods in Physics Research Section A: Accelerators, Spectrometers, Detectors and Associated Equipment* 520 (2004), Nr. 1, 125 - 131. DOI: 10.1016/j.nima.2003.11.273. – ISSN 0168–9002. – Proceedings of the 10th International Workshop on Low Temperature Detectors (page 22)

[85] Gastaldo, L. ; Blaum, K. ; Doerr, A. ; Düllmann, Ch. E. ; Eberhardt, K. ; Eliseev, S. ; Enss, C. ; Faessler, Amand ; Fleischmann, A. ; Kempf, S. ; Krivoruchenko, M. ; Lahiri, S. ; Maiti, M. ; Novikov, Yu. N. ; Ranitzsch, P. C.-O. ; Simkovic, F. ; Szusc, Z. ; Wegner, M.: The Electron Capture ^{163}Ho Experiment ECHo. In: *Journal of Low Temperature Physics* 176 (2014), Sep, Nr. 5, 876–884. DOI: 10.1007/s10909-014-1187-4. – ISSN 1573–7357 (page 22)

[86] Alpert, B. ; Balata, M. ; Bennett, D. ; Biasotti, M. ; Boragno, C. ; Brofferio, C. ; Ceriale, V. ; Corsini, D. ; Day, P. K. ; De Gerone, M. ; Dressler, R. ; Faverzani, M. ; Ferri, E. ; Fowler, J. ; Gatti, F. ; Giachero, A. ; Hays-Wehle, J. et al.: HOLMES. In: *The European Physical Journal C* 75 (2015), Mar, Nr. 3, 112. DOI: 10.1140/epjc/s10052-015-3329-5. – ISSN 1434–6052 (page 22)

[87] Croce, M. P. ; Rabin, M. W. ; Mocko, V. ; Kunde, G. J. ; Birnbaum, E. R. ; Bond, E. M. ; Engle, J. W. ; Hoover, A. S. ; Nortier, F. M. ; Pollington, A. D. ; Taylor, W. A. ; Weisse-Bernstein, N. R. ; Wolfsberg, L. E. ; Hays-Wehle, J. P. ; Schmidt, D. R. ; Swetz, D. S. ; Ullom, J. N. ; Barnhart, T. E. ; Nickles, R. J.: Development of Holmium-163 Electron-Capture Spectroscopy with Transition-Edge Sensors. In: *Journal of Low Temperature Physics* 184 (2016), Aug, Nr. 3, 958–968. DOI: 10.1007/s10909-015-1451-2. – ISSN 1573–7357 (page 22)

[88] Monreal, Benjamin ; Formaggio, Joseph A.: Relativistic cyclotron radiation detection of tritium decay electrons as a new technique for measuring the neutrino mass. In: *Phys. Rev. D* 80 (2009), Sep, 051301. DOI: 10.1103/PhysRevD.80.051301 (page 22)

[89] Asner, D. M. ; Bradley, R. F. ; Viveiros, L. de ; Doe, P. J. ; Fernandes, J. L. ; Fertl, M. ; Finn, E. C. ; Formaggio, J. A. ; Furse, D. ; Jones, A. M. ; Kofron, J. N. ; LaRoque, B. H. ; Leber, M. ; McBride, E. L. ; Miller, M. L. ; Mohanmurthy, P. ; Monreal, B. ; Oblath, N. S. ; Robertson, R. G. H. ; Rosenberg, L. J. ; Rybka, G. ; Rysewyk, D. ; Sternberg, M. G. ; Tedeschi, J. R. ; Thümmler, T. ; VanDevender, B. A. ; Woods, N. L.: Single-Electron Detection and Spectroscopy via Relativistic Cyclotron Radiation. In: *Phys. Rev. Lett.* 114 (2015), Apr, 162501. DOI: 10.1103/PhysRevLett.114.162501 (page 22)

[90] Esfahani, Ali A. ; Asner, David M. ; Böser, Sebastian ; Cervantes, Raphael ; Claessens, Christine ; Viveiros, Luiz de ; Doe, Peter J. ; Doeleman, Shepard

; Fernandes, Justin L. ; Fertl, Martin ; Finn, Erin C. ; Formaggio, Joseph A. ; Furse, Daniel et al.: Determining the neutrino mass with cyclotron radiation emission spectroscopy—Project 8. In: *Journal of Physics G: Nuclear and Particle Physics* 44 (2017), Nr. 5, 054004. DOI: 10.1088/1361-6471/aa5b4f (page 22)

[91] Kraus, C. ; Bornschein, B. ; Bornschein, L. ; Bonn, J. ; Flatt, B. ; Kovalik, A. ; Ostrick, B. ; Otten, E.W. ; Schall, J.P. ; Thümmler, T. ; Weinheimer, C.: Final results from phase II of the Mainz neutrino mass search in tritium β decay. In: *The European Physical Journal C - Particles and Fields* 40 (2005), Nr. 4, S. 447–468. DOI: 10.1140/epjc/s2005-02139-7 (page 22, 25)

[92] Aseev, V.N. ; Belesev, A.I. ; Berlev, A.I. ; Geraskin, E.V. ; Golubev, A.A. ; Likhovid, N.A. ; Lobashev, V.M. ; Nozik, A.A. ; Pantuev, V.S. ; Parfenov, V.I. ; Skasyrskaya, A.K. ; Tkachov, F.V. ; Zadorozhny, S.V.: Upper limit on the electron antineutrino mass from the Troitsk experiment. In: *Physical Review D* 84 (2011), S. 112003. DOI: 10.1103/PhysRevD.84.112003 (page 22, 52)

[93] Otten, E.W. ; Weinheimer, C.: Neutrino mass limit from tritium β decay. In: *Reports on Progress in Physics* 71 (2008), Nr. 8, S. 086201. DOI: 10.1088/0034-4885/71/8/086201 (page 23)

[94] Robertson, R. G. H. ; Bowles, T. J. ; Stephenson, G. J. ; Wark, D. L. ; Wilkerson, J. F. ; Knapp, D. A.: Limit on ν_e mass from observation of the β decay of molecular tritium. In: *Phys. Rev. Lett.* 67 (1991), Aug, 957–960. DOI: 10.1103/PhysRevLett.67.957 (page 23, 25)

[95] Holzschuh, E. ; Fritschi, M. ; Kündig, W.: Measurement of the electron neutrino mass from tritium β-decay. In: *Physics Letters B* 287 (1992), Nr. 4, 381 - 388. DOI: 10.1016/0370-2693(92)91000-Y. – ISSN 0370–2693 (page 23, 25)

[96] Kawakami, H. ; Kato, S. ; Ohshima, T. ; Shibata, S. ; Ukai, K. ; Morikawa, N. ; Nogawa, N. ; Haga, K. ; Nagafuchi, T. ; Shigeta, M. ; Fukushima, Y. ; Taniguchi, T.: New upper bound on the electron anti-neutrino mass. In: *Physics Letters B* 256 (1991), Nr. 1, 105 - 111. DOI: 10.1016/0370-2693(91)90226-G. – ISSN 0370–2693 (page 23, 25)

[97] Stoeffl, Wolfgang ; Decman, Daniel J.: Anomalous Structure in the Beta Decay of Gaseous Molecular Tritium. In: *Phys. Rev. Lett.* 75 (1995), Oct, 3237–3240. DOI: 10.1103/PhysRevLett.75.3237 (page 23, 25)

[98] The KATRIN Collaboration ; Arenz, M et al.: First transmission of electrons and ions through the KATRIN beamline. In: *Journal of Instrumentation* 13 (2018), Nr. 04, P04020. DOI: 10.1088/1748-0221/13/04/P04020 (page 25)

[99] Bonn, J. ; Bornschein, B. ; Bornschein, L. ; Fickinger, L. ; Flatt, B. ; Kazachenko, O. ; Kovalik, A. ; Kraus, Ch. ; Otten, E.W. ; Schall, J.P. ; Ulrich, H. ; Weinheimer, Ch.: The Mainz neutrino mass experiment. In:

Nuclear Physics B - Proceedings Supplements 91 (2001), Nr. 1, 273 - 279. DOI: 10.1016/S0920-5632(00)00951-8. – ISSN 0920–5632. – Neutrino 2000 (page 25)

[100] Lobashev, VM ; Aseev, VN ; Belesev, AI ; Berlev, AI ; Geraskin, EV ; Golubev, AA ; Kazachenko, OV ; Kuznetsov, Yu E. ; Ostroumov, RP ; Rivkis, LA et al.: Direct search for mass of neutrino and anomaly in the tritium beta-spectrum. In: *Physics Letters B* 460 (1999), Nr. 1, 227 - 235. DOI: 10.1016/S0370-2693(99)00781-9. – ISSN 0370–2693 (page 25)

[101] Lobashev, V.M ; Aseev, V.N ; Belesev, A.I ; Berlev, A.I ; Geraskin, E.V ; Golubev, A.A ; Kazachenko, O.V ; Kuznetsov, Yu.E ; Ostroumov, R.P ; Rivkis, L.A ; Stern, B.E ; Titov, N.A ; Zadoroghny, C.V ; Zakharov, Yu.I: Direct search for neutrino mass and anomaly in the tritium beta-spectrum: Status of "Troitsk neutrino mass" experiment. In: *Nuclear Physics B - Proceedings Supplements* 91 (2001), Nr. 1, 280 - 286. DOI: 10.1016/S0920-5632(00)00952-X. – ISSN 0920–5632. – Neutrino 2000 (page 25)

[102] Picard, A. ; Backe, H. ; Barth, H. ; Bonn, J. ; Degen, B. ; Edling, Th. ; Haid, R. ; Hermanni, A. ; Leiderer, P. ; Loeken, Th. ; Molz, A. ; Moore, R.B. ; Osipowicz, A. ; Otten, E.W. ; Przyrembel, M. ; Schrader, M. ; Steininger, M. ; Weinheimer, C.: A solenoid retarding spectrometer with high resolution and transmission for keV electrons. In: *Nuclear Instruments and Methods in Physics Research Section B: Beam Interactions with Materials and Atoms* 63 (1992), Nr. 3, S. 345–358. DOI: 10.1016/0168-583X(92)95119-C (page 26)

[103] Higaki, H. ; Ito, K. ; Kira, K. ; Okamoto, H.: Electrons Confined with an Axially Symmetric Magnetic Mirror Field. In: *AIP Conference Proceedings* 1037 (2008), Nr. 1, 106-114. DOI: 10.1063/1.2977830 (page 27)

[104] Wandkowsky, Nancy: *Study of background and transmission properties of the KATRIN spectrometers*, Karlsruher Institut für Technologie (KIT), Diss., 2013. URN: nbn:de:swb:90-366316 (page 30, 41, 52, 69, 93)

[105] Babutzka, M. ; Bahr, M. ; Bonn, J. ; Bornschein, B. ; Dieter, A. ; Drexlin, G. ; Eitel, K. ; Fischer, S. ; Glück, F. ; Grohmann, S. ; Hötzel, M. ; James, T.M. ; Käfer, W. ; Leber, M. ; Monreal, B. ; Priester, F. ; Röllig, M. ; Schlösser, M. ; Schmitt, U. ; Sharipov, F. ; Steidl, M. ; Sturm, M. ; Telle, H.H. ; Titov, N.: Monitoring of the operating parameters of the KATRIN Windowless Gaseous Tritium Source. In: *New Journal of Physics* 14 (2012), Nr. 10, S. 103046. DOI: 10.1088/1367-2630/14/10/103046 (page 30, 33)

[106] Sturm, Michael: *Aufbau und Test des Inner-Loop-Systems der Tritiumquelle von KATRIN*, Karlsruher Institut für Technologie (KIT), Diss., 2010. URN: nbn:de:swb:90-193551 (page 32)

[107] Grohmann, S. ; Bode, T. ; Schön, H. ; Süsser, M.: Precise temperature measurement at 30 K in the KATRIN source cryostat. In: *Cryogenics* 51 (2011), Nr. 8, S. 438–445. DOI: 10.1016/j.cryogenics.2011.05.001 (page 32)

[108] Bode, T.: *Optimierung des 2-Phasen-Kühlkonzepts für den WGTS-Demonstrator von KATRIN*, Karlsruher Institut für Technologie (KIT), Diploma Thesis, 2011 (page 32)

[109] Grohmann, S.: Stability analyses of the beam tube cooling system in the KATRIN source cryostat. In: *Cryogenics* 49 (2009), Nr. 8, S. 413–420. DOI: 10.1016/j.cryogenics.2009.06.001 (page 32)

[110] Hackenjos, Moritz T.: *KATRIN "First Light" - Commissioning and Modelling of the Beamline*, Karlsruher Institut für Technologie (KIT), Diss., 2017. DOI: 10.5445/IR/1000078933 (page 32)

[111] Hötzel, Markus: *Simulation and analysis of source-related effects for KATRIN*, Karlsruher Institut für Technologie (KIT), Diss., 2012. URN: nbn:de:swb:90-312594 (page 32, 56, 76)

[112] Schlösser, Magnus ; Seitz, Hendrik ; Rupp, Simone ; Herwig, Philipp ; Alecu, Catalin G. ; Sturm, Michael ; Bornschein, Beate: In-Line Calibration of Raman Systems for Analysis of Gas Mixtures of Hydrogen Isotopologues with Sub-Percent Accuracy. In: *Analytical Chemistry* 85 (2013), Nr. 5, 2739-2745. DOI: 10.1021/ac3032433. – PMID: 23320553 (page 32)

[113] Schlösser, M. ; Rupp, S. ; Seitz, H. ; Fischer, S. ; Bornschein, B. ; James, T.M. ; Telle, H.H.: Accurate calibration of the laser Raman system for the Karlsruhe Tritium Neutrino Experiment. In: *Journal of Molecular Structure* 1044 (2013), Nr. 0, S. 61–66. DOI: 10.1016/j.molstruc.2012.11.022 (page 32)

[114] Roellig, Marco: *Studien zu einem Röntgendetektorsystem zur Überwachung der KATRIN Tritiumquelle*, Karlsruher Institut für Technologie (KIT), Diploma Thesis, 2011. `http://www.katrin.kit.edu/publikationen/dth_m_roellig.pdf` (page 32)

[115] Kosmider, Andreas: *Tritium Retention Techniques in the KATRIN Transport Section and Commissioning of its DPS2-F Cryostat*, Karlsruher Institut für Technologie (KIT), Diss., 2012. URN: nbn:de:swb:90-289595 (page 33, 35)

[116] Mertens, S. ; Drexlin, G. ; Fränkle, F.M. ; Furse, D. ; Glück, F. ; Görhardt, S. ; Hötzel, M. ; Käfer, W. ; Leiber, B. ; Thümmler, T. ; Wandkowsky, N. ; Wolf, J.: Background due to stored electrons following nuclear decays in the KATRIN spectrometers and its impact on the neutrino mass sensitivity. In: *Astroparticle Physics* 41 (2013), S. 52–62. DOI: 10.1016/j.astropartphys.2012.10.005 (page 33)

[117] Luo, X. ; Day, Chr. ; Hauer, V. ; Malyshev, O.B. ; Reid, R.J. ; Sharipov, F.: Monte Carlo simulation of gas flow through the KATRIN DPS2-F differential pumping system. In: *Vacuum* 80 (2006), Nr. 8, S. 864–869. DOI: 10.1016/j.vacuum.2005.11.044 (page 34)

[118] Ubieto Díaz, Marta: *Off-line commissioning of a non-destructive FT-ICR detection system for monitoring the ion concentration in the KATRIN beamline*, Ruperto-Carola University of Heidelberg, Diss., 2011. URN: nbn:de:bsz:16-opus-129425 (page 34)

[119] Ubieto-Díaz, M. ; Rodríguez, D. ; Lukic, S. ; Nagy, S. ; Stahl, S. ; Blaum, K.: A broad-band FT-ICR Penning trap system for KATRIN. In: *International Journal of Mass Spectrometry* 288 (2009), Nr. 1–3, S. 1–5. DOI: 10.1016/j.ijms.2009.07.003 (page 34)

[120] Windberger, Alexander: *Berechnungen und Simulationen zum Verhalten von Ionen in der differenziellen Pumpstrecke des KATRIN-Experiments*, Karlsruher Institut für Technologie (KIT), Diploma Thesis, 2011. `http://www.katrin.kit.edu/publikationen/dth-windberger.pdf` (page 34)

[121] Reimer, Stefan: *Ein elektrostatisches Dipolsystem zur Eliminierung von Ionen in der DPS2-F des KATRIN Experimentes*, Karlsruher Institut für Technologie (KIT), Diploma Thesis, 2009. `http://www.katrin.kit.edu/publikationen/dth-reimer.pdf` (page 34)

[122] Luo, X. ; Day, C.: Test particle Monte Carlo study of the cryogenic pumping system of the Karlsruhe tritium neutrino experiment. In: *Journal of Vacuum Science & Technology A* 26 (2008), Nr. 5, S. 1319–1325. DOI: 10.1116/1.2956628 (page 34)

[123] Prall, M. ; Renschler, P. ; Glück, F. ; Beglarian, A. ; Bichsel, H. ; Bornschein, L. ; Chaoui, Z. ; Drexlin, G. ; Fränkle, F.M. ; Görhardt, S. ; Mertens, S. ; Steidl, M. ; Thümmler, T. ; Wüstling, S. ; Weinheimer, C. ; Zadorozhny, S.: The KATRIN pre-spectrometer at reduced filter energy. In: *New Journal of Physics* 14 (2012), Nr. 7, S. 073054. DOI: 10.1088/1367-2630/14/7/073054 (page 36)

[124] Behrens, Jan D.: *Design and commissioning of a mono-energetic photoelectron source and active background reduction by magnetic pulse at the KATRIN spectrometers*, Westfälische Wilhelms-Universität Münster, Diss., 2016. `https://www.katrin.kit.edu/publikationen/phd_behrens.pdf` (page 36, 43, 93, 119, 126)

[125] Hilk, Daniel Franz R.: *Electric field simulations and electric dipole investigations at the KATRIN main spectrometer*, Karlsruher Institut für Technologie (KIT), Diss., 2017. DOI: 10.5445/IR/1000065869 (page 36, 43, 44, 93, 128)

[126] Mertens, Susanne: *Study of Background Processes in the Electrostatic Spectrometers of the KATRIN experiment*, Karlsruher Institut für Technologie (KIT), Diss., 2012. URN: nbn:de:swb:90-270589 (page 36, 69, 92, 93, 126)

[127] Görhardt, Stefan: *Background Reduction Methods and Vacuum Technology at the KATRIN Spectrometers*, Karlsruher Institut für Technologie (KIT), Diss., 2014. `http://nbn-resolving.org/urn:nbn:de:swb:90-380506` (page 36)

[128] Glück, F. ; Drexlin, G. ; Leiber, B. ; Mertens, S. ; Osipowicz, A. ; Reich, J. ; Wandkowsky, N.: Electromagnetic design of the large-volume air coil system of the KATRIN experiment. In: *New Journal of Physics* 15 (2013), Nr. 8, S. 083025. DOI: 10.1088/1367-2630/15/8/083025 (page 37)

[129] Erhard, M. ; Behrens, J. ; Bauer, S. ; Beglarian, A. ; Berendes, R. ; Drexlin, G. ; Glück, F. ; Gumbsheimer, R. ; Hergenhan, J. ; Leiber, B. ; Mertens, S. ; Osipowicz, A. ; Plischke, P. ; Reich, J. ; Thümmler, T. ; Wandkowsky, N. ; Weinheimer, C. ; Wüstling, S.: Technical design and commissioning of the KATRIN large-volume air coil system. In: *Journal of Instrumentation* 13 (2018), Nr. 02, P02003. DOI: 10.1088/1748-0221/13/02/P02003 (page 37)

[130] Valerius, K.: The wire electrode system for the KATRIN main spectrometer. In: *Progress in Particle and Nuclear Physics* 64 (2010), Nr. 2, 291 - 293. DOI: 10.1016/j.ppnp.2009.12.032. – ISSN 0146–6410 (page 37)

[131] Valerius, K.: Electromagnetic design and inner electrode for the KATRIN main spectrometer. In: *Progress in Particle and Nuclear Physics* 57 (2006), Nr. 1, 58 - 60. DOI: 10.1016/j.ppnp.2005.11.011. – ISSN 0146–6410. – International Workshop of Nuclear Physics 27th course (page 37, 92)

[132] Zacher, Michael: *Electromagnetic design and field emission studies for the inner electrode system of the KATRIN main spectrometer*, Westfälische Wilhelms-Universität Münster, Diploma Thesis, 2009. `http://www.uni-muenster.de/Physik.KP/AGWeinheimer/theses/Diplom_Michael_Zacher.pdf` (page 38)

[133] Valerius, Kathrin: *Spectrometer-related background processes and their suppression in the KATRIN experiment*, Westfälische Wilhelms-Universität Münster, Diss., 2009. `http://nbn-resolving.de/urn:nbn:de:hbz:6-28479494638` (page 38)

[134] Wolf, J.: Size Matters: The Vacuum System of the KATRIN Neutrino Experiment. In: *Journal of the Vacuum Society of Japan* 52 (2009), Nr. 5, S. 278–284. DOI: 10.3131/jvsj2.52.278 (page 38)

[135] Luo, X. ; Bornschein, L. ; Day, Ch. ; Wolf, J.: KATRIN NEG pumping concept investigation. In: *Vacuum* 81 (2007), Nr. 6, S. 777–781. DOI: 10.1016/j.vacuum.2005.11.053 (page 38)

[136] Day, Ch. ; Luo, X. ; Conte, A. ; Bonucci, A. ; Manini, P.: Determination of the sticking probability of a Zr–V–Fe nonevaporable getter strip. In: *Journal of Vacuum Science & Technology A: Vacuum, Surfaces, and Films* 25 (2007), Nr. 4, 824-830. DOI: 10.1116/1.2748799 (page 38)

[137] The KATRIN Collaboration ; Arenz, M et al.: Commissioning of the vacuum system of the KATRIN Main Spectrometer. In: *Journal of Instrumentation* 11 (2016), Nr. 04, P04011. DOI: 10.1088/1748-0221/11/04/P04011 (page 38)

[138] Zbořil, Miroslav: *Solid electron sources for the energy scale monitoring in the KATRIN experiment*, Westfälische Wilhelms-Universität Münster, Diss., 2011. URN: nbn:de:hbz:6-91469497689 (page 38)

[139] Slezak, Martin ; Vénos, Drahoslav: *Monitoring of the energy scale in the KATRIN neutrino experiment*, Charles University in Prague, Diss., Dec 2015. `http://hdl.handle.net/20.500.11956/77972` (page 38)

[140] Erhard, Moritz: *Untersuchung der Langzeitstabilität des nuklearen Standards für die Energieskala des KATRIN-Experiments*, Karlsruher Institut für Technologie (KIT), Diploma Thesis, 2012. `http://www.katrin.kit.edu/publikationen/dth-erhard.pdf` (page 38, 39)

[141] Slezák, Martin: *The source of monoenergetic electrons for the monitoring of spectrometer in the KATRIN neutrino experiment*, Charles University in Prague, Diploma Thesis, 2011. `http://www.katrin.kit.edu/publikationen/dth-slezak.pdf` (page 38)

[142] Goullon, Johannes D.: *Installation and commissioning of the monitor spectrometer*, Karlsruher Institut für Technologie (KIT), Diploma Thesis, 2010. `http://www.katrin.kit.edu/publikationen/dth-goullon.pdf` (page 38)

[143] Schupp, Michael: *Inbetriebnahme des Monitorspektrometers und erste Messungen*, Karlsruher Institut für Technologie (KIT), Diploma Thesis, 2011. `http://www.katrin.kit.edu/downloads/dth-schupp.pdf` (page 38)

[144] Bauer, Stephan: *Aufbau und Inbetriebnahme des zweiten Präzisions-Hochspannungsteilers bis 65 kV für das KATRIN-Experiment*, Westfälische Wilhelms-Universität Münster, Diploma Thesis, 2010. `http://www.uni-muenster.de/Physik.KP/AGWeinheimer/theses/Diplom_Stephan_Bauer.pdf` (page 38)

[145] The KATRIN Collaboration ; Arenz, M et al.: Calibration of high voltages at the ppm level by the difference of ^{83m}Kr conversion electron lines at the KATRIN experiment. In: *The European Physical Journal C* 78 (2018), May, Nr. 5, 368. DOI: 10.1140/epjc/s10052-018-5832-y. – ISSN 1434–6052 (page 38)

[146] Amsbaugh, J.F. et al.: Focal-plane detector system for the KATRIN experiment. In: *Nuclear Instruments and Methods in Physics Research Section A: Accelerators, Spectrometers, Detectors and Associated Equipment* 778 (2015), S. 40–60. DOI: 10.1016/j.nima.2014.12.116 (page 39)

[147] Harms, Fabian: *Assembly and First Results of the KATRIN Focal-Plane Detector System at KIT*, Karlsruher Institut für Technologie (KIT), Diploma Thesis, 2012. `http://www.katrin.kit.edu/publikationen/dth_Fabian_Harms.pdf` (page 40)

[148] Görhardt, Stefan: *Reduktion der durch Radon induzierten Untergrundprozesse in den KATRIN Spektrometern*, Karlsruher Institut für Technologie (KIT), Diploma Thesis, 2010. `http://www.katrin.kit.edu/publikationen/dth-goerhardt.pdf` (page 41)

[149] Fränkle, F.M. ; Bornschein, L. ; Drexlin, G. ; Glück, F. ; Görhardt, S. ; Käfer, W. ; Mertens, S. ; Wandkowsky, N. ; Wolf, J.: Radon induced background processes in the KATRIN pre-spectrometer. In: *Astroparticle Physics* 35 (2011), Nr. 3, S. 128–134. DOI: 10.1016/j.astropartphys.2011.06.009 (page 41)

[150] Mertens, S. ; Beglarian, A. ; Bornschein, L. ; Drexlin, G. ; Fränkle, F.M. ; Furse, D. ; Glück, F. ; Görhardt, S. ; Krömer, O. ; Leiber, B. ; Schlösser, K. ; Thümmler, T. ; Wandkowsky, N. ; Wüstling, S.: Stochastic Heating by ECR as a Novel Means of Background Reduction in the KATRIN spectrometers. In: *Journal of Instrumentation* 7 (2012), S. P08025. DOI: doi:10.1088/1748-0221/7/08/P08025 (page 41)

[151] Wandkowsky, N. ; Drexlin, G. ; Fränkle, F.M. ; Glück, F. ; Groh, S. ; Mertens, S.: Validation of a model for radon-induced background processes in electrostatic spectrometers. In: *Journal of Physics G: Nuclear and Particle Physics* 40 (2013), Nr. 8, S. 085102. DOI: 10.1088/0954-3899/40/8/085102 (page 41)

[152] Kleesiek, Marco: *A Data-Analysis and Sensitivity-Optimization Framework for the KATRIN Experiment*, Karlsruher Institut für Technologie (KIT), Diss., 2014. URN: nbn:de:swb:90-433013 (page 42, 43, 56, 126, 127)

[153] Kleesiek, M. ; Behrens, J. ; Drexlin, G. ; Eitel, K. ; Erhard, M. ; Formaggio, J. A. ; Glück, F. ; Groh, S. ; Hötzel, M. ; Mertens, S. ; Poon, A. W. P. ; Weinheimer, C. ; Valerius, K.: *β-Decay Spectrum, Response Function and Statistical Model for Neutrino Mass Measurements with the KATRIN Experiment.* 2018. – arXiv:1806.00369 (page 42, 43, 55, 67, 126)

[154] Furse, Daniel ; Groh, Stefan ; Trost, Nikolaus ; Babutzka, Martin ; Barrett, John ; Behrens, Jan ; Buzinsky, Nicholas ; Corona, Thomas ; Enomoto, Sanshiro ; Erhard, Moritz ; Formaggio, Joseph ; Glueck, Ferenc ; Harms, Fabian ; Heizmann, Florian ; Hilk, Daniel ; Käfer, Wolfgang

; Kleesiek, Marco ; Leiber, Benjamin ; Mertens, Susanne ; Oblath, Noah ; Renschler, Pascal ; Schwarz, Johannes ; Slocum, Penny ; Wandkowsky, Nancy ; Wierman, Kevin ; Zacher, Michael: Kassiopeia: A modern, extensible C++ particle tracking package. In: *New Journal of Physics* (2017). DOI: 10.1088/1367-2630/aa6950 (page 43, 50, 69, 71, 72)

[155] Furse, Daniel: *Techniques for direct neutrino mass measurement utilizing tritium β-decay*, Massachusetts Institute of Technology, Diss., 2015. `http://hdl.handle.net/1721.1/99313` (page 43, 48)

[156] Groh, Stefan: *Modeling of the response function and measurement of transmission properties of the KATRIN experiment*, Karlsruher Institut für Technologie (KIT), Diss., 2015. URN: nbn:de:swb:90-465464 (page 43, 52, 56, 60, 67, 69, 71, 76, 116, 126)

[157] Corona, Thomas J.: *Tools for Electromagnetic Field Simulation in the KATRIN Experiment*, Massachusetts Institute of Technology, Master Thesis, 2009. `http://www.katrin.kit.edu/publikationen/mth-corona.pdf` (page 43, 44)

[158] Barrett, John P.: *A spatially resolved study of the KATRIN main spectrometer using a novel fast multipole method*, Massachusetts Institute of Technology, Diss., 2017. `http://hdl.handle.net/1721.1/114314` (page 43, 85)

[159] Poljak, Dragan ; Brebbia, Carlos A.: *Boundary element methods for electrical engineers*. Bd. 4. WIT Press, 2005. – ISBN 978–1–84564–033–0 (page 44)

[160] Glück, Ferenc: Axisymmetric electric field calculation with zonal harmonic expansion. In: *Progress In Electromagnetics Research B* 32 (2011), 319–350. DOI: 10.2528/PIERB11042106 (page 44)

[161] Formaggio, J.A. ; Lazic, P. ; Corona, T.J. ; Stefancic, H. ; Abraham, H. ; Glück, F.: Solving for micro- and macro-scale electrostatic configurations using the robin hood algorithm. In: *Progress In Electromagnetics Research B* 39 (2012), S. 1–37. DOI: 10.2528/PIERB11112106 (page 45)

[162] Renschler, Pascal: *KESS - A new Monte Carlo simulation code for low-energy electron interactions in silicon detectors*, Karlsruher Institut für Technologie (KIT), Diss., 2011. URN: nbn:de:swb:90-249597 (page 46)

[163] Elder, F. R. ; Gurewitsch, A. M. ; Langmuir, R. V. ; Pollock, H. C.: Radiation from Electrons in a Synchrotron. In: *Phys. Rev.* 71 (1947), Jun, 829–830. DOI: 10.1103/PhysRev.71.829.5 (page 47)

[164] Dirac, P. A. M.: Classical theory of radiating electrons. In: *Proceedings of the Royal Society of London A: Mathematical, Physical and Engineering Sciences* 167 (1938), Nr. 929, 148–169. DOI: 10.1098/rspa.1938.0124. – ISSN 0080–4630 (page 47, 48)

[165] Johnson, Philip R. ; Hu, B. L.: Stochastic theory of relativistic particles moving in a quantum field: Scalar Abraham-Lorentz-Dirac-Langevin equation, radiation reaction, and vacuum fluctuations. In: *Phys. Rev. D* 65 (2002), Feb, 065015. DOI: 10.1103/PhysRevD.65.065015 (page 48)

[166] Yaghjian, Arthur D.: *Relativistic dynamics of a charged sphere: updating the Lorentz-Abraham model*. Bd. 11. Springer Science & Business Media, 1992. DOI: 10.1007/978-0-387-73967-0. – ISBN 978–0–387–73967–0 (page 48)

[167] Rohrlich, F.: The dynamics of a charged sphere and the electron. In: *American Journal of Physics* 65 (1997), Nr. 11, 1051-1056. DOI: 10.1119/1.18719 (page 48)

[168] Medina, Rodrigo: Radiation reaction of a classical quasi-rigid extended particle. In: *Journal of Physics A: Mathematical and General* 39 (2006), Nr. 14, 3801. DOI: 10.1088/0305-4470/39/14/021 (page 48)

[169] Heizmann, Johannes: *Modeling of inelastic electron-hydrogen scattering and of the energy loss function of 18.6 keV electrons for the KATRIN experiment*, Karlsruher Institut für Technologie (KIT), Bachelor Thesis, 2015 (page 52, 74)

[170] Harms, Fabian: *Characterization and Minimization of Background Processes in the KATRIN Main Spectrometer*, Karlsruher Institut für Technologie (KIT), Diss., 2015. URN: nbn:de:swb:90-500274 (page 52, 83, 85, 89, 90, 92, 93, 95, 96, 97, 98, 118, 123)

[171] Basunia, M. S.: Nuclear Data Sheets for A = 210. In: *Nuclear Data Sheets* 121 (2014), 561 - 694. DOI: https://doi.org/10.1016/j.nds.2014.09.004. – ISSN 0090–3752 (page 52)

[172] Chen, Mau H. ; Crasemann, Bernd ; Mark, Hans: Relativistic radiationless transition probabilities for atomic K-and L-shells / OREGON UNIV EUGENE DEPT OF PHYSICS. Version: 1979. `http://www.dtic.mil/docs/citations/ADA090894`. 1979. – Forschungsbericht (page 53)

[173] McGuire, Eugene J.: Atomic M-Shell Coster-Kronig, Auger, and Radiative Rates, and Fluorescence Yields for Ca-Th. In: *Phys. Rev. A* 5 (1972), Mar, 1043–1047. DOI: 10.1103/PhysRevA.5.1043 (page 53)

[174] Käfer, Wolfgang: *Sensitivity studies of the KATRIN experiment*, Karlsruher Institut für Technologie (KIT), Diss., 2012. URN: nbn:de:swb:90-260214 (page 56)

[175] Hannen, V. ; Heese, I. ; Weinheimer, C. ; Riis, A. S. ; Valerius, K.: Deconvolution of the energy loss function of the KATRIN experiment. In: *Astroparticle Physics* 89 (2017), 30 - 38. DOI: 10.1016/j.astropartphys.2017.01.010. – ISSN 0927–6505 (page 59, 60, 63, 64, 65, 66)

[176] Saenz, A. ; Froelich, P.: Effect of final-state interactions in allowed β decays. I. General formalism. In: *Physical Review C* 56 (1997), S. 2132–2161. DOI: 10.1103/PhysRevC.56.2132 (page 60)

[177] Saenz, A. ; Froelich, P.: Effect of final-state interactions in allowed β decays. II. Reliability of the β-decay spectrum for T_2. In: *Physical Review C* 56 (1997), S. 2162–2184. DOI: 10.1103/PhysRevC.56.2162 (page 60)

[178] Saenz, A. ; Jonsell, S. ; Froelich, P.: Improved Molecular Final-State Distribution of HeT^+ for the β-Decay Process of T_2. In: *Physical Review Letters* 84 (2000), S. 242–245. DOI: 10.1103/PhysRevLett.84.242 (page 60)

[179] Press, William H. ; Teukolsky, Saul A. ; Vetterling, William T. ; Flannery, Brian P.: *Numerical recipes 3rd edition: The art of scientific computing*. Cambridge university press, 2007. – ISBN 9780521880688 (page 65)

[180] Sleijpen, Gerard L. ; Fokkema, Diederik R.: BiCGstab (l) for linear equations involving unsymmetric matrices with complex spectrum. In: *Electronic Transactions on Numerical Analysis* 1 (1993), Nr. 11, 2000. `http://emis.ams.org/journals/ETNA/vol.1.1993/pp11-32.dir/pp11-32.html` (page 65)

[181] Oskooi, Ardavan F. ; Roundy, David ; Ibanescu, Mihai ; Bermel, Peter ; Joannopoulos, J.D. ; Johnson, Steven G.: Meep: A flexible free-software package for electromagnetic simulations by the FDTD method. In: *Computer Physics Communications* 181 (2010), Nr. 3, 687 - 702. DOI: 10.1016/j.cpc.2009.11.008. – ISSN 0010–4655 (page 65)

[182] Geiger, J.: Streuung von 25 keV-Elektronen an Gasen. In: *Zeitschrift für Physik* 181 (1964), Aug, Nr. 4, 413–425. DOI: 10.1007/BF01380873. – ISSN 0044–3328 (page 67, 77, 78, 79)

[183] Tawara, H. ; Itikawa, Y. ; Nishimura, H. ; Yoshino, M.: Cross Sections and Related Data for Electron Collisions with Hydrogen Molecules and Molecular Ions. In: *Journal of Physical and Chemical Reference Data* 19 (1990), Nr. 3, 617-636. DOI: 10.1063/1.555856 (page 67, 68)

[184] Schlösser, Magnus ; Seitz, Hendrik ; Rupp, Simone ; Herwig, Philipp ; Alecu, Catalin G. ; Sturm, Michael ; Bornschein, Beate: In-Line Calibration of Raman Systems for Analysis of Gas Mixtures of Hydrogen Isotopologues with Sub-Percent Accuracy. In: *Analytical Chemistry* 85 (2013), Nr. 5, 2739-2745. DOI: 10.1021/ac3032433. – PMID: 23320553 (page 67)

[185] Schlösser, M. ; James, T.M. ; Fischer, S. ; Lewis, R.J. ; Bornschein, B. ; Telle, H.H.: Evaluation method for Raman depolarization measurements including geometrical effects and polarization aberrations. In: *Journal of Raman Spectroscopy* 44 (2013), Nr. 3, 453–462. DOI: 10.1002/jrs.4201 (page 67)

[186] Aseev, VN ; Belesev, AI ; Berlev, AI ; Geraskin, EV ; Kazachenko, OV ; Kuznetsov, Yu E. ; Lobashev, VM ; Ostroumov, RP ; Titov, NA ; Zadorozhny, SV et al.: Energy loss of 18 keV electrons in gaseous T and quench condensed D films. In: *The European Physical Journal D - Atomic, Molecular, Optical and Plasma Physics* 10 (2000), Mar, Nr. 1, 39–52. DOI: 10.1007/s100530050525. – ISSN 1434–6079 (page 67, 69, 77, 78, 79)

[187] LxCat: *H2 cross sections extracted from PROGRAM MAGBOLTZ, VERSION 8.9.* `www.lxcat.net`, October 2017 (page 68, 73, 74, 75, 78)

[188] Liu, J. W.: Total Inelastic Cross Section for Collisions of H_2 with Fast Charged Particles. In: *Phys. Rev. A* 7 (1973), Jan, 103–109. DOI: 10.1103/PhysRevA.7.103 (page 68, 69, 70, 72, 77, 78)

[189] Liu, J. W.: Total cross sections for high-energy electron scattering by H_2 ($^1\Sigma_g^+$), N_2 ($^1\Sigma_g^+$), and O_2 ($^3\Sigma_g^-$). In: *Phys. Rev. A* 35 (1987), Jan, 591–597. DOI: 10.1103/PhysRevA.35.591 (page 69, 74, 75, 77, 78)

[190] Rudd, M. E.: Differential and total cross sections for ionization of helium and hydrogen by electrons. In: *Phys. Rev. A* 44 (1991), Aug, 1644–1652. DOI: 10.1103/PhysRevA.44.1644 (page 70, 72, 75, 77, 78, 153)

[191] Chantry, P. J.: Doppler Broadening in Beam Experiments. In: *The Journal of Chemical Physics* 55 (1971), Nr. 6, 2746-2759. DOI: 10.1063/1.1676489 (page 76)

[192] Read, F. H.: Doppler and other broadening effects in electron scattering experiments. In: *Journal of Physics B: Atomic and Molecular Physics* 8 (1975), Nr. 7, 1034. DOI: 10.1088/0022-3700/8/7/009 (page 76)

[193] Robertson, R.G.H. ; Knapp, D.A.: Direct Measurements of Neutrino Mass. In: *Annual Review of Nuclear and Particle Science* 38 (1988), Nr. 1, S. 185–215. DOI: 10.1146/annurev.ns.38.120188.001153 (page 76)

[194] Kraus, Marcel: *Energy-Scale Systematics at the KATRIN Main Spectrometer*, Karlsruher Institut für Technologie (KIT), Diss., 2016. DOI: 10.5445/IR/1000054447 (page 76)

[195] Erhard, Moritz G.: *Influence of the magnetic field on the transmission characteristics and the neutrino mass systematic of the KATRIN experiment*, Karlsruher Institut für Technologie (KIT), Diss., 2016. DOI: 10.5445/IR/1000065003 (page 85, 125, 126, 127)

[196] Fränkle, Florian M.: *Background Investigations of the KATRIN Pre-Spectrometer*, Karlsruher Institut für Technologie (KIT), Diss., 2010. URN: nbn:de:swb:90-193929 (page 92)

[197] Beck, M. ; Valerius, K. ; Bonn, J. ; Essig, K. ; Glück, F. ; Ortjohann, H.W. ; Ostrick, B. ; Otten, E.W. ; Thümmler, T. ; Zbořil, M. ; Weinheimer, C.: Effect of a sweeping conductive wire on electrons stored in a Penning-like trap between the KATRIN spectrometers. In: *The European Physical Journal A* 44 (2010), Nr. 3, S. 499–511. DOI: 10.1140/epja/i2010-10959-1 (page 92)

[198] Fränkle, F.M. ; Glück, F. ; Valerius, K. ; Bokeloh, K. ; Beglarian, A. ; Bonn, J. ; Bornschein, L. ; Drexlin, G. ; Habermehl, F. ; Leber, M.L. ; Osipowicz, A. ; Otten, E.W. ; Steidl, M. ; Thümmler, T. ; Weinheimer, C. ; Wilkerson, J.F. ; Wolf, J. ; Zadorozhny, S.V.: Penning discharge in the KATRIN pre-spectrometer. In: *Journal of Instrumentation* 9 (2014), Nr. 7, S. P07028. DOI: 10.1088/1748-0221/9/07/P07028 (page 92)

[199] Leiber, Benjamin: *Investigations of background due to secondary electron emission in the KATRIN-experiment*, Karlsruher Institut für Technologie (KIT), Diss., 2014. URN: nbn:de:swb:90-424154 (page 93)

[200] Linek, Johanna: *Investigation of the muon induced background at the KATRIN main spectrometer*, Karlsruher Institut für Technologie (KIT), Master Thesis, 2015. `http://www.katrin.kit.edu/publikationen/mth-Linek.pdf` (page 93)

[201] KATRIN Collaboration: *Gamma-induced backgrounds in the KATRIN Main Spectrometer*. 2018 (page 93)

[202] Ziegler, James F. ; Ziegler, M.D. ; Biersack, J.P.: SRIM – The stopping and range of ions in matter (2010). In: *Nuclear Instruments and Methods in Physics Research Section B: Beam Interactions with Materials and Atoms* 268 (2010), Nr. 11, 1818 - 1823. DOI: 10.1016/j.nimb.2010.02.091. – ISSN 0168–583X. – 19th International Conference on Ion Beam Analysis (page 95, 96)

[203] Weg, W.F. van d. ; Rol, P.K.: On the excited state of sputtered particles. In: *Nuclear Instruments and Methods* 38 (1965), 274 - 276. DOI: 10.1016/0029-554X(65)90154-0. – ISSN 0029–554X (page 95, 102)

[204] Müller, Axel: *Investigation of the secondary electron emission characteristics of the KATRIN main spectrometer*, Karlsruher Institut für Technologie (KIT), Diploma Thesis, 2016. `https://www.katrin.kit.edu/publikationen/mth_mueller_axel.pdf` (page 96)

[205] Wikimedia: *Uranium decay chain*. `https://commons.wikimedia.org/wiki/File:Decay_chain(4n+2,_Uranium_series).svg`. Version: 2008 (page 97)

[206] J., Kerber S. ; John, Tverberg: Stainless steel : Surface analysis. In: *Advanced materials and processes* 158 (2000), Nr. 5, 33–36. `http://www.refdoc.fr/Detailnotice?idarticle=11095987`. – ISSN 0882–7958. – eng (page 98)

[207] *Kapitel* 3. In: Yu, Ming L.: *Charged and excited states of sputtered atoms*. Berlin, Heidelberg : Springer Berlin Heidelberg, 1991. – ISBN 978–3–540–46881–3, S. 91–160. – DOI: 10.1007/3540534288_17 (page 100)

[208] Rao, G. N. ; Govindarajan, J. ; Reddy, M. N.: Optogalvanic spectroscopy of sputtered atoms. In: *Hyperfine Interactions* 38 (1987), Dec, Nr. 1, 539–552. DOI: 10.1007/BF02394860. – ISSN 1572–9540 (page 100)

[209] Berthold, W. ; Wucher, A.: Energy- and angle-dependent excitation probability of sputtered metastable silver atoms. In: *Phys. Rev. B* 56 (1997), Aug, 4251–4260. DOI: 10.1103/PhysRevB.56.4251 (page 100)

[210] Gallagher, Thomas F.: *Rydberg atoms*. Bd. 3. Cambridge University Press, 2005. – ISBN 9780521021661 (page 101, 111, 113)

[211] Einstein, Albert ; Ehrenfest, Paul: Zur Quantentheorie des Strahlungsgleichgewichts. In: *Zeitschrift für Physik* 19 (1923), Dec, Nr. 1, 301–306. DOI: 10.1007/BF01327565. – ISSN 0044–3328 (page 101)

[212] Bethe, Hans A. ; Salpeter, Edwin E.: *Quantum mechanics of one-and two-electron atoms*. Springer Science & Business Media, 2012. DOI: 10.1007/978-3-662-12869-5. – ISBN 978–3–662–12869–5 (page 101, 113)

[213] Gordon, Walter: Zur Berechnung der Matrizen beim Wasserstoffatom. In: *Annalen der Physik* 394 (1929), Nr. 8, 1031-1056. DOI: 10.1002/andp.19293940807 (page 106, 110)

[214] Hoang-Binh, D.: A program to compute exact hydrogenic radial integrals, oscillator strengths, and Einstein coefficients, for principal quantum numbers up to $n \approx 1000$. In: *Computer Physics Communications* 166 (2005), Nr. 3, S. 191 – 196. DOI: 10.1016/j.cpc.2004.11.005. – ISSN 0010–4655 (page 106)

[215] Marxer, Hermann ; Spruch, Larry: Semiclassical estimation of the radiative mean lifetimes of hydrogenlike states. In: *Phys. Rev. A* 43 (1991), Feb, 1268–1274. DOI: 10.1103/PhysRevA.43.1268 (page 107)

[216] Burgess, A: Tables of hydrogenic photoionization cross-sections and recombination coefficients. In: *Memoirs of the Royal Astronomical Society* 69 (1965), 1. `http://adsabs.harvard.edu/full/1965MmRAS..69....1B` (page 110)

[217] Lanczos, Cornel: Zur Intensitätsschwächung der Spektrallinien in hohen elektrischen Feldern. In: *Zeitschrift für Physik* 68 (1931), Mar, Nr. 3, 204–232. DOI: 10.1007/BF01390967. – ISSN 0044–3328 (page 111)

[218] Dierckx, Paul: *Curve and surface fitting with splines*. Oxford University Press, 1995. – ISBN 9780198534402 (page 116)

[219] Behrens, J. ; Ranitzsch, P. C.-O. ; Beck, M. ; Beglarian, A. ; Erhard, M. ; Groh, S. ; Hannen, V. ; Kraus, M. ; Ortjohann, H.-W. ; Rest, O. ; Schlösser, K. ; Thümmler, T. ; Valerius, K. ; Wierman, K. ; Wilkerson, J. F. ; Winzen, D. ; Zacher, M. ; Weinheimer, C.: A pulsed, mono-energetic and angular-selective UV photo-electron source for the commissioning of the KATRIN experiment. In: *The European Physical Journal C* 77 (2017), Jun, Nr. 6, 410. DOI: 10.1140/epjc/s10052-017-4972-9. – ISSN 1434–6052 (page 119)

[220] Schwarz, Johannes S.: *The Detector System of the KATRIN Experiment - Implementation and First Measurements with the Spectrometer*, Karlsruher Institut für Technologie (KIT), Diss., 2014. URN: nbn:de:swb:90-427724 (page 123, 128)

[221] Brodbeck, R.M. ; Schommer, G.R.: Radioactive decontamination of metals by electropolishing / Mound Laboratory, Monsanto Chemical Company. Version: 1 1949. DOI: 10.2172/115570. University of North Texas Libraries, 1 1949 (1). – Forschungsbericht. – OSTI as DE96001528 (page 125)

[222] Pollithy, Anna: *KATRIN Background Characterization*. DOI: 10.5281/zenodo.1300813. Version: Juni 2018 (page 128)

Danksagung

Zuguterletzt ist es mir ein wichtiges Anliegen mich bei allen zu bedanken die mich während meiner Promotion privat wie auch kollegial unterstützt haben. Dies gilt selbstredend für die gesamte KATRIN Kollaboration aber auch insbesondere

- Prof. Dr. Guido Drexlin für die Möglichkeit der Promotion und das unentwegte Vorantreiben der Rydbergthematik
- Prof. Dr. Ullrich Husemann für die Übernahme des Korefferats
- Dr. Kathrin Valerius für ihr nachhaltiges Interesse an der Modellierung der Elektronenstreuung und die Korrekturen.
- Dr. Ferenc Glück für die vielen fachlichen Diskussionen und die Korrekturen.
- Dr. Stefan Groh und Dr. Marco Kleesiek für die Einführung in Kassiopeia und Hilfe bei der Zähmung widerspenstigen C++ codes.
- Dr. Florian Fränkle, Dr. Fabian Harms, Dr. Moritz Erhard und Dr. Marcel Kraus für die gemeinsame Bewältigung der Messphasen.
- Dr. Florian Fränkle, Dr. Jan Behrens und Florian Heizmann für den Einsatz bei der gemeinsamen Administration des Rechenclusters für die Arbeitsgruppe.
- Dr. Moritz Hackenjos für den Einsatz bei den FirstLight Messungen und ein offenes Ohr.

Ferner gilt mein Dank meiner Mutter Susanne Trost, meinem Bruder Hans Trost und ganz besonders meiner Partnerin Martina Meiritz die mich immer und unter zum Teil großer Anstrengung unterstützt haben, insbesondere in der schwierigen Schreibphase über die Geburt unseres Sohnes Fridolin und den Tod meines Vaters Dr. Med. Christian Trost hinweg. Seiner Ermunterung verdanke ich unzweifelhaft die Neugier und das Interesse an Naturwissenschaften die mich letztlich zu dieser Arbeit gebracht haben, weshalb ich sie ihm an dieser Stelle widmen möchte.